12-15-2014

Theoretical Investigation of the Catalytic, Liquid-Phase Hydrodeoxygenation of Organic Acids and Esters

Sina Behtash
University of South Carolina - Columbia

THEORETICAL INVESTIGATION OF THE CATALYTIC, LIQUID-PHASE HYDRODEOXYGENATION OF ORGANIC ACIDS AND ESTERS

by

Sina Behtash

Bachelor of Science
Sharif University of Technology, 2009

Submitted in Partial Fulfillment of the Requirements

For the Degree of Doctor of Philosophy in

Chemical Engineering

College of Engineering and Computing

University of South Carolina

2014

Accepted by:

Andreas Heyden, Major Professor

John R. Monnier, Committee Member

Christopher T. Williams, Committee Member

John R. Regalbuto, Committee Member

Mark A. Berg, Committee Member

John W. Weidner, Committee Member

Lacy Ford, Vice Provost and Dean of Graduate Studies

DEDICATION

To my wife, April, for her unconditional love and support.

تقدیم به مادرم که همیشه برای من الگوی از خود گذشتگی، ایمان، صداقت و سخت کوشیدن است.

به پدرم برای حمایت‌هایش و خواهرانم برای محبت هایشان.

ACKNOWLEDGEMENTS

First and foremost, I would like to express my deepest appreciation for my adviser, Dr. Andreas Heyden for the opportunity to work with him. His knowledge, enthusiasm, passion, integrity, encouragement, and unfailing accessibility to discuss research, provided a creative and productive environment and enabled me to accomplish my Ph.D.

I would like to thank my committee members, Dr. Monnier, Dr. Williams, Dr. Rgalbuto, Dr. Berg, and Dr. Weidner for their guidance, time, and help.

Next, I would like to thank Dr. Jianmin Lu, and Dr. Yuliana Lugo-Jose who contributed to my thesis with their research work.

I would like to also thank the Chemical Engineering Department staff including: Marcia Rowen, Loretta L. Hardcastle, Vernon Dorrell, Kay P. Dorrell, Brian Loggans, Carol Stork, and Sandra Knotts. Thank you for assisting me with technical and administrative issues.

Finally, many thanks to my friends and colleagues at the University of South Carolina, specifically: Saeedreza Abbaspour, Lutfi Erden, Danial Barati, Kumud Kanneganti, Shuo Cao, Osman Mamun, Eric Walker, Mohammad Saleheen, Yuliana Lugo-Jose, Abraham Rodriguez, Jose Contreras, and Verionica Rodriguez-Rivera.

ABSTRACT

With worldwide fossil fuel resources dwindling and greenhouse gas emissions rising, it is urgent to find renewable liquid fuel alternatives from e.g. biomass to meet the world's growing energy demand. Lipid feedstocks and pyrolysis oils from woody biomass can be utilized for the production of second-generation biofuels via a catalytic hydrodeoxygenation (HDO) process. The conversion of fatty acids and esters plays an important role in the activity and selectivity of these processes. Understanding the HDO reaction mechanism of organic acids and esters on metal surfaces is a prerequisite for the rational design of new HDO catalysts specifically designed for upgrading pyrolysis oils or lipid feedstocks.

We theoretically studied the HDO of propionic acid and methyl propionate, our model acid and ester molecules, on flat and step metal surfaces in the absence and presence of solvents. Our theoretical results suggest that the activity of palladium flat and step surfaces are very similar under typical reaction conditions. Decarbonylation was identified to be the dominant mechanism, and in our sensitivity analysis, CH_3CH_2CO-OH bond dissociation as well as dehydrogenation of the α-carbon were found to be the most rate-controlling steps in all reaction media. Finally, with the help of an experimental kinetic isotope study on propionic acid, we confirmed the results of our sensitivity analysis.

TABLE OF CONTENTS

LIST OF TABLES

LIST OF FIGURES

CHAPTER 1

INTRODUCTIONS

1.1 OVERVIEW

Developments in society, major changes in agriculture, manufacturing, mining, transportation and technology, have had a profound effect on economic conditions in recent centuries. By changing from a labor and animal based economy to machine and industrial based economy, energy demand has increased dramatically. Fossil fuel fueled the industrial revolution and formed the foundation of modern industrial economies; however, the slow rate of the fossil fuels regeneration cycle makes them non-renewable recourses. Fossil fuel recourses such as coal, petroleum, and natural gas, take millions of years to be formed, and over the recent centuries, they have been consumed at a rate that is orders of magnitude higher than their natural regeneration cycle [1, 2].

Recent statistical energy reviews indicate that most of the countries in the world are strongly dependent on fossil fuels. Fossil fuels supplied 83 % of the total energy of the United States[2, 3] and almost 80 percent of energy produced in the European Union in different energy sectors[2, 4]. For example in the US, Petroleum provides 94 percent of transportation, 40 percent of Industrial, 18% of residential and 1 percent of electric power sector [5].

According to the increase in consumption rate of fossil fuels, it is obvious that the dependency of the world on fossil fuel resources increases every year. Last year, the

world oil consumption rate grew by 2.7%, also, natural gas consumption increased by 7.4%, which is the most rapid increase since 1984 [6].

Continuous and rapid over exploitation of fossil fuels brings up serious concerns about the depletion of fossil fuel resources. The reserve-to-production ratio (R/P), which indicates the remaining amount of non-renewable energy recourses, has dropped at a dramatic rate over the last 3 decades all around the world[6].

R/P ratios by region are shown in Figure 1.1, 1.2 and 1.3 for oil, natural gas and coal resources.

Currently available world reserves of fossil fuel resources are sufficient to meet 46.2 years for oil, 58.6 years for natural gas and 118 years for global coal production [6]. Research continues to be concentrated on depletion of oil and other resources. A group of scientists are pessimistic and claim an imminent peak at 2020 and subsequent terminal decline in the global production of conventional oil[7]. On the other side, optimists believe that liquid fuels production is sufficient to meet global demand in the 21st century[7]; however, it is imminent that fossil fuels will continue to diminish as time progresses.

Next, cogeneration of CO_2 in stoichiometric ratio to carbon used in fossil fuels is another main societal concern. Carbon dioxide is a greenhouse gas. Greenhouse gases are those that can absorb and emit radiation within the thermal infrared light. High concentration of greenhouse gases in the atmosphere can cause the greenhouse effect. The greenhouse effect is a process by which thermal radiation from a planetary surface is absorbed by atmospheric greenhouse gases, and is re-radiated in all directions. Since part of this re-radiation is back towards the surface, energy is transferred to the surface and

the lower atmosphere. As a result, it can alter the energy of the climate system and consequently, rises the average temperature of earth which is known as global warming[1, 8, 9].

As a result of the rapid growth in the usage of fossil fuels, CO_2 emissions have exponentially increased in the last century. The accumulated global CO_2 emissions from fossil resources have grown by 600 % from 1925 to 2000 [1]. Consequently, the global average temperature has increased over the last century and scientists believe that most of the observed increase in global average temperature is due to increases in greenhouse gas concentration produced from human activities.[1, 9]

Fig 1.4 shows observed continental and global changes in surface temperature for the period 1906-2005.

Global warming is likely one of the most dangerous threats that human will face in the future. Effects of global warming are difficult to completely predict because of the complexity of the climate. However it is known that it will have a large effect on water, resources, food supplies, economy and health.

Environmental impacts of fossil fuel utilization not only can affect the atmosphere and temperature but also, the water recourses all around the globe. Oil may accidently release to the environment especially in marine areas, from tankers, offshore platforms, drilling rigs and wells due to human activities. Oil can poison the animals and sea bird bodies and damage the wildlife species. Oil spill disasters change the ecosystem of marine and coastal areas and the cost of the consequent effects on the environment is very large. One of the worst recent oil spills in the world is the Gulf of Mexico disaster in

2010. Most recent data show that approximately 6,000 sea turtles, 26,000 dolphins and whales, 82,000 birds, and countless fish and invertebrates may have been harmed.[10]

Fig1.5 gives an idea that how much oil was released in the Gulf of Mexico.

Concerns about non-renewable resources are not limited to availability and environmental issues. Considering that fossil fuels are not equally distributed in the world and also, the high dependency of the US and Europe on fossil fuels, clearly shows the importance of fossil fuels in the stability and political situation of the world.

According to concerns and issues mentioned above, it is clear that society needs new sources of energy. New alternative energy resources need to be renewable and eco-friendly. Equally important, efficient production of new potential resources should be technologically possible and economically viable.

The most reliable candidates for alternative energy resources are: Solar, hydro, wind, geothermal and biomass[1, 11]. The amount of renewable energy resources on earth is much more than fossil resources but there are facts that limit the large exploitation of these resources. The availability of these resources is limited to location, seasonal and climate changes. For example, cloudy days reduce solar power and calm days reduce wind power. Also, these resources might be located in remote areas like a desert. Next, the lack of a cheap technology required for production, conversion, storage and transportation is the current challenge in utilization of renewable resources. Research continues to achieve a sustainable and efficient production of renewable resources.

Among those potential alternative sources mentioned above, solar energy and biomass have received significant attention in recent years and it is expected that we will see the dominance of biomass as a renewable energy resource[1, 11].

Biomass is organic material made from plants and animals. All water and land-based organisms, vegetation, trees, algae, municipal solid waste, animal waste, sewage, forestry and agricultural residues are biomass resources[12]. Energy stored in biomass comes from carbohydrates from the photosynthesis reaction which is of the same origin as fossil fuels. Consequently, biomass is more compatible with existing conversion technology in comparison to other renewable resources [13, 14]. Existing facilities can convert biomass to fuel with small adaption costs which is of key importance for the growth of biomass utilization.

Biomass resources include different types of chemical compounds including oxygenated lipids and different types of carbohydrates such as sugars and lignocelluloses. Food crops such as sugar cane and corn grains constitute the first generation of biomass feed stock. Fermentation of sugars to ethanol by microorganism was the first bioprocess to make biofuels. Later, another biofuel was produced by tranesterification of vegetable oil and animal fats with methanol to long chain alkyl esters, which is called biodiesel. Ethanol and biodiesel implemented successfully in the energy system. The U.S. Annual energy review report 2011 shows that the biodiesel and ethanol share is 23 % of the total renewable energy consumption[5]. Recent data show that ethanol production has increased from 331 to 1.22 Trillion BTU in the period of 2005-2010 [5]. Also, the international energy outlook predicts the growth of ethanol production [15]; however, first generation biofuels are not ideal alternatives for fossil fuels because of compatibility issues and expensive sourcing. That is why they have been mostly used as a blend with hydrocarbon fuels[2, 16, 17].

Utilization of corn and sugar cane biomass for large scale production can increase the price of these edible sources due to competition with food and land. Also, biodiesel production from vegetable oils derived from food sources is limited by the expensive price of vegetable oils. This is one of the reasons for a decrease in biodiesel production in the last 2-3 years[5, 18, 19].

The oxygenated structure of ethanol and biodiesel makes them much more miscible in water in comparison to hydrocarbon fuels which can cause serious damage to the vehicle engine. Next, ethanol can cause corrosion to some metals. So compatibility of first generation fuels with the infrastructure is not complete and large scale utilization of ethanol in the transportation system needs an expensive modification in many parts such as vehicle engines, pipe lines, and storage tanks [2, 16, 17].

Regardless of the compatibility problem with current infrastructure, the energy density of biodiesel and ethanol is less than that of fossil fuels. The energy density of biomass is on average 15-20 $MJkg^{-1}$ which is considerably lower than crude oil (42 $MJkg^{-1}$)[20].

Issues in large scale utilization of first generation biofuels have driven researchers to develop technologies to convert non-edible and inexpensive biomass resources to biofuels that are more similar to liquid hydrocarbon fuels[21].

Lignocelluloses and non-edible oils have received attention recently and research continues to develop processes to convert them to ethanol and green fuels (e.g. green gasoline and green diesel) so called second generation biofuels. Green fuels are often chemically identical to current hydrocarbon fuels[21].

Lignocelluloses resources are cheap and abundant in comparison to edible resources[22]. Agricultural residues, wood and municipal paper wastes are available, and mostly composed of cellulose, hemicelluloses and lignin[1].

Fats and oils contain a glycerol molecule bonded to three fatty acid chains. This structure is called triglyceride[1, 23]. Biodiesel and green fuel can be made from any oil lipid resource (edible and non-edible)[24]. Most used sources of edible vegetable oils are: Canola, soybean, palm, sunflower seeds, corn, peanut, coconut, and safflower. Also microalgae oil, Jatropha Curcas, Pongamia Pinnata, Neem oil and Castor oils are non-edible biomass sources [25-28]. Among all the edible and non-edible sources, algae offer great promise due to high oil yield per acre of cultivation. (1000-6500 gallons/acre/year compared to 48 for soybean and 102 for sunflower); however, a commercially viable system and technology has not yet immerged, but academia and industry are increasing their focus on algal biofuels research [29-33].

Different thermal, biological, and catalytic processes for utilization of lignocelluloses, sugars and vegetable oil, have been developed over the recent years. There are four main types of processes: microbial processing, liquid phase processing, pyrolysis, and gasification [1, 2, 22]. Fig. 1.6 shows the typical routes for conversion of biomass into liquid hydrocarbon fuels.

Gasification of biomass to syngas (H_2/CO) at high temperature (1100-1500 K), followed by the Fischer-Tropsch process of syngas can convert lignocellulosic biomass to different sized hydrocarbons[1, 2, 34].

Also, lingnocellulosic biomass can be treated at temperatures of 648-800 K under different processing condition to dehydrate, depolymerize and break the C-C bond

to form a bio-oil. Bio-oil is highly oxygenated and includes, organic acids, esters, aldehydes, alcohols, ketones and aromatics. Bio-oil needs another upgrading process to remove oxygen which is often a liquid-phase hydrodeoxygenation process[1, 35-37].

Gasification and F-T are highly sensitive to impurities and might produce contaminants and toxics in the outlet stream[38, 39]. In contrast, liquid phase routes are catalytic reactions at mild reaction conditions which allow for better control of conversion and selectivity.

Due to the importance of mild reaction conditions for low cost production, aqueous-phase processing has recently received attention. Aqueous-phase processing of biomass derivatives includes different types of catalytic reactions. Different pathways are discovered and they are named by the intermediates produced during the process. After dehydration of aqueous sugars, it is possible to produce levulinic acid, γ-valerolactone, and hydroxymethylfulfural via catalytic reactions over different metal and metal oxide catalysts. All of these intermediates can be converted to fuels by different catalytic reactions [40-46].

Fig.1.7 shows the different routes of aqueous phase processing of biomass into liquid hydrocarbon fuels.

Lignocellulosic resources are the main focus in biomass research due to availability and the low price; however, complexity of lignocellulosic biomass feedstock is a barrier in large scale utilization. Various types of reactions such as hydrolysis, gasification, pyrolysis and upgrading are required to convert the raw material to the desired hydrocarbons. While the lipids have simple structures such as triglyceride, fatty acids and esters, which do not need pre-treatment[1, 2, 22]

As research on production of algae is making progress, the dream of having cheap lipid feed stock is coming true. It is expected that algae, waste oil and plant oil will produce a significant fraction of biofuels in the future[29-33].

Current technology and science for lipid treatment is mostly dedicated to transesterification. Transesterification of vegetable oils with ethanol and methanol has been widely studied and has been successfully implemented in bio-refineries to produce bio-diesel. While, the transesterifaction process has been widely implemented, it needs important improvements such as: increasing thermal stability, avoiding soap formation, enhancement of mass transfer, milder operation conditions, decreasing the waste stream and lowering the cost. Also, in addition to these difficulties, there are several issues in compatibility of fatty acid methyl esters (FAMEs) used in diesel due to low stability and corrosion problems[47-51].

Also, regardless of reaction condition and limitations, biodiesel as the main product of the transesterification process, has many unfavorable properties such as bad thermal, oxidation, and storage stability because of double bonds, sensibility to hydrolysis because of the ester bond, bad cold properties, etc[47-51].

The above mentioned limitations, are the reason that alternative routes for lipid treatment have become an area of interest. Recently, a promising liquid phase processing route has been developed to upgrade aqueous glycerol obtained from transesterification, to liquid hydrocarbon fuels (it is shown in Fig. 1.7)[52]. In this respect glycerol will convert to syngas through aqueous phase reformation. This reaction can produce syngas at low temperature. Integration of this reaction with Fischer-Tropsch can

produce liquid hydrocarbons [2, 52]; however, this process still suffers from transesterification difficulties.

Other than transesterification, lipid based biomass can be treated in aqueous phase which is known as hydroprocessing. Hydroprocessing is a series of reactions such as, hydrogenation, hydrogenolysis, deoxygenation, desulfurization and denitrogeneration which uses high pressure hydrogen to remove S, O, and N heteroatoms of the feedstock[47, 53, 54].

Hydrodeoxygenation(HDO) is an example of hydroprocessing with the ultimate goal to eliminate all oxygen atoms from the feedstock molecules at moderate reaction conditions while minimizing bi-products and waste[47].

Since the oxygen in petroleum is typically less than 3000 ppmw, traditionally less attention has been paid to HDO compared to hydrodesulfurization and hydrodenitrogenation in the petroleum industry[55]. However, this process is very critical in hydroprocessing of biomass since a neat biomass feed stock may contain up to 500,000 ppmw oxygen with minimal amount of sulfur[55].

In contrast to transesterification, liquid phase processing can be operated at milder reaction conditions. Also, it has the potential to produce fuels that are identical to gasoline. From an environmental point of view, this process releases less greenhouse gases per energy equivalent in comparison to the transesterification process or in other word, it is more eco-friendly. Consequently, HDO can be one of the candidate routes to convert triglyceride based feeds to liquid hydrocarbons[56, 57].

In addition, developments in science and technology of HDO can be useful for various parts of a future bio-refinery because applications of this process are not limited

to lipids and triglycerides based feed stocks. It can also be used in lignocellulosic biomass refineries, to upgrade the bio-oil obtained from pyrolysis or even as an extra process after transesterification to convert the bio-diesel to Green diesel [2, 47, 58].

Currently, triglyceride based biomass feed stocks can be hydroprocessed in the presence ("co-processing") or absence ("stand-alone") of petroleum fractions [47, 54, 55, 59]. Both processes need large amounts of hydrogen and reduction of hydrogen consumption is one of the challenges in this area. Stand-alone mode offers the advantage of high process flexibility while, from an economic point of view, co-processing seems to be more reasonable due to the existence of petroleum refinery units. However the sulfur content of the final product, effect of water and carbon oxides on the catalyst life time and separation of carbon oxides from the recycle gas are the main issues that have to be dealt with [54, 59]. As a result, there is an apparent need for new catalytic processes for this new industry.

In this respect, as most of the oxygen containing species of vegetable oils and triglyceride, have high reactivity, attention should be paid to achieve high product selectivity with the least consumption of hydrogen. A correct understanding of the reaction mechanisms and pathways of the hydrodeoxygenation can help to develop catalysts which can target the rate limiting steps and overcome the barriers to decrease the hydrogen consumption and facilitate this process.

Three different pathways have been proposed for HDO: hydrogenation, decarboxylation, and decarbonylation. HDO research continues and scientists have studied effects of different reaction conditions, feed stock composition, catalyst and support on activity of reactants and selectivity of products. However, there is not enough

knowledge about the details of the pathways and it is clear that more theoretical and experimental research are needed in this area in order to develop a reasonable HDO process which can be used at an industry scale.

It is believed that a systematic computational and theoretical investigation of the HDO mechanism of fatty acids and esters, which are the main compounds of a triglyceride feed stocks, permits the identification of descriptors that determine the:
(a) HDO activity and (b) the selectivity of different possible pathways. Reaction pathways and important descriptors of activity and selectivity will let us to develop a new selective low-cost HDO process which has the potential to be used in industry to transform the renewable triglyceride based feed stock to hydrocarbon fuels.

This study has mainly focused on the computational investigation of the hydrodeoxygenation of acids and esters over Palladium. The hypothesis is that results of the Pd pathways are applicable to other noble metals and bimetallics similar to Pd. Also, methyl propionate and propanoic acid were purposely chosen as model molecules. A study of smaller molecules is obviously more convenient but we decided not to choose a model molecule smaller than three and four carbon atoms, since the effects of a beta carbon on C-O and C-C cleavages were unknown. So the smallest molecules which have two carbon atoms (alpha and beta carbons) next to carbonyl function, Methyl propionate and Propionic acid, were selected. Fig 1.8 shows our model molecules.

To summarize, the objectives and tasks of this study are:

- Theoretical investigation of the reaction mechanisms and key reaction intermediates of the HDO of propionic acid and methyl propionate on Pd.

- Identification of activity and selectivity descriptors for the decarboxylation, decarbonylation and hydrogenation/dehydration of organic acids and esters.
- Investigation of the effect of surface structure on the activity and selectivity
- Identification of the effect of a liquid solvent on activity and selectivity descriptors.

1.2 CURRENT STATE OF KNOWLEDGE

Hydrodeoxygenation reactions of fatty acids and esters have been studied widely, and investigations have focused on the effects of temperature, pressure, catalysts and supports on conversion and selectivity of the HDO. However, a promising HDO process has not yet been developed. Recently, with development of ever faster computers, chemists and chemical engineers have been able to investigate every single elementary reaction in a network of reactions involved in a complex chemical process. Computational studies allow the researchers to understand the fundamental science behind, e.g., the HDO to develop and design new and reliable catalysts for utilization of biomass. In the following section, the current science and knowledge of the HDO for triglyceride based feed stocks will be discussed.

The simplest example of methyl esters is methyl formate ($C_2H_4O_2$). This molecule has been widely investigated in the 70s and 80s. Different reactions and catalysts have been proposed for activation of this molecule toward deoxygenation processes. Methyl formate can decomposed and undergo different decomposition pathways [60, 61] which release different amounts of CO, CO_2, methane and methanol. The best catalyst to deoxygenate methyl formate is reported to be Ru based catalysts at 180-230^{o}C. It has also

been shown that methyl formate can easily convert to acid, aldehydes, and alchohols which again can decompose to CO and CO_2 [60]. This result is consistent with Murzin et al., who report that ethyl stearate mainly converts to acids[62]. This study shows that aldehydes and alchohols are the most likely intermediates in the HDO process. Formation and stability of these intermediates determines the dominancy of different pathways involved the hydrodeoxygenation pathways. The HDO process can be operated under different reaction conditions and over different catalysts such as, transition metals and bimetallic and also different supports, so multiple studies have specifically focused on effects of all of these parameters in activity and selectivity of the HDO process. The most recent studies in this area will be discussed in the following sections starting, with supported noble metal followed by bimetallic catalysts.

Murzin et al. widely studied the decarboxylation and decarbonylation of different fatty acids and esters[62-66]. Activity and selectivity of steric acid and ethyl stearate over Pd/C catalysts for the production of linear hydrocarbons has been one of the focuses of the Murzin studies. The effects of support, acidity and reaction atmosphere have also been studied. The highest yields of n-heptadecane (97%) were obtained for the decarboxylation of steric acid over Pd/C at 300^{o}C under a helium atmosphere in a batch reactor. While ethyl stearate showed less conversion and selectivity towards linear hydrocarbons due to the conversion of ethyl stearate to steric acid. They conclude that, depending on the atmosphere, there are different reaction pathways for catalytic transformation of ethyl stearate and steric acid illustrated in figure 1.9. As is shown, ethyl stearate can convert to stearic acid or n-heptadecane, ethylene and CO_2 or n-heptadecane, ethanol and CO[62].

Another study by Lestari and Murzin reports 95% and 98% conversion of stearic acid and palmetic acid (C16 and C18) to aliphatic hydrocarbons containing one carbon less than the corresponding acids at 17 bar of 5 % H_2 in argon and 300^{o}C over 4% Pd/C. They also report that the reaction rates of different fatty acids were independent of the fatty acid length[67].

Other than saturated acids and esters, Snare and Murzin also investigated unsaturated renewables like oleic acid, linoleic acid and methyl oleate over 5% Pd/C. Reactions were carried out at constant pressure and temperature in the following domain, 15-17 bar and 300-360^{o}C , respectively[65]. Conversion of Linoleic acid to Oleic, elaidic and stearic acid can produce heptadecane. Another possible mechanism involves formation of cis and trans Vaccenic acid to produce heptadecane. The main product of both mechanisms was n-heptadecane but minor amounts of unsaturated isomers, C17 aromatic and heavy oxygenate products have been detected as well. Figure 1.10 shows the mechanism proposed for oleic and linoleic acids.

Resasco and co-workers investigated deoxygenation of methyl octanoate and methyl stearate over Pt on Al_2O_3 and TiO_2 supports. They report that the conversion of both methyl esters results in hydrocarbons with one carbon less than the fatty acid of the corresponding ester as the main products. The most interesting result in this study is the observation of ketonization reaction and formation of heavy oxygenates. With 97.8 % conversion of pure methyl octanoate at T=603 K an d p =101 kPa, the products were distributed as: 89.5% of C7, 5% of C8, 0.2 % of octanol and octanal, and 1 % of octanoic acid. They conclude that the formation of C7 products comes from direct decarboxylation

and decarbonylations of esters and acids, and alchohol and C8 produced comes from direct C-O hydrogenolysis of alchohol and aldehydes[68].

Fig.1.11 shows the proposed process for methyl octanoate.

To achieve maximum conversion of C7 and C8 which are the desired hydrocarbons, the condensation of the intermediate and production of heavy oxygenates should be minimized. Heavy ketone is formed via the interaction of two adjacent carboxylate species on the surface[68, 69]. Ketonization reactions are favored only under a hydrogen-deficient environment. That's why the yield of ketones and heavy oxygenates over Pt/Al_2O_3 decreases in presence of hydrogen[68]. Also, since none of the hydrogenated ketones and secondary alcohols have been found, the heavy hydrocarbons have likely been formed via hydrogenolysis of the C-O bond. In this context, Barteau et al. also observed propane, obtained by hydrogenolysis of acetone over Pd/CeO_2 and Co/CeO_2 catalysts [70].

In addition, support materials can significantly change the functionality of the noble metal. For example the study of methyl octanoate on Pt/TiO_2 shows less selectivity toward C8 and higher yields of heavy oxygenates in comparison to Pt/Al_2O_3. It is hypothesized that the reason for this behavior is related to spilled-over hydrogen effects. In this case, some hydrogen atoms diffuse to some of the support materials and reduce the oxide support. As a result the availability of hydrogen decreases and the rate of ketonization and formation of heavy oxygenates increases[70].

Finally in another study of Rassaco et. al, on Pt, Pd, and Cu catalysts over silica support, it is reported that Pt was the most active for hydrogenation of the C=C bond at

473 K However, Cu was a good catalyst for oxygen removal by hydrogenation of the C=O bond[71].

Kubica et al. mainly studied Co/Mo and Ni/Mo bimetallics over different supports such as Al_2O_3 and silica in different sizes and shapes [59, 72-76]. In one of the studies by Kubric et al[59], deoxygenation of triglyceride (rape seed) over organized mesoporous-alumina-supported CoMo and MCM-41 supported CoMo have been considered. The alumina supported catalysts have shown better performance than the silica supported one with respect to conversion and selectivity. Selective conversion was achieved at 310^oC and 7 MPa. Main products were hydrocarbons with a different number of carbons (C17 and C18). The number of carbons in the products is related to the reaction pathways. Since they barely saw carbon monoxide in the products and since the origin of the produced CO could not be identified, they could not rule out or confirm the decarbonylation pathways. In addition, it is interesting that undesirable aromatic or other hydrocarbon products were not formed over both alumina and silica Co/Mo supported catalysts. Figure 2.3 shows the suggested reaction mechanism.

In another study of this group[72], Ni/Mo over alumina were compared to Ni and Mo monometallics over Al_2O_3. The experiment was performed at 260-280 ^oC and 3.5 MPa in a fixed bed reactor. The activity of the catalyst decreased in the order NiMo/ Al_2O_3 > Mo/ Al_2O_3 > Al_2O_3. C17 and and C18 were again the main products and a reaction mechanism similar to Fig. 1.12 was proposed.

In addition to common sulfided bimetallics, Ru-Sn has shown promising activity toward hydrogenation of fatty acids and ester. Ferrero et al [77] in the early 90s studied the reduction of carboxylic acids over alumina supported Sn-Ru and they claimed that

hydrogenation to aldehydes on Sn-Ru occurs at 513 K which is lower than the common hydrogenation temperature on Ni-Mo(573-673).

Tahara et al. [78-80] studied the hydrogenation of methyl laurate, methyl oleate, methyl cyclohexane-carboxylate, methyl iso-butylate and methyl benzoate over alumina supported Sn-Ru. Methyl oleate and methyl laurate showed high activity toward hydrogenation of the C=O group; however, the main products were alcohol with a selectivity of 96% and 98%, respectively. Moreover, alumina was the most effective support for Sn-Ru compared to silica-alumina, zirconia, magnesia and titania(MC-90).

Finally, Miyake et al.[81] investigated the effect of Pt addition to a $Ru/Sn/Al_2O_3$ catalyst. The main product was lauryl alcohol which is consistent with previous studies; however, lauryl laurate and lauric acid were formed as well. $5\%Ru\text{-}7\%Sn\text{-}2\%Pt/\gamma Al_2O_3$ has shown the highest conversion and selectivity compared to different compositions of Ru-Sn-Pt, Ru-Sn and Sn-Pt bimetallics and Pt monometallic catalysts.

Pallasana and Neurock have studied a large network of elementary reactions for the hydrogenation of acetic acid on Pd(111). They performed DFT calculations with the Becke and Pedrew functional (BP) for cluster calculations, and the Pedrew-Wang(PW-91 functional) for periodic slab calculations. Fig.1.13 shows the proposed reaction mechanism; however, a microkinetic model has not been developed to determine rate determining steps and the plausible pathways but, it has been reported that the C-O bond activation is likely the rate limiting step (ΔH= 68 kJ/mol and E_a (activation barrier)=142 kJ/mol)[82].

In another study by Tysoe and Neurock[83], the surface chemistry of vinyl acetate on clean Pd(111) is explored experimentally and computationally. Temperature

programmed desorption (TPD) and reflection adsorption infrared spectroscopy (RAIRS) combined with DFT calculation have been used to calculate the reaction energies, activation barriers, and vibrational frequencies. The calculated heat of adsorption (63.4 kJ/mol) is in agreement with measured one (65 KJ/mol). Figure 1.14 shows the proposed mechanism for the activation of vinyl acetate on Pd(111).

Santiago et el.[84] studied the reduction of methyl acetate and ethyl acetate on silica supported copper experimentally and computationally. DFT calculations were performed on a Cu_{13} cluster and for both methyl acetate and ethyl acetate they observed the activation via the C-O bond close to the carbonyl group. Table 1.1 shows elementary reactions, heat of reactions, and activation barriers for the suggested reaction mechanism.

Next, Gurshani et al. [85] studied the activation of ethanol, acetic acid and ethyl acetate on silica-supported Pt. The periodic DFT calculations were performed on a 2×2×2 slab with PW-91 functional. Both the ethyl acetate and methyl acetate activate starting from the C-O bond cleavage on the surface. Also, a kinetic model has been developed and it is reported that CH_4 and CO are expected to be the main products of the reactions. They also conclude that the reason CO is the main product is because the C-C bond activation on Pt is 50 kJ/mol easier than on Cu. Table 1.2 and figure 1.15, show the details in the mechanism.

As computer resources have become more available, DFT calculation can be carried out for larger molecules over larger slabs and clusters and recently, Xu et al. carefully investigated various pathways for the activation of methyl acetate. they report that the activation of methyl acetate on Pd(111) is limited by the dehydrogenation of the alpha, beta and methoxy carbons. Dehydrogenation from the methoxy end leads to a

selective C-O dissociation to produce methoxy and acetaldehyde; however, dehydrogenation of the alpha and beta carbon was shown to be an unselective pathway which goes through further dehydrogenation. Unfortunately, a thorough microkinetic model has not been developed[86].

Table 1.1 ΔH and activation barriers of elementary reactions involved reduction of Ethyl acetate and Methyl acetate on supported Cu[84].

Step	Reaction	$E_{forward}$ (kJ/mol)	$E_{reverse}$ (kJ/mol)	ΔH (kJ/mol)	Kinetic sensitivity
1	$C_2H_5OH_{(g)} + 2* \rightleftharpoons C_2H_5O* + H*$	32[b]	22	10[c]	0.01
2	$C_2H_5O* + * \leftrightharpoons CH_3CHO* + H*$	0[d]	24	−24[e]	0.03
3	$CH_3CHO* \rightleftharpoons CH_3CHO_{(g)} + *$	20	0[f]	20[c]	0
4	$CH_3CHO* + * \rightarrow C_2H_{6(g)} + H_2O_{(g)} + 2* - 2H_{2(g)}$	38 ± 2	183	−145[e]	1.02
5	$CH_3CHO* + * \leftrightharpoons CH_3C*O + H*$	20[d]	79	−59[e]	0.33
6	$CH_3C*O\ CO* \rightarrow + CH_{4(g)} - 0.5H_{2(g)}$	100[d]	190	−90[b]	1.02
7	$CH_3COOH_{(g)} + 3* \rightleftharpoons CH_3CO*O* + H*$	9[b]	85	−76[b]	0
8	$CH_3COOH_{(g)} + 2* \leftrightharpoons CH_3C*O + HO*$	100[g]	60	40[e]	0
9	$CH_3COOC_2H_{5(g)} + 2* \rightarrow CH_3C*O + C_2H_5O*$	81[h]	47	34[e]	0
10	$CH_3COOC_2H_{5(g)} + 2* \rightarrow CH_3CO*O* + C_2H_{6(g)} - 0.5H_{2(g)}$	103[i]	227	−124[e]	0
11	$H_{2(g)} + 2* \rightleftharpoons 2H*$	0[f]	66	−66 ± 5	0
12	$CO_{(g)} + * \rightleftharpoons CO*$	0[f]	118	−118 ± 2	0
13	$HO* + H* \rightleftharpoons H_2O_{(g)} + 2*$	1	30[j]	−29[b]	0

Table1.2 Summary of heats of reaction for the reactions on Pt as estimated from DFT for ethanol, acetic acid and ethyl acetate[85].

Step	Reaction	DFT (kJ/mol)	EtOH (kJ/mol)	AcOH (kJ/mol)	EA (kJ/mol)
1	$C_2H_5OH_{(g)} + 2* \leftrightharpoons C_2H_5O* + H*$	22	**10**	22	22
2	$C_2H_5O* + * \leftrightharpoons CH_3CHO* + H*$	−41	−24	−42	−43
3	$CH_3CHO* \leftrightharpoons CH_3CHO_{(g)} + *$	32	**20**	32	32
4	$CH_3CHO* + * \leftrightharpoons C_2H_{6(g)} + H_2O_{(g)} + 2* - 2H_{2(g)}$	−163	−145	−135	−134
5	$CH_3CHO* + * \leftrightharpoons CH_3C*O + H*$	−69	−59	−37	−44
6	$CH_3C*O \leftrightharpoons CO* + CH_{4(g)} - 0.5H_{2(g)}$	−90	−90	−90	−90
7	$CH_3COOH_{(g)} + 3* \leftrightharpoons CH_3CO*O* + H*$	−76	−76	−76	−76
8	$CH_3COOH_{(g)} + 2* \leftrightharpoons CH_3C*O + HO*$	35	40	43	37
9	$CH_3COOC_2H_{5(g)} + 2* \leftrightharpoons CH_3C*O + C_2H_5O*$	37	34	49	43
10	$CH_3COOC_2H_{5(g)} + 2* \leftrightharpoons CH_3CO*O* + C_2H_{6(g)} - 0.5H_{2(g)}$	−94	−124	−128	−127
11	$H_{2(g)} + 2* \leftrightharpoons 2H*$	−85	**−66**	**−60**	**−60**
12	$CO_{(g)} + * \leftrightharpoons CO*$	−194	**−118**	**−111**	**−118**
13	$HO* + H* \leftrightharpoons H_2O_{(g)} + 2*$	−29	−29	−29	−29

1.4 FIGURES

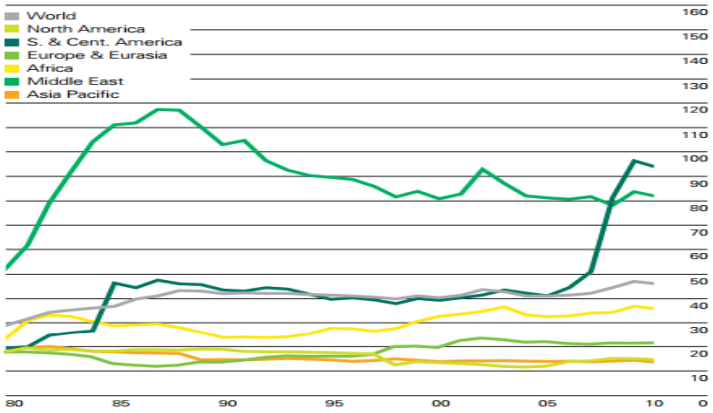

Figure 1.1 Oil Reserve-to-production ratios by region(1980-2010)[6]

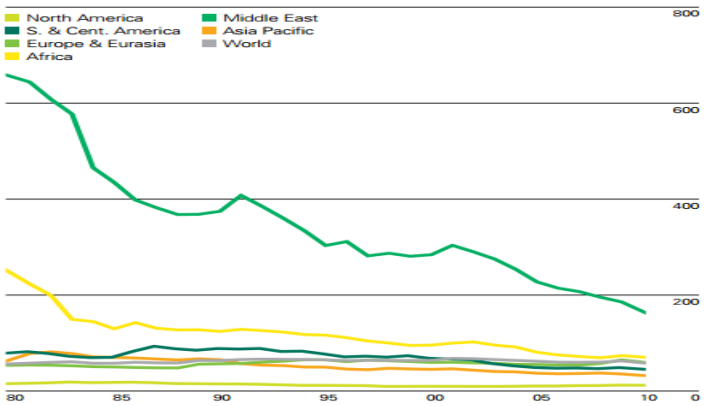

Figure 1.2 Natural Gas reserve-to-production ratios by region(1980-2010)[6]

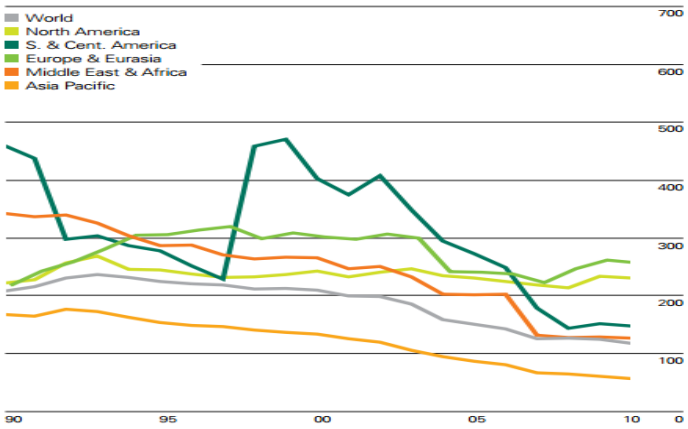

Figure 1.3 Coal reserve-to-production ratios by region(1990-2010)[6]

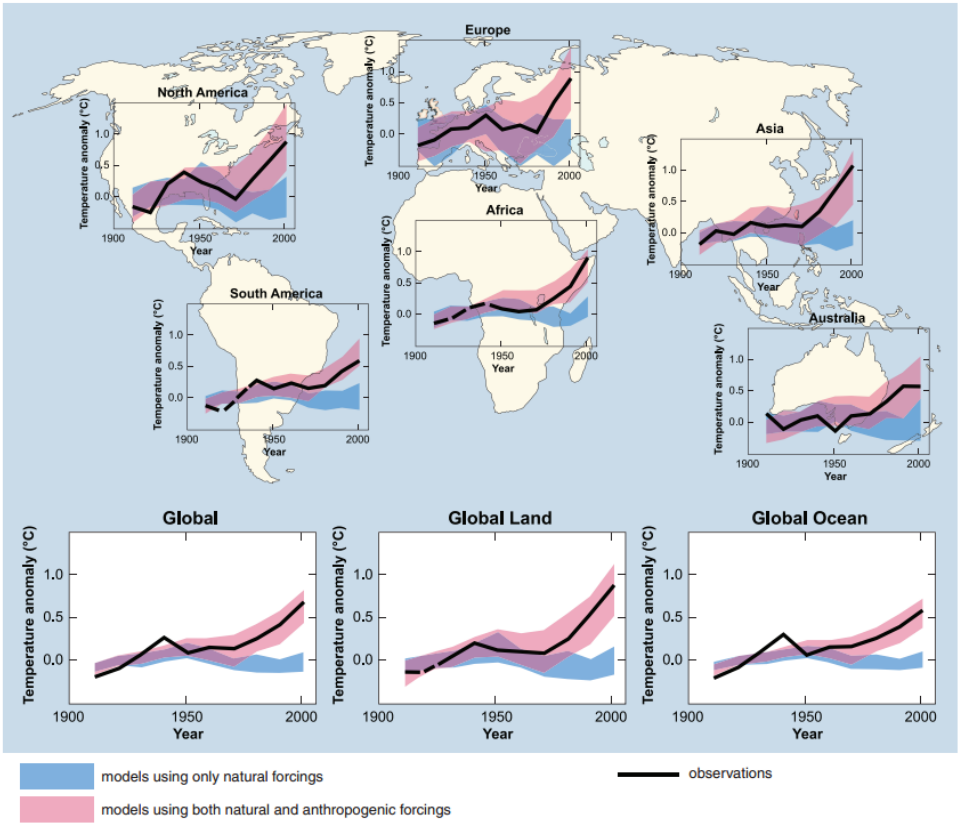

Figure 1.4 Continental and global changes in surface temperature(1906-2005)[9]

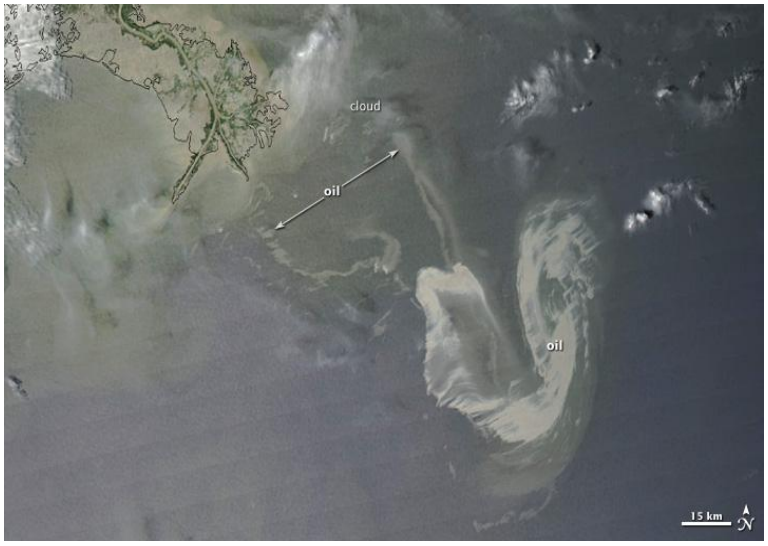

Figure 1.5 NASA released image of the oil reaching the shore in the Gulf of Mexico[87]

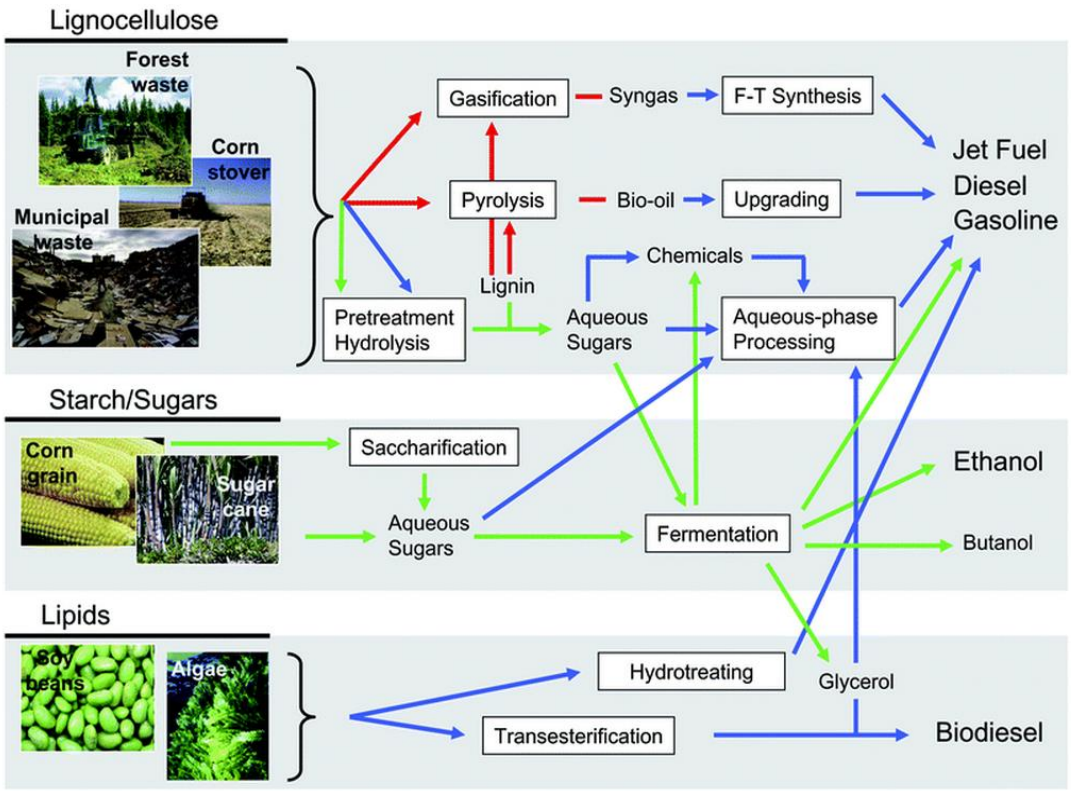

Figure 1.6. Different routes of biomass conversion to liquid hydrocarbons [2].

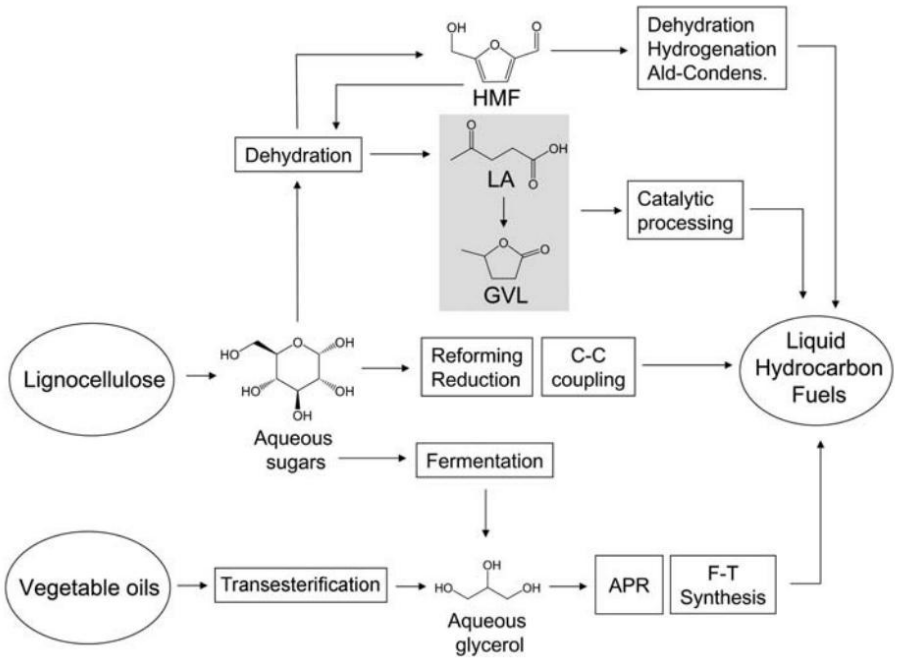

Figure 1.7 Heterogeneous catalytic routes of biomass conversion[2]

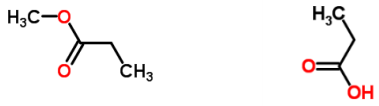

Figure 1.8 Methyl propionate and propianic acid

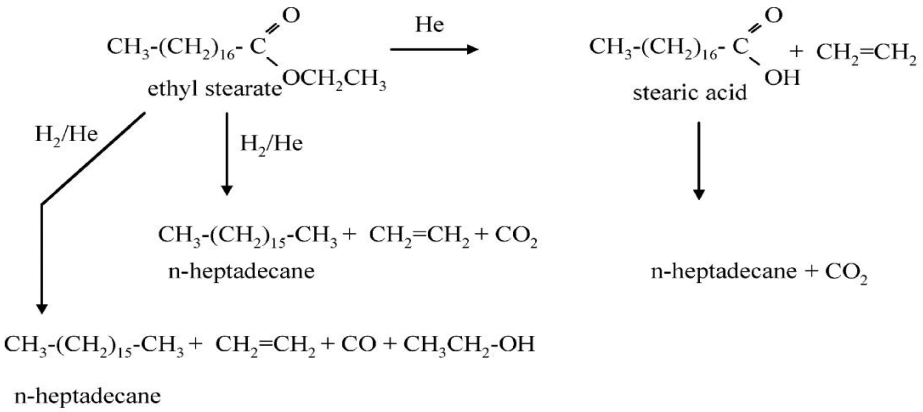

Figure 1.9 proposed mechanism of ethyl stearate and steric acid by Murzin et al. [62].

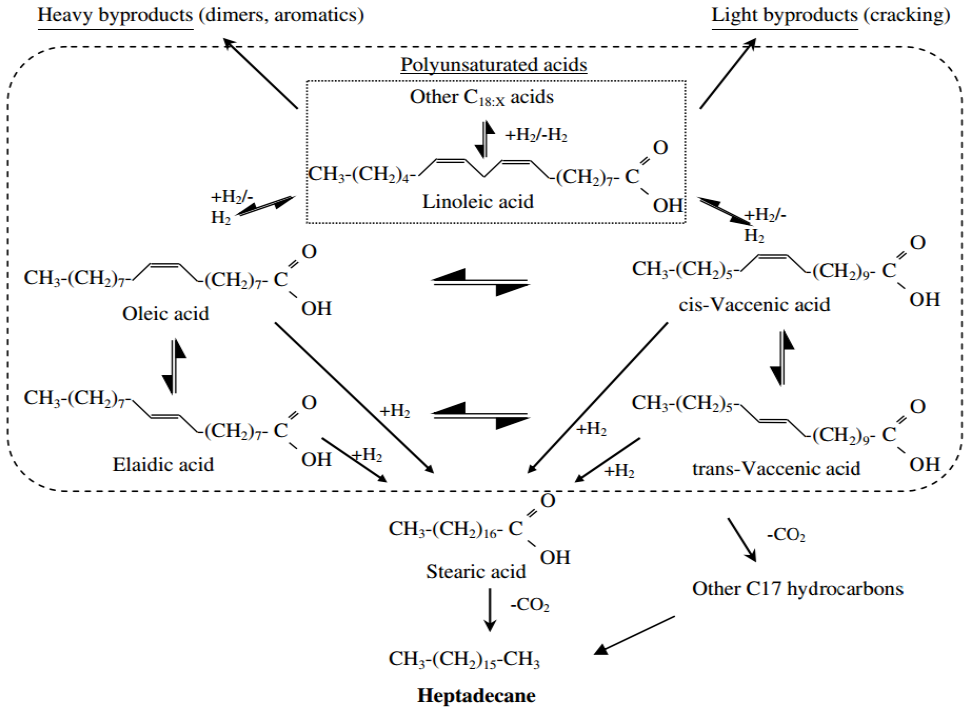

Figure 1.10 Linoleic and oleic acid conversion to C17 and C18 hydrocarbons over Pd/C[65]

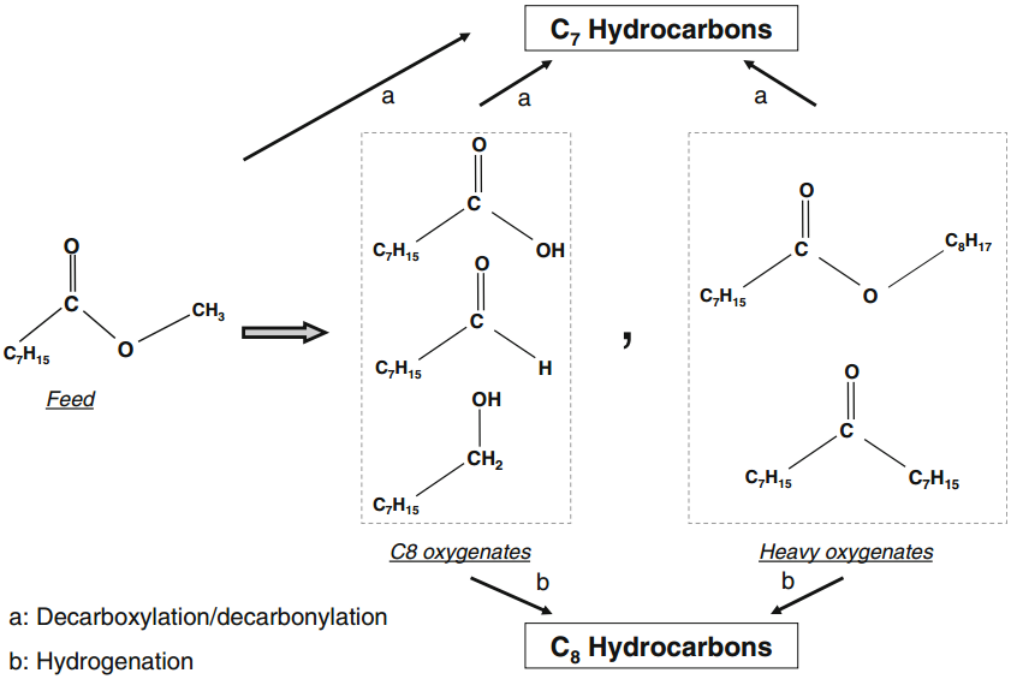

Figure 1.11 Methyl octanoate HDO mechanism over Pt/Al_2O_3 [68]

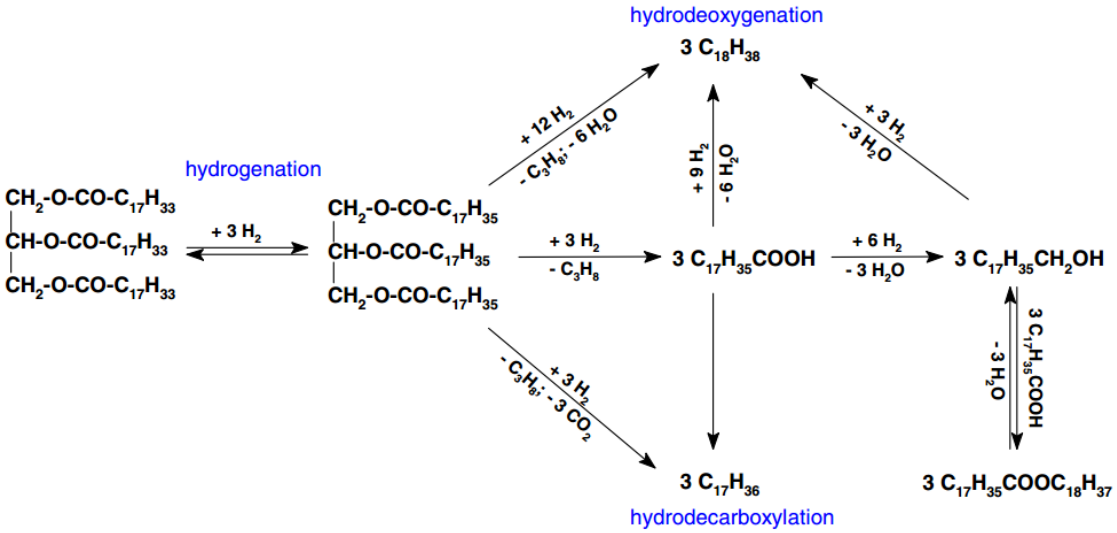

Figure 1.12 Decarboxylation and hydrodeoxygeneation of triglyceride[59, 72]

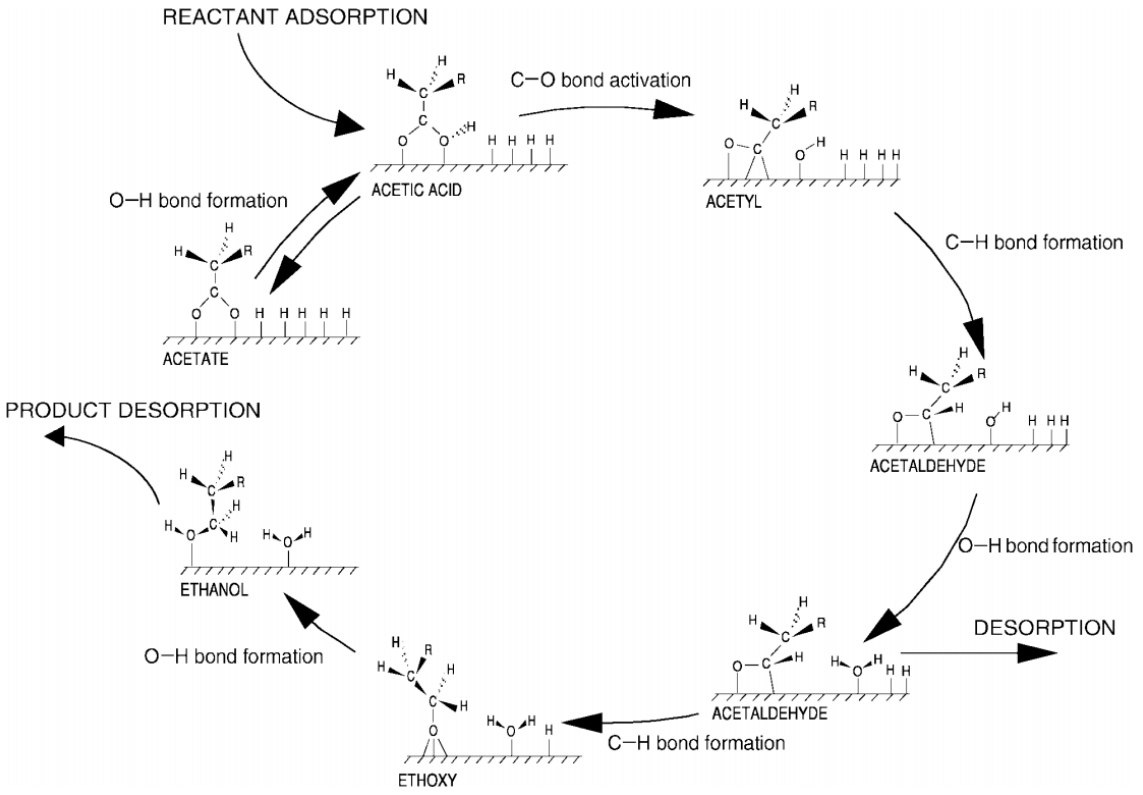

Figure 1.13 Acid acetic hydrogenolysis on Pd(111) [82]

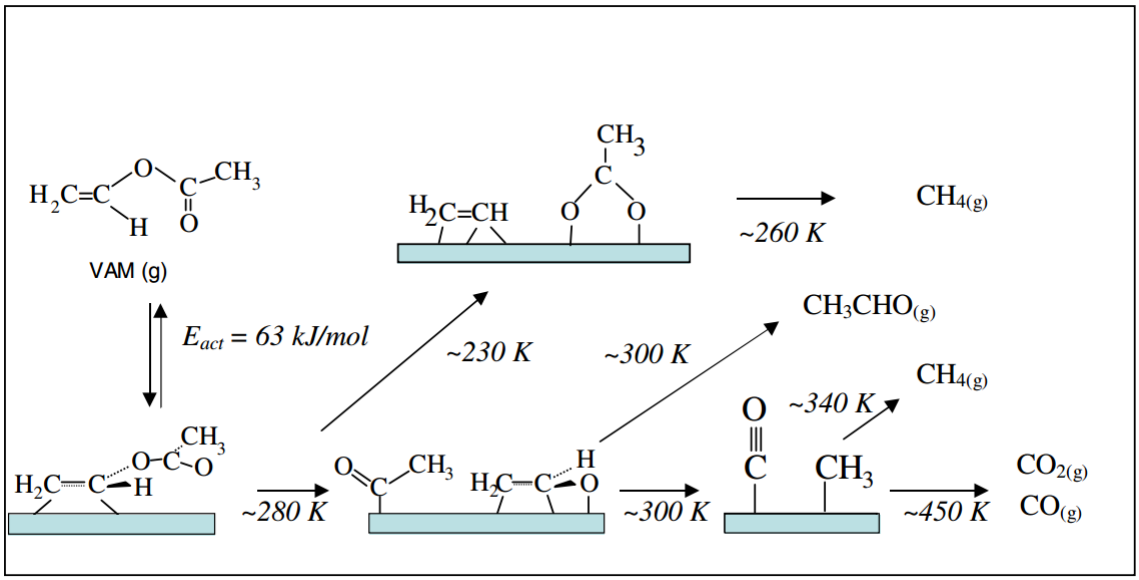

Figure 1.14 Two different mechanism for vinyl acetate HDO on Pd(111)[83]

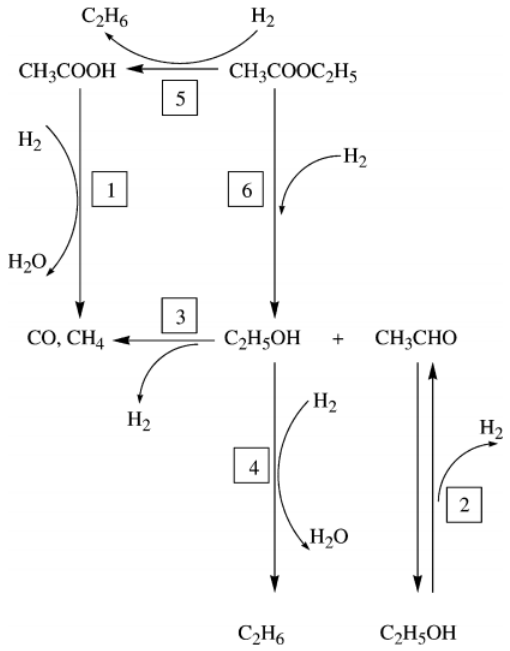

Figure 1.15 Ethyl acetate, acetic acidand ethanol HDO over silica supported Pd[85]

CHAPTER 2

METHODOLOGY

2.1 THEORETICAL BACKGROUND

2.1.1 DENSITY FUNCTIONAL THEORY (DFT)

The basis of Density functional theory (DFT) is the proof by Hohenberg and Kohn[88, 89] that the ground state electronic energy is determined completely by the electron density (ρ)[88]. The significance of the Hohenberg-Kohn Theory is perhaps best illustrated by comparison to the wave function approach. A wave function for an N-electron system contains 3N coordinates while, density only depends on three coordinates. The term "functional" refers to a function of a function, which means that the energy has a functional dependence on ρ, and then ρ is the function of the coordinates of the electrons[90]. In the following section, the fundamental of density functional theory and Kohn-Sham theory are described briefly.

The foundation for the use of DFT in computational chemistry was the Kohn-Sham theory[91]. To understand the Kohn-Sham Theory first, the total electronic energy should be defined. Total energy can be divided into three parts: kinetic energy T[ρ], attraction between nuclei and electrons $E_{ne}[\rho]$, and electron-electron repulsion $E_{ee}[\rho]$. The term $E_{ee}[\rho]$ may be divided into a Coulomb and an exchange part, J[ρ] and K[ρ].

In Kohn-Sham theory the $E_{ne}[\rho]$ and J[ρ] are given by their classical expressions[88]:

$$E_{ne}[\rho] = \sum_a \frac{Z_a \rho(r)}{|R_a - r|} dr \tag{2.1}$$

$$J[\rho] = \frac{1}{2} \int\int \frac{\rho(r)\rho(r')}{|r - r'|} dr dr' \tag{2.2}$$

Also kinetic energy is calculated under the assumption of non-interacting electrons from the equation below:

$$T_S = \sum_{i=1}^{N} \langle \phi_i | -\frac{1}{2} \nabla^2 | \phi_i \rangle \tag{2.3}$$

For example for an electron in a boxlike potential the kinetic energy is:

$$T = \frac{3}{10} (3\pi^2)^{\frac{2}{3}} \int \rho^{\frac{5}{3}} d\tau \tag{2.4}$$

In reality the electrons are interacting and equation 2.1 does not provide the total kinetic energy however, it provides ~99% of the correct answer[88]. The difference between the exact kinetic energy and calculated by assuming non-interacting electrons, is adsorbed into an exchange-correlation term. So, the general DFT energy expression can be written as[88]:

$$E_{DFT} = T_S[\rho] + E_{ne}[\rho] + J[\rho] + E_{XC}[\rho] \tag{2.5}$$

There is no exact expression for E_{XC}; however, several approximate expressions have been developed in order to describe the exchange correlation energy[90].

The simplest DFT approximation is the local density approximation (LDA) which is

$$E_{XC} = -\frac{9}{8} \left(\frac{3}{\pi}\right)^{\frac{1}{5}} \alpha \int \rho(1)^{\frac{4}{3}} d\tau \tag{2.6}$$

where α is unity when a free-electron gas model is used and values of about 0.7 are

generally used for molecules. In LDA it is assumed that the density can locally be treated as a uniform electron gas, or equivalently, density is a slowly varying function[88]. The LDA is not generally of high enough accuracy to be useful for determining structural properties and dissociation energies of molecules. One obvious way to improve the correlation functional is to make it depend not only on the local value, but also on the extent to which the density is changing, i.e., the gradient of the density[92]. This approach is known as "generalized gradient approximation". Most gradient corrected functionals are constructed with the correction being a term added to the LDA functional, i.e.,

$$E_{XC}^{GGA}[\rho(r)] = E_{XC}^{LSD}[\rho(r)] + \Delta E_{XC}\left[\frac{\nabla\rho(r)}{\rho^{\frac{4}{3}}(r)}\right] \tag{2.7}$$

Another class of approximations to exchange-correlation functionals, are hybrid methods. Using the Hellmann-Feyman theorem, the exchange-correlation energy can be computed as

$$E_{XC} = \int_0^1 \langle \Psi(\lambda) | V_{XC}(\lambda) | \Psi(\lambda) \rangle d\lambda \tag{2.8}$$

where λ describes the extent of interelectronic interaction, ranging from 0 (none) to 1 (exact)[92]. This equation is an exact connection between the exchange correlation energy and corresponding potential energy which is known as *Adiabatic Connection Formula.* Different approximations have been developed to find an expression for E_{XC} by evaluating the integral in equation 2.8. Exchange functional models which are derived from equation 2.8 usually include exact Hartree-Fock exchange and exchange and correlations from other sources such as LDA, GGA and empirical functionals and they

are often called hybrid methods[88]. Eq. 2.9 shows one of the famous hybrid functionals, B3LYP.

$$E_{xc}^{B3LYP} = E_{xc}^{LDA} + a_0(E_x^{HF} - E_x^{LDA}) + a_x(E_x^{GGA} - E_x^{LDA}) + a_c(E_c^{GGA} - E_c^{LDA}) \qquad (2.9)$$

In recent years different types of approximation have been developed to modify the kinetic energy term and exchange functional terms; however, there is no systematic approach for achieving the exact solution for the Schrodinger equation through the use of a more accurate exchange functional or kinetic energy expressions.

As it shown before, all the terms in total electronic energy depend on density, which means there is no need to determine the wave function. However, it is difficult to obtain high accuracy on the basis of this approach, so in practice it is common to determine the density from the wave functions that are obtained from self-consistent field calculations[90]. These self-consistent field calculations in DFT are similar to Hartree-Fock calculations.

Figure 2.1 shows the flowchart for self-consistent field (SCF) DFT calculations

2.1.1.1 Transition State Search

An important problem in theoretical chemistry is understanding the transition process of chemical reactions. The system of atoms and molecules is more likely to move along the paths with the lowest intermediate free energy maximum, and especially the one that minimizes the total action along the path[93]. This pathway is the so-called minimum energy path (MEP). The MEP describes the mechanism of reaction, and the energy barrier along the path can be used to calculate the reaction rate[94]. There are several approaches for finding MEPs. In this study, nudge elastic band (NEB) and dimer

methods have been used to locate the transition state. In the following section these methods are described briefly.

The NEB is a method to find a MEP between a pair of stable states[94]. In the context of reaction rates, this pair has an initial and a final state, both of which are local minima on the potential energy surface[94]. The NEB is a chain-of-states method[95, 96] in which a string of images (geometric configurations of the system) is used to describe a reaction pathway. These configurations are connected by spring forces to ensure equal spacing along the reaction path. Upon convergence of the NEB to MEP, the images describe the reaction mechanism. (See figure 2.2)

The NEB force on image i contains two independent components,

$$F_i^{NEB} = F_i^{\perp} + F_i^{S||} \tag{2.10}$$

where $F_i^{\perp}$ is the component of the force due to the potential perpendicular to the band,

$$F_i^{\perp} = -\nabla(R_i) + -\nabla(R_i).\hat{\tau}_i.\hat{\tau}_i \tag{2.11}$$

and $F_i^{S||}$ is the spring force parallel to the band,

$$F_i^{S||} = k(|R_{i+1} - R_i| - |R_i - R_{i-1}|)\hat{\tau}_i \tag{2.12}$$

where R_i is the position of the *i*th image and k is the spring constant[94].

While the NEB method is robust and has been successful, there are situations where the elastic band does not converge well to the MEP. When the force parallel to the MEP is large compared to the force perpendicular to the MEP, kinks can form and as the minimization is applied, they can continue oscillate back and forth, preventing the band from converging to the MEP[97]. Another approach, to avoid this problem is climbing image NEB (CI-NEB). In this method, the highest energy image l feels no spring forces and climbs to the saddle via a reflection in the force along the tangent[94],

$$F_l^{CI} = -F_l - 2F_l.\hat{\tau}_i.\hat{\tau}_i \tag{2.13}$$

Finding the precise value of the energy at the transition state, can be tedious with the NEB method. Enough images need to be included to get high enough resolution near the maximum for the interpolation to give an accurate value. Also, many force evaluations can be wasted converging images far from the transition state. So it can be advantageous to first use only a few iterations of the NEB method, enough to get a rough estimate of the shape of the MEP, and then turn to another method which can efficiently converge to the transition state[94].

The dimer method is a good candidate for this co-operative strategy. Similar to NEB methods, it requires only forces to find the transition state[94];however, dimer method involves just two images of the system "dimer" refers to these images[98].

The dimer method, depicted in Fig. 2.3 is a pair of images separated from their common midpoint R by a distance ΔR. The vector $\hat{N}$ which defines the dimer orientation is a unit vector pointing from one image at R_2 to the other image at R_1. When a transition state launched from an initial configuration, with no prior knowledge of what $\hat{N}$ might be, a random unit vector is assigned to $\hat{N}$ and the corresponding dimer images are formed

$$R_1 = R + \Delta R\ \hat{N} \qquad \text{and} \qquad R_2 = R - \Delta R \tag{2.14}$$

Initially, and whenever the dimer is moved to a new location, the forces acting on the dimer and the energy of the dimer are evaluated. These quantities are calculated from the energy and the force (E_1, F_1, E_2 and F_2) acting on the two images,

$$E_0 = \frac{E}{2} + \frac{\Delta R}{4}(F_1 - F_2).\hat{N} \tag{2.15}$$

The advantage of dimer method is that all the properties of dimer are derived from the forces and energy of two images and there is no need to evaluate the energy and force at the midpoint between two images which consequently decreases the number of required force evaluations[98].

2.1.1.2 VIBRATIONAL FREQUENCY CALCULATIONS

Atoms vibrate around their equilibrium positions. From a quantum mechanic perspective, the vibrations that are possible around an atom's equilibrium position contribute to the material's energy even at 0K via zero-point energies. Frequencies of vibrations usually are measured experimentally using spectroscopy. These frequencies are often of great interest. In our study zero-point energies are taken into account and also vibrational frequencies have been used to calculate the rate of elementary reactions. Here, the theory behind the DFT calculation of vibrational frequency will be explained.

For a set of N atoms, a vector with 3N components, $r=(r_1,\ldots,r_{3N})$ can define the Cartesian coordinate of the system of atoms. If locating the atoms at r_0 is a local minimum in the energy of atoms, then it is convenient to define a new coordinate $x= r-r_0$. The Taylor expansion of the atoms about the minimum at r_0 is to second order,

$$E=E_0+\frac{1}{2}\sum_{i}^{3N}\sum_{i}^{3N}\left[\frac{\partial^2 E}{\partial x_i \partial x_j}\right]_{x=0} x_i x_j \qquad (2.16)$$

The term, in this expression involving the first derivatives is zero because the system is at equilibrium. The second derivatives can be defined as a $3N\times3N$ matrix known as hessian matrix,

$$H_{ij} = [\frac{\partial^2 E}{\partial x_i \partial x_j}]_{x=0} \tag{2.17}$$

Also, the matrix form of equation of motion is,

$$\frac{d^2 X}{dt^2} = -AX \tag{2.18}$$

Where the elements of matrix A are $A_{ij} = \frac{H_{ij}}{\sqrt{mi}.\sqrt{mj}}$. The matrix A is known as mass-weighted Hessian matrix. The special solutions of equation of motions are called normal modes and the general solution of the equation of motion and frequencies can be calculated as,

$$X(t) = \sum_i [a_i \cos(wt) + b_i \sin(wt)]e_i \tag{2.19}$$

$$\upsilon_i = \sqrt{\lambda_i} / 2\pi \tag{2.20}$$

where λ_i and e_i are eigenvalues and eigenvectors of Matrix A and a_i and b_i are a collection of constants that are uniquely determined by the initial position and velocity of atoms[99].

To calculate the vibrational frequencies using DFT, we first have to find the bond length and minimize the molecule's energy. Then the hessian matrix should be calculated. Unfortunately, it is not easy to evaluate the second derivatives of the energy with respect to atomic position. However, a good estimate of the second derivative is using a finite-difference approximation:

$$\left(\frac{d^2 E}{db^2}\right)_{b0} = \frac{E(b_0 + \delta b) - 2E(b_0) + E(b_0 - \delta b)}{(\delta b)^2} \tag{2.21}$$

As $\delta b \rightarrow 0$ the values of second derivative becomes more accurate. $\delta b = 0.001$ Å has shown a reasonable accuracy. With this approximation, the elements of the Hessian matrix can be estimated and eigenvalues and eigenvectors can be calculated to find frequencies[99].

2.1.2 Solvation Models

2.1.2.1 Continuum Models

In the previous sections DFT and its applications, have been reviewed briefly. Despite the tremendous progress made in this field, there is a severe draw-back. The quantum chemistry developed by theoretical chemists is primarily suited for vacuum and dilute gases. Taking the advantages of periodic boundary conditions, different DFT codes have been developed for crystalline systems by solid-state physicists. However, most industrially relevant chemical processes do not happen in gas phase or in crystals, but mainly in the liquid phase or amorphous solid phase where the quantum chemical methods are not suitable. Since, the representation of condensed liquid systems by large ensembles of molecules converges very slowly with an increase in ensemble size[100].

The major approaches in Computational Chemistry in treating of solvent effects are:

supermolecule, continuum models, Molecular Mechanics, and recently appeared various hybrid constructions.

In the supermolecule approach one places some number of solvent molecules together with the solute in the QM calculation. While, in many cases, it can give some insights on solvent effects even with a limited number of solvent molecules, quantitative

results require a large number of solvent molecules to be included increasing the computational cost beyond the present day limits[100, 101].

Molecular Mechanics methods, due to the simplicity of the atom-centred force field, allow us to include quite a large number of solvent molecules into consideration. However, the simplicity of the MM approach does not allow the MM methods to get an adequate description of many processes, such as bond breaking in chemical reaction. Regarding solvent effects, accounting for the mutual polarization of the solute and solvent molecules requires a considerable complication in the MM theory which again increases the cost of such calculations[101].

Hybrid QM/MM methods are quite a fresh branch on the tree of Computational Chemistry. It is a promising approach. However, QM/MM calculations are not easy to setup and they are costly[101].

Finally, continuum solvation models, the combination of QM methods with continuum solvation theory, have proven to be successful. The basic idea of the continuum models is the Max Born equation for the free energy of solvation of ions, ΔG_S^{ion} [102]

$$\Delta G_S^{ion} = -\frac{\varepsilon_S - 1}{\varepsilon_S}\frac{Q^{ion^2}}{2R^{ion}} \qquad (2.22)$$

Here, ε_S is the dielectric constant of the solvent, Q^{ion} is the total charge of the ion. R^{ion} is the effective ion-radius which is the radius of a spherical boundary between the solute and solvent[102]. The boundary around the solute is the so-called cavity and as is shown in Eq. 2.22 the free energy of solvation is essentially dependent on the cavity size.Later Born's idea was taken up by Kirkwood and Onsager [103-105] by taking into account

electrostatic multiple moments. Born-like models have become able to treat typical molecular shapes reasonably well; however, they are always in danger of generating electrostatic artifacts as soon as less-common shapes of solutes are involved[100].

Another class of continuum solvation models, use the Poison equation of classical electrostatics to express the electrostatic potential as a function of the charge density and dielectric constant.

$$\nabla^2\phi(r) = -\frac{4\pi\rho(r)}{\varepsilon} \tag{2.23}$$

where ε is the dielectric constant of the medium[92].

The most widely used scheme for the self-consistent reaction field implementation of the Poison equation is the surface area boundary element approach. This was first formalized by Miertus, Scrocco and Tomassi, and these authors referred to their construction as the polarized continuum model[92].

Surely, it has limitations in applicability, but where it works it allows us to get an estimate of solvent effects at a cheap computational price. The cheap price is achieved by exclusion of information on explicit configurations of the solvent molecules because the solvent is described as a uniform medium characterized by some macroscopic properties[101].

Recently another class of continuum models, so-called conductor-like screening models (COSMO), have been developed by Andreas Klamt. These models approximate the surrounding space of the solute by an infinite dielectric constant. Such a situation considerably simplifies the necessary electrostatic equations. Also, these models seem to be more computationally robust[92]. In this study, COSMO and COSMO-RS calculations

have been used to calculate the solvent effect. In the following section, COSMO and COSMO-RS models will be explained.

2.1.2.2 COSMO AND COSMO-RS

The idea of the COSMO model originates from a simple question: *What is the interaction energy of an arbitrary charge distribution within a surrounding conducting sphere of radius R?*

Andreas Klamt found a general exact expression for this question by the method of mirror changes.

$$\Delta E = -\frac{1}{2}\sum_{ij}\frac{q_i q_j R}{\sqrt{R^4 - 2R^2 r_i r_j + r_i^2 r_j^2}} \tag{2.24}$$

Here, r_i denotes the position vector of the charges q_i with respect to the center of the sphere, and r_i is the distance from the center. The boundary condition is also different from previous continuum methods because it is assumed that spherical cavities are conductors[100],

$$0 = \Phi^X + \Phi(q) = \Phi^X + Aq \tag{2.25}$$

where Φ^X denotes the surface potential arising from the charge distribution of a solute X inside the cavity, and A is the Coulomb interaction matrix. After scaling the solute potential with a dielectric scaling factor,

$$Aq = f(\varepsilon)\Phi^X \tag{2.26}$$

this equation can be solved by inversion of the symmetric matrix A [100]. So the solute-conductor energy can be expressed as,

$$E_S^X = \Phi^X q = -f(\varepsilon)\Phi^X A^{-1}\Phi^X \tag{2.27}$$

and the total free energy, ΔG_S^X is $\frac{1}{2}E_S^X$. Also, in all quantum mechanic codes, there is an operator (B) which generate the potential Φ^X from the charge density[100]. This operator can be used to express the free energy of solvation as a function of charge density,

$$G_S^X = -\frac{1}{2} f(\varepsilon) Q^X B^t A^{-1} B Q^X = \frac{1}{2} Q^X D Q^X \tag{2.28}$$

With definition of matrix D in the last equation, this expression is similar to the Coulomb interaction,

$$E_{Coulomb}^X = \frac{1}{2} Q^X C Q^X . \tag{2.29}$$

This formal analogy is helpful since the COSMO model can now be easily implemented in a DFT code as an addition to the Coulomb interaction[100].

The COSMO accuracy can be improved by using more realistic cavity structures. Different types of cavities such as, icosahedron, pentakisdodecahedron and iso-density cavities have been used in the COSMO codes. Basically the cavity structures in COSMO model are similar to PCM and isodensity PCM (IPCM)[100].

Overall, this model has shown promising results for water however it seems that COSMO fails to predict the behavior of non-polar solvents and polar solutes in polar solvents. The reason is that this model is unable to take Vander *Waals* and *hydrogen bondig* interactions into account. Also, the cavity structures lead to a misfit error in the contact surfaces between cavities[100]. Fig. 2.4 shows this electrostatic misfit due to cavity structure.

Next generation of conductor-like models incorporate, the COSMO result with the statistical thermodynamics of interacting surfaces to calculate a more accurate and realistic solution properties. First model was developed by Klamt and it is so-called COSMO-RS(COSMO for real solvent). In the next section, this model will be described briefly.

COSMO-RS is a theory which describes the interactions in a fluid as local contact interaction of molecular surfaces. (see Fig. 2.4) Interaction energies are quantified by the values of the two screening charge densities σ and σ' which can be calculated by COSMO calculation. Klamt et al. claim that interaction energies can be described by the formula,

$$E_{\text{int}}(\sigma,\sigma') = e_{misfit}(\sigma,\sigma') + e_{H-bond}(\sigma,\sigma') = \frac{\alpha'}{2}(\sigma+\sigma') + C_{H-bond}\min(\sigma\sigma'+\sigma_{H-bond}^2,0) \tag{2.30}$$

α' and C_{H-bond} are parameterized based on DFT/COSMO calculation with Becke-Perdew (BP) functional and a triple-zeta valence polarization[100].

The key of this statistical thermodynamic approach used in COSMO-RS is the reduction of interacting molecules to pairs of interacting surface pieces. An expression for the Chemical potential of a unit piece of surface of kind σ in the solvent S was developed by Klamt,

$$\mu_S(\sigma) = -k_b T \ln \int d\sigma' P_S(\sigma) \exp\left\{-\frac{E_{\text{int}}(\sigma,\sigma') - \mu_S(\sigma')}{KT}\right\} \tag{2.31}$$

where $P_S(\sigma)$ is the profile of σ. The difference between the value of real chemical potential and ideal chemical potential (without interaction) can be found by summation of the chemical potentials of a segment i,

$$\mu_i^R(S;T) = \sum_{\upsilon} n_i^{\upsilon}\mu_i^{\upsilon}(S;T) = \int p^i(\sigma)\mu(\sigma)d\sigma \tag{2.32}$$

Consequently, with calculation of Chemical potential, free energy of solvation of compound i in solvent S and also all of the arbitrary liquid-liquid equilibrium properties such as activity coefficient, heat of mixing, solubility etc, can be calculated[100].

2.2 Computational Method

2.2.1 Gas-Phase Calculations

All density functional theory calculations have been conducted using the Vienna Ab Initio Simulation Package (VASP).[106-108] The Kohn-Sham valence states are expanded in a plane wave basis sets with the energy cut-off of up to 400eV. The interaction between core electrons is described with projector-augmented wave (PAW)[107, 109] methods. The exchange correlation energy is calculated within the generalized gradient approximation (GGA) using the functional form proposed by Perdew and Wang which is known as Perdew-Wang 91 (PW91).[110, 111] The lattice constant, obtained from the optimization of the fcc-Pd bulk, is 3.953 $\AA$ which is in reasonable agreement with the experimental value of 3.891 $\AA$. The surface Brillouin zone is sampled with 4×4×1 Monkhorst-pack kpoint grid. Pd (111) is modeled by a four layer slab with a (3×4) surface unit cell and the palladium layers separated by a 15 $\AA$ vacuum. The 12 Pd atoms in each layer allow for a coverage of 1/12 ML for adsorbates.

Pd(211) is modeled by an 8 atomic layer slab (corresponding to approximately four layers in closed packed (111) direction) with a (2×3) surface unit cell and a 15 $\AA$ vacuum gap between palladium layers. The Pd (211) surface Brillouin zone is sampled with 3×5×1 Monkhorst-pack k-point grid The bottom four Pd layers were fixed to their bulk configuration during all calculations while the top four atomic layers were free to

relax in all directions. We note that we did not consider Pd hydride formation since at the investigated reaction conditions of low hydrogen pressure of 0.2 bar and 473 K hydride formation is thermodynamically not favorable. All self-consistent field (SCF) calculations for geometry optimizations were converged to 1×10^{-3} kJ/mol and for transition state identification the convergence criterion was set to be 1×10^{-5} kJ/mol.

The bottom two Pd layers were fixed to their bulk configuration during all calculations while top two layers were free to relax in all directions. Adsorption energies of all intermediates were calculated at their most stable geometry by the following equation:

$$E_{\text{ads}} = E_{\text{slab+adsorbate}} - E_{\text{slab}} - E_{\text{adsorbate(gas)}} \tag{2.33}$$

where $E_{\text{slab+adsorbate}}$ is the total energy of the adsorbed intermediate on the Pd slab, E_{slab} is the total energy of the Pd slab and $E_{\text{adsorbate(gas)}}$ is the total energy of the adsorbate in the gas phase. Transition states are located by combination of CI-NEB[112] and dimer[98, 113] methods and finally, vibrational frequency calculations have been performed to clearly identify stable intermediate and transition state structures. The zero-point energy correction for all the structures was taken into account by using the following equation:

$$\Delta E_{ZPE} = \sum_i \frac{1}{2} h \nu_i \tag{2.34}$$

where h is the Plank constant and ν_i is the vibrational frequency of mode i. We note that all the energy values in this paper are zero-point energy corrected.

For surface reactions, the forward rate constant (k_{for}) of each reaction is calculated using harmonic transition state theory (hTST)[114]

$$k_{\text{for}} = \frac{k_{\text{B}}T}{h}\frac{q_{\text{TS,vib}}}{q_{\text{IS,vib}}}e^{-\frac{E_{\text{a\_for}}}{k_{\text{B}}T}} \tag{2.35}$$

where k_{B} is the Boltzmann constant, T denotes the reaction temperature, h is the Planck constant, $E_{\text{a\_for}}$ stands for the zero-point energy-corrected activation barrier for the forward reaction derived from DFT calculations, and $q_{\text{TS,vib}}$ and $q_{\text{IS,vib}}$ are the (harmonic) vibrational partition functions for the transition state and the initial state, respectively, i.e., q_{vib} is calculated as

$$q_{\text{vib}} = \prod_i \frac{1}{1-e^{\frac{-h\nu_i}{k_{\text{B}}T}}} \tag{2.36}$$

where ν_{i} is the vibrational frequency of each vibrational mode of the adsorbed intermediate derived from our DFT calculations.

The reverse rate constant (k_{rev}) is calculated similarly and the thermodynamic equilibrium constant K is given as

$$K = \frac{k_{\text{for}}}{k_{\text{rev}}}$$

(5)

For an adsorption reaction A(g)+*→A*, the equilibrium constant K is defined as

$$K = \frac{(q_{\text{vib}})_{A^*}}{(q_{\text{vib}}q_{\text{rot}}q_{\text{trans}})_{A(g)}}e^{\frac{-\Delta E_{\text{ads}}}{k_B T}} \tag{2.37}$$

where $(q_{\text{vib}})_{\text{A*}}$ is the vibrational partition function of adsorbed A, and q_{vib}, q_{rot}, q_{trans} stand for vibrational, rotational, and translational partition functions, respectively. ΔE_{ads} represents the zero-point corrected adsorption energy. For an adsorption reaction A(g)+*→A*, the forward rate is given by collision theory with a sticking probability of 1.

$$k_{\text{for}} = \frac{1}{N_0\sqrt{2\pi m_A k_B T}} \tag{2.38}$$

where N_0 is the number of sites per area (1.478×10^{19} m^2) and m_A denotes the molecular weight of A. The reverse rate constant is again given as

$$k_{\text{rev}} = \frac{k_{\text{for}}}{K} \tag{2.39}$$

With the forward and reverse rate constants defined, we solve the full set of steady-state rate equations to obtain the surface coverages of all possible reaction intermediates and the fraction of free sites using the BzzMath library[115] developed by Buzzi-Ferraris. No assumptions were made regarding rate-limiting steps.

2.2.2 Liquid-Phase Calculations

Cluster model DFT calculations were carried out using TURBOMOLE 6.0.[116-118] The Pd (111) cluster model surfaces have been modeled by a two layered cluster with a 5×5 surface. These structures were constructed by removal of the periodic boundaries from the periodic slabs that were obtained from our previous plane-wave (VASP)[107, 108] calculations.[119] All adsorbates were represented by all-electron TZVP[120-122] basis sets while for Pd we used a relativistic small core potential (ECP) together with a basis set of same quality as the adsorbates for the valence electrons. The Coulomb potential was approximated with the RI-J approximation with auxiliary basis sets [123-125].. Single point energy calculations were performed with a self-consistent field energy convergence criterion of 1.0×10^{-6}. Finally, for each cluster model energy calculations on various spin surfaces were performed to identify the lowest energy spin state for further calculations.

For cluster models in the liquid phase, COSMO calculations were performed on the same spin surface as for the vacuum cluster calculations. The dielectric constant was set to infinity to provide the input for the COSMO-RS calculations. For cavity construction, the default radii-based cavities were used.

For surface reactions, the forward rate constant (k_{for}) of each reaction is calculated as,

$$k_{for} = \frac{k_B T}{h} e^{-\frac{\Delta G^{\ddagger}}{k_B T}} \tag{2.40}$$

where k_B is the Boltzmann constant, T denotes the reaction temperature, h is the Planck constant, and $\Delta G^{\ddagger}$ represents the free energy of activation for a specific temperature and reaction environment. I.e., in the presence of solvents, the free energy of activation ($\Delta G^{\ddagger}_{solvent}$) and free energy of reaction ($\Delta G_{rxn\text{-}solvent}$) were calculated as,

$$\Delta G^{\ddagger}_{Solvent} = \Delta G^{\ddagger}_{Gas} + G_{TS}(solv) - G_{IS}(solv), \tag{2.41}$$

and

$$\Delta G_{rxn\text{-}solvent} = \Delta G_{Gas} + G_{FS}(solv) - G_{IS}(solv) \tag{2.42}$$

where, $G_{IS}(solv)$, $G_{FS}(solv)$, and $G_{TS}(solv)$ are the solvation energies of the initial, final, and transition states, respectively, that were obtained from the difference in energy of the COSMO-RS and gas-phase cluster calculations, and $\Delta G^{\ddagger}_{Gas}$ and ΔG_{Gas} are the free energy of activation and reaction under gas phase conditions, respectively.

In the presence of a solvent, the free energy of adsorption for A(g)+*→A* is calculated as,

$$\Delta G_{ads-solvent} = \Delta G_{ads-gas} + G_{A^*}(solv) - G_{Pd}(solv) \tag{2.43}$$

where $\Delta G_{ads-gas}$ is the free energy of adsorption under gas phase conditions and $G_{A*}(solv)$ and $G_{Pd}(solv)$ are as before the solvation energies of the adsorbed molecule A and Pd surface immersed in the solvent, respectively.

With the forward and reverse rate constants defined, rates of the elementary reactions can be expressed by mean-field rate laws. Considering that some of the adsorbed intermediates occupy multiple active sites, the rate expressions and steady state molecular balance equations are highly nonlinear. To solve the set of steady state differential reactor equations and to obtain the surface coverages of the intermediates, we used the BzzMath library[115] developed by Buzzi-Ferraris. No assumptions were made regarding rate-limiting steps.

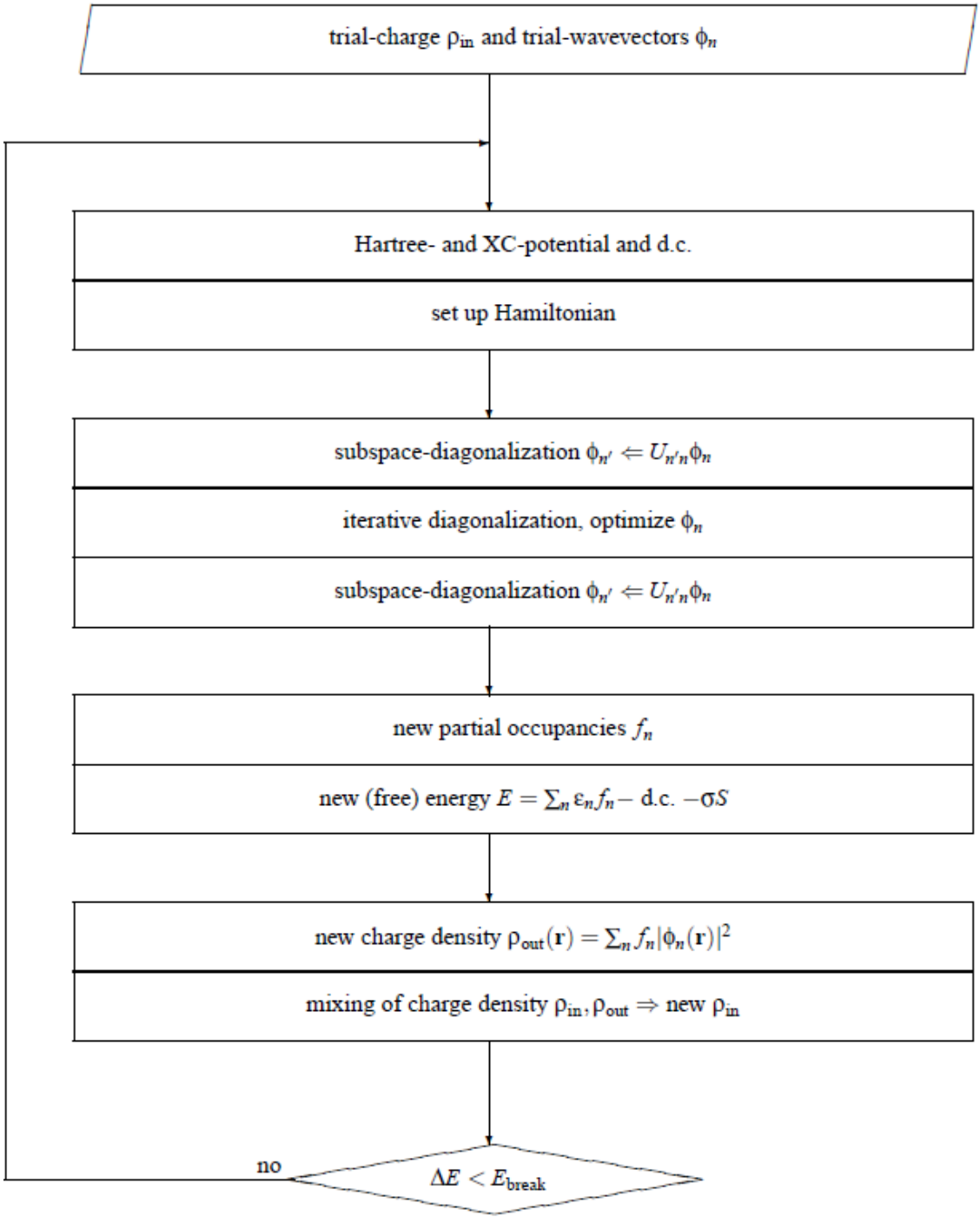

Figure 2.1 Calculation of KS- ground-state energy from SCF DFT[126]

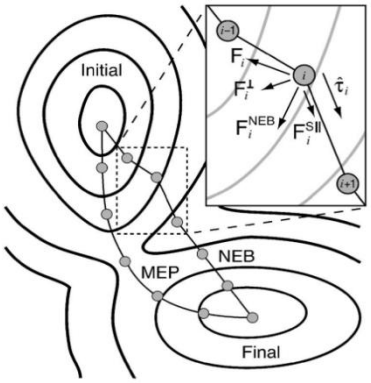

Figure 2.2 Two components make up the nudged elastic band force F^{NEB}: the spring force $F_i^{S\parallel}$, along the tangent $\hat{\tau}_i$, and the perpendicular force $F_i^{\perp}$ [94].

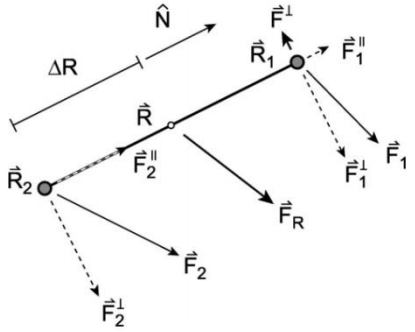

Figure 2.3 Definition of the various position and force vectors of the dimer[98]

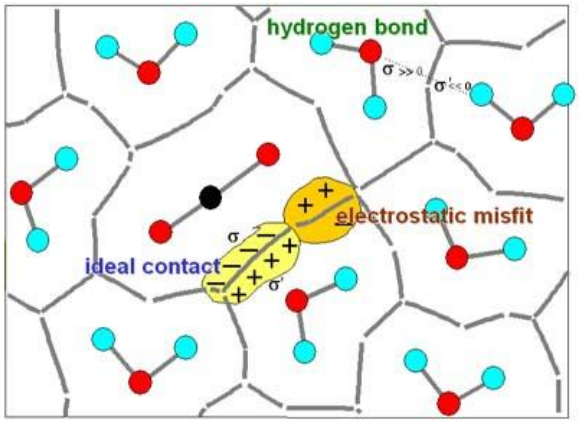

Figure 2.4 Schematic picture of the interactions of solute and solvent. Adapted from[100]

CHAPTER 3

INVESTIGATION OF THE REACTION MECHANISM OF GAS-PHASE, CATALYTIC HYDRODEOXYGENATION OF PROPANOIC ACID[1]

[1] Behtash, S.; Lu, J.; Faheem, M.; Heyden, A. Green Chemistry 2014, 16, 605. Partly reprinted here with permission of publisher.

[1] Lu, J. M.; Behtash, S.; Faheem, M.; Heyden, A. Journal of Catalysis 2013, 305, 56. Partly reprinted here with permission of publisher.

[1] Lu, J. M.; Behtash, S.; Heyden, A. Journal of Physical Chemistry C 2012, 116, 14328. Partly reprinted here with permission of publisher.

3.1 INTRODUCTION

The increasing consumption of fossil fuels in the last decades has caused a rapid depletion of easily accessible, non-renewable, fossil resources. As a result, fuels derived from renewable raw materials such as biomass are of significant academic and industrial interest. First generation biofuels (fatty acid methyl esters, FAMEs) are typically produced by transesterification of triglycerides (the main constituent of vegetable oils and animal fats) with methanol or ethanol, and are usually used as an additive to petroleum diesel. Unfortunately, FAMEs suffer from disadvantages such as higher viscosity, higher cloud point temperature, poor oxidation stability, and lower energy density.[127, 128] Therefore, there is interest in the conversion of triglycerides and fatty acids to oxygen free hydrocarbons identical to diesel, also known as 1.5^{th} generation biofuels.

During the deoxygenation of esters and in the presence of hydrogen, fatty or carboxylic acids form as intermediates whose conversion is often found to be particularly slow. As a result, we study here the hydrodeoxygenation (HDO) of carboxylic acids in the form of propionic acid. Three plausible mechanisms for HDO of carboxylic acids have been identified – decarbonylation (DCN), decarboxylation (DCX), and reductive deoxygenation without C-C cleavage (RDO). In the DCN and DCX mechanism, oxygen atoms are removed in the form of CO and CO_2 which leads to products one carbon atom shorter than the acid molecule. In contrast, in the RDO mechanism oxygen atoms are removed in the form of water without carbon loss. However, more hydrogen is consumed in the RDO mechanism.

As one of the early efforts, Maier and colleagues have found that Pd/SiO_2 catalysts are highly selective for the deoxygenation of carboxylic acids[129]. Recently,

Murzin's group has conducted an extensive investigation on the liquid phase deoxygenation of various long chain fatty acids on Pd/C catalysts, e.g., lauric acid[130], palmitic acid[66, 131], and stearic acid[131, 132]. Overall, they suggest that the DCX is preferred over the DCN and RDO. Similarly, Ford *et al.*[133] found in the study of the deoxygenation of C_{18}-C_{10} fatty acids that the DCX is preferred but that the CO_2 selectivity decreases with decreasing fatty acid carbon number. In contrast, Boda *et al*.[134] Recently studied the catalytic hydroconversion of octanoic acid to hydrocarbons over a similar Pd/C catalyst and suggested that the DCN is the favored reaction mechanism. The occurrence of the water-gas shift under reaction conditions makes it difficult to specify whether the observed CO and CO_2 are produced by DCX or DCN.

Mean-field microkinetic modeling permits extrapolating atomistic DFT information to describe a catalysts behavior under realistic temperatures and partial pressures and therefore allows a "first-principles" determination of the dominant reaction pathways, rate-limiting elementary steps, surface coverages, reaction orders. Although, the uncertainties in DFT-derived rate parameters and mean-field catalyst models are not insignificant, microkinetic modeling often provides significant insights into the reaction mechanism of a catalytic reaction under realistic temperatures and pressures. For example, microkinetic models have successfully been developed for various industrial reactions, such as the water-gas shift [135-137], ammonia synthesis[138], and methanol decomposition[139].

In this chapter, we present a detailed microkinetic model based on parameters exclusively derived from first-principles DFT calculations for two HDO reaction mechanisms - DCN and DCX - of propanoic acid to ethane over Pd(111). [119, 140]

All of the elementary steps and intermediates involved in DCN and DCX of propanoic acid are shown in Figure 3.1. The DFT-derived parameters for the reactions are listed in Table 3.1. Although the DCN and DCX mechanisms are interconnected, key steps in each mechanism are distinguishable. For example, C-OH bond dissociations in propanoic acid and its derivatives (CH_xCH_yCOOH, x=[1,2,3], y=[0,1,2]) form CH_xCH_yCO intermediates which produce CO and C_2 hydrocarbons after a C-C bond dissociation and are therefore key steps in the DCN mechanism. Similarly, key steps unique to the DCX mechanism are O-H bond dissociations to form CH_xCH_yCOO intermediates followed by C-C cleavage to form CO_2. Also, we grouped C-C bond dissociations to form CH_xCH_y and COOH on the surface in the DCX mechanism considering that COOH dissociates on Pd (111) easier to CO_2 and hydrogen than to CO and OH.

3.2 MICROKINETIC MODELING

We developed a microkinetic model for all elementary steps involved in both the DCX and DCN networks (previously the networks were studied independently) with forward and reverse rate parameters shown in Table 3.2.

All calculations were carried out at 473K which is a typical experimental temperature[62, 67, 141-145] and we selected partial pressures of propanoic acid, water, and CO_2 of 1 bar and a CO partial pressure of 0.1 bar which corresponds to a condition of about 10% conversion. Additionally, all simulations were carried out under low (0.001 bar) and medium (1 bar) hydrogen partial pressures to investigate the effect of hydrogen partial pressure on the reaction mechanism. For simplicity, all results corresponding to

the low partial pressure of hydrogen environment are displayed in this paper in [ ] bracket next to the results of the medium hydrogen partial pressure. Finally, for all simulations we employed a method similar to Grabow *et al.[146]* for determining coverage dependent adsorption energies of CO, H, and CH_3C.[140]

Figure 3.2 illustrates the turnover frequencies of all elementary steps under gas-phase conditions. The overall TOF was calculated to be 1.30×10^{-6} s^{-1} at medium hydrogen partial pressure [2.13×10^{-5} s^{-1} at low hydrogen partial pressure]. The TOF of the DCN pathways are 1.28×10^{-6} s^{-1} [2.11×10^{-5} s^{-1}] and the TOF of DCX pathways are 2.26×10^{-8} s^{-1} [1.43×10^{-7} s^{-1}], illustrating that the rate of the DCN is two orders of magnitude higher than the DCX. Next, we find the dominant reaction mechanism to be independent of the partial pressure of hydrogen to involve propanoic acid to undergo three dehydrogenation steps of α and β-carbons to form CHCHCOOH, followed by C-OH cleavage, and C-CO bond dissociation to produce C_2 products (CH_3CH_2COOH → $CH_3CHCOOH$ → $CH_2CHCOOH$ → CHCHCOOH → CHCHCO → CHCH). 31% [43% in the low hydrogen scenario] of the surface was free of adsorbed intermediates and the coverages of the most abundant surface species are adsorbed hydrogen, CO, and CH_3C were calculated to be 23% [7%], 34% [35%], and 12% [14%], respectively.

3.3 Apparent Activation Barrier, Reaction Orders, and Sensitivity Analysis

Apparent activation barriers were computed in the temperature range of 423 to 523 K in all reaction environments and hydrogen partial pressures.

$$E_a = RT^2\left(\frac{\partial \ln(r)}{\partial T}\right)_{p_i} \tag{3.1}$$

Next, the reaction order with respect to hydrogen was calculated at 473 K for the low hydrogen partial pressure in the range of 0.0005 to 0.002 bar and for the medium hydrogen partial pressure in the range of 0.5 to 2 bar using equation 3.10. Similarly, the reaction order of propanoic acid and CO were calculated at 473 K and a pressure range of 0.5 to 2 bar and 0.0001 to 1 bar, respectively.

$$\alpha_i = \left(\frac{\partial \ln(r)}{\partial \ln(p_i)} \right)_{T, p_{j \neq i}} \tag{3.2}$$

Finally, Campbell's degrees of rate and thermodynamic control[147-149], X_{RC} and X_{TRC}, were used to determine the rate controlling steps and intermediates in the mechanism. Rate controlling steps and intermediates are those transition states and intermediates that most strongly influence the reaction rate and are potential activity descriptors.

$$X_{\mathrm{RC},i} = \frac{k_i}{r} \left(\frac{\partial r}{\partial k_i} \right)_{K_i, k_j \neq k_i} \quad , \quad X_{\mathrm{TRC},n} = \frac{1}{r} \left(\frac{\partial r}{\partial \left(\frac{-G_n^0}{RT} \right)} \right)_{G^0_{m \neq n}, G_i^{0,\mathrm{TS}}} \tag{3.3}$$

where r is the overall rate of reaction, k_i is the forward rate constant for step i, K_i equilibrium constant for step i, R is the gas constant, T denotes the reaction temperature, and $G_n{}^0$ is the free energy of adsorbate n.

Medium partial pressure of hydrogen (p_{H2} = 1 bar)

At a reaction temperature of 473 K and a hydrogen partial pressure of 1 bar, our model predicts an apparent activation energy of 0.84 eV in a gas phase environment. The reaction order with respect to propanoic acid is +1.0, with respect to CO it is +0.31, and

finally with respect to H_2 it is -0.80. These results are in good agreement to our previous study[140]. Next, the C-OH bond dissociation as well as α- and β-carbon dehydrogenation steps are found to be rate-controlling. For example, the X_{RC} values for the C-OH cleavage reactions 17 ($CHCHCOOH^{***} + 2^* \rightarrow CHCHCO^{****} + OH^*$), reaction 5 ($CH_3CHCOOH^{**} + ^* \rightarrow CH_3CHCO^{**} + OH^*$), and reaction 11 ($CH_2CHCOOH^{***} + ^* \rightarrow CH_2CHCO^{***} + OH^*$) were calculated to be 0.49, 0.23, and 0.17, respectively. The X_{RC} value of the dehydrogenation of the α-carbon in propanoic acid (reaction 2) is rate controlling with X_{RC} = 0.32 and the first and second dehydrogenation steps of the β-carbon in $CH_3CHCOOH$ are rate controlling with X_{RC} = 0.09 (reaction 6) and X_{RC} = 0.06 (reaction 12), respectively. We note that the sum of the degree of rate control is larger one due to numerical inaccuracies of our nonlinear equation solver; however, the trends should not be affected by these numerical issues.

Also, these results are in agreement with previous calculations[82, 150] from Pallassana and Neurock and Olcay et al. who found that the C-OH bond cleavage is rate controlling for the HDO of acetic acid. Our model in addition highlights the importance of dehydrogenation steps. Finally, the thermodynamic rate control analysis suggests that the adsorption free energy of H* and CO* have a significant effect on the overall rate with X_{TRC} = -1.52 and 0.21, respectively, such that destabilizing the adsorbed hydrogen or stabilizing CO improves the overall reaction rate. CO is generally known to be a surface poison; however, due to repulsive lateral interactions with adsorbed H* and the negative reaction order with respect to hydrogen we observe that destabilizing adsorbed H* is more important than stabilizing CO*.

Low partial pressure of hydrogen (p_{H2} = 0.001bar)

At a low partial pressure of hydrogen, the coverage of hydrogen drops from 23% (p_{H2} = 1 bar) to 7%. Also, the available free sites increased from 31% to 42%. However, the coverage of CO is not significantly affected and in fact, slightly increases from 34% to 35%. Now, the thermodynamic rate control analysis suggests that destabilizing both CO* and H* improves the overall rate with X_{TRC} = -0.03 and -0.33, respectively. Also, the dehydrogenation of the α-carbon in propanoic acid is clearly the most rate controlling step with X_{RC} = 1.0 and C-OH bond dissociation becoming less important with X_{RC} = 0.05 for reaction 17.

Finally, our model predicts an apparent activation barrier of 0.62 eV (which is lower than at higher hydrogen partial pressures) and orders of reaction for CO and H_2 that are close to zero (i.e., -0.02 and -0.13, respectively). The calculated propanoic acid reaction order is again 1.

3.4 CONCLUSION

We performed a systematic investigation of both the decarbonylation and decarboxylation mechanisms of propanoic acid over Pd catalysts and developed a microkinetic model with parameters derived from DFT calculations and transition state theory. We incorporated the coverage dependence of the CO and H adsorption energies and the lateral interactions of CO and H, CO and CH_3C, and CH_3C and H in the microkinetic models.

Under all conditions is the decarbonylation the dominant HDO mechanism with the most favored pathway following dehydrogenation steps prior to C-OH and C-CO

bond cleavages, i.e., CH_3CH_2COOH → $CH_3CHCOOH$ → $CH_2CHCOOH$ → CHCHCOOH → CHCHCO → CHCH → → CH_3CH_3 / CH_2CH_2. Finally, a sensitivity analysis suggests that at a low hydrogen partial pressure is the dehydrogenation of α-carbon in propanoic acid most rate controlling. With increasing hydrogen partial pressure, the C-OH bond dissociation becomes most rate controlling and the importance of C-H bond cleavages is diminished. As a result, both C-H and C-OH bond dissociations are likely activity descriptors for a future computational catalyst discovery and design study.

3.5 TABLES

Table 3.1 Reaction free energies in eV for all elementary reaction steps in the hydrodeoxygenation of propanoic acid over Pd (111) model surfaces at a temperature of 473 K.

#	Reaction	Gas	
		ΔG_{rxn}	$\Delta G^{\ddagger}$
0	$CH_3CH_2COOH+*\rightarrow CH_3CH_2COOH*$	0.94	N/A
1	$CH_3CH_2COOH* + 3*\rightarrow CH_3CH_2CO*** + OH*$	0.35	0.89
2	$CH_3CH_2COOH* + 2*\rightarrow CH_3CHCOOH** + H*$	-0.11	0.61
3	$CH_3CH_2CO*** \rightarrow CH_3CH_2* + CO* + *$	-0.66	1.01
4	$CH_3CH_2CO*** \rightarrow CH_3CHCO** + H*$	0.02	0.83
5	$CH_3CHCOOH** + *\rightarrow CH_3CHCO** + OH*$	0.47	0.86
6	$CH_3CHCOOH** + 2*\rightarrow CH_2CHCOOH*** + H*$	-0.35	0.57
7	$CH_3CHCOOH** + 2*\rightarrow CH_3CCOOH*** + H*$	-0.06	1.14
8	$CH_3CHCO** + * \rightarrow CH_3CH** + CO*$	-0.84	1.00
9	$CH_3CHCO** + 2*\rightarrow CH_3CCO*** + H*$	-0.39	0.61
10	$CH_3CHCO** + 2*\rightarrow CH_2CHCO*** + H*$	-0.29	0.57
11	$CH_2CHCOOH*** + *\rightarrow CH_2CHCO*** + OH*$	0.53	1.20
12	$CH_2CHCOOH*** + *\rightarrow CHCHCOOH*** + H*$	0.04	0.89
13	$CH_3CCOOH*** + *\rightarrow CH_3CCO*** + OH*$	0.14	0.77
14	$CH_3CCO***\rightarrow CH_3C* + CO* + *$	-1.37	0.47
15	$CH_2CHCO*** + *\rightarrow CH_2CH*** + CO*$	-0.80	0.80
16	$CH_2CHCO*** + 2*\rightarrow CHCHCO**** + H*$	0.02	0.68
17	$CHCHCOOH*** + 2*\rightarrow CHCHCO**** + OH*$	0.51	1.07
18	$CHCHCO**** \rightarrow CHCH*** + CO*$	-1.13	0.19
19	$CHCH*** + H*\rightarrow CH_2CH*** + *$	0.31	0.95
20	$CH_2CH*** + H* \rightarrow CH_2CH_2** + 2*$	-0.03	0.87
21	$CH_2CH***\rightarrow CH_2C** + H*$	-0.43	0.45
22	$CH_2C** + H*\rightarrow CH_3C* + 2*$	-0.24	0.87
23	$CH_2CH*** + H* \rightarrow CH_3CH** + 2*$	-0.26	0.79
24	$CH_3C* + H* \rightarrow CH_3CH**$	0.92	1.09
25	$CH_3CH** + H* \rightarrow CH_3CH_2* + 2*$	0.16	0.87
26	$CH_3CH_2* + H* \rightarrow CH_3CH_3* + *$	0.05	0.64
27	$CH_3CH_2* + 2* \rightarrow CH_2CH_2** + H*$	-0.45	0.42
28	$CH_3CH_2COOH* + 2* \rightarrow CH_3CH_2COO** + H*$	-0.40	0.35
29	$CH_3CH_2COO** \rightarrow CH_3CH_2* + CO_2*$	0.18	1.40
30	$CH_3CH_2COO** + 2* \rightarrow CH_3CHCOO*** + H*$	0.39	1.22
31	$CH_3CHCOOH** + * \rightarrow CH_3CHCOO** + H*$	0.10	0.79
32	$CH_3CHCOOH** + * \rightarrow CH_3CH ** + COOH*$	0.28	1.37
33	$CH_3CHCOO*** \rightarrow CH_3CH** + CO_2*$	-0.37	0.94
34	$CH_3CHCOO*** + * \rightarrow CH_3CCOO*** + H*$	-0.07	0.85
35	$CH_3CCOOH*** + * \rightarrow CH_3CCOO*** + H*$	0.04	0.89
36	$CH_3CCOOH*** \rightarrow CH_3C* + COOH**$	-0.58	0.90
37	$CH_2CHCOOH*** + * \rightarrow CH_2CH*** + COOH*$	0.70	2.07
38	$CH_3CCOO*** \rightarrow CH_3C* + CO_2* + *$	-1.12	0.63
39	$COOH** \rightarrow CO_2* + H*$	-0.55	0.35
40	$COOH** \rightarrow CO* + OH*$	-0.65	0.40
41	$OH* + H* \rightarrow H_2O* + *$	-0.20	0.69

#	Reaction	Gas	
		ΔG_{rxn}	$\Delta G^{\ddagger}$
42	$CH_3CH_3^* \rightarrow CH_3CH_3 + *$	-0.79	N/A
43	$CH_2CH_2^{**} \rightarrow CH_2CH_2 + 2*$	0.01	N/A
44	$H_2O^* \rightarrow H_2O + *$	-0.49	N/A
45	$CO_2^* \rightarrow CO_2 + *$	-0.81	N/A
46	$CHCH^* \rightarrow CHCH + *$	1.16	N/A
47	$CO^* \rightarrow CO + *$	-1.19	N/A
48	$H_2 + 2* \rightarrow 2H*$	-0.58	N/A

Table 3.2 Equilibrium and forward rate constants for the elementary steps in the HDO of propanoic acid over Pd (111) model surfaces at a temperature of 473 K.

Reaction #	Gas	
	K_{eq}	$k_{forward}$ (s^{-1})
0	8.98×10^{-11}	9.52×10^{7}
1	2.10×10^{-4}	3.14×10^{3}
2	1.39×10^{1}	3.04×10^{6}
3	1.01×10^{7}	1.76×10^{2}
4	6.05×10^{-1}	1.34×10^{4}
5	9.14×10^{-6}	6.16×10^{3}
6	5.81×10^{3}	8.43×10^{6}
7	4.06	6.85
8	8.58×10^{8}	2.03×10^{2}
9	1.32×10^{4}	3.51×10^{6}
10	1.33×10^{3}	8.80×10^{6}
11	2.09×10^{-6}	1.68
12	4.16×10^{-1}	3.31×10^{3}
13	2.98×10^{-2}	6.70×10^{4}
14	3.95×10^{14}	9.98×10^{7}
15	3.52×10^{8}	2.91×10^{4}
16	6.61×10^{-1}	5.57×10^{5}
17	3.32×10^{-6}	4.33×10^{1}
18	1.12×10^{12}	8.65×10^{10}
19	4.76×10^{-4}	8.33×10^{2}
20	2.28	4.99×10^{3}
21	3.39×10^{4}	1.73×10^{8}
22	3.30×10^{2}	5.89×10^{3}
23	5.46×10^{2}	1.94×10^{7}
24	1.64×10^{-10}	2.51×10^{1}
25	1.95×10^{-2}	5.46×10^{3}
26	3.17×10^{-1}	1.46×10^{6}
27	6.40×10^{4}	3.26×10^{8}
28	1.92×10^{4}	1.99×10^{9}
29	1.08×10^{-2}	1.13×10^{-2}
30	6.55×10^{-5}	9.39×10^{-1}
31	9.04×10^{-2}	3.95×10^{4}
32	9.80×10^{-4}	2.33×10^{-2}
33	8.49×10^{3}	1.05×10^{3}
34	6.23	8.87×10^{3}
35	3.43×10^{-1}	3.29×10^{3}
36	1.47×10^{6}	2.84×10^{3}
37	3.33×10^{-8}	7.99×10^{-10}
38	9.13×10^{11}	1.76×10^{6}
39	7.28×10^{5}	1.63×10^{9}
40	8.00×10^{6}	4.84×10^{8}
41	1.48×10^{2}	4.20×10^{5}

Reaction #	Gas	
	K_{eq}	$k_{forward}$ (s^{-1})
42	2.44×10^{8}	3.65×10^{16}
43	7.22×10^{-1}	1.12×10^{8}
44	1.73×10^{5}	3.35×10^{13}
45	2.50×10^{8}	3.24×10^{16}
46	1.60×10^{-6}	9.98×10^{-15}

3.6 FIGURES

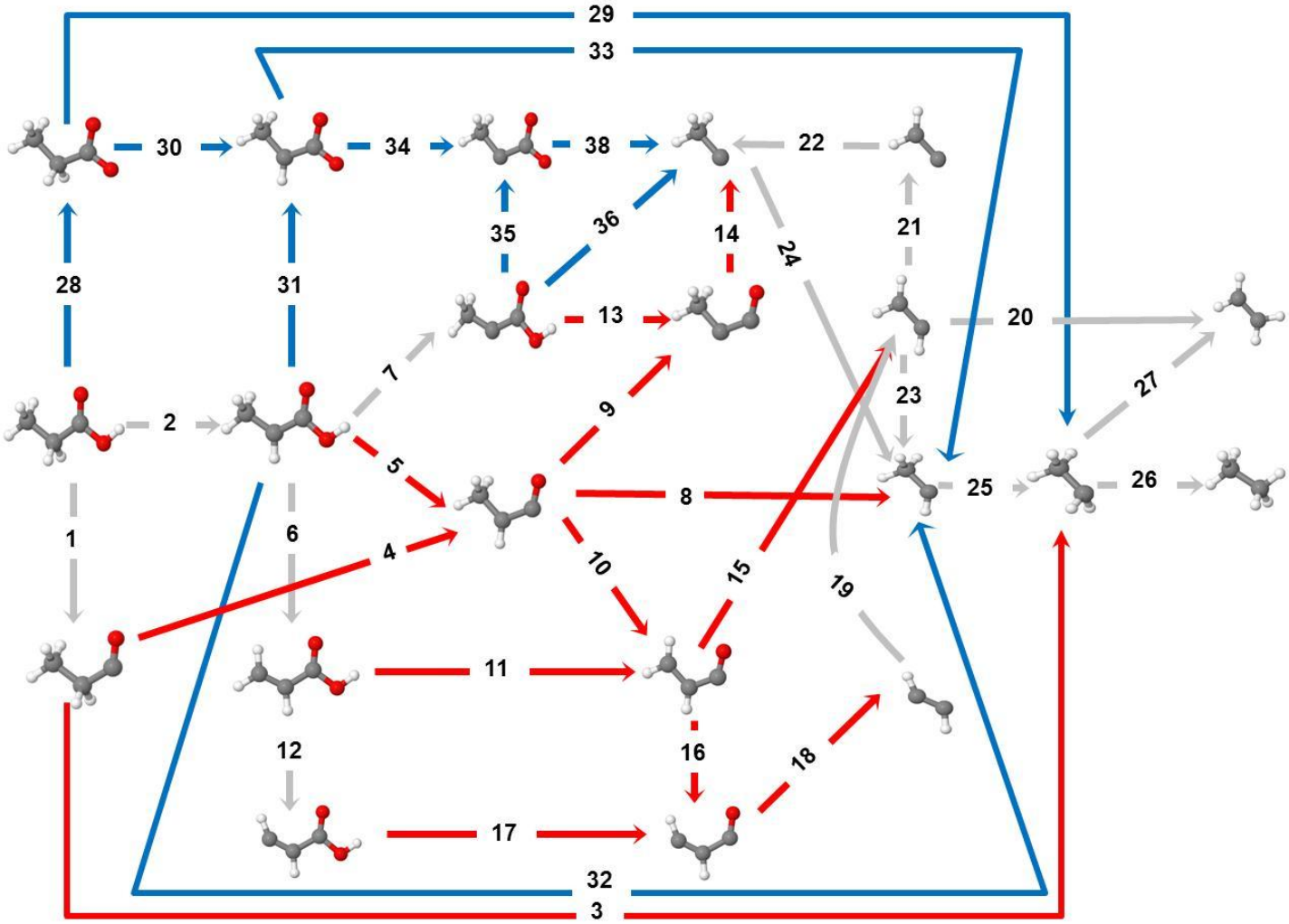
29
33
30
34
38
22
28
31
35
36
14
24
21
13
20
7
9
2
23
27
5
8
25
26
1
6
4
10
15
19
11
12
16
18
17
32
3

Figure 3.1 Network of elementary reaction steps considered in the hydrodeoxygenation of propanoic acid over Pd (111). The elementary reactions which are involved in DCN mechanism are shown with the blue color arrows, DCX reactions are illustrated with the red color arrows, and those reaction which are involved in both of the mechanisms such as, dehydrogenation of propionaic acid and its derivatives, and removal of hydrocarbon pool are shown with the gray color arrows.

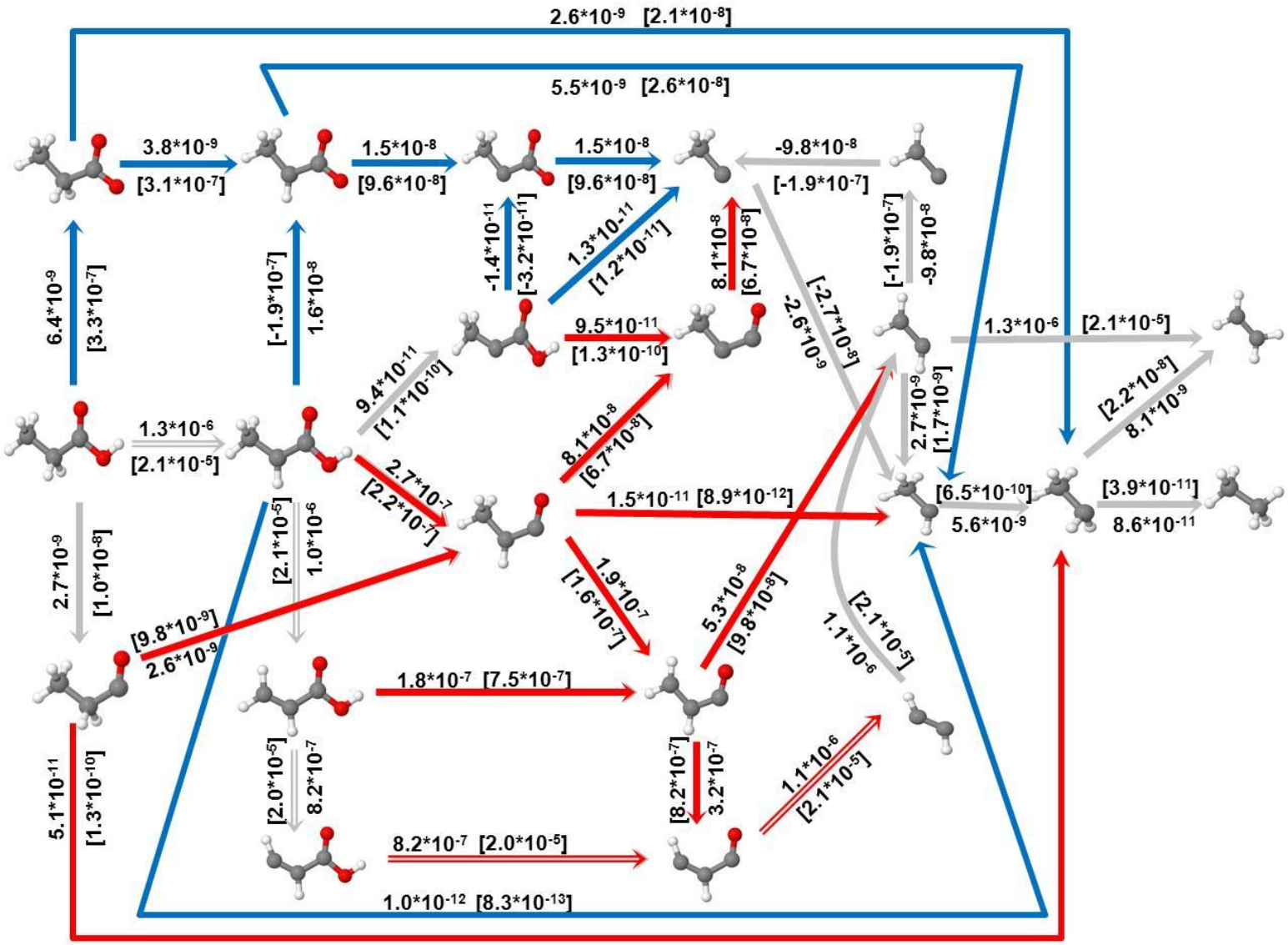
2.6*10-9 [2.1*10-8]
5.5*10-9 [2.6*10-8]
3.8*10-9
[3.1*10-7]
1.5*10-8
[9.6*10-8]
1.5*10-8
[9.6*10-8]
-9.8*10-8
[-1.9*10-7]
6.4*10-9
[3.3*10-7]
[-1.9*10-7]
1.6*10-8
-1.4*10-11
[-3.2*10-11]
1.3*10-11
[1.2*10-11]
8.1*10-8
[6.7*10-8]
[-1.9*10-7]
-9.8*10-8
-2.6*10-9
[-2.7*10-8]
9.5*10-11
[1.3*10-10]
9.4*10-11
[1.1*10-10]
1.3*10-6
[2.1*10-5]
2.7*10-9
[1.7*10-9]
[2.2*10-8]
8.1*10-9
1.3*10-6
[2.1*10-5]
8.1*10-8
[6.7*10-8]
2.7*10-7
[2.2*10-7]
1.5*10-11 [8.9*10-12]
[6.5*10-10]
5.6*10-9
[3.9*10-11]
8.6*10-11
2.7*10-9
[1.0*10-8]
[2.1*10-5]
1.0*10-6
1.9*10-7
[1.6*10-7]
5.3*10-8
[9.8*10-8]
[2.1*10-5]
1.1*10-6
[9.8*10-9]
2.6*10-9
1.8*10-7 [7.5*10-7]
5.1*10-11
[1.3*10-10]
[2.0*10-5]
8.2*10-7
[8.2*10-7]
3.2*10-7
1.1*10-6
[2.1*10-5]
8.2*10-7 [2.0*10-5]
1.0*10-12 [8.3*10-13]

Figure 3.2 TOFs (s^{-1}) for various elementary steps in the HDO of propanoic acid in absence of any solvents at a temperature of 473 K and a propanoic acid gas phase pressure of 1 bar and a hydrogen partial pressure of 1 bar or 0.001 bar (numbers inside the square brackets []). All other reaction conditions are given in section 3.3. The elementary reactions which are involved in DCN mechanism are shown with the blue color arrows, DCX reactions are illustrated with the red color arrows, and those reactions which are involved in both of the mechanisms such as, dehydrogenation of propionaic acid and its derivatives, and removal of hydrocarbon pool are shown with the gray color arrows. The reactions that are involved in the most dominant pathway are illustrated with a double-line arrow. The TOF_{DCN} was calculated to be 1.28×10^{-6} s^{-1} [2.11×10^{-5} s^{-1}] while the TOF_{DCX} was 2.26×10^{-8} s^{-1} [1.43×10^{-7} s^{-1}] (TOF_{DCN}/TOF_{DCX} = 56.4 [148])

CHAPTER 4

INVESTIGATION OF THE REACTION MECHANISM OF GAS-PHASE, CATALYTIC HYDRODEOXYGENATION OF METHYL PROPIONATE [1]

[1] Behtash, S.; Lu, J.; Heyden, A. *Catalysis Science & Technology* 2014, *4*, 3981. Reprinted here with permission of publisher.

ABSTRACT

Esters are one of the key components of lipid-rich biomass feedstocks that are potential raw materials for production of green fuels. We present a thorough density functional theory and microkinetic modeling study of the hydrodeoxygenation (HDO) of organic esters over Pd (111) model surfaces. Methyl propionate was chosen as our model molecule since it permits the study of the effect of both α- and β-carbon dehydrogenations on the HDO of esters while still being computationally accessible. An extensive network of elementary reactions was investigated and a microkinetic model was developed at reaction conditions of 473K, a methyl propionate partial pressure of 0.01 bar, and a hydrogen partial pressure of 0.2 bar to identify the dominant pathway and surface abundant species. Our microkinetic model suggests that decarbonylation pathways of methyl propionate are favored over decarboxylation pathways. We found the most dominant pathway to involve methyl propionate to undergo two dehydrogenation steps of both α- and β-carbons to form $CH_2CHCOOCH_3$, followed by C-O and C-C cleavages to produce C2 hydrocarbons and methoxy that eventually get hydrogenated to ethane and methanol ($CH_3CH_2COOCH_3 \rightarrow CH_3CHCOOCH_3 \rightarrow CH_2CHCOOCH_3 \rightarrow CH_2CHCO+OCH_3 \rightarrow \ldots \rightarrow CH_3CH_3+CO+CH_3OH$). The most abundant surface intermediates were identified to be H and CO and CH_3C. Finally, a sensitivity analysis of our models suggests that the dehydrogenation of α-carbon of methyl propionate, as well as propanoyl-methoxy bond dissociation control the overall rate on Pd (111).

KEYWORDS: biomass; lipids; triglyceride; ester; methyl propionate; palladium; density functional theory; hydrodeoxygenation; decarbonylation; decarboxylation;

4.1 INTRODUCTION

Energy demand continues to significantly increase due to societal developments. As a result, fossil fuels have been overused and nowadays most countries are strongly dependent on fossil fuel imports.[151, 152] Rising concerns over depletion of current fossil fuel resources and also environmental impacts of fossil fuel utilization have drawn substantial attention to conversion of biomass to biofuels to at least partially meet the world's growing energy demand. First generation biofuels such as bio-ethanol and biodiesel have been implemented successfully in the energy system. However, they generally suffer from compatibility issues and low energy density.[2, 127, 128, 153] Recently, biofuels research has been focused on the development of the science and technology for conversion of biomass into second-generation biofuels that are identical to gasoline and diesel and which are often called green diesel or green gasoline.[22]

Lipid-rich biomass feedstocks such as vegetable oils are one potential raw material for production of green fuels. In spite of their current relatively high price,[154] it is expected that the availability of lipid feedstocks will increase in the near future due to recent progress in large-scale production of non-edible lipid-rich biomass such as algae,[29, 31, 33] Jatropha and Camelina oils.[25, 26, 28] Lipids contain considerable amounts of oxygenates such as triglycerides/organic esters and fatty acid. To convert the lipids into hydrocarbons identical to fossil-derived transportation fuels, removal of oxygen atoms from the feedstock molecules is required. Significant research efforts have been done to convert vegetable oils into liquid hydrocarbons employing a hydroprocess with conventional hydrotreating catalysts such as sulfided $NiMo/Al_2O_3$ and $CoMo/Al_2O_3$.[47, 54, 59] However, by using conventional, sulfided hydrotreating

catalysts, the sulfur content of the final products is remarkable. Additionally, other disadvantages such as short catalyst life time and problems in separation of carbon oxides from the recycle gas have been reported.[54, 59] Consequently, there is an apparent need for new hydrodeoxygenation (HDO) catalysts for triglycerides/organic esters and fatty acids.

To rationally design a metal catalyst for hydrotreating of lipids, it is necessary to obtain a fundamental understanding of the reaction mechanisms on the catalyst surface. Previously, various reaction routes such as decarbonylation (DCN), decarboxylation (DCX), and reductive deoxygenation (RDO) have been proposed for the catalytic hydrodeoxygenation (HDO) of triglycerides to alkanes.[54] There is a consensus that RDO is not the dominant reaction mechanism over most metal catalysts;[54], [62], [155] however, it is currently not clear whether DCX or DCN are the dominant pathways. A thorough theoretical investigation of the catalytic HDO of fatty acids and esters can provide the required knowledge about the activity of the oxygen functionality in organic acids and esters. Also, the results of such studies can be used for the design of new metal catalysts for upgrading wood-derived bio-oils that contain considerable amounts of acids and esters.[156] In our recent publications,[119, 157] we investigated the HDO of organic acids in the absence and presence of solvents. In this study, we focused on understanding the reaction mechanism for the catalytic HDO of organic esters under gas phase condition with the help of first principles calculations. Previously, the activation of esters over various metal catalysts has been investigated by a number of research groups. For example, Murzin et al. investigated the HDO of ethyl stearate over Pd/C catalysts in a detailed experimental study.[62] Their observations suggested that the reaction

mechanism is complex and the DCN is the dominant catalytic cycle in the presence of hydrogen while DCX is favored in the absence of hydrogen. Similar results have been obtained in a study[155] of methyl stearate and methyl octanoate over Pd/Al_2O_3. Next, the catalytic conversion of methyl acetate to alcohols over palladium was theoretically investigated by Xu et al.[86] They reported that the activation of methyl acetate over Pd (111) is limited by the dehydrogenation of the alpha, beta and methoxy carbons. Dehydrogenation from the methoxy end leads to a selective C-O dissociation to produce methoxy and acetaldehyde; however, dehydrogenation of the alpha and beta carbon was shown to be an unselective pathway, i.e., further activation of the dehydrogenated species could not be determined without a detailed microkinetic modeling analysis.

In this paper, we present a thorough density functional theory (DFT) and microkinetic modeling study of the HDO of organic esters over Pd (111) model surfaces. Methyl Propionate was purposefully chosen as our model molecule. Methyl Propionate is the smallest organic ester that has two carbon atoms (alpha and beta carbons) next to the carbonyl function that allows us to investigate whether dehydrogenation of alpha and beta carbons can affect C-O and C-C bond dissociations and overall activity. All possible C-C, C-O and dehydrogenation/hydrogenation steps for methyl propionate and derivatives have been investigated in detail to obtain an extensive chemical reaction network. Next, the results of the DFT calculations were used to obtain reaction rate parameters such as elementary reaction rate constants. Finally, these parameters were incorporated in a microkinetic model to obtain the overall turnover frequency, dominant reaction pathway, and most abundant species on the surface.

4.2 METHODS

4.2.1 DFT CALCULATIONS

All density functional theory calculations have been conducted using the Vienna Ab Initio Simulation Package (VASP).[106-108] The Kohn-Sham valence states are expanded in a plane wave basis sets with the energy cut-off of up to 400eV. The interaction between core electrons is described with projector-augmented wave (PAW)[107, 109] methods. The exchange correlation energy is calculated within the generalized gradient approximation (GGA) using the functional form proposed by Perdew and Wang which is known as Perdew-Wang 91 (PW91).[110, 111] The lattice constant, obtained from the optimization of the fcc-Pd bulk, is 3.953 $\mathring{A}$ which is in reasonable agreement with the experimental value of 3.891 $\mathring{A}$. The surface Brillouin zone is sampled with $4\times4\times2$ Monkhorst-pack kpoint grid. Pd (111) is modeled by a four layer slab with a (3×4) surface unit cell and the palladium layers separated by a 15 $\mathring{A}$ vacuum. The 12 Pd atoms in each layer allow for a coverage of 1/12 ML for adsorbates. The bottom two Pd layers were fixed to their bulk configuration during all calculations while top two layers were free to relax in all directions. Adsorption energies of all intermediates were calculated at their most stable geometry by the following equation:

$$E_{ads} = E_{slab+adsorbate} - E_{slab} - E_{adsorbate(gas)} \quad (4.1)$$

where $E_{slab+adsorbate}$ is the total energy of the adsorbed intermediate on the Pd slab, E_{slab} is the total energy of the Pd slab and $E_{adsorbate(gas)}$ is the total energy of the adsorbate in the gas phase. Transition states are located by combination of CI-NEB[112] and dimer[98, 113] methods and finally, vibrational frequency calculations have been performed to

clearly identify stable intermediate and transition state structures. The zero-point energy correction for all the structures was taken into account by using the following equation:

$$\Delta E_{ZPE} = \sum_i \frac{1}{2} h \nu_i \tag{4.2}$$

where h is the Plank constant and ν_i is the vibrational frequency of mode i. We note that all the energy values in this paper are zero-point energy corrected.

4.2.2 MICROKINETIC MODELING

For surface reactions, the forward rate constant (k_{for}) of each reaction is calculated using harmonic transition state theory (hTST)[114]

$$k_{for} = \frac{k_B T}{h} \frac{q_{TS,vib}}{q_{IS,vib}} e^{-\frac{E_{a\_for}}{k_B T}} \tag{4.3}$$

where k_B is the Boltzmann constant, T denotes the reaction temperature, h is the Planck constant, E_{a_for} stands for the zero-point energy-corrected activation barrier for the forward reaction derived from DFT calculations, and $q_{TS,vib}$ and $q_{IS,vib}$ are the (harmonic) vibrational partition functions for the transition state and the initial state, respectively, i.e., q_{vib} is calculated as

$$q_{vib} = \prod_i \frac{1}{1 - e^{\frac{-h\nu_i}{k_B T}}} \tag{4.4}$$

where ν_i is the vibrational frequency of each vibrational mode of the adsorbed intermediate derived from our DFT calculations.

The reverse rate constant (k_{rev}) is calculated similarly and the thermodynamic equilibrium constant K is given as

$$K = \frac{k_{for}}{k_{rev}} \tag{4.5}$$

For an adsorption reaction A(g)+*→A*, the equilibrium constant K is defined as

$$K = \frac{(q_{\text{vib}})_{A^*}}{(q_{\text{vib}} q_{\text{rot}} q_{\text{trans}})_{A(g)}} e^{\frac{-\Delta E_{\text{ads}}}{k_B T}} \tag{4.6}$$

where $(q_{\text{vib}})_{A^*}$ is the vibrational partition function of adsorbed A, and q_{vib}, q_{rot}, q_{trans} stand for vibrational, rotational, and translational partition functions, respectively. ΔE_{ads} represents the zero-point corrected adsorption energy. For an adsorption reaction A(g)+*→A*, the forward rate is given by collision theory with a sticking probability of 1.

$$k_{\text{for}} = \frac{1}{N_0 \sqrt{2\pi m_A k_B T}} \tag{4.7}$$

where N_0 is the number of sites per area (1.478×10^{19} m^2) and m_A denotes the molecular weight of A. The reverse rate constant is again given as

$$k_{\text{rev}} = \frac{k_{\text{for}}}{K} \tag{4.8}$$

With the forward and reverse rate constants defined, we solve the full set of steady-state rate equations to obtain the surface coverages of all possible reaction intermediates and the fraction of free sites using the BzzMath library[115] developed by Buzzi-Ferraris. No assumptions were made regarding rate-limiting steps.

4.3 Results

4.3.1 Adsorption and Desorption Reactions

Methyl propionate (MP) adsorbs weakly on Pd (111) (E_{ads}=-0.52 eV). In the most stable *cis* configuration of adsorbed methyl propionate the carbonyl oxygen binds to a single Pd atom (atop-site) with the molecular plane perpendicular to the surface (Figure

4.1.1). In the *trans* configuration (Figure 4.1.2), the two oxygen atoms of methyl propionate are located above a pair of adjacent Pd atoms (bridge-site) with an zero-point corrected adsorption energy of E_{ads}=-0.50 eV. Another possible configuration is the *chair* configuration, (Figure 4.1.3) in which the two oxygen atoms and the carbonyl carbon atom bind to three palladium atoms (E_{ads}=-0.50 eV). The weak π-bonded interactions of the C=O group with the surface[82] explains the quite small adsorption energy of MP (the three adsorption configurations of MP and all intermediates involved in the hydrodeoxygenation of MP are shown in Figure 4.1).

We will later show in our microkinetic analysis (Section 4.4.1), that we identified methanol, CO, ethane and ethene to be the main products of HDO of methyl propionate over Pd (111) model surfaces. Methanol adsorbs weakly on Pd (111) with zero-point corrected adsorption energy of -0.32 eV. In the adsorption configuration, the oxygen atom binds to one Pd atom (atop site). Ethane also physisorbs on palladium and adsorption energy of this intermediate is -0.17 eV. However, ethene and CO adsorb stronger with adsorption energies of -0.98 and -1.97 eV respectively. Additionally, the H_2 that was fed to the reactor with methyl propionate adsorbs dissociatively with an adsorption energy of -1.13 eV. Finally we note that the reaction parameters for all of the adsorption and desorption reactions, as well as their correspondent rate constants that were used in our microkinetic model, are presented in Table 4.1 and 4.2 (Step 65-73).

4.3.2 Elementary Surface Reactions

The investigated elementary reactions in the HDO of methyl propionate can be grouped into three different types of bond dissociations: C-O bond dissociations (e.g.

$CH_3CH_2COOCH_3 \rightarrow CH_3CH_2CO + OCH_3$), C-H bond dissociations (e.g. $CH_3CH_2COOCH_3 \rightarrow CH_3CHCOOCH_3$), and C-C bond dissociations (e.g. $CH_3CH_2CO \rightarrow CH_3CH_2 + CO$). The Zero-point corrected DFT-derived reaction energies, activation barriers, transition state (TS) imaginary frequencies, and TS bond lengths for all types of the elementary reactions investigated in HDO of methyl propionate, are listed in Table 4.1. Additionally, a schematic of the transition state geometry configurations are illustrated in Figure 4.2.

C-O BOND DISSOCIATIONS:

Adsorbed methyl propionate can go through two different C-O bond dissociations to either form propionate and methyl (Step 1: $CH_3CH_2COOCH_3$** + 1* ↔ CH_3CH_2COO** + CH_3*) or propanoyl and methoxy (Step 2: $CH_3CH_2COOCH_3$** + 2*↔ CH_3CH_2CO*** + CH_3O*). Our DFT result suggests that the propanoyl-methoxy bond is easier to cleave as the activation barrier of this step ($E_{act\text{-}step2}$= 0.73 eV) is remarkably smaller than the activation barrier of the methyl-propionate bond dissociation ($E_{act\text{-}step1}$= 1.54 eV). The trend in the activation barriers stays the same for other dehydrogenated derivatives of methyl propionate, such as $CH_3CHCOOCH_3$, $CH_2CH_2COOCH_3$, $CH_2CH_2COOCH_3$, and $CH_2CHCOOCH_3$ (Table 4.1). Consequently, propanoyl-methoxy type C-O bond dissociations are expected to be more favored in comparison to propionate-methyl type C-O bond dissociations.

Next, propanoyl (CH_3CH_2CO) goes through dehydrogenation and C-C bond cleavages to produce CO, and is one of the key intermediates in the decarbonylation (DCN) mechanism, while propionate undergoes dehydrogenation and C-C dissociation

steps to produce CO_2 and is essential to decarboxylation (DCX) reactions. Considering that production of propanoyl from methyl propionate and its dehydrogenated intermediates is more favored than production of propionate, we predict the DCN to be the dominant mechanism. In section 4.4.1, we verified our prediction by a microkinetic modeling analysis under realistic reaction conditions.

C-H BOND DISSOCIATIONS:

Adsorbed methyl propionate can be dehydrogenated via its α-, β-, and methoxy-end carbon. The dehydrogenation of the α-carbon (Step 3: $CH_3CH_2COOCH_3$** + 2* ↔ $CH_3CHCOOCH_3$*** + H*) is slightly exothermic (ΔE_0= -0.07 eV) and the activation barrier for this reaction is relatively small (0.70 eV). Dehydrogenation of the β-carbon (Step 4: $CH_3CH_2COOCH_3$** + 2* ↔ $CH_2CH_2COOCH_3$*** + H*) is slightly endothermic (ΔE_0=0.12 eV) and the activation barrier of this step is 0.78 eV. Finally, dehydrogenation of the methoxy-end carbon (Step 5: $CH_3CH_2COOCH_3$** + 2* ↔ $CH_3CH_2COOCH_2$*** + H*) is an almost thermoneutral process (ΔE_0=0.02 eV) with an activation barrier of 0.72 eV. We found that all dehydrogenations of α-, β-, and methoxy-end carbon have similarly small activation barriers and consequently, it is not possible to determine the dominant dehydrogenation pathway without developing a microkinetic model. However, all of these steps are less endothermic than the propanoyl-methoxy dissociation (ΔE_0=0.19) and consequently, we expect the dehydrogenation of methyl propionate to be slightly more favored than the propanoyl-methoxy dissociation.

The dehydrogenated derivatives of methyl propionate, $CH_3CHCOOCH_3$, $CH_2CH_2COOCH_3$, and $CH_3CH_2COOCH_2$, can go through C-O bond dissociations or

further dehydrogenation steps. All possible elementary reactions for these intermediates are identified and the reaction parameters of these elementary steps are listed in Table 4.1. Our DFT results (as well as our microkinetic modeling analysis in section 4.4.1) suggest that both $CH_2CH_2COOCH_3$ and $CH_3CHCOOCH_3$ go through further dehydrogenation to form $CH_2CHCOOCH_3$, as Step 8 ($CH_3CHCOOCH_3$*** + 1* ↔ $CH_2CHCOOCH_3$*** + H*, ΔE_0= -0.47 eV and E_{act}=0.46 eV), and Step 18 ($CH_2CH_2COOCH_3$*** + 1* ↔ $CH_2CHCOOCH_3$*** + H*, ΔE_0= -0.67 eV and E_{act}=0.34 eV) are exothermic and have very small activation barriers. We again considered various possible elementary reactions for further activation of $CH_2CHCOOCH_3$, but we will show below that these intermediates will go through C-O bond dissociation to form methoxy and CH_2CHCO where it next goes through C-C bond dissociation to form CH_2CH and CO.

In contrast to $CH_2CH_2COOCH_3$ and $CH_3CHCOOCH_3$, we predict that $CH_3CH_2COOCH_2$ undergoes a C-O bond dissociation to form propanoyl and OCH_2 (Step 28: $CH_3CH_2COOCH_2$*** + 3* ↔ CH_3CH_2CO*** + OCH_2***) since this step is exothermic by -0.31 eV and has a small activation barrier of 0.15 eV.

C-C BOND DISSOCIATIONS:

Propanoyl (CH_3CH_2CO) and other dehydrogenated derivatives of propanoyl, such as CH_3CHCO, CH_3CCO, CH_2CHCO, and CHCHCO can go through C-C bond dissociations to produce C_2 fragments and CO on the surface (Step30, 32, 34, 36, and 37). Dissociation of the C-C bond in propanoyl (Step 30) is exothermic, ΔE_0= -0.60, but this step has a large activation barrier of 1.01 eV. Dehydrogenation of the α- and β- carbon of

propanoyl facilitate the C-C bond dissociation. For instance the dissociation of the C-C bond of CH_3CCO (Step 37: $CH_3CCO^{***} \leftrightarrow CH_3C^* + CO^* + 1^*$) has an activation barrier of 0.44 eV. So it is expected that propanoyl will go through further dehydrogenation steps of the α- and β- carbons prior to C-C bond cleavages. In the microkinetic modeling analysis of the investigated reaction network of the HDO of methyl propionate we included various C-C bond dissociations, such as propionate decomposition to CH_3CH_2 and CO_2 (Step 61); however, as we explained before, our DFT results indicates that it is not probable that other C-C bond cleavages play an important role in the HDO of methyl propionate (Reaction parameters of all investigated C-C bond cleavages are listed in Table 4.1).

4.4 Discussions

4.4.1 Microkinetic Modeling

We previously[158] developed mean-field microkinetic models for the reaction mechanism of the decarboxylation and decarbonylation of propionic acid over Pd (111) model surfaces under realistic experimental gas phase conditions. In this study, we used the same methodology for developing a microkinetic model for the HDO of methyl propionate. All calculations were carried out at 473 K and partial pressures of methyl propionate and hydrogen of 0.01 and 0.2 bar, respectively, which are typical experimental conditions.[62, 67, 141-145, 159] Since we did not include a water-gas shift model in our microkintic model, we had to set the partial pressures of CO and CO_2 to 0.001 bar which correspondents to approximately 10% conversion. Computed turnover frequencies (TOF) of all elementary steps are summarized in Table 4.2.

The most abundant surface intermediates were adsorbed hydrogen, CO, and CH_3C with surface coverages of 67%, 20%, and 7% respectively. We note that we used a method similar to Grabow *et al.*[160] for determining coverage dependent adsorption energies of CO, H, and CH_3C. More details about adsorbate-adsorbate interactions can be found in our previously published paper.[158] A schematic of the most dominant reaction pathways is illustrated in Figure 4.3. The overall TOF is calculated to be 3.42×10^{-7} s^{-1} on Pd (111). As shown in Figure 4.3, the adsorbed methyl propionate molecule can be dehydrogenated from the α, β or methoxy-end (Step 3, 4, and 5 respectively) or it can go through propanoyl-methoxy bond dissociations (Step 2). Accordingly, there are four competing pathways and this study can only suggest that the most dominant pathway might involve methyl propionate to undergo two dehydrogenation steps of first α- and then β-carbon to form $CH_2CHCOOCH_3$ followed by C-O bond dissociation to form CH_2CHCO and OCH_3. CH_2CHCO goes through C-C bond cleavage to produce C2 hydrocarbons (Step 34) while the methoxy group gets hydrogenated to form methanol (Step 57). The TOF of methanol formation (Step 57: $CH_3O + H \rightarrow CH_3OH$) is $TOF_{Step57}=2.47\times10^{-7}$ s^{-1}, which is one order of magnitude larger than the competing dehydrogenation of methoxy to formaldehyde (Step 54: $CH_3O \rightarrow CH_2O + H$, $TOF_{Step57}=1.45\times10^{-8}$ s^{-1}). According to our DFT results (Table 4.1), formation of methanol from methoxy (Step 57) and decomposition of methoxy to CO (Step 54-56) are thermodynamically competitive; however, our microkinetic modeling result shows that methanol formation is favored due to an excess of hydrogen on the surface (dominant pathway:

$CH_3CH_2COOCH_3 \rightarrow CH_3CHCOOCH_3 \rightarrow CH_2CHCOOCH_3 \rightarrow CH_2CHCO+OCH_3 \rightarrow \ldots \rightarrow CH_3CH_3+CO+CH_3OH$, TOF=$1.85\times10^{-7}$ s^{-1}, red pathway in Figure 4.3).

In the second competitive pathway, methyl propionate gets dehydrogenated at the methoxy end to form $CH_3CH_2COOCH_2$ followed by C-O bond dissociation to form propanoyl (CH_3CH_2CO) and formaldehyde. Next, propanoyl gets dehydrogenated prior to C-C bond cleavage to form C_2 hydrocarbons and CO. Formaldehyde again can be further dehydrogenated to produce CO ($CH_3CH_2COOCH_3 \rightarrow CH_3CH_2COOCH_2 \rightarrow CH_3CH_2CO+OCH_2 \rightarrow \ldots \rightarrow CH_3CH_3+2CO$, green pathway in Figure 4.3). The computed TOF of the dominant pathway is only 2.4 times larger than for this pathway.

In the third pathway, methyl propionate directly dissociates to form methoxy and propanoyl ($CH_3CH_2COOCH_3 \rightarrow CH_3CH_2CO \rightarrow \ldots \rightarrow CH_3CH_3+CO+CH_3OH$, TOF=$6.43\times10^{-8}$ s^{-1}, black pathway in Figure 4.3). Later, the methoxy group gets hydrogenated to form methanol and the propanoyl species gets dehydrogenated followed by C-C bond cleavage to produce C2 hydrocarbons and CO.

In the last competitive pathway, methyl propionate first undergoes a dehydrogenation via its β-carbon, followed by another dehydrogenation from its α-carbon to produce $CH_2CHCOOCH_3$. This intermediate goes through C-O bond dissociation to form CH_2CHCO and methoxy. We note that the only difference of this pathway and the most dominant pathway is in the order of dehydrogenation steps. In the dominant pathway, first α-carbon and then β-carbon gets dehydrogenated while in this pathway first the β-carbon and then the α-carbon get dehydrogenated. However, it is less probable that methyl propionate first goes through dehydrogenation of the β-carbon as the TOF of this

pathway is an order of magnitude smaller than the most dominant pathway ($CH_3CH_2COOCH_3 \rightarrow CH_2CH_2COOCH_3 \rightarrow CH_2CHCOOCH_3 \rightarrow CH_2CHCO+OCH_3 \rightarrow \ldots \rightarrow CH_3CH_3+CO+CH_3OH$, TOF=$1.39\times10^{-8}$ s^{-1}, blue pathway in Figure 4.3).

Finally, the most dominant decarboxylation pathway is: $CH_3CH_2COOCH_3 \rightarrow CH_3CH_2COOCH_2 \rightarrow CH_3CH_2COO+CH_2 \rightarrow \ldots \rightarrow CH_3CH_3+CO_2+CH_4$ (TOF=3.49×10^{-10}) where the rate of this pathway is 3 orders of magnitude smaller than competing decarbonylation pathways. Overall, we conclude that the dominant catalytic cycles are decarbonylation pathways and in all of these pathways, dehydrogenation of α- and β-carbon play an important role in further activity of adsorbed intermediates. In the next section, we investigate the importance of the dehydrogenation steps in the overall activity.

4.4.2 Apparent Activation Barrier, Reaction Orders, and Sensitivity Analysis

The apparent activation barrier was computed in the temperature range of 423 to 523 K.

$$E_a = RT^2\left(\frac{\partial \ln(r)}{\partial T}\right)_{p_i} \tag{4.9}$$

Our model predicts an apparent activation energy of 1.01 eV. Next, the reaction order with respect to hydrogen was calculated at 473 K in the range of 0.05 to 0.4 bar. Similarly, the reaction order of propanoic acid and CO were calculated at 473 K and a pressure range of 0.005 to 0.1 bar and 0.0001 to 0.1 bar, respectively.

$$\alpha_i = \left(\frac{\partial \ln(r)}{\partial \ln(p_i)} \right)_{T, p_{j \neq i}} \tag{4.10}$$

Our model predicts a reaction order with respect to methyl propionate of +1.0, with respect to CO of -0.49, and finally with respect to H_2 of -0.07.

To understand the sensitivity of our model and to determine rate controlling steps and intermediates in the mechanism, we computed Campbell's degrees of rate and thermodynamic control,[147-149] X_{RC} and X_{TRC}. Rate controlling steps and intermediates are those transition states and intermediates that most strongly influence the reaction rate and are potential activity descriptors.

$$X_{\mathrm{RC},i} = \frac{k_i}{r} \left(\frac{\partial r}{\partial k_i} \right)_{K_i, k_j \neq k_i} \quad , \quad X_{\mathrm{TRC},n} = \frac{1}{r} \left(\frac{\partial r}{\partial \left(\frac{-G_n^0}{RT} \right)} \right)_{G_{m \neq n}^0, G_i^{0,\mathrm{TS}}} \tag{4.11}$$

where r is the overall rate of reaction, k_i is the forward rate constant for step i, K_i equilibrium constant for step i, R is the gas constant, T denotes the reaction temperature, and G_n^0 is the free energy of adsorbate n. The result of our Campbell's degree of rate control analysis suggests that the most controlling steps are propanoyl-methoxy type C-O bond dissociation and dehydrogenation of α-, β-, and methoxy-end carbons of methyl propionate. Reaction 2 ($CH_3CH_2COOCH_3$** + 2*↔ CH_3CH_2CO*** + CH_3O*), propanoyl-methoxy dissociation, is the most rate-controlling C-O bond dissociation step with the X_{RC} of 0.17. Additionally, Reaction 12 ($CH_2CHCOOCH_3$*** + 1* ↔ CH_2CHCO*** +CH_3O*) and Reaction 28 ($CH_3CH_2COOCH_2$*** + 3* ↔ CH_3CH_2CO*** + OCH_2***) are also rate-controlling with the X_{RC} of 0.09 and 0.02 respectively, such that the sum of C-O rate-control is 0.28.

Under the investigated reaction conditions of 473 K and excess of hydrogen, we found that dehydrogenation steps are even more rate-controlling than C-O bond dissociations. Dehydrogenation of the α-carbon of methyl propionate (Reaction 2) is the most rate-controlling dehydrogenation step with an X_{RC} of 0.35. Dehydrogenation of the methoxy-end carbon of methyl propionate (Reaction 5) has an X_{RC} of 0.19, and finally, dehydrogenation of the β-carbon of methyl propionate (Reaction 4) and also dehydrogenation of the β-carbon of $CH_3CHCOOCH_3$*** (Reaction 8: $CH_3CHCOOCH_3$*** + 1* ↔ $CH_2CHCOOCH_3$*** + H*) have a X_{RC} of 0.05 and 0.03 respectively. We note that the sum of the degrees of rate control is slightly smaller than one (0.9) due to numerical inaccuracies of our nonlinear equation solver; however, the trends should not be affected by these numerical issues.

The analysis above suggests the following: Considering that all of the rate-controlling dehydrogenation steps are chemically similar and involve bonding of a hydrogen and carbon atom to the metal surface, we expect that all of these dissociations can be described by one independent activity descriptor, e.g., the dehydrogenation of the α-carbon of methyl propionate. Similarly, all of the rate-controlling C-O bond dissociations are chemically similar and involve bonding of both an oxygen and carbon atom to the metal surface, such that we expect all of these dissociations can be described by another independent activity descriptor, e.g., the C-O dissociation of the propanoyl-methoxy bond.

Finally, the thermodynamic rate control analysis suggests that the adsorption free energy of CO* has a significant effect on the overall rate with X_{TRC} = -0.57 such that destabilizing the adsorbed CO improves the overall reaction rate.

4.4.3 BEP Relationships

In our effort to provide correlations for predicting activation barriers without having to perform expensive transition state searches and also to better understand the accuracy of these correlations, we show in Figure 4.4 Brønsted-Evans-Polanyi (BEP) relations that aim at linearly correlating the activation barrier of all C-H, C-C, and C-O bond dissociations to their reaction energies on Pd (111).[161, 162] The obtained BEP relation for C-H dissociation is $E_{act}=0.43\times\Delta E_0+0.76$. The mean absolute error (MAE) of this relation is 0.10 eV and the largest error in all the data point is 0.27 eV which originates from CH_2O dissociation to CHO and H. Next, the BEP relation for all C-C bond cleavage steps is $E_{act}=0.26\times\Delta E_0+1.03$ with a MAE of 0.11 eV and a maximum error of 0.23 eV. The dissociation of CH_3CCO to CH_3C and CO has the maximum absolute error among all C-C bond cleavage steps. Finally, the C-O bond dissociation data points can be fitted to $E_{act}=0.42\times\Delta E_0+0.58$ with a MAE of 0.12 eV. The largest error is 0.29 eV which comes from the dissociation of $CH_3CH_2COOCH_2$ to CH_3CH_2CO and OCH_2.

4.5 CONCLUSIONS

The hydrodeoxygenation of methyl propionate was investigated over a Pd (111) surface model from first principles. An extensive network of elementary reactions was studied and a microkinetic model was developed to study the reaction mechanism at a reaction temperature of 473K. We found the most dominant pathway to involve methyl propionate to undergo two dehydrogenation steps of both its α and β-carbon to form $CH_2CHCOOCH_3$ followed by a C-O bond dissociation to form CH_2CHCO and OCH_3, next, CH_2CHCO goes through C-C bond cleavage to produce C2 hydrocarbons. Surface

methoxy species get hydrogenated to form methanol, i.e., the most dominant pathway is $CH_3CH_2COOCH_3 \rightarrow CH_3CHCOOCH_3 \rightarrow CH_2CHCOOCH_3 \rightarrow CH_2CHCO+OCH_3 \rightarrow \ldots \rightarrow CH_3CH_3+CO+CH_3OH$, TOF=$1.85\times10^{-7}$ s^{-1}. Decarbonylation is the dominant mechanism and methanol, CO, and C_2 hydrocarbons are predicted to be the main reaction products of the HDO of methyl propionate over Pd (111). H, CO, and CH_3C were identified to be the most abundant surface intermediates. The apparent activation barrier was calculated to be 1.01 eV. Finally, our sensitivity analysis suggests that dehydrogenation of α-carbon of methyl propionate and the propanoyl-methoxy bond dissociation are rate-controlling steps and possible activity descriptors.

4.6 ACKNOWLEDGEMENTS

This work has been supported by the National Science Foundation under Grant No. CBET-1159863 and in part by the USC future fuels program and USC NanoCenter. Computational resources have been provided by the National Energy Research Scientific Computing Center (NERSC) which is supported by the Office of Science of the U.S. Department of Energy and in part by XSEDE resources provided by the National Institute for Computational Sciences (NICS), Texas advanced Computing Center (TACC), and the Purdue University under grant number TG-CTS090100. Finally, computing resources from the USC NanoCenter and USC's High Performance Computing Group are gratefully acknowledged.

4.7 TABLES

TABLE 4.1 Zero-point energy corrected activation barriers, reaction energies, transition-state imaginary frequencies, and TS bond lengths of all elementary steps investigated for the HDO of methyl propionate. * symbolizes an active site and ** symbolizes two occupied active sites, etc.

#	Reaction	E_{act} (eV)	ΔE_0 (eV)	ν (cm^{-1})	TS bond (Å)
Step 1	$CH_3CH_2COOCH_3$** + 1* ↔ CH_3CH_2COO** + CH_3*	1.54	-0.45	521 *i*	2.08
Step 2	$CH_3CH_2COOCH_3$** + 2*↔ CH_3CH_2CO*** + CH_3O*	0.73	0.19	161 *i*	2.05
Step 3	$CH_3CH_2COOCH_3$** + 2* ↔ $CH_3CHCOOCH_3$*** + H*	0.70	-0.07	950 *i*	1.55
Step 4	$CH_3CH_2COOCH_3$** + 2* ↔ $CH_2CH_2COOCH_3$*** + H*	0.78	0.12	776 *i*	1.59
Step 5	$CH_3CH_2COOCH_3$** + 2* ↔ $CH_3CH_2COOCH_2$*** + H*	0.72	0.02	844 *i*	1.56
Step 6	$CH_3CHCOOCH_3$*** + 1* ↔ CH_3CHCOO*** + CH_3*	1.63	0.00	539 *i*	2.02
Step 7	$CH_3CHCOOCH_3$*** + 1* ↔ CH_3CHCO*** + CH_3O*	0.74	0.27	187 *i*	2.08
Step 8	$CH_3CHCOOCH_3$*** + 1* ↔ $CH_2CHCOOCH_3$*** + H*	0.46	-0.47	1019 *i*	1.51
Step 9	$CH_3CHCOOCH_3$*** + 1* ↔ $CH_3CHCOOCH_2$*** + H*	0.75	-0.02	856 *i*	1.53
Step 10	$CH_2CHCOOCH_3$*** + 2* ↔ $CH_2CHCOOCH_2$**** + H*	0.96	0.13	958 *i*	1.54
Step 11	$CH_2CHCOOCH_3$*** + 2* ↔ $CHCHCOOCH_3$**** + H*	0.85	0.03	743 *i*	1.79
Step 12	$CH_2CHCOOCH_3$*** + 1* ↔ CH_2CHCO*** +CH_3O*	0.91	0.41	241 *i*	2.09

Step 13	$CH_3CHCOOCH_2$*** + 2* ↔ $CH_2CHCOOCH_2$**** + H*	0.38	-0.33	951 *i*	1.54
Step 14	$CH_3CHCOOCH_2$*** + 3* ↔ CH_3CHCO*** + OCH_2***	0.47	-0.19	252 *i*	1.97
Step 15	$CHCHCOOCH_3$**** + 2* ↔ CHCH*** + $COOCH_3$***	0.91	-0.06	453 *i*	2.00
Step 16	$CH_2CHCOOCH_2$**** + 3* → CH_2CH*** + $COOCH_2$****	0.93	0.01	335 *i*	2.09
Step 17	$CH_2CHCOOCH_2$**** + 2* ↔ CH_2CHCO*** + OCH_2***	0.47	-0.20	222 *i*	2.06
Step 18	$CH_2CH_2COOCH_3$*** + 1* ↔ $CH_2CHCOOCH_3$*** + H*	0.34	-0.67	965 *i*	1.49
Step 19	$CH_2CH_2COOCH_3$*** + 1* ↔ $CH_2CH_2COOCH_2$*** + H*	0.83	0.00	1037 *i*	1.54
Step 20	$CH_2CH_2COOCH_3$*** + 2* ↔ CH_2CH_2** + $COOCH_3$***	0.98	-0.42	429 *i*	2.04
Step 21	$CH_2CH_2COOCH_3$*** + 1* ↔ CH_2CH_2CO*** + CH_3O*	0.58	0.20	190 *i*	2.05
Step 22	$CH_2CH_2COOCH_2$*** + 1* ↔ $CH_2CHCOOCH_2$**** + H*	0.67	-0.54	993 *i*	1.61
Step 23	$CH_2CH_2COOCH_2$*** + 3* ↔ CH_2CH_2** +$COOCH_2$****	0.91	-0.55	453 *i*	2.05
Step 24	$CH_2CH_2COOCH_2$*** + 3* ↔ CH_2CH_2CO*** + OCH_2***	0.26	-0.30	244 *i*	1.88
Step 25	$CH_3CH_2COOCH_2$*** + 1* ↔ $CH_3CHCOOCH_2$*** + H*	0.59	-0.11	750 *i*	1.59
Step 26	$CH_3CH_2COOCH_2$*** + 1* ↔ $CH_2CH_2COOCH_2$*** + H*	0.89	0.10	670 *i*	1.64
Step 27	$CH_3CH_2COOCH_2$*** + 1* ↔ CH_3CH_2COO** + CH_2**	0.70	-0.57	217 *i*	2.30
Step 28	$CH_3CH_2COOCH_2$*** + 3* ↔ CH_3CH_2CO*** + OCH_2***	0.15	-0.31	259 *i*	1.82
Step 29	CH_3CH_2CO*** + 1* ↔ CH_3CHCO*** + H*	0.81	0.01	901 *i*	1.57
Step 30	CH_3CH_2CO*** ↔ CH_3CH_2* + CO* + 1*	1.01	-0.60	372 *i*	2.34

Step 31	$CH_3CHCO^{***} + 1^* \leftrightarrow CH_2CHCO^{***} + H^*$	0.46	-0.34	766 *i*	1.47
Step 32	$CH_3CHCO^{***} \leftrightarrow CH_3CH^{**} + CO^*$	1.02	-0.81	410 *i*	2.30
Step 33	$CH_3CHCO^{***} + 1^* \leftrightarrow CH_3CCO^{***} + H^*$	0.52	-0.38	848 *i*	1.66
Step 34	$CH_2CHCO^{***} + 1^* \leftrightarrow CH_2CH^{***} + CO^*$	0.78	-0.74	491 *i*	1.98
Step 35	$CH_2CHCO^{***} + 2^* \leftrightarrow CHCHCO^{****} + H^*$	0.68	0.01	631 *i*	1.59
Step 36	$CHCHCO^{****} \leftrightarrow CHCH^{***} + CO^*$	0.57	-1.09	462 *i*	2.05
Step 37	$CH_3CCO^{***} \leftrightarrow CH_3C^* + CO^* + 1^*$	0.44	-1.37	396 *i*	1.73
Step 38	$CH_2CH_2CO^{***} \leftrightarrow CH_2CH_2^{**} + CO^*$	0.76	-1.22	471 *i*	2.13
Step 39	$CH_2CH_2CO^{***} + 1^* \leftrightarrow CH_2CHCO^{***} + H^*$	0.66	-0.46	942 *i*	1.61
Step 40	$COOCH_3^{***} + 2^* \leftrightarrow COOCH_2^{***} + H^*$	0.58	-0.13	900 *i*	1.56
Step 41	$COOCH_3^{***} \leftrightarrow CO^* + CH_3O^* + 1^*$	0.56	-0.60	205 *i*	2.04
Step 42	$COOCH_3^{***} \leftrightarrow CO_2^* + CH_3^* + 1^*$	1.48	-0.38	554 *i*	1.92
Step 43	$COOCH_2^{****} \leftrightarrow CO^* + OCH_2^{***}$	0.29	-0.95	345 *i*	1.78
Step 44	$COOCH_2^{****} \leftrightarrow CO_2^* + CH_2^{**} + 1^*$	0.89	-0.35	432 *i*	2.03
Step 45	$CHCH^{***} + H^* \leftrightarrow CH_2CH^{***} + 1^*$	0.82	0.30	1025 *i*	1.57
Step 46	$CH_2CH^{***} \leftrightarrow CH_2C^{**} + H^*$	0.46	-0.43	970 *i*	1.48
Step 47	$CH_2C^{**}+H^* \leftrightarrow CH_3C^{**} + 2^*$	0.88	-0.23	966 *i*	1.70
Step 48	$CH_2CH^{***} + H^* \leftrightarrow CH_2CH_2^{**} + 2^*$	0.88	-0.02	787 *i*	1.75

Step 49	$CH_2CH^{***} + H^* \leftrightarrow CH_3CH^{**} + 2^*$	0.79	0.26	982 *i*	1.55
Step 50	$CH_3C^{***} + H^* \leftrightarrow CH_3CH^{**} + 2^*$	1.11	0.94	196 *i*	1.13
Step 51	$CH_3CH^{**} + H^* \leftrightarrow CH_3CH_2^* + 2^*$	0.86	0.21	801 *i*	1.69
Step 52	$CH_2CH_2^{**} + H^* \leftrightarrow CH_3CH_2^* + 2^*$	0.88	0.48	924 *i*	1.53
Step 53	$CH_3CH_2^* + H^* \leftrightarrow CH_3CH_3^* + 1^*$	0.60	0.04	941 *i*	1.59
Step 54	$CH_3O^* + 3^* \leftrightarrow CH_2O^{***} + H^*$	0.44	-0.48	914 *i*	1.46
Step 55	$CH_2O^{***} + 1^* \leftrightarrow CHO^{***} + H^*$	0.67	-0.87	603 *i*	1.64
Step 56	$CHO^{***} \leftrightarrow CO^* + H^* + 1^*$	0.16	-1.42	684 *i*	1.36
Step 57	$CH_3O^* + H^* \leftrightarrow CH_3OH^* + 1^*$	0.60	0.01	726 *i*	1.61
Step 58	$CH_2^{**} + H^* \leftrightarrow CH_3^* + 2^*$	0.78	0.10	788 *i*	1.84
Step 59	$CH_3^* + H^* \leftrightarrow CH_4^* + 1^*$	0.58	-0.03	938 *i*	1.57
Step 60	$CH_3CH_2COO^{**} \leftrightarrow CH_3CH_2^* + CO_2^*$	1.43	0.24	435 *i*	1.93
Step 61	$CH_3CH_2COO^{**} + 2^* \leftrightarrow CH_3CHCOO^{***} + H^*$	1.22	0.38	811 *i*	1.64
Step 62	$CH_3CHCOO^{***} + \leftrightarrow CH_3CH^{**} + CO_2^*$	0.96	-0.32	449 *i*	2.10
Step 63	$CH_3CHCOO^{***} + 1^* \leftrightarrow CH_3CCOO^{***} + H^*$	0.85	-0.08	784 *i*	1.75
Step 64	$CH_3CCOO^{***} \leftrightarrow CH_3C^* + CO_2^* + 1^*$	0.65	-1.17	575 *i*	2.09
Step 65	$CH_3CH_2COOCH_3 + 2^* \leftrightarrow CH_3CH_2COOCH_3^{**}$	N/A	-0.52	N/A	N/A
Step 66	$CH_3CH_3 + 1^* \leftrightarrow CH_3CH_3^*$	N/A	-0.17	N/A	N/A

Step 67	$CH_2CH_2 + 2* \leftrightarrow CH_2CH_2**$	N/A	-0.98	N/A	N/A
Step 68	$CHCH + 3* \leftrightarrow CHCH***$	N/A	-1.67	N/A	N/A
Step 69	$CH_4 + 1* \leftrightarrow CH_4*$	N/A	-0.08	N/A	N/A
Step 70	$CH_3OH + 1* \leftrightarrow CH_3OH*$	N/A	-0.32	N/A	N/A
Step 71	$CO + 1* \leftrightarrow CO*$	N/A	-1.97	N/A	N/A
Step 72	$CO_2 + 1* \leftrightarrow CO_2*$	N/A	0.02	N/A	N/A
Step 73	$H_2 + 2* \rightarrow 2H*$	N/A	-1.13	N/A	N/A

TABLE 4.2 Equilibrium, forward rate constants, and calculated net rate (turnover frequency) for the elementary steps in the HDO of methyl propionate over Pd (111) model surfaces at a temperature of 473 K**.**

	Reaction	**K_{eq}**	**k_f (s^{-1})**	**TOF (s^{-1})**
Step 1	$CH_3CH_2COOCH_3$** + 1* ↔ CH_3CH_2COO** + CH_3*	1.08×10^{-5}	2.08×10^{-4}	6.17×10^{-15}
Step 2	$CH_3CH_2COOCH_3$** + 2*↔ CH_3CH_2CO*** + CH_3O*	7.63×10^{-3}	3.96×10^{4}	6.43×10^{-8}
Step 3	$CH_3CH_2COOCH_3$** + 2* ↔ $CH_3CHCOOCH_3$*** + H*	1.52	1.37×10^{5}	1.85×10^{-7}
Step 4	$CH_3CH_2COOCH_3$** + 2* ↔ $CH_2CH_2COOCH_3$*** + H*	1.91×10^{-2}	1.01×10^{4}	1.39×10^{-8}
Step 5	$CH_3CH_2COOCH_3$** + 2* ↔ $CH_3CH_2COOCH_2$*** + H*	9.81×10^{-2}	5.02×10^{4}	7.85×10^{-8}
Step 6	$CH_3CHCOOCH_3$*** + 1* ↔ CH_3CHCOO*** + CH_3*	2.41	4.00×10^{-5}	1.35×10^{-18}
Step 7	$CH_3CHCOOCH_3$*** + 1* ↔ CH_3CHCO*** + CH_3O*	2.49×10^{-3}	1.30×10^{5}	4.37×10^{-9}
Step 8	$CH_3CHCOOCH_3$*** + 1* ↔ $CH_2CHCOOCH_3$*** + H*	3.98×10^{4}	4.64×10^{7}	1.80×10^{-7}
Step 9	$CH_3CHCOOCH_3$*** + 1* ↔ $CH_3CHCOOCH_2$*** + H*	4.89×10^{-1}	3.04×10^{4}	9.07×10^{-10}
Step 10	$CH_2CHCOOCH_3$*** + 2* ↔ $CH_2CHCOOCH_2$**** + H*	1.27×10^{-2}	2.69×10^{2}	1.39×10^{-9}
Step 11	$CH_2CHCOOCH_3$*** + 2* ↔ $CHCHCOOCH_3$**** + H*	1.90×10^{-1}	5.29×10^{3}	1.25×10^{-11}
Step 12	$CH_2CHCOOCH_3$*** + 1* ↔ CH_2CHCO*** +CH_3O*	1.28×10^{-4}	1.98×10^{3}	1.92×10^{-7}
Step 13	$CH_3CHCOOCH_2$*** + 2* ↔ $CH_2CHCOOCH_2$**** + H*	1.03×10^{3}	2.69×10^{8}	1.76×10^{-9}

Step 14	$CH_3CHCOOCH_2$*** + 3* ↔ CH_3CHCO*** + OCH_2***	3.77×10^{2}	1.10×10^{8}	5.01×10^{-11}
Step 15	$CHCHCOOCH_3$**** + 2* ↔ CHCH*** + $COOCH_3$***	1.24×10^{1}	2.77×10^{3}	1.25×10^{-11}
Step 16	$CH_2CHCOOCH_2$**** + 3* ↔ CH_2CH*** + $COOCH_2$****	2.59	6.95×10^{2}	3.12×10^{-16}
Step 17	$CH_2CHCOOCH_2$**** + 2* ↔ CH_2CHCO*** + OCH_2***	7.51×10^{2}	3.84×10^{8}	3.15×10^{-9}
Step 18	$CH_2CH_2COOCH_3$*** + 1* ↔ $CH_2CHCOOCH_3$*** + H*	3.17×10^{6}	8.55×10^{8}	1.30×10^{-8}
Step 19	$CH_2CH_2COOCH_3$*** + 1* ↔ $CH_2CH_2COOCH_2$*** + H*	1.14×10^{-1}	1.93×10^{3}	7.42×10^{-13}
Step 20	$CH_2CH_2COOCH_3$*** + 2* ↔ CH_2CH_2** + $COOCH_3$***	3.87×10^{4}	9.87×10^{1}	2.09×10^{15}
Step 21	$CH_2CH_2COOCH_3$*** + 1* ↔ CH_2CH_2CO*** + CH_3O*	7.44×10^{-3}	2.41×10^{6}	9.34×10^{-10}
Step 22	$CH_2CH_2COOCH_2$*** + 1* ↔ $CH_2CHCOOCH_2$**** + H*	3.52×10^{5}	8.95×10^{5}	-3.23×10^{-15}
Step 23	$CH_2CH_2COOCH_2$*** + 3* ↔ CH_2CH_2** +$COOCH_2$****	5.74×10^{6}	3.30×10^{3}	2.85×10^{-19}
Step 24	$CH_2CH_2COOCH_2$*** + 3* ↔ CH_2CH_2CO*** + OCH_2***	8.44×10^{3}	1.18×10^{10}	1.02×10^{-12}
Step 25	$CH_3CH_2COOCH_2$*** + 1* ↔ $CH_3CHCOOCH_2$*** + H*	7.56	3.86×10^{6}	9.06×10^{-10}
Step 26	$CH_3CH_2COOCH_2$*** + 1* ↔ $CH_2CH_2COOCH_2$*** + H*	2.22×10^{-2}	5.89×10^{2}	2.73×10^{-13}
Step 27	$CH_3CH_2COOCH_2$*** + 1* ↔ CH_3CH_2COO** + CH_2**	2.74×10^{6}	7.28×10^{5}	3.49×10^{-10}
Step 28	$CH_3CH_2COOCH_2$*** + 3* ↔ CH_3CH_2CO*** + OCH_2***	8.01×10^{3}	5.37×10^{10}	7.72×10^{-8}
Step 29	CH_3CH_2CO*** + 1* ↔ CH_3CHCO*** + H*	3.08×10^{-1}	7.47×10^{3}	1.05×10^{-7}

Step 30	$CH_3CH_2CO^{***} \leftrightarrow CH_3CH_2^* + CO^* + 1^*$	4.73×10^{6}	1.36×10^{2}	3.61×10^{-8}
Step 31	$CH_3CHCO^{***} + 1^* \leftrightarrow CH_2CHCO^{***} + H^*$	2.06×10^{3}	5.51×10^{7}	-6.17×10^{-8}
Step 32	$CH_3CHCO^{***} \leftrightarrow CH_3CH^{**} + CO^*$	6.68×10^{8}	3.55×10^{2}	6.62×10^{-11}
Step 33	$CH_3CHCO^{***} + 1^* \leftrightarrow CH_3CCO^{***} + H^*$	1.05×10^{4}	1.68×10^{7}	1.71×10^{-7}
Step 34	$CH_2CHCO^{***} + 1^* \leftrightarrow CH_2CH^{***} + CO^*$	6.37×10^{7}	3.06×10^{4}	5.85×10^{-8}
Step 35	$CH_2CHCO^{***} + 2^* \leftrightarrow CHCHCO^{****} + H^*$	9.03×10^{-1}	5.54×10^{5}	5.83×10^{-8}
Step 36	$CHCHCO^{****} \leftrightarrow CHCH^{***} + CO^*$	7.59×10^{11}	5.57×10^{6}	5.83×10^{-8}
Step 37	$CH_3CCO^{***} \leftrightarrow CH_3C^* + CO^* + 1^*$	1.00×10^{15}	1.76×10^{8}	1.71×10^{-7}
Step 38	$CH_2CH_2CO^{***} \leftrightarrow CH_2CH_2^{**} + CO^*$	2.19×10^{13}	1.81×10^{5}	9.85×10^{-10}
Step 39	$CH_2CH_2CO^{***} + 1^* \leftrightarrow CH_2CHCO^{***} + H^*$	5.46×10^{4}	3.89×10^{5}	-4.99×10^{-11}
Step 40	$COOCH_3^{***} + 2^* \leftrightarrow COOCH_2^{***} + H^*$	1.69×10^{1}	1.42×10^{6}	3.02×10^{-15}
Step 41	$COOCH_3^{***} \leftrightarrow CO^* + CH_3O^* + 1^*$	4.20×10^{6}	1.77×10^{7}	1.25×10^{-11}
Step 42	$COOCH_3^{***} \leftrightarrow CO_2^* + CH_3^* + 1^*$	1.21×10^{5}	1.87×10^{-3}	1.33×10^{-21}
Step 43	$COOCH_2^{****} \leftrightarrow CO^* + OCH_2^{***}$	1.85×10^{10}	1.75×10^{10}	3.36×10^{-15}
Step 44	$COOCH_2^{****} \leftrightarrow CO_2^* + CH_2^{**} + 1^*$	1.11×10^{4}	3.62×10^{3}	7.89×10^{-21}
Step 45	$CHCH^{***} + H^* \leftrightarrow CH_2CH^{***} + 1^*$	8.26×10^{-4}	2.03×10^{4}	5.83×10^{-8}

Step 46	$CH_2CH^{***} \leftrightarrow CH_2C^{**} + H^*$	3.07×10^{4}	1.73×10^{8}	-2.39×10^{-7}
Step 47	$CH_2C^{**}+H^* \leftrightarrow CH_3C^{**} + 2^*$	8.27×10^{2}	5.44×10^{3}	-2.39×10^{-7}
Step 48	$CH_2CH^{***} + H^* \leftrightarrow CH_2CH_2^{**} + 2^*$	6.28	5.64×10^{3}	2.08×10^{-7}
Step 49	$CH_2CH^{***} + H^* \leftrightarrow CH_3CH^{**} + 2^*$	5.10×10^{-3}	3.71×10^{4}	1.48×10^{-7}
Step 50	$CH_3C^{***} + H^* \leftrightarrow CH_3CH^{**} + 2^*$	6.32×10^{-11}	3.50	-1.12×10^{-7}
Step 51	$CH_3CH^{**} + H^* \leftrightarrow CH_3CH_2^* + 2^*$	2.30×10^{-2}	1.74×10^{4}	3.60×10^{-8}
Step 52	$CH_2CH_2^{**} + H^* \leftrightarrow CH_3CH_2^* + 2^*$	2.05×10^{-5}	3.54×10^{3}	-2.31×10^{-8}
Step 53	$CH_3CH_2^* + H^* \leftrightarrow CH_3CH_3^* + 1^*$	2.18	3.67×10^{6}	1.10×10^{-7}
Step 54	$CH_3O^* + 3^* \leftrightarrow CH_2O^{***} + H^*$	7.42×10^{4}	1.02×10^{8}	1.45×10^{-8}
Step 55	$CH_2O^{***} + 1^* \leftrightarrow CHO^{***} + H^*$	1.20×10^{9}	9.66×10^{6}	9.49×10^{-8}
Step 56	$CHO^{***} \leftrightarrow CO^* + H^* + 1^*$	9.35×10^{14}	1.24×10^{12}	9.49×10^{-8}
Step 57	$CH_3O^* + H^* \leftrightarrow CH_3OH^* + 1^*$	5.74×10^{-2}	4.23×10^{5}	2.47×10^{-7}
Step 58	$CH_2^{**} + H^* \leftrightarrow CH_3^* + 2^*$	6.45×10^{-1}	1.12×10^{5}	3.49×10^{-10}
Step 59	$CH_3^* + H^* \leftrightarrow CH_4^* + 1^*$	4.38×10^{1}	1.50×10^{7}	3.49×10^{-10}
Step 60	$CH_3CH_2COO^{**} \leftrightarrow CH_3CH_2^* + CO_2^*$	1.75×10^{-2}	2.49×10^{-2}	6.09×10^{-8}
Step 61	$CH_3CH_2COO^{**} + 2^* \leftrightarrow CH_3CHCOO^{***} + H^*$	2.14×10^{-5}	2.46×10^{-1}	3.49×10^{-10}

Step 62	$CH_3CHCOO^{***} + \leftrightarrow\ CH_3CH^{**} + CO_2^*$	1.50×10^{4}	1.41×10^{3}	2.67×10^{-10}
Step 63	$CH_3CHCOO^{***} + 1^* \leftrightarrow\ CH_3CCOO^{***} + H^*$	8.51	7.97×10^{3}	8.25×10^{-11}
Step 64	$CH_3CCOO^{***} \leftrightarrow\ CH_3C^* + CO_2^* + 1^*$	1.04×10^{13}	1.65×10^{6}	8.25×10^{-11}
Step 65	$CH_3CH_2COOCH_3 + 2^* \leftrightarrow CH_3CH_2COOCH_3^{**}$	1.81×10^{-5}	8.73×10^{7}	3.42×10^{-7}
Step 66	$CH_3CH_3 + 1^* \leftrightarrow CH_3CH_3^*$	2.79×10^{-7}	1.50×10^{8}	1.10×10^{-7}
Step 67	$CH_2CH_2 + 2^* \leftrightarrow CH_2CH_2^{**}$	2.79×10^{1}	1.55×10^{8}	2.32×10^{-7}
Step 68	$CHCH + 3^* \leftrightarrow CHCH^{***}$	2.59×10^{12}	1.61×10^{8}	5.29×10^{-14}
Step 69	$CH_4 + 1^* \leftrightarrow CH_4^*$	8.51×10^{-6}	2.05×10^{8}	3.49×10^{-10}
Step 70	$CH_3OH + 1^* \leftrightarrow CH_3OH^*$	5.89×10^{-5}	1.45×10^{8}	2.47×10^{-7}
Step 71	$CO + 1^* \leftrightarrow CO^*$	5.33×10^{12}	1.55×10^{8}	Equilibrium
Step 72	$CO_2 + 1^* \leftrightarrow CO_2^*$	2.79×10^{-6}	1.30×10^{8}	3.49×10^{-10}
Step 73	$H_2 + 2^* \rightarrow 2H^*$	1.65×10^{6}	5.80×10^{8}	Equilibrium

4.8 FIGURES

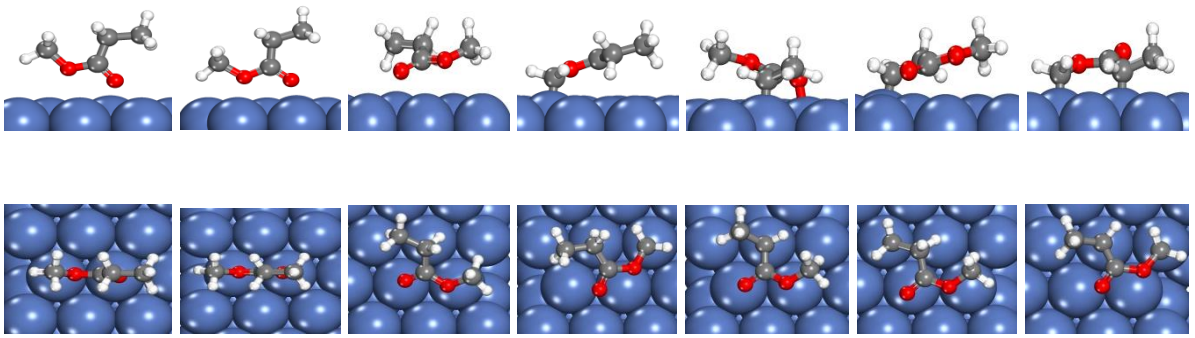

(1) (2) (3) (4) (5) (6) (7)

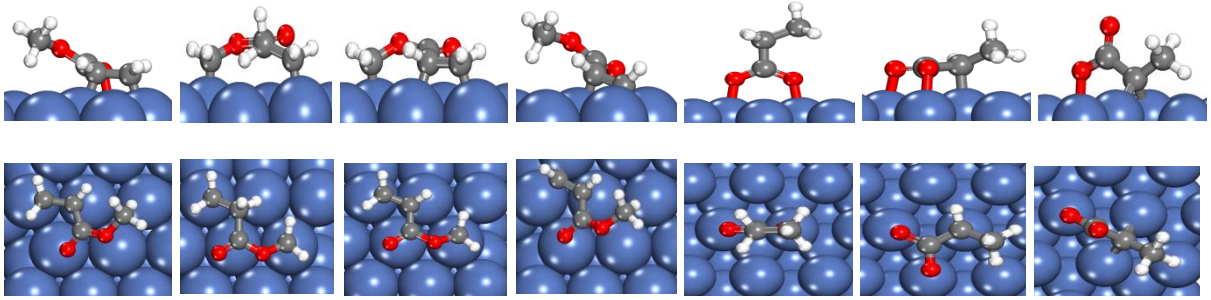

(8) (9) (10) (11) (12) (13) (14)

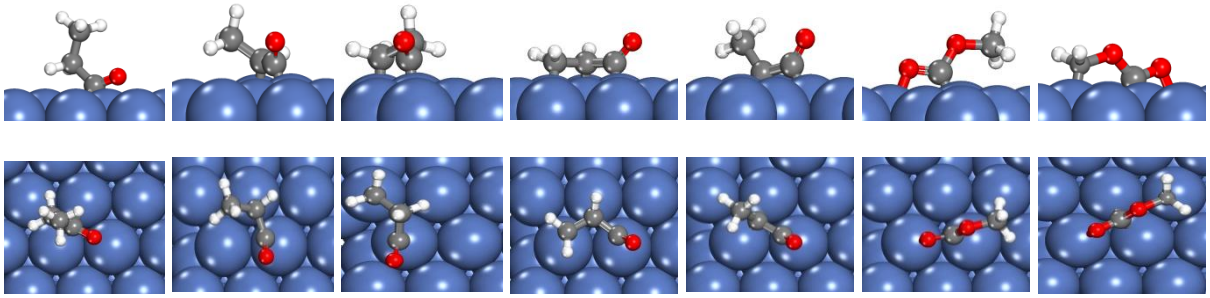

(15) (16) (17) (18) (19) (20) (21)

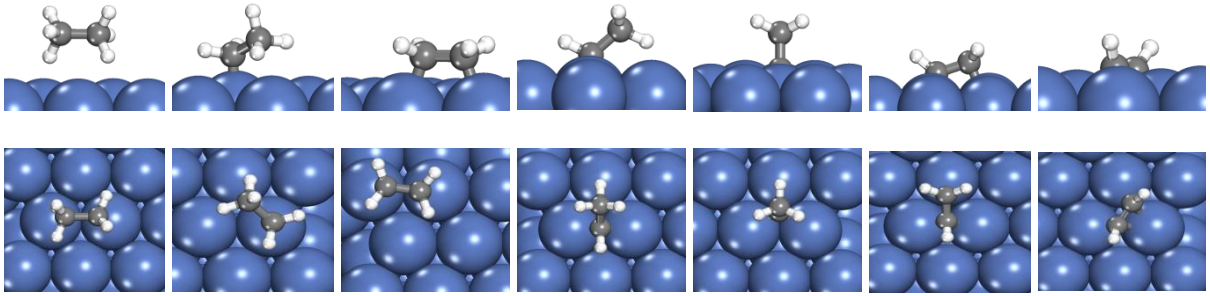

(22) (23) (24) (25) (26) (27) (28)

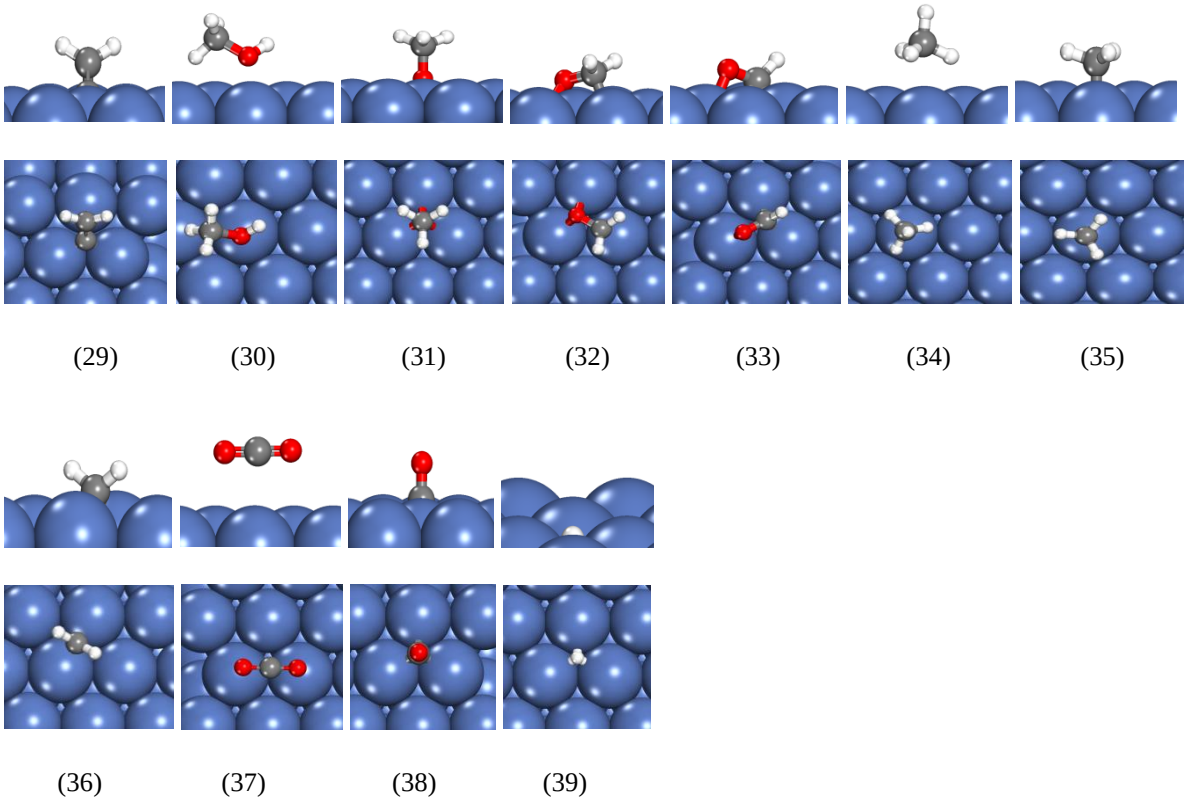

Figure 4.1 Side and top view of most stable adsorption structure of intermediates involved in HDO of methyl propionate over Pd (111). (1) Methyl Propionate-Cis ($CH_3CH_2COOCH_3$); (2) Methyl Propionate-Trans ($CH_3CH_2COOCH_3$); (3) Methyl Propionate-Chair ($CH_3CH_2COOCH_3$); (4) Methylene Propionate ($CH_3CH_2COOCH_2$); (5) Methylcarboxylethyledene ($CH_3CHCOOCH_3$); (6) Methylcarboxylethene ($CH_2CH_2COOCH_3$); (7) Methylenecarboxylethyledne ($CH_3CHCOOCH_2$); (8) Methylcarboxylvinyl ($CH_2CHCOOCH_3$); (9) Methylenecarboxylethene ($CH_2CH_2COOCH_2$); (10) Methylenecarboxylvinyl ($CH_2CHCOOCH_2$); (11) Methylcarboxylethyne ($CHCHCOOCH_3$); (12)Propionate (CH_3CH_2COO); (13) Carboxylethylidene

(CH_3CHCOO); (14) Carboxylethenyl (CH_3CCOO); (15) Propanoyl (CH_3CH_2CO); (16) Carbonylethylidene (CH_3CHCO); (17) Carbonylethene (CH_2CH_2CO); (18) Carbonylvinyl (CH_2CHCO); (19) Carbonylethenyl (CH_3CCO); (20) carboxylmethyl ($COOCH_3$); (21) carboxylmethylene ($COOCH_2$); (22) Ethane (CH_3CH_3); (23) Ethyl (CH_3CH_2); (24) Ethene (CH_2CH_2); (25) Ethylidene (CH_3CH); (26) Ethenyl (CH_3C); (27) Vinyl CH_2CH; (28) Ethyne (CHCH); (29) CH_2C; (30) Methanol (CH_3OH); (31) Methoxy (CH_3O); (32) Formaldehyde (CH_2O); (33) Formyl (CHO); (34) Methane (CH_4); (35) Methyl (CH_3); (36) Methylene (CH_2); (37) Carbon dioxide (CO_2); (38) Carbon monoxide(CO); (39)Hydrogen atom(H);

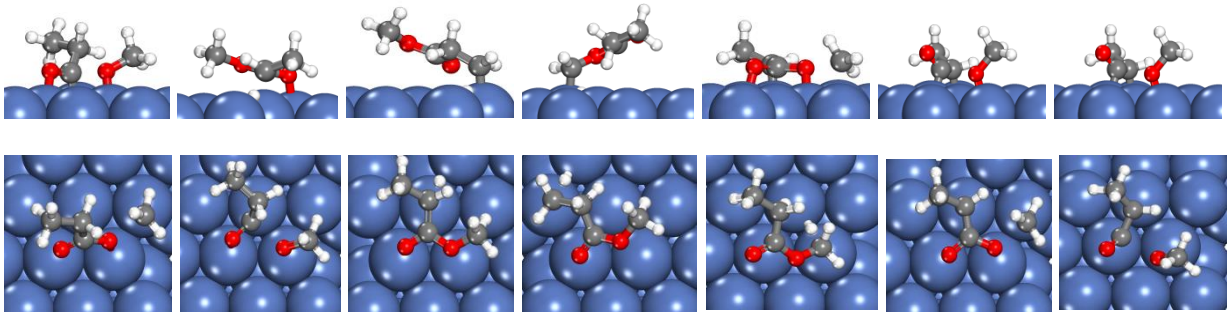

(1) (2) (3) (4) (5) (6) (7)

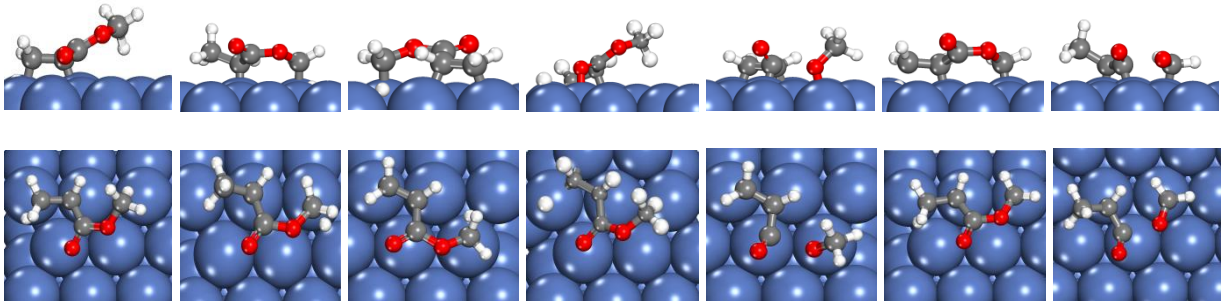

(8) (9) (10) (11) (12) (13) (14)

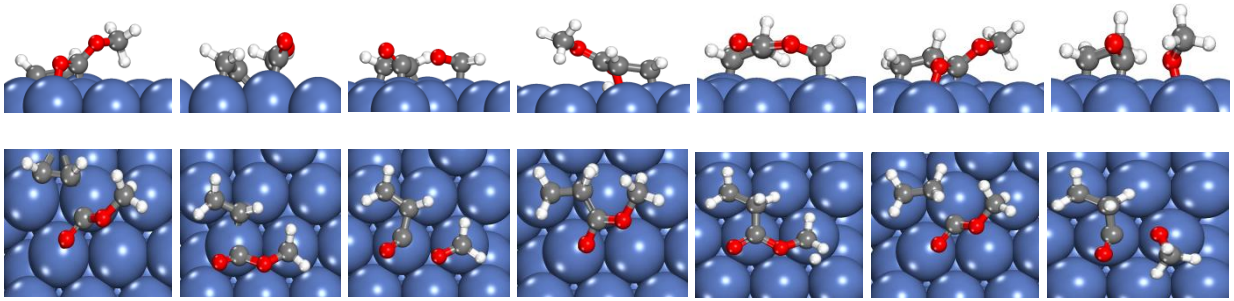

(15) (16) (17) (18) (19) (20) (21)

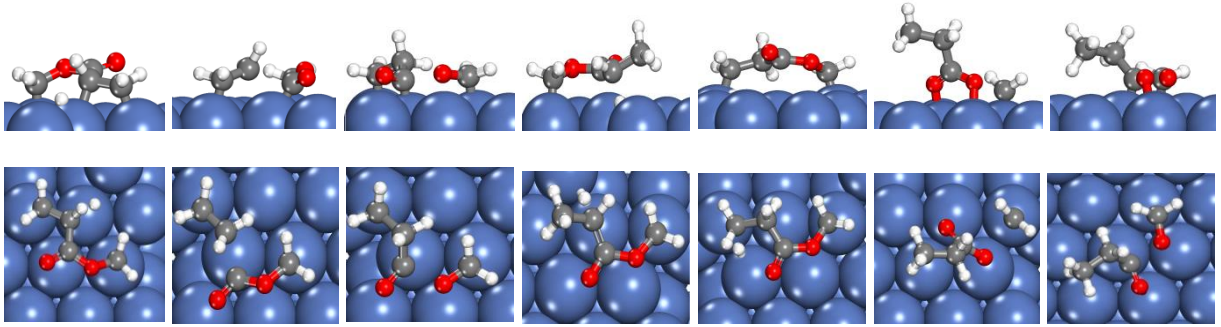

(22) (23) (24) (25) (26) (27) (28)

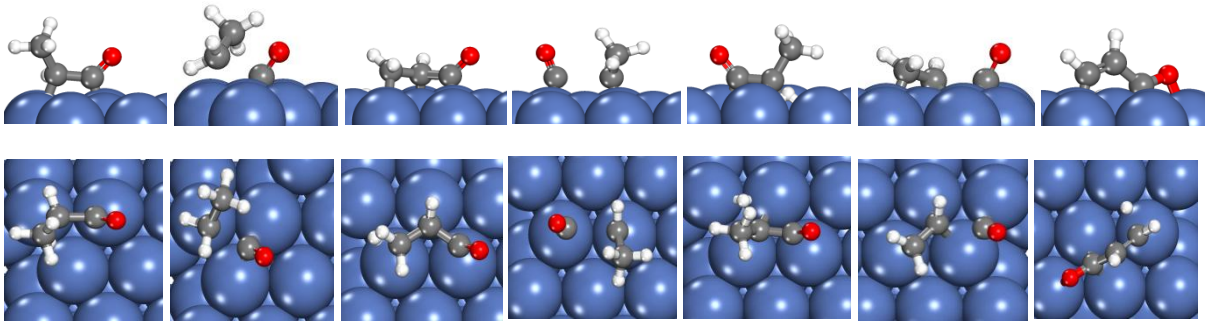

(29) (30) (31) (32) (33) (34) (35)

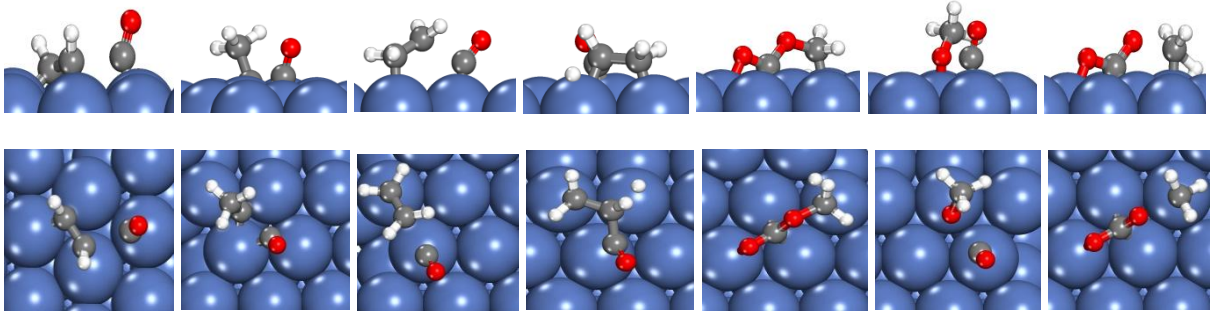

(36) (37) (38) (39) (40) (41) (42)

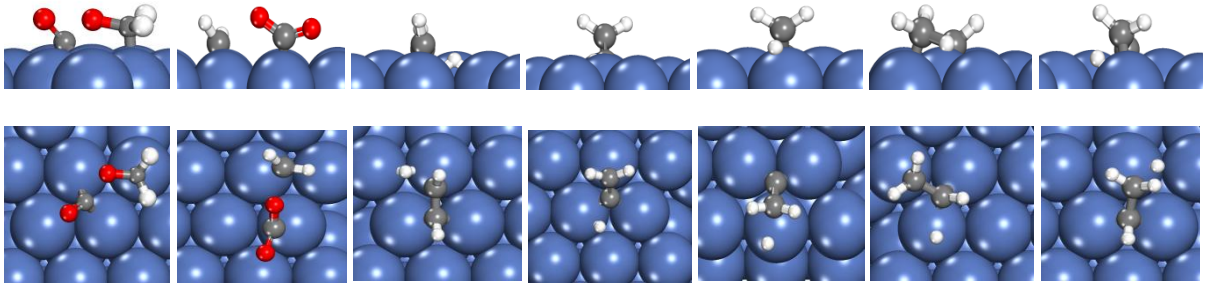

(43) (44) (45) (46) (47) (48) (49)

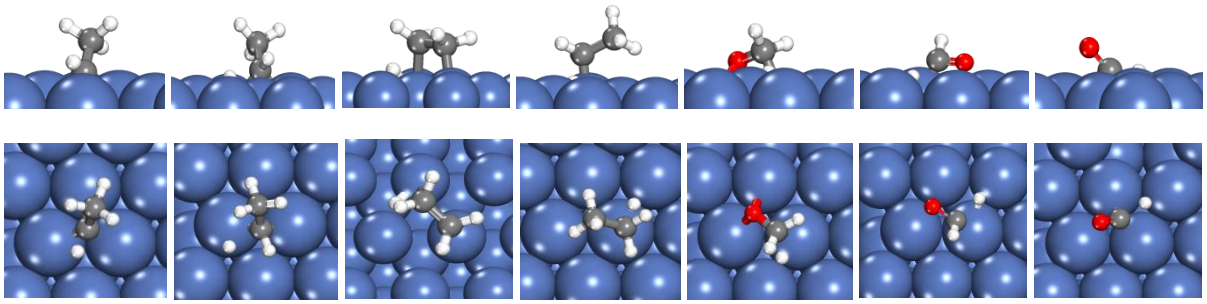

(50) (51) (52) (53) (54) (55) (56)

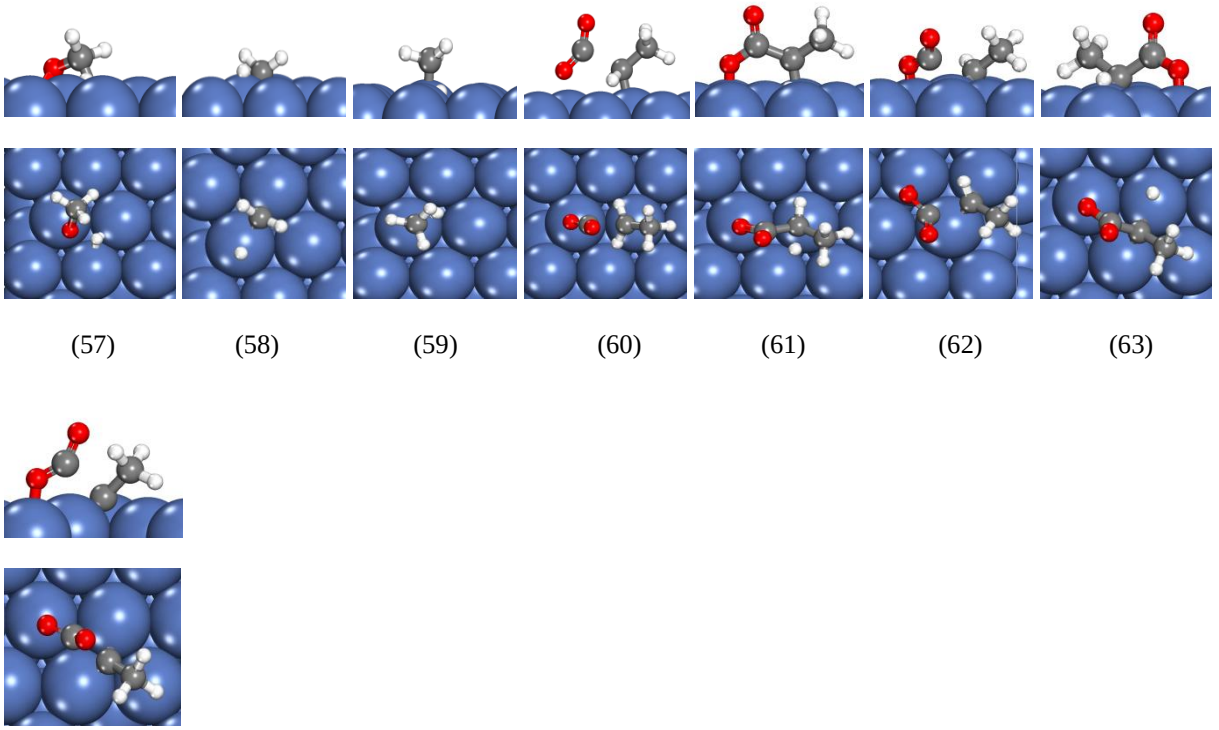

Figure 4.2 Snapshots of transition states of the elementary reactions involved in hydrodeoxygenation of methyl propionate on Pd (111) surface. Upper panels are for side views and lower ones for top views. Numbers correspond to the reaction numbers shown in Table 4.1.

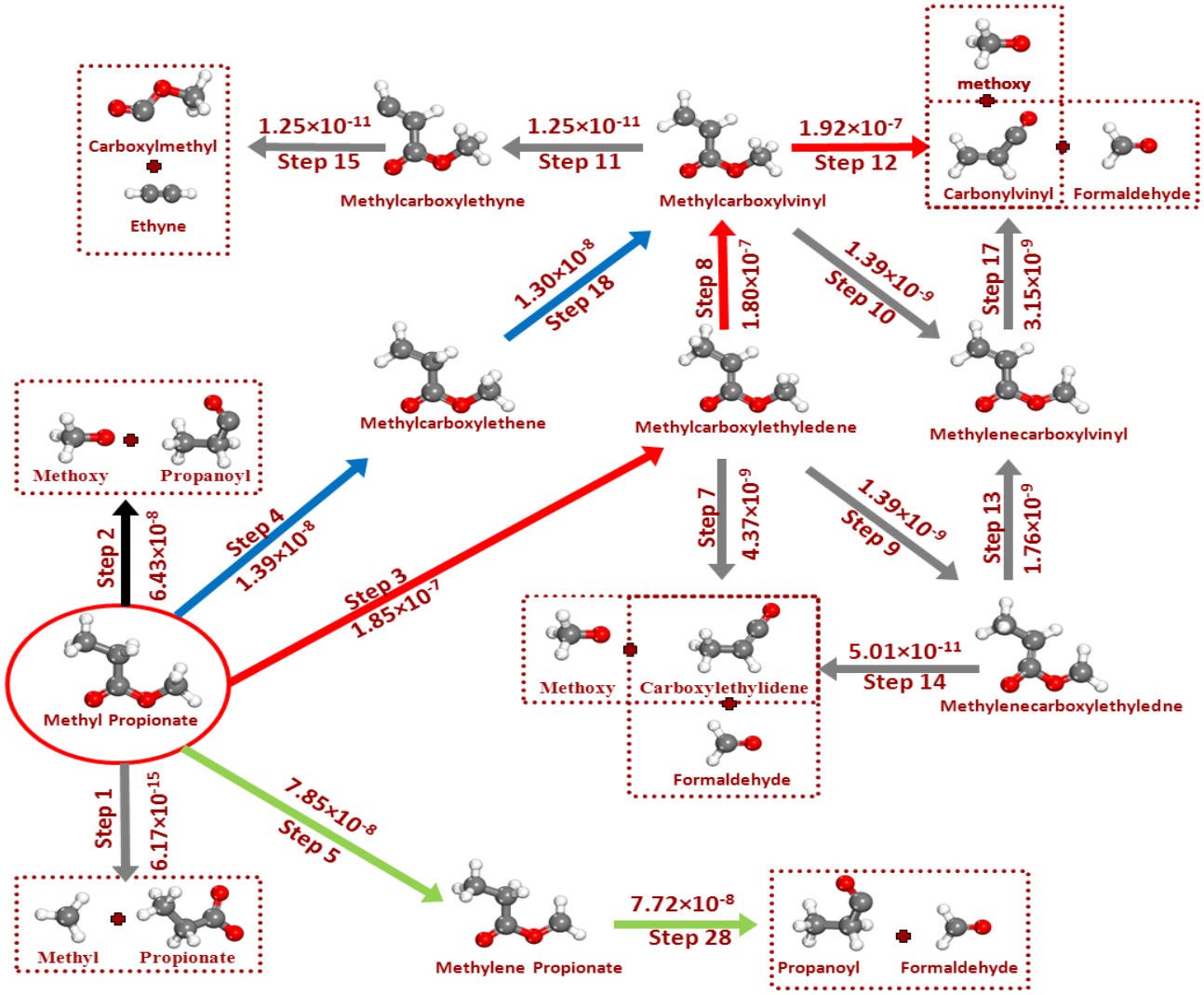
Carboxylmethyl
Ethyne
1.25×10-11
Step 15
Methylcarboxylethyne
1.25×10-11
Step 11
Methylcarboxylvinyl
1.92×10-7
Step 12
methoxy
Carbonylvinyl
Formaldehyde
1.30×10-8
Step 18
Step 8
1.80×10-7
1.39×10-9
Step 10
Step 17
3.15×10-9
Methylcarboxylethene
Methylcarboxylethyledene
Methylenecarboxylvinyl
Methoxy
Propanoyl
Step 2
6.43×10-8
Step 4
1.39×10-8
Step 3
1.85×10-7
Step 7
4.37×10-9
1.39×10-9
Step 9
Step 13
1.76×10-9
Methoxy
Carboxylethylidene
Formaldehyde
5.01×10-11
Step 14
Methylenecarboxylethyledne
Methyl Propionate
Step 1
6.17×10-15
7.85×10-8
Step 5
Methyl
Propionate
Methylene Propionate
7.72×10-8
Step 28
Propanoyl
Formaldehyde

Figure 4.3 Schematic representation of the most important reaction pathways in the network considered in the HDO of methyl propionate over Pd (111). We note that in our microkinetic calculations, we included all the elementary steps illustrated in Table 4.1; however, this Figure is a schematic of elementary steps involved in the dominant pathways of the HDO of methyl propionate. TOFs (s^{-1}) shown for various elementary steps are computed at a temperature of 473 K, a methyl propionate gas phase pressure of 0.01 bar and a hydrogen partial pressure of 0.2 bar. TOFs (s^{-1}) for elementary reactions not shown in this figure are illustrated in Table 4.2. The most dominant pathway is shown in red color ($CH_3CH_2COOCH3 \rightarrow CH_3CHCOOCH_3 \rightarrow CH_2CHCOOCH_3 \rightarrow CH_2CHCO+OCH_3 \rightarrow \ldots \rightarrow CH_3CH_3+CO+CH_3OH$). Other competitive pathways are shown in black, blue, and green. Reaction pathways of the intermediates shown in rectangles are explained in detail in sections 4.3.2.

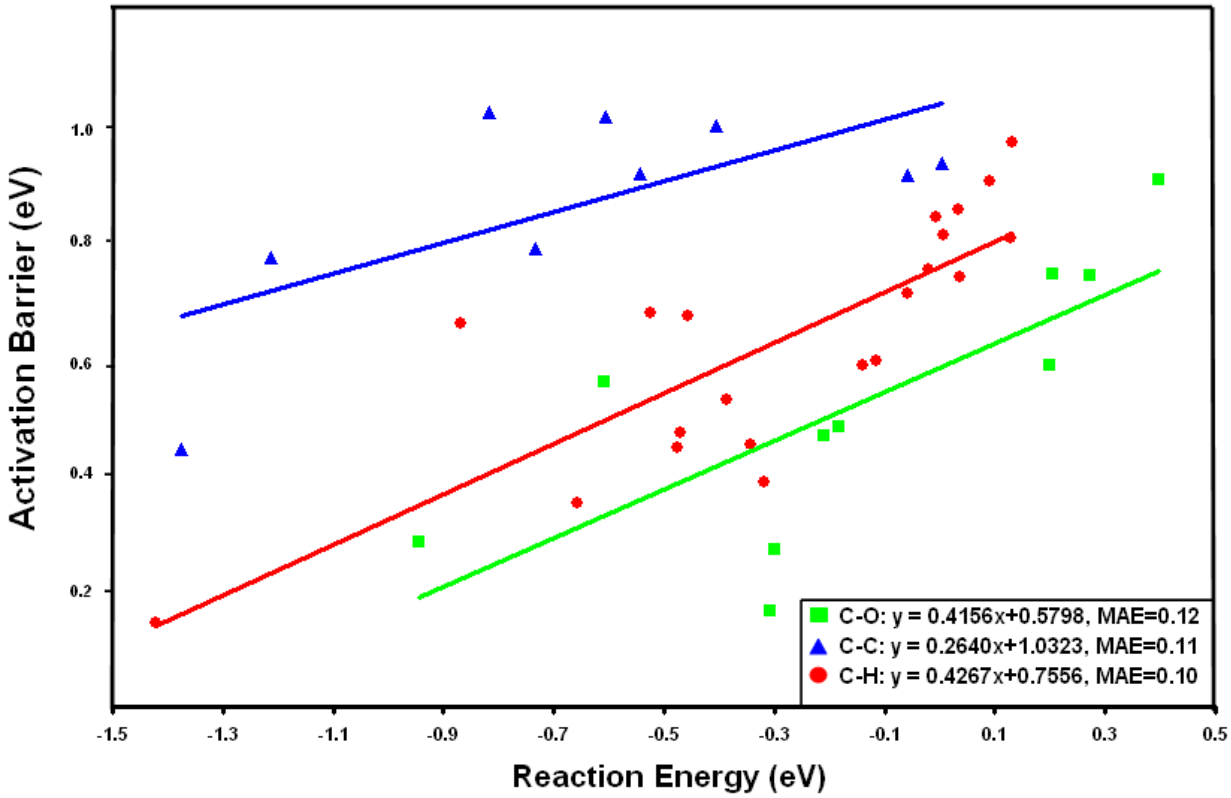

Figure 4.4 Brønsted-Evans-Polanyi (BEP) correlation for C-O (green line), C-C (blue line) and C-H (red line) bond dissociations. The zero-point energy corrected activation barriers of investigated reactions have been plotted vs. zero-point energy corrected reaction energies.

CHAPTER 5

UNRAVELING THE MECHANISM OF PROPANOIC ACID HYDRODEOXYGENATION USING DEUTERIUM KINETIC ISOTOPE EFFECTS[1]

[1] Y. K. Lugo-José, S. Behtash, M. Nicholson, J. R. Monnier, A. Heyden, and C. T. Williams To be submittedto Journal of Molecular Catalysis A .

ABSTRACT

A combined experimental and computational kinetic isotope effect (KIE) study was performed for the catalytic hydrodeoxygenation (HDO) of deuterium-labeled propanoic acid (PAc-2, 2-D2) over Pd catalyst. For the experimental study, the kinetics were measured in a plug flow reactor over a 5 wt% Pd/C catalyst at 200ºC and 1 atm under differential conversion using a reactor feed consisting of 1.2% PAc and 5% or 20% H_2, with the balance of He. The Pd/C catalyst had a dispersion of 16.9% and a mean particle size of 6.8 nm, suggesting a very high percentage of exposed Pd(111) facets. Different experimental KIE values for the high (k_H/k_D = 1.16 ± 0.07) and low (k_H/k_D = 1.62 ± 0.05) partial pressures of hydrogen were observed. Density functional theory calculations were performed to obtain the reaction parameters of the elementary steps involved in the HDO of PAc on Pd (111), and a microkinetic model was developed to estimate the KIE for the low hydrogen partial pressure case from first principles. The computed result (k_H/k_D = 1.49) is in good agreement with the experiment. In addition, the product distribution showed to be C_2H_6 and CO suggesting decarbonylation (DCN) is the main reaction pathway. This provides strong evidence for the proposed mechanism for the formation of C_2H_6 on Pd(111) and supported Pd with a high percentage of that exposed crystal face presented in the nanoparticles.

5.1 INTRODUCTION

An extensive amount of research has explored the catalytic performance for the hydrodeoxygenation (HDO) of biomass-derived carboxylic acids and acid esters[163, 164]. Supported palladium is one of the most investigated catalysts in the area of catalytic hydrodeoxygenation of biomass derived platform molecules[165-176]. For instance, early studies showed that supported palladium offers a strong activity and selectivity for the HDO of PAc[177-181]. While kinetic studies reveal overall reaction rates, reaction orders, and apparent activation barriers, they do not provide enough information for determining the fundamental elementary steps involved in the reaction mechanism[182, 183]. For HDO reactions, the network of these underlying steps is complex and not yet fully understood.

In our previous DFT studies,[119, 158, 184] the HDO of PAc was investigated over Pd (111) model surfaces. The elementary reaction steps involved in the decarbonylation (DCN) and decarboxylation (DCX) were identified from first principles. A microkinetic model was developed to determine the dominant pathway and rate-controlling steps under realistic reaction conditions of 200 ºC and low, medium, and high partial pressures of hydrogen (0.001, 1 and 30 bar) in the presence and absence of solvents. Our results suggest that under gas phase reaction conditions, DCN is favored over the DCX, while in the presence of water, DCN and DCX mechanisms become essentially competitive.[184] This is in agreement with our experimental study of the gas-phase HDO of PAc over supported group VIII noble metals, where we found that on various metals the DCN pathway dominates.[159]

Additionally, computations found that in all reaction environments, and at a low hydrogen partial pressure, dehydrogenation of the α-carbon in PAc is the most rate-controlling step. With increasing hydrogen partial pressure, C-OH bond dissociation becomes most rate-controlling and the importance of C-H bond cleavage is diminished.[184] The dissociation of the C-OH bond is one of the key reactions in the DCN and was previously also identified as the rate-determining step for the HDO of acetic acid.[82, 150] Our studies, however, clearly suggest that at all conditions, dehydrogenation steps of the α-carbon of the acid have at least some importance for the HDO to hydrocarbons. Barteau et al. and Zhong et al. have also examined the deoxygenation of carboxylic acids over Pd[163, 185, 186]. They suggest that a carboxylate intermediate dehydrogenates, which is accompanied by C-O bond cleavage, resulting in CO and hydrocarbon formation by C-C bond cleavage.

The present study explores the deuterium kinetic isotope effect (KIE) [187-192],[193, 194] for the HDO of PAc in order to further confirm the importance of C-H bond cleavage in the reaction pathway. PAc substituted with deuterium at the α-carbon position (CH_3CD_2COOH) was deoxygenated over 5wt% Pd/C catalyst and its reaction rate compared with that obtained from unlabeled PAc (CH_3CH_2COOH). From these data, experimental rate constant ratio (k_H/k_D) was determined under various hydrogen partial pressures. Density functional theory (DFT) calculations were performed for labeled PAc and its intermediates on Pd (111) to obtain the reaction parameters of all the elementary steps involved. The DFT-derived parameters were then implemented in a microkinetic model that allowed prediction of k_H/k_D under the same conditions used for the experiments. The experimental and computational results are consistent with each other,

and confirm the importance of C-H bond cleavage in governing the rates of HDO of PAc on Pd.

5.2 METHODS

5.2.1 MATERIAL AND CATALYST CHARACTERIZATION

The experimental conditions have been previously reported in detail and thus will only be discussed briefly[178]. Propanoic Acid (CH_3CH_2COOH, 99%) and propanoic acid-2, 2-d2 (CH_3CD_2COOH, 98%) were purchased from Alfa Aesar and Cambridge Isotope Laboratories, respectively, and used without further purification. The gases for the reactor studies were H_2 (UHP), He (UHP), and Ar (UHP) supplied by Airgas National Welders. The 5wt% Pd/C catalyst (CP-97, SA_{BET} = 615 $m^{2/}g$) was supplied by BASF and reduced *in-situ* at 350ºC. The dispersion and particle size of 5wt% Pd/C was determined by pulsed hydrogen titration of oxygen pre-covered sites utilizing a Micromeritics 2920 AutoChem II Analyzer.

5.2.2 REACTION EVALUATION

The reaction rate experiments were performed in a single pass, packed bed, plug flow reactor system connected to a GC system [178]. The experiments were carried out under differential (<5%) conversion at 200ºC under atmospheric pressure. Two sets of experiments were conducted: (1) 1.2% PAc/20%H_2/balance He and (2) 1.2% PAc/5%H_2/balance He in a total flow of 50 sccm. This catalyst under these reaction conditions has previously been shown to be free of both external and internal mass transfer effects [178]. The reaction rate was determined based on the formation of

product (which is proportional to the rate of acid disappearance) in μmol product formed/min·gcat. The TOF was determined based on the reaction rate per active site of the 5wt% Pd/C catalyst. Unlabeled and labeled PAc were kept in separate vapor-liquid equilibrium (VLE) saturators and the concentrations of the both acids (e.g. labeled and unlabeled) in the gas feed were set equal prior to starting the reaction. Once the reaction with unlabeled PAc reached steady-state, the reactor feed was switched to the labeled PAc. This process was cycled until steady state reaction was attained for each species. In this way, the KIE can be determined as the ratio between the unlabeled and labeled reaction rates (i.e., k_H/k_D).

Measurements of the isotopic composition of the products were conducted by mass spectroscopy. To ensure only the products were analyzed by MS, the PAc (unreacted) was condensed in a cold trap (-55ºC). This was verified by analyzing the gas effluent with gas chromatography to confirm only products such as C_2H_6 and CO were detected. The gas products were diluted with argon carrier gas before being sampled by a Stanford Research Systems RGA100 mass spectrometer with an electron multiplier. The detailed description of this apparatus and sampling procedure is included in the Supplemental Information. The masses 29, 30 and 31 were monitored to track various ethane species, while water, nitrogen, oxygen, hydrogen and argon were also monitored. For the MS study the PAc conversion was increased (~10%) by adjusting the catalyst loading (0.9g).

5.2.3 COMPUTATIONAL METHODOLOGY

All density functional theory calculations have been conducted with the Vienna Ab Initio Simulation Package (VASP).[106, 107, 195] The Kohn-Sham valence states are expanded in a plane wave basis sets with an energy cut-off of up to 400 eV. The interaction between core electrons is described with projector-augmented wave (PAW)[107, 109] method. The exchange correlation energy is calculated within the generalized gradient approximation (GGA) using the functional form proposed by Perdew and Wang, which is known as Perdew-Wang 91 (PW91).[88, 110, 111] Similar pseudopotentials were used for hydrogen and deuterium atoms with only the mass modified for deuterium atoms.

The lattice constant obtained from the optimization of the fcc-Pd bulk is 3.953 $\AA$, which is in reasonable agreement with the experimental value of 3.891 $\AA$. The surface Brillouin zone is sampled with $4\times4\times2$ Monkhorst-pack k-point grid. Pd (111) is modeled by a 4-layer slab with a (3×4) surface unit cell and the palladium layers separated by a 15 $\AA$ vacuum.

The bottom two layers were fixed to their bulk configuration during all calculations while the top two layers were free to relax in all directions. Adsorption energies of all intermediates were calculated at their most stable geometry by the following equation:

$$E_{ads} = E_{slab+adsorbate} - E_{slab} - E_{adsorbate}(g) \quad (5.1)$$

where $E_{\text{slab+adsorbate}}$ is the total energy of the adsorbed intermediate on the Pd slab, E_{slab} is the total energy of the Pd slab and $E_{\text{adsorbate}}$(g) is the total energy of the adsorbate in the gas phase.

Transition states were obtained from our previous DFT studies[119, 158, 184] on PAc and finally, vibrational frequency calculations have been performed to obtain the frequency modes for all labeled intermediates and transition state structures.

The zero-point energy correction for all the structures was taken into account by using the following equation:

$$\Delta E_{ZPE} = \sum_i \frac{1}{2} h\nu_i \quad (5.2)$$

where h is the Plank constant and ν_i is the vibrational frequency of mode i.

5.2.4 MICROKINETIC MODELING

For surface reactions, the forward rate constant (k_{for}) of each reaction is calculated as:

$$k_{for} = \frac{k_B T}{h} \frac{q_{TS,vib}}{q_{IS,vib}} e^{\frac{-E_{a\_for}}{k_B T}} \quad (5.3)$$

where k_B is the Boltzmann constant, T denotes the reaction temperature, h is the Planck constant, E_{a_for} stands for the zero-point-energy-corrected activation barrier for the forward reaction derived from DFT calculations, and $q_{TS,vib}$ and $q_{IS,vib}$ are the (harmonic) vibrational partition functions for the transition state and the initial state, respectively, i.e., q_{vib} is calculated as:

$$q_{vib} = \prod_i \frac{1}{1 - e^{\frac{-h\nu_i}{k_B T}}} \quad (5.4)$$

where ν_i is the vibrational frequency of each vibrational mode of the adsorbed intermediate derived from our DFT calculations.

The reverse rate constant (k_{rev}) is calculated similarly and the thermodynamic equilibrium constant K is given by:

$$K = \frac{k_{for}}{k_{rev}} \tag{5.5}$$

For an adsorption reaction A(g)+*→A*, the equilibrium constant K is defined as:

$$K = \frac{(q_{vib})_{A^*}}{(q_{vib}q_{vib}q_{vib})_{A(g)}} e^{\frac{-\Delta E_{ads}}{k_B T}} \tag{5.6}$$

where $(q_{\text{vib}})_{\text{A*}}$ is the vibrational partition function of adsorbed A, and q_{vib}, q_{rot}, q_{trans} stand for vibrational, rotational, and translational partition functions, respectively. ΔE_{ads} represents the zero-point corrected adsorption energy, R is the ideal gas constant, and T denotes temperature.

For an adsorption reaction A(g)+*→A*, the forward rate is given by collision theory with a sticking probability of 1.

$$k_{for} = \frac{1}{N_0\sqrt{2\pi m_A k_B T}} \tag{5.7}$$

where N_0 is the number of sites per area (1.478×10^{19} m^{-2}) and m_{A} denotes the molecular weight of A.

The reverse rate constant is again given as:

$$k_{rev} = \frac{k_{for}}{K} \tag{5.8}$$

With the forward and reverse rate constants defined, we solve the full set of steady-state rate equations to obtain the surface coverage of all possible reaction intermediates and the fraction of free sites using the BzzMath library[115] developed by Buzzi-Ferraris. No assumptions were made regarding rate-limiting steps.

5.3 RESULT

5.3.1 KINETIC ISOTOPE EFFECT MEASUREMENTS

Figure 5.1A shows the results of the reaction rate over time during switching between unlabeled (CH_3CH_2COOH) and labeled (CH_3CD_2COOH) PAc at 200ºC and 1 atm with a reactor feed of 1.2% PAc/20% H_2/balance He. The reaction resulted in differential conversion (<5%) with a 100% selectivity toward C_2H_6, with CO indicating decarbonylation (DCN) as the major reaction pathway as described previously[178]. The reaction rates based on the products formed and TOF are summarized in Table 5.1. The labeled PAc reaction rate (1.39±0.05 μmol/min·gcat) was calculated from the average of measurements between 45 and 50 hr on stream, while the unlabeled PAc reaction rate (1.61±0.16 μmol/min·gcat) was calculated from the average of measurements between 37 and 44 hrs on stream. Taking the ratio of these two values, the KIE effect was found to be k_H/k_D = 1.16 ±0.07. Given this small value, as a comparison, Figure 5.1B shows the measurement of acid feed concentration (labeled and unlabeled PAc) as a function of time during the same experiment. The feed concentration analysis were conducted every 2 hours to verify there was no change. The variability from labeled to unlabeled feed composition is around 3.0% and a mass balance between 0.99-1.01 is obtained. Given that the reaction order with respect to PAc is ~0.5 order under these conditions [178], such variability does not account for the observed rate difference. Nevertheless, this small ratio of k_H/k_D = 1.16 ±0.07, indicates that the isotopic substitution at the α-carbon position had little effect under these conditions.

In our previous DFT study, we performed a sensitivity analysis on HDO of propionic acid over Pd (111) model surfaces, [184]. Our model suggested that by

lowering the partial pressures of hydrogen, the influence of the dehydrogenation of α-carbon on the overall TOF will increase. To further explore the KIE effect and trend in its relationship with partial pressure of hydrogen, steady-state measurements at 200ºC and 1 atm total pressure were conducted at lower hydrogen partial pressure. Figure 5.2A shows reaction rate data as a function of time during switching between unlabeled and labeled PAc using a feed consisting of 1.2% PAc/5% H_2/balance He, The labeled PAc reaction rate (0.80±0.09 μmol/min·gcat) was calculated from the average of measurements between 16 and 19 hr on stream, while the unlabeled PAc reaction rate (1.28±0.15 μmol/min·gcat) was calculated from the average of measurements between 19.5 and 22 hrs on stream. A k_H/k_D ratio of 1.62 ±0.05 is obtained, suggesting that a significant KIE is present at this lower partial pressure of hydrogen. Once again, Figure 5.2B shows the measurement of acid feed concentration as a function of time during the same experiment revealing negligible variation. The significant KIE therefore indicates that the rate controlling step involves dehydrogenation of the α-carbon (i.e., C-H bond breaking). Indeed, a lower partial pressure of hydrogen should allow for the dehydrogenation of the α-carbon to occur to a greater extent, accounting for the increased KIE.

5.3.2 Kinetic Isotope Effect Calculations

The positive experimental KIE values obtained above point to the kinetic importance of α-carbon dehydrogenation in the HDO of PAc. According to our previous DFT studies[158, 184], we know that the dehydrogenation of the α-carbon is not the only rate-controlling step under the investigated reaction conditions of 200ºC and partial pressures of 0.01 bar of acid and 0.05 bar of H_2. Indeed, the observation that the k_H/k_D

ratio varies under different reaction conditions appears to be similar to the changes in the computed degree of rate control[196] of the α-carbon dehydrogenation. Thus, the interpretation of the observed KIE is not straightforward. To initially obtain a meaningful range for the KIE in our system, two limiting theoretical cases were considered. In Section 5.3.2.1, an upper limit for the KIE is predicted for the case where α-carbon dehydrogenation is the only rate-controlling step. Next, in Section 5.3.2.2, it is shown that the k_H/k_D ratio is expected to be approximately 1 when C-H bond dissociation is not rate controlling. While labeling PAc could in principle affect other rate-controlling steps through a so-called secondary kinetic isotope effect, this is also shown to be negligible in this system for the limiting case of C-OH bond dissociation being the rate limiting step. Finally, Section 5.3.2.3 presents a detailed DFT and microkinetic modeling study to estimate the KIE under reaction conditions for a Pd (111) surface from first principles.

5.3.2.1 Upper Limit for Primary Kinetic Isotope Effect

Assuming that the dehydrogenation of the α-carbon is the only rate controlling step in the HDO of PAc, the ratio of the turn over frequencies of CH_3CH_2COOH and CH_3CD_2COOH can be approximated using transition state theory[114, 197, 198] as:

$$\frac{TOF_{CH_3CH_2COOH}}{TOF_{CH_3CD_2COOH}} \approx \frac{k_H}{k_D} \approx \frac{e^{\frac{-(E_a+\Delta ZPE_H)}{K_BT}}}{e^{\frac{-(E_a+\Delta ZPE_D)}{K_BT}}} = e^{\frac{-h}{2K_BT}\nu_H(\frac{\nu_D}{\nu_H}-1)} \quad (5.9)$$

where E_a is the activation barrier, ΔZPE_H is the zero-point energy correction to the activation barrier for the unlabeled PAc, ΔZPE_D is the zero-point energy correction to the activation barrier for the labeled PAc, k_B is the Boltzmann constant, T denotes the

temperature, h is the Planck constant, and ν_H and ν_D are the C_α -H and C_α-D vibrational frequencies, respectively, in PAc.

The maximum C-H frequency observed in carboxylic acids[199] is 3000 cm^{-1}. In addition,

$$\frac{\nu_D}{\nu_H} \approx \sqrt{\frac{\mu_H}{\mu_D}} \quad , \quad \frac{1}{\mu_H} = \frac{1}{m_H} + \frac{1}{m_{CH_3CHCOOH}} \quad , \; and \; \frac{1}{\mu_D} = \frac{1}{m_D} + \frac{1}{m_{CH_3CDCOOH}} \qquad (5.10)$$

where μ_D and μ_H are the reduced masses for $CH_3CDCOOH$--D and $CH_3CHCOOH$—H, respectively, and m_H, m_D, $m_{CH3CHCOOH}$, $m_{CH3CDCOOH}$ are the molecular masses in g mol^{-1} of H (1), D (2), $CH_3CHCOOH$ (73), and $CH_3CDCOOH$ (74), respectively. Combining equations (5.10) with equation (5.9) then yields the the maximum KIE = $\frac{TOF_{CH_3CH_2COOH}}{TOF_{CH_3CD_2COOH}}$ is calculated to be 3.73. This value is considerably (by over a factor of two) than that observed experimentally, suggesting that α-carbon dehydrogenation is not the only rate controlling step.

5.3.2.2 Secondary Kinetic Isotope Effect

To estimate the maximum secondary KIE effect for labeled PAc assuming C-OH bond dissociation, we use Equation 5.9 with a C-OH bond frequency of 1360 cm^{-1} (which is the largest frequency observed in experimental studies[199] for carboxylic acids which ranges from 1000 to 1360 cm^{-1}). Next, the ratio of ν_D over ν_H can be approximated as:

$$\frac{1}{\mu_H} = \frac{1}{m_{OH}} + \frac{1}{m_{CH_3CH_2CO}} \quad , \; and \; \frac{1}{\mu_D} = \frac{1}{m_{OH}} + \frac{1}{m_{CH_3CD_2CO}} \qquad (5.11)$$

where $m_{OH,}$ $m_{CH3CH2CO}$, $m_{CH3CD2CO}$ are the molecular masses of OH, CH_3CH_2CO, and CH_3CD_2CO which are 17, 57 and 59 g/mol, respectively. As a result, the KIE for the secondary kinetic isotope effect is calculated to be 1.01 which is negligible.

5.3.2.3 DFT AND MICROKINETIC MODELING STUDY

Our previous[119, 158, 184] study analyzed the elementary reaction steps involved in the DCN and DCX of PAc on Pd (111) from first principles. To computationally investigate the activity of labeled PAc, the adsorption and TS geometries obtained previously for unlabeled PAc [119, 158, 184] were used. DFT frequency calculations were performed for all intermediates involved in the HDO of labeled PAc to obtain the frequencies of the labeled intermediates needed to compute the zero-point energy corrections and vibrational partition functions of the labeled species. The calculated free energies of reaction (ΔG_{rxn}) and free energies of activation ($G^{\ddagger}$) for all the labeled elementary reactions, as well as the reaction parameters for the corresponding unlabeled reactions, are listed in Table 5.2.

Previously, it was found[158, 184] that the dehydrogenation of the α-carbon of PAc ($CH_3CH_2COOH^* + 2^* \rightarrow CH_3CHCOOH^{**} + H^*$) is one of the rate-controlling steps. At 200ºC, this step has a free energy of reaction, ΔG_{rxn}, of -0.02 eV and a free energy of activation of 0.70 eV. The correspondent labeled reaction, i.e., the de-deuteriation of the α-carbon of labeled PAc (Reaction 2: $CH_3CD_2COOH^* + 2^* \rightarrow CH_3CHCOOH^{**} + D^*$), has a free energy of reaction, ΔG_{rxn}, of -0.01 eV and a free energy of activation of 0.77 eV indicating that the overall turnover frequency (TOF) of labeled PAc will be slightly slower than that of unlabeled PAc as the barrier of this step was increased by nearly 0.1 eV.

To investigate the overall effects of changes in the reaction parameters on the TOFs, previously[157, 158, 200] developed microkinetic models for the HDO of PAc over Pd (111) were applied to labeled and unlabeled PAc under the reaction conditions

identical to the above experimental study (Section 5.3.1). Accordingly, simulations were carried out at 200ºC and partial pressures of H_2 and PAc of 0.05 (5% H_2) and 0.01 (1% PAc) bar, respectively. The partial pressures of H_2O, CO_2 and CO were set to 10^{-3}; however, the analysis shows that the microkinetic modeling result is insensitive to the partial pressures of these intermediates in the range of 10^{-4} to 10^{-2} bar. In doing so, the partial pressures of these products are fixed, which is necessary since the model does not contain a reaction network for the water-gas shift reaction. Finally, the primary kinetic isotope effect, KIE = $\frac{TOF_{CH_3CH_2COOH}}{TOF_{CH_3CD_2COOH}}$ was calculated to be 1.49 under the experimental reaction conditions. This value is in very good agreement with our experimental result of 1.62 under the same reaction conditions. Table 5.3 summarizes and compare the KIE obtained based on the computational, calculated and experimental approach.

5.3.3 Extent of Dehydrogenation

Given the confirmation of α-carbon dehydrogenation as an important rate controlling step, the extent of this step under actual reaction conditions was further probed experimentally. Mass spectrometric analysis was performed on the reaction products formed for the HDO of labeled and unlabeled PAc, since GC cannot distinguish between various deuterium-labeled ethane products. Masses corresponding to CH_3CH_3 (m/e = 30), CH_3CDH_2 (m/e = 31), and CH_3CD_2H (m/e = 32) were considered. If one C-D bond is broken at the rate-determining step, the product CH_3CDH_2 should be detected. Similarly, if two C-D bonds are broken at the rate-determining step, the product CH_3CH_3 is detected. Lastly, if there is no C-D bond broken at the rate determining step, the

product CH_3CD_2H is detected. The latter, however, was not able to be detected since it overlapped with a background of signal at m/e = 32 arising from oxygen in the MS chamber. Nevertheless, it is highly unlikely that this species was formed, given that it requires C-C bond breaking to occur to form a CH_3CD_2 fragment before H addition, which is not favorable. According to our DFT calculations (Table 5.2), the C-C bond dissociation in deuterated propanoyl (Reaction 3: $CH_3CD_2CO^{***} \rightarrow CH_3CD_2^* + CO^* + *$) has the activation barrier of 0.99 eV, while the activation barrier of C-C bond dissociation in Reaction 14 ($CH_3CCO^{***} \rightarrow CH_3C^* + CO^* + *$) was lowered to 0.47 eV. This suggests that propionic acid or propanoyl most likely go through dehydrogenation steps prior to C-C bond dissociations. In this context, if CH_3CD_2 would be a dominant product, no KIE would be observed; however, we observe a clear primary KIE. It is assumed that there is no H-D exchange between H_2 and CH_3CD_2COOH in the chemisorbed state.

Analysis of the mass spectrum recorded for the HDO of labeled PAc shows that both CH_3CDH_2 and CH_3CH_3 are produced. As can be seen from Table 5.3, the CH_3CDH_2:CH_3CH_3 ratio is 1:2. Thus, C-C bond rupture in CH_3-CH_2-COOH is favored by a factor of two after both hydrogens of the α-C-H have been broken. These results also strongly support the idea that C-H bond-breaking occurs before C-C rupture.

5.4 CONCLUSIONS

Kinetic isotope effects in the HDO of deuterated PAc over Pd catalyst were examined with both experimental and computational approaches. Excellent agreement was found between the KIE found experimentally over Pd/C (k_H/k_D = 1.62) versus that

estimated by DFT calculations coupled with microkinetic models for Pd(111) (k_H/k_D = 1.49). The results confirm that the dehydrogenation of the α-carbon in PAc is one of the rate-controlling steps, especially under lower partial pressures of hydrogen. In addition, measurements of product distribution suggest that the reaction proceeds through the decarbonylation pathway, and that the associated C-C rupture is most favorable if both of the α-C-H bonds are broken. These results reaffirm the advantage of isotope labeling experiments for elucidation of kinetically important steps in catalytic reactions. In particular, the coupling of experiments with modern computational modeling allows for a more detailed and deeper analysis than was previously possible. Further research will focus on similar types of combined studies to elucidate the reaction mechanism of HDO, as well as other reactions important to catalytic biomass conversion.

5.5 ACKNOWLEDGEMENTS

The authors wish to thank the financial support from National Science Foundation (NSF) grant number CHE-1153012. Yuliana Lugo-José thanks the Sloan Foundation and the NSF Southeastern Alliance for Graduate Education and the Professoriate (SEAGEP) for financial support. The authors thank Professor Jim Ritter from the University of South Carolina for providing the Residual Gas Analyzer (RGA) equipment for the MS experiments.

5.6 TABLES

Table 5.1 Deuterium isotope effect for PAc HDO over 5wt% Pd/C, 16.9%, 6.8nm. Reaction conditions: 200ºC and 1 atm, Total flow: 50 sccm. <5% conversion, 100% selectivity C_2H_6. [a] Rxn rate - µmol/min·gcat.
Rxn 1- CH_3CH_2COOH/H_2, Rxn 2= CH_3CD_2COOH/H_2.

	X_{H2}/bal. He:							
	20% H_2/balance He				**5% H_2/balance He**			
Rxn	Feed conc. (*%PAc*)	Rxn rate[a]	*TOF* *(min^{-1})*	k_H/k_D Exp.	Feed conc. (*%PAc*)	Rxn rate[a]	*TOF* *(min^{-1})*	k_H/k_D Exp.
1	1.19±0.02	1.61±0.16	0.020±0.002	1.16±0.07	1.22±0.02	1.28±0.15	0.016±0.002	1.62±0.05
2	1.16±0.03	1.39±0.05	0.018±0.002		1.23±0.01	0.80±0.09	0.010±0.001	

Table 5.2 Reaction free energies (eV), equilibrium and forward rate constants for all elementary reaction steps in the hydrodeoxygenation of labeled PAc over Pd (111) model surfaces at a temperature of 200ºC. For comparison reaction free energies and free energies of activation are also shown for unlabeled PAc.
Note: * symbolizes a free site.

#	Reaction	Labeled PAc		Unlabeled PAc		Labeled PAc	Labeled PAc
		ΔG_{rxn}	$G^{\ddagger}$	ΔG_{rxn}	$G^{\ddagger}$	K_{eq}	$k_{forward}$ (s^{-1})
1	$CH_3CD_2COOH^* + 3^* \rightarrow CH_3CD_2CO^{***} + OH^*$	0.45	0.95	0.45	0.97	1.78×10^{-5}	7.30×10^{2}
2	$CH_3CD_2COOH^* + 2^* \rightarrow CH_3CHCOOH^{**} + D^*$	-0.01	0.77	-0.02	0.70	1.25	6.95×10^{4}
3	$CH_3CD_2CO^{***} \rightarrow CH_3CD_2^* + CO^* + ^*$	-0.68	0.99	-0.68	1.02	1.85×10^{7}	2.58×10^{2}
4	$CH_3CD_2CO^{***} \rightarrow CH_3CDCO^{**} + D^*$	0.07	0.89	0.04	0.84	1.99×10^{-1}	3.63×10^{3}
5	$CH_3CDCOOH^{**} + ^* \rightarrow CH_3CDCO^{**} + OH^*$	0.23	0.88	0.23	0.87	2.83×10^{-6}	3.89×10^{3}
6	$CH_3CDCOOH^{**} + 2^* \rightarrow CH_2CDCOOH^{***} + H^*$	-0.35	0.57	-0.36	0.57	5.64×10^{3}	7.61×10^{6}
7	$CH_3CDCOOH^{**} + 2^* \rightarrow CH_3CCOOH^{***} + D^*$	0.01	1.21	-0.03	1.16	7.88×10^{-1}	1.20
8	$CH_3CDCO^{**} + ^* \rightarrow CH_3CD^{**} + CO^*$	-0.83	0.99	-0.84	0.98	7.64×10^{8}	2.81×10^{2}
9	$CH_3CDCO^{**} + 2^* \rightarrow CH_3CCO^{***} + D^*$	-0.34	0.61	-0.37	0.57	3.73×10^{3}	2.90×10^{6}
10	$CH_3CDCO^{**} + 2^* \rightarrow CH_2CDCO^{***} + H^*$	-0.26	0.58	-0.27	0.58	6.57×10^{2}	6.69×10^{6}
11	$CH_2CDCOOH^{***} + ^* \rightarrow CH_2CDCO^{***} + OH^*$	0.61	1.22	0.61	1.22	3.30×10^{-7}	9.51×10^{-1}
12	$CH_2CDCOOH^{***} + ^* \rightarrow CHCDCOOH^{***} + H^*$	0.06	0.91	0.06	0.91	2.17×10^{-1}	1.98×10^{3}
13	$CH_3CCOOH^{***} + ^* \rightarrow CH_3CCO^{***} + OH^*$	0.18	0.82	N/A	N/A	1.34×10^{-2}	1.75×10^{4}
14	$CH_3CCO^{***} \rightarrow CH_3C^* + CO^* + ^*$	-1.39	0.47	N/A	N/A	5.76×10^{14}	1.01×10^{8}
15	$CH_2CDCO^{***} + ^* \rightarrow CH_2CD^{***} + CO^*$	-0.79	0.84	-0.76	0.87	2.52×10^{8}	1.03×10^{4}
16	$CH_2CDCO^{***} + 2^* \rightarrow CHCDCO^{****} + H^*$	0.01	0.68	0.00	0.68	8.79×10^{-1}	5.10×10^{5}
17	$CHCDCOOH^{***} + 2^* \rightarrow CHCDCO^{****} + OH^*$	0.55	1.10	0.55	1.09	1.34×10^{-6}	2.03×10^{1}
18	$CHCDCO^{****} \rightarrow CHCD^{***} + CO^*$	-1.11	0.59	-1.11	0.57	7.16×10^{11}	4.93×10^{6}
19	$CHCH^{***} + H^* \rightarrow CH_2CH^{***} + ^*$	0.32	0.93	N/A	N/A	4.27×10^{-4}	1.34×10^{3}
20	$CH_2CH^{***} + H^* \rightarrow CH_2CH_2^{**} + 2^*$	-0.11	0.86	N/A	N/A	1.40×10^{1}	7.10×10^{3}
21	$CH_2CH^{***} \rightarrow CH_2C^{**} + H^*$	-0.42	0.45	N/A	N/A	3.07×10^{4}	1.73×10^{8}

22	$CH_2C^{**} + H^* \rightarrow CH_3C^* + 2^*$	-0.27	0.87	N/A	N/A	8.27×10^{2}	5.44×10^{3}
23	$CH_2CH^{***} + H^* \rightarrow CH_3CH^{**} + 2^*$	0.22	0.78	N/A	N/A	4.27×10^{-3}	4.81×10^{4}
24	$CH_3C^* + H^* \rightarrow CH_3CH^{**}$	0.92	1.11	N/A	N/A	1.68×10^{-10}	1.59×10^{1}
25	$CH_3CH^{**} + H^* \rightarrow CH_3CH_2^* + 2^*$	0.12	0.85	N/A	N/A	5.45×10^{-2}	8.85×10^{3}
26	$CH_3CH_2^* + H^* \rightarrow CH_3CH_3^* + *$	-0.03	0.64	N/A	N/A	2.20	1.64×10^{6}
27	$CH_3CH_2^* + 2^* \rightarrow CH_2CH_2^{**} + H^*$	-0.44	0.45	N/A	N/A	4.87×10^{4}	1.72×10^{8}
28	$CH_3CD_2COOH^* + 2^* \rightarrow CH_3CD_2COO^{**} + H^*$	-0.35	0.35	-0.34	0.43	5.10×10^{3}	1.68×10^{9}
29	$CH_3CD_2COO^{**} \rightarrow CH_3CD_2^* + CO_2^*$	0.17	1.41	0.16	1.37	1.62×10^{-2}	9.46×10^{-3}
30	$CH_3CD_2COO^{**} + 2^* \rightarrow CH_3CDCOO^{***} + D^*$	0.47	1.33	0.44	1.28	9.30×10^{-6}	6.79×10^{-2}
31	$CH_3CDCOOH^{**} + * \rightarrow CH_3CDCOO^{**} + H^*$	0.13	0.85	0.12	0.84	3.79×10^{-2}	8.74×10^{3}
32	$CH_3CDCOOH^{**} + * \rightarrow CH_3CD^{**} + COOH^*$	0.31	1.40	0.40	1.38	4.64×10^{-4}	1.26×10^{-2}
33	$CH_3CDCOO^{***} \rightarrow CH_3CD^{**} + CO_2^*$	-0.39	0.89	-0.39	0.92	1.43×10^{4}	3.16×10^{3}
34	$CH_3CDCOO^{***} + * \rightarrow CH_3CCOO^{***} + D^*$	-0.05	0.89	-0.09	0.85	3.84	2.99×10^{3}
35	$CH_3CCOOH^{***} + * \rightarrow CH_3CCOO^{***} + H^*$	0.07	1.01	N/A	N/A	1.85×10^{-1}	1.55×10^{2}
36	$CH_3CCOOH^{***} \rightarrow CH_3C^* + COOH^{**}$	-0.58	0.98	N/A	N/A	1.65×10^{6}	3.29×10^{2}
37	$CH_2CDCOOH^{***} + * \rightarrow CH_2CD^{***} + COOH^*$	0.45	1.79	0.75	2.10	1.78×10^{-5}	9.12×10^{-7}
38	$CH_3CCOO^{***} \rightarrow CH_3C^* + CO_2^* + *$	-1.13	0.64	N/A	N/A	1.15×10^{12}	1.65×10^{6}
39	$COOH^{**} \rightarrow CO_2^* + H^*$	-0.57	0.37	N/A	N/A	1.09×10^{6}	1.07×10^{9}
40	$COOH^{**} \rightarrow CO^* + OH^*$	-0.63	0.39	N/A	N/A	4.66×10^{6}	6.64×10^{8}
41	$OH^* + H^* \rightarrow H_2O^* + *$	-0.28	0.66	N/A	N/A	1.06×10^{3}	9.00×10^{5}
42	$CH_3CD^{**} + H^* \rightarrow CH_3CDH^* + 2^*$	0.12	0.84	0.12	0.85	5.64×10^{-2}	1.05×10^{4}
43	$CH_3CDH^* + H^* \rightarrow CH_3CDH_2^* + *$	-0.03	0.63	-0.03	0.64	2.35	1.79×10^{6}
44	$CH_2CD^{***} + H^* \rightarrow CH_2CDH^{**} + 2^*$	-0.10	0.86	-0.11	0.86	1.15×10^{1}	7.46×10^{3}
45	$CH_2CD^{***} + H^* \rightarrow CH_3CD^{**} + 2^*$	0.22	0.78	0.22	0.78	4.62×10^{-3}	4.71×10^{4}
46	$CH_3CDH^* + 2^* \rightarrow CH_2CDH^{**} + H^*$	-0.44	0.45	-0.44	0.45	4.40×10^{4}	1.49×10^{8}
47	$CH_2CDH_2^* + 2^* \rightarrow CH_2CDH^{**} + H^*$	-0.43	0.46	-0.44	0.45	4.05×10^{4}	1.25×10^{8}
48	$CH_2CDH_2^* + H^* \rightarrow CH_3CDH_2^* + *$	-0.03	0.64	-0.03	0.64	2.16	1.80×10^{6}

49	CHCD*** + H*→ CH_2CD*** + *	0.32	0.93	0.32	0.93	4.00×10^{-4}	1.35×10^{3}
50	CHCD*** + H*→ CHCDH*** + *	0.32	0.93	0.32	0.93	4.25×10^{-4}	1.29×10^{3}
51	CHCDH*** + H* → $CHCDH_2$** + 2*	0.22	0.78	0.22	0.78	4.89×10^{-3}	4.84×10^{4}
52	$CHCDH_2$** + H* → CH_2CDH_2* + 2*	0.12	0.85	0.12	0.85	5.46×10^{-2}	9.14×10^{3}
53	CH_3CD_2* + H* → CH_3CD_2H* + *	-0.03	0.63	-0.03	0.64	2.29	1.88×10^{6}
54	CH_3CD_2* + 2* → CH_3CD** + D*	-0.09	0.77	-0.12	0.73	8.20	6.22×10^{4}
55	CH_3CD_2H* + * → CH_3CDH* + D*	0.07	0.72	0.03	0.67	2.02×10^{-1}	2.33×10^{5}
56	CH_2CD_2** + 2* → CH_2CD*** + D*	0.99	0.13	0.11	0.97	3.96×10^{-2}	2.56×10^{2}
57	CH_2CD***→ CH_2C** + D*	-0.39	0.49	-0.42	0.45	1.57×10^{4}	5.71×10^{7}
58	CH_3CD** → CH_3C* + D*	-0.89	0.19	-0.92	0.19	2.81×10^{9}	8.73×10^{10}
59	CH_3CD_2COOH+*→CH_3CD_2COOH*	0.76	N/A	0.74	N/A	8.85×10^{-9}	9.40×10^{7}
60	CH_3CH_3 + * → CH_3CH_3*	0.63	N/A	N/A	N/A	2.09×10^{-7}	1.50×10^{8}
61	CH_2CH_2 + 2* → CH_2CH_2**	-0.08	N/A	N/A	N/A	7.74	1.55×10^{8}
62	H_2O + * → H_2O*	0.41	N/A	N/A	N/A	4.14	1.93×10^{8}
63	CO_2 + * → CO_2*	0.74	N/A	N/A	N/A	1.33×10^{-8}	1.24×10^{8}
64	CO* → CO + *	-1.19	N/A	N/A	N/A	828.13	1.55×10^{8}
65	H_2 + 2* → 2H*	-0.58	N/A	N/A	N/A	6.04	5.80×10^{8}
66	CH_3CDH_2 + * → CH_3CDH_2*	-0.63	N/A	0.63	N/A	2.19×10^{-7}	1.47×10^{8}
67	CH_3CD_2H + * → CH_3CD_2H*	-0.63	N/A	0.63	N/A	1.76×10^{-7}	1.45×10^{8}
68	CH_2CDH + 2* → CH_2CDH**	-0.08	N/A	-0.08	N/A	6.81	1.52×10^{8}
69	CH_2CD_2 + 2* → CH_2CD_2**	-0.08	N/A	-0.08	N/A	6.90	1.50×10^{8}
70	CHCD + * → CHCD*	-1.15	N/A	-1.16	N/A	1.87×10^{12}	1.58×10^{8}
71	HD + 2* → H* + D*	-0.57	N/A	-0.58	N/A	1.24×10^{6}	4.73×10^{8}

Table 5.3 Comparison of KIE values based on experimental, calculated and theoretical approach.
* based on the Upper Limit for the Primary Kinetic Isotope Effect calculations.

Gas phase comp. 1.2% PAc/5% H_2/balance He		
k_H/k_D ***Experimental***	$\boldsymbol{k_H/k_D}$ *Theoretical(comp.)*	$\boldsymbol{k_H/k_D}$ *Calculated**
1.62	1.49	3.73

5.7 FIGURES

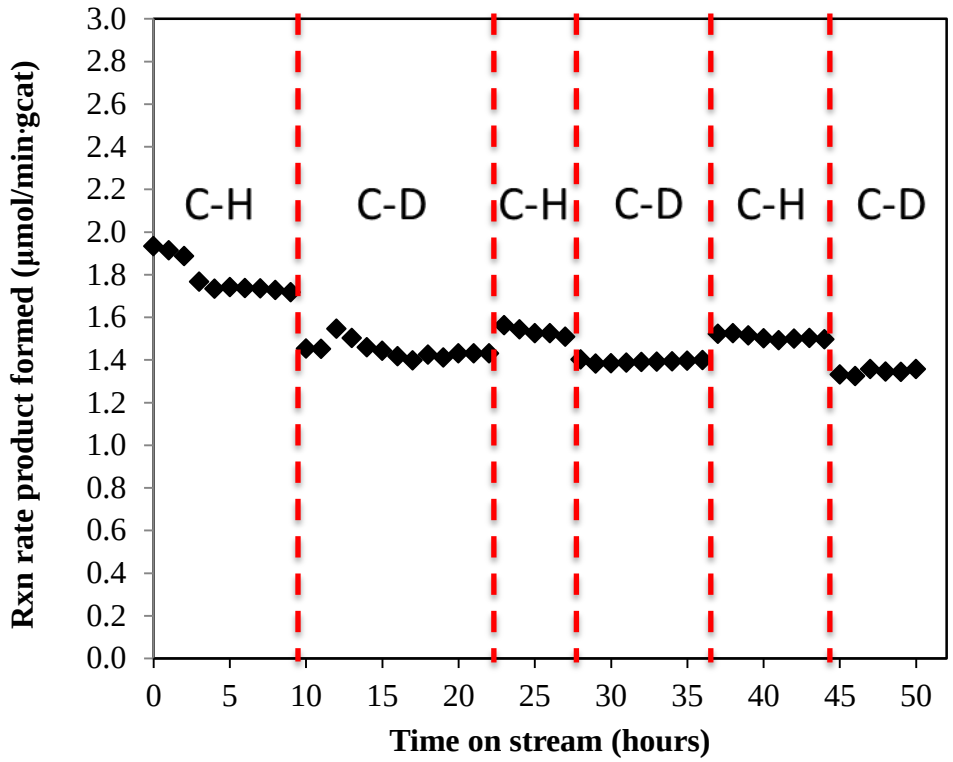
Rxn rate product formed (µmol/min·gcat)
Time on stream (hours)
C-H
C-D
C-H
C-D
C-H
C-D
0.0
0.2
0.4
0.6
0.8
1.0
1.2
1.4
1.6
1.8
2.0
2.2
2.4
2.6
2.8
3.0
0
5
10
15
20
25
30
35
40
45
50

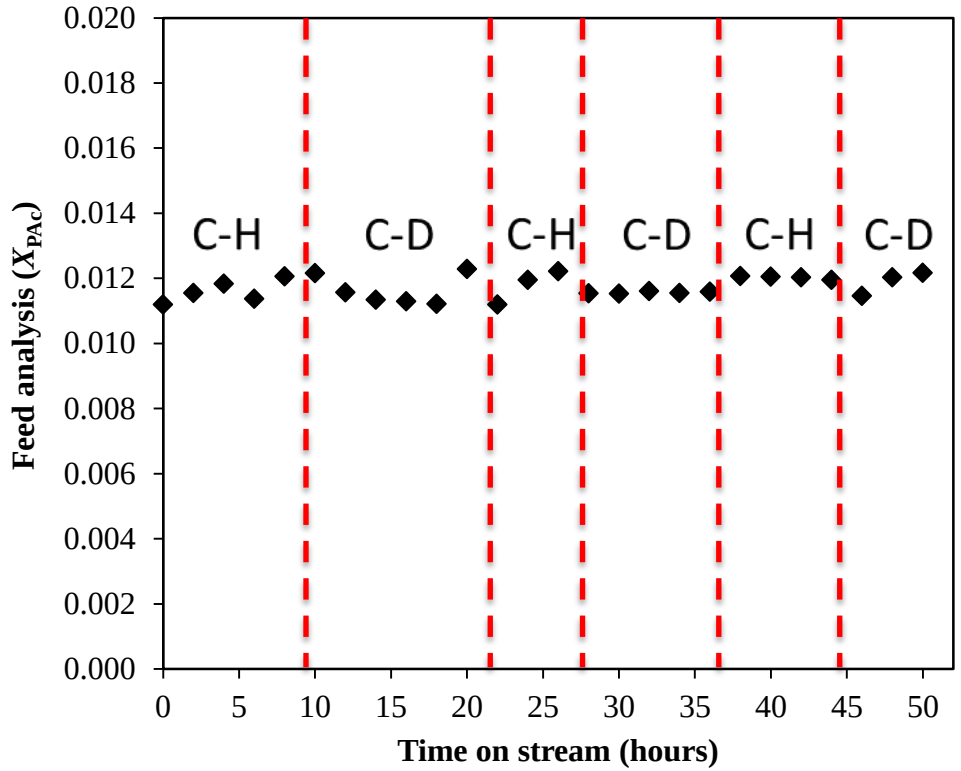

Figure 5.1 A) Reaction rate measurements as a function of time on stream for HDO during switching between unlabeled (C-H) and labeled (C-D) PAc. B) Feed analysis as a function of time on stream during the same experiment. Reaction conditions: 200ºC, 1 atm, ~1.2% PAc, 20% H_2, balance He.

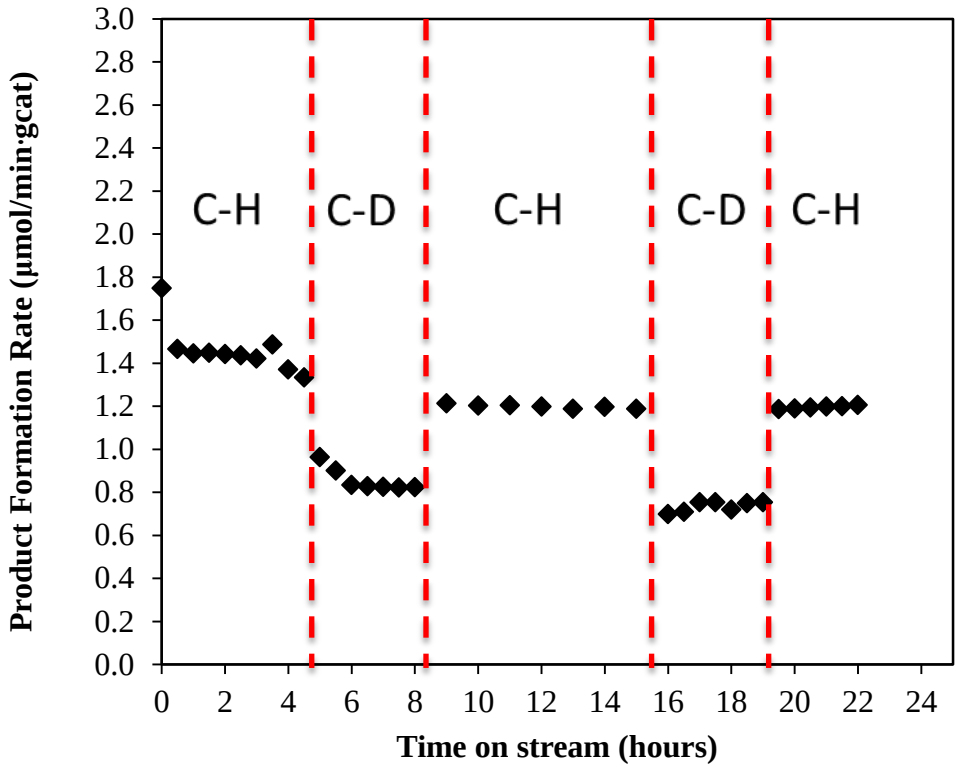
Product Formation Rate (µmol/min·gcat)
3.0
2.8
2.6
2.4
2.2
2.0
1.8
1.6
1.4
1.2
1.0
0.8
0.6
0.4
0.2
0.0
C-H
C-D
C-H
C-D
C-H
0
2
4
6
8
10
12
14
16
18
20
22
24
Time on stream (hours)

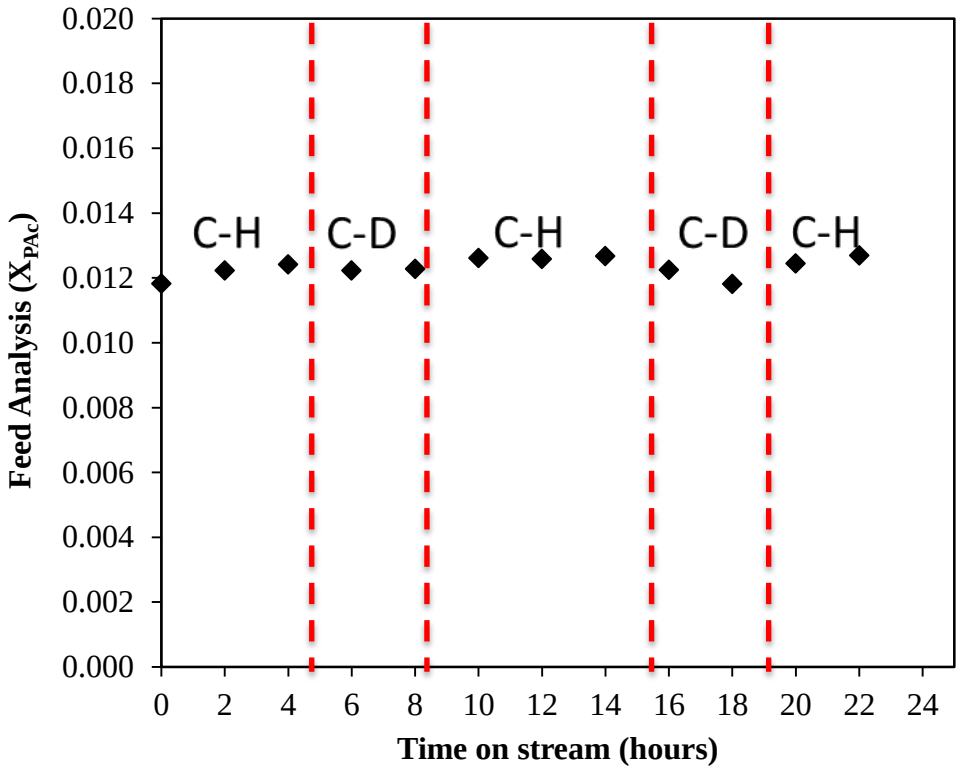

Figure 5.2 A) Reaction rate measurements as a function of time on stream for HDO during switching between unlabeled (C-H) and labeled (C-D) PAc. B) Feed analysis as a function of time on stream during the same experiment. Reaction conditions: 200ºC, 1 atm, ~1.2% PAc, 5% H_2, balance He.

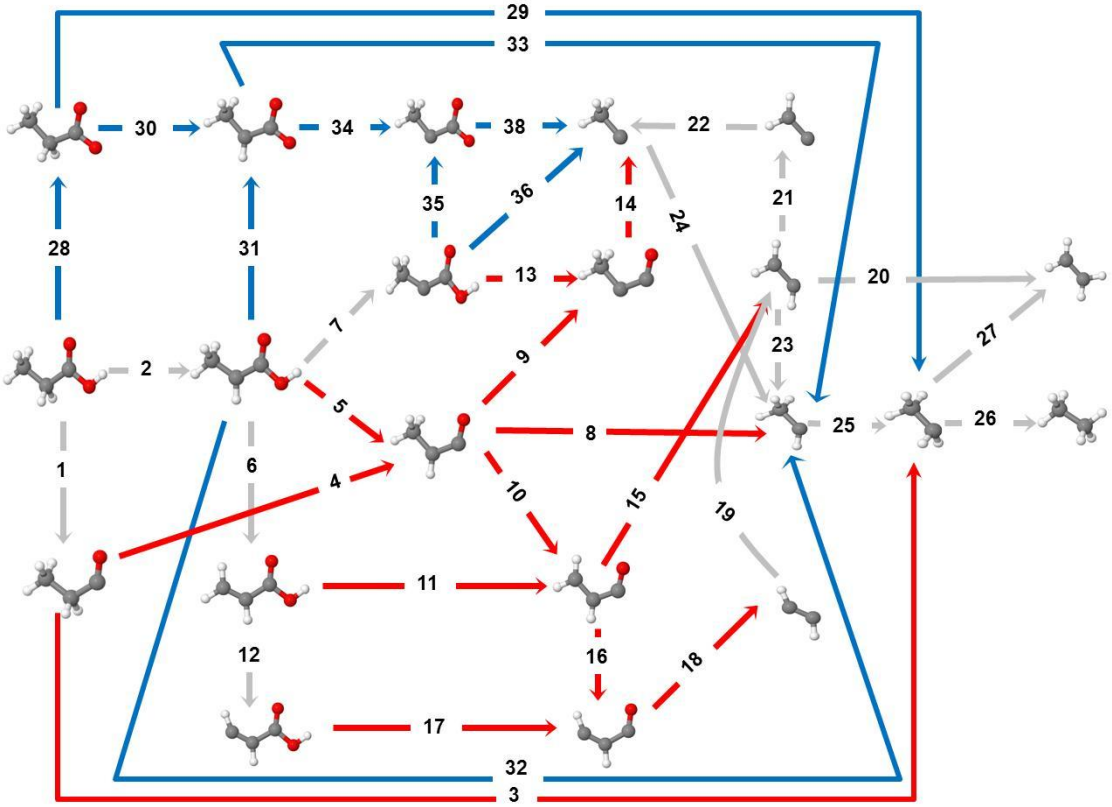

Figure 5.3 Network of elementary reaction steps considered in the hydrodeoxygenation of PAc over Pd (111). Elementary reactions involved in the DCX mechanism are shown with blue color arrows, DCN reactions are illustrated with red color arrows, and those reactions involved in both mechanisms such as dehydrogenation reactions and removal of the hydrocarbon pool are shown with gray color arrows.

CHAPTER 6

EFFECTS OF SURFACE STRUCTURE ON HYDRODEOXYGENATION OF PROPANOIC ACID OVER PALLADIUM CATALYSTS[1]

[1] S. Behtash, J. Lu, J. R. Monnier, C. T. Williams , and A. Heyden.
To be submittedto Journal of Physical Chemistry C.

ABSTRACT

The effect of palladium surface structure on the hydrodeoxygenation of propionic acid has been investigated by studying the mechanism over Pd(111) and Pd(211) model surfaces. We developed a microkinetic model based on parameters obtained from density functional theory and harmonic transition state theory and studied the reaction mechanism at a characteristic experimental reaction temperature of 473 K. The activity of active sites on flat surface models was found to be 3-8 times higher than the activity of stepped surface models, suggesting that the hydrodeoxygenation of propionic acid over a palladium catalyst is not very sensitive to surface structure. Very good agreement between computations and experiments could be obtained for our Pd(111) model if we include dispersion interactions between the gas species and the metal surface approximately by using the PBE-D3 functional for adsorption/desorption processes. Our model calculations predict that on both stepped and flat surfaces, the dominant deoxygenation mechanism proceeds by a decarbonylation pathway; however, on stepped surface models decarboxylation and decarbonylation are essentially competitive. A sensitivity analysis of our models suggests that C-OH and C-H bond cleavages control the overall rate over both Pd(111) and (211) catalyst surface models. In addition, on Pd(211) the C-C bond dissociation of propionate to CH_3CH_2 and CO_2—a key step in the decarboxylation mechanism—is also partially rate controlling.

KEYWORDS:

Surface structure; organic acids; palladium; density functional theory; step; terrace; decarbonylation; decarboxylation; microkinetic modeling

6.1 INTRODUCTION

The energy demand continues to increase due to the world's development, leading to an overexploitation of fossil fuels.[151, 201] Rising concerns over dwindling fossil fuel resources and realization of the environmental impact of fossil fuel utilization have drawn substantial attention to the conversion of biomass to biofuels as an alternative process for meeting the world's growing energy and liquid fuels demand.

Lipids are one promising biomass feedstock for production of biofuels that are identical to gasoline and diesel, and are therefore often called green diesel or green gasoline.[22] Practical lipids for fuel production consist of oxygenates such as triglycerides, organic esters and fatty acids. To convert these lipids into hydrocarbon fuels identical to fossil-derived transportation fuels, at least some of the oxygen atoms have to be removed from the feedstock molecules. Significant research efforts have been invested to convert vegetable oils into liquid hydrocarbons using a hydrodeoxygenation (HDO) process with conventional hydrotreating catalysts such as sulfided $NiMo/Al_2O_3$ and $CoMo/Al_2O_3$.[47, 54, 59] However, these hydrotreating catalysts increase the sulfur content in the final products. Also, the catalyst life-time is relatively short and problems in separating carbon oxides from the recycle gas have been reported.[54, 59] Consequently, there is an apparent need for new catalysts for the HDO of triglycerides, organic esters and fatty acids.

To design a metal catalyst for the HDO of organic acids and esters, it is necessary to first obtain a fundamental understanding of the reaction mechanism for the HDO of organic acids and esters on the catalyst surface. In our previous studies,[119, 158, 184, 202] we investigated the HDO of organic acids and esters over Pd(111) model surfaces

from first principles and obtained results that agreed qualitatively with experimental observations.[159, 203] Our model reactant for organic acids has been propionic acid that we found to possess a long enough hydrocarbon chain to obtain results that can likely be extrapolated to longer chain hydrocarbons. We found two major mechanisms for the HDO which are the decarbonylation (DCN) and the decarboxylation (DCX) pathways. Our results suggested that under gas phase reaction conditions DCN is favored over the DCX, while in the presence of water both DCN and DCX mechanisms are competitive.[184] In all reaction environments and at a low hydrogen partial pressure, a dehydrogenation of the α-carbon in propanoic acid is the most rate controlling step. With increasing hydrogen partial pressure, the C-OH bond dissociation becomes most rate controlling and the importance of C-H bond cleavages is reduced.[184]

While our previous studies[119, 158, 184] on the HDO of propionic acid on flat surface models agreed qualitatively with experimental observations, computed turnover frequencies have been low and predicted acid reaction orders have been too high. Considering furthermore that there is some consensus in the literature[15, 162, 204-209] that step surfaces are more active than flat surfaces, we decided to investigate the effect of Pd surface structure on the HDO activity of Pd catalysts and to test if better agreement between experiment and theory can be achieved. According to the d-band theory,[210] the binding energy of adsorbates can be correlated to the d-band center of the metal catalysts. The closer the d-band center to the Fermi level, the stronger the chemisorption and (following transition state scaling relations[211]) the lower the elementary activation barrier. Since the d-band center of the more open Pd(211) surface is closer to the Fermi level than its flat surface, active sites on steps and kinks are expected to possess a higher

activity.[212] However, while many elementary steps might possess a lower activation barrier on Pd(211) than on Pd(111), a "too active" surface is poisoned in which case the removal of the reaction products is the rate controlling step. For example, for NO dissociation and acetylene hydrogenation on Pd catalysts, steam reforming and graphite formation on Ni, ammonia synthesis and decomposition on Ru catalysts, stepped surface sites have been identified to be the most active sites,[15, 162, 204-209] while for methane dissociation on Ni, synthesis of H_2O_2 from H_2 and O_2 over Pd catalysts, flat, closed-packed surface sites have been reported[213-215] to be more active.

Considering the difficulty in predicting the active sites in heterogeneous catalysis, it is often necessary to study various active site models. It is the objective of this paper to investigate the effect of stepped, low-coordinated Pd sites on the activity and reaction mechanism of the HDO of propionic acid. In particular, we present a detailed density functional theory (DFT) and microkinetic modeling study of the HDO of propanoic acid over a Pd (211) surface model that has previously been found to be an active surface for a number of catalytic reactions such as, NO dissociation, and ethylene decomposition.[162, 205, 206, 209]

6.2 METHODS

6.2.1 DFT CALCULATIONS

All density functional theory calculations have been conducted using the Vienna Ab Initio Simulation Package (VASP).[106, 107, 195] The Kohn-Sham valence states are expanded in a plane wave basis sets with an energy cut-off of 400 eV. The interaction between core electrons is described with the projector-augmented wave (PAW)[107, 109]

method. The exchange correlation energy is calculated within the generalized gradient approximation (GGA) using the functional form proposed by Perdew and Wang which is known as Perdew-Wang 91 (PW91).[88, 110, 111] The lattice constant obtained from the optimization of the fcc-Pd bulk is 3.953 *Å*, which is in reasonable agreement with the experimental value of 3.891 *Å*. The surface Brillouin zone is sampled with $3\times5\times1$ Monkhorst-pack k-point grid. Pd(211) is modeled by an 8 atomic layer slab (corresponding to approximately four layers in closed packed (111) direction) with a ($2\times$ 3) surface unit cell and a 15 *Å* vacuum gap between palladium layers. The bottom four Pd layers were fixed to their bulk configuration during all calculations while the top four atomic layers were free to relax in all directions. We note that we did not consider Pd hydride formation since at the investigated reaction conditions of low hydrogen pressure of 0.2 bar and 473 K hydride formation is thermodynamically not favorable. All self-consistent field (SCF) calculations for geometry optimizations were converged to 1×10^{-3} kJ/mol and for transition state identification the convergence criterion was set to be 1×10^{-5} kJ/mol. Adsorption energies of all intermediates were calculated at their most stable geometry using the following equation:

$$E_{ads} = E_{slab+adsorbate} - E_{slab} - E_{adsorbate(gas)} \tag{6.1}$$

where $E_{slab+adsorbate}$ is the total energy of the adsorbed intermediate on the Pd slab, E_{slab} is the total energy of the Pd slab and $E_{adsorbate(gas)}$ is the total energy of the adsorbate in the gas phase. Transition states are located by a combination of the CI-NEB[112] and dimer[216-218] methods. Vibrational frequency calculations have been performed for all stable intermediates and transition state structures. All energies reported in this paper have been zero-point corrected using the following equation:

$$\Delta E_{ZPE} = \sum_i \frac{1}{2} h \nu_i \tag{6.2}$$

where h is the Plank constant and ν_i is the vibrational frequency of mode *i*. Frequencies below 100 cm^{-1} are shifted to 100 cm^{-1} during the partition function calculations to minimize errors associated with the harmonic approximation for small frequencies.[219]

6.2.1 MICROKINETIC MODELING

For surface reactions, the forward rate constant (k_{for}) of each reaction is calculated as

$$k_{for} = \frac{k_B T}{h} \frac{q_{TS,vib}}{q_{IS,vib}} e^{-\frac{E_a}{k_B T}} \tag{6.3}$$

where k_B is the Boltzmann constant, T denotes the reaction temperature, h is the Planck constant, E_a stands for the zero-point energy corrected activation barrier for the forward reaction derived from DFT calculations, and $q_{TS,vib}$ and $q_{IS,vib}$ are the (harmonic) vibrational partition functions for the transition state and the initial state, respectively. I.e., q_{vib} is calculated as

$$q_{vib} = \prod_i \frac{1}{1 - e^{\frac{-h\nu_i}{k_B T}}} \tag{6.4}$$

where ν_i is the vibrational frequency of each vibrational mode of the adsorbed intermediate derived from our DFT calculations. The reverse rate constant (k_{rev}) is calculated similarly and the thermodynamic equilibrium constant K is given as

$$K = \frac{k_{\text{for}}}{k_{\text{rev}}} \tag{6.5}$$

For an adsorption reaction A(g)+*⇌ A*, the equilibrium constant K is computed as

$$K = \frac{(q_{\text{vib}})_{A^*}}{(q_{\text{vib}} q_{\text{rot}} q_{\text{trans}})_{A(g)}} e^{\frac{-\Delta E_{\text{ads}}}{k_B T}} \tag{6.6}$$

where $(q_{\text{vib}})_{A^*}$ is the vibrational partition function of adsorbed A, and q_{vib}, q_{rot}, q_{trans} stand for vibrational, rotational, and translational partition functions of the gas molecule A, respectively. ΔE_{ads} represents the zero-point corrected adsorption energy. For an adsorption reaction, A(g)+*⇌ A*, the forward rate is given by collision theory with a sticking probability of 1.

$$k_{\text{for}} = \frac{1}{N_0 \sqrt{2\pi m_A k_B T}} \tag{6.7}$$

where N_0 is the number of sites per area (1.75×10^{19} m^{-2}) and m_A denotes the molecular weight of A. The reverse rate constant is again given as

$$k_{\text{rev}} = \frac{k_{\text{for}}}{K} \tag{6.8}$$

All rate parameters computed from DFT are listed in Table 6.3.

With the forward and reverse rate constants defined, we solve the full set of steady-state rate equations at a given set of gas phase partial pressures to obtain the surface coverages of all possible reaction intermediates, the fraction of free sites, and the turnover frequency using the BzzMath library[115] developed by Buzzi-Ferraris. No assumptions were made regarding rate-controlling steps.

6.3 Results and Discussion

The reaction network investigated in this study is identical to the one from our previous study on the mechanism of the DCN and DCX of propanoic acid over Pd(111) model surfaces.[184] All elementary steps and intermediates involved in the DCN and DCX of propanoic acid are shown in Figure 6.1. The adsorption energies, chemical formula, and binding modes of all intermediates are given in Table 6.1 for both the Pd(111) and (211) surfaces. We have employed the nomenclature $\eta_i\mu_j$ to designate that *i* atoms of the adsorbate are binding to *j* atoms of the metal surface. Also, a schematic of the adsorption and transition state configurations of all stationary points on the Pd(211) surface are shown in Figure 6.2 and 6.3, respectively. Finally, DFT-derived reaction energies, activation barriers, transition state (TS) imaginary frequencies, and the length of the dissociating bond in the TS structure for the elementary reactions are listed in Table 6.2 and 6.3.

6.3.1 Adsorption Energies

As expected, Table 6.1 shows that most intermediates adsorb stronger on Pd(211) than on Pd(111). The only exceptions are H and CH_3C whose adsorption energies decrease by 0.06 and 0.07 eV, respectively. The maximum change in adsorption energies was obtained for OH whose adsorption strength increases by 0.53 eV on Pd (211). In the remainder of this section, the changes in adsorption energies are discussed for all classes of intermediates.

CH_3CH_2COOH AND ITS DEHYDROGENATED DERIVATIVES:

The reaction network of the HDO of propionic acid (Figure 6.1) consists of various dehydrogenated derivatives of CH_3CH_2COOH such as, $CH_3CHCOOH$, $CH_2CHCOOH$, CH_3CCOOH, and CHCHCOOH. These intermediates adsorb relatively strong on Pd(211). The binding energy of propionic acid increased by 0.37 eV on Pd(211) relative to the Pd(111) surface. $CH_3CHCOOH$, $CH_2CHCOOH$ and CH_3CCOOH are also more stable on Pd(211) by 0.46, 0.28, and 0.21 eV, respectively.

CH_3CH_2COO AND ITS DEHYDROGENATED DERIVATIVES:

CH_3CH_2COO and its dehydrogenated derivatives, which are the products of CH_3CH_2COO—H bond dissociations, are key intermediates in the DCX mechanism. These intermediates go through C-C bond dissociations to form C_2 hydrocarbon fragments and CO_2 on the surface. CH_3CH_2COO, CH_3CHCOO, and CH_3CCOO are stabilized on Pd(211) relative to Pd(111) by -0.51, -0.35, and -0.41 eV, respectively.

CH_3CH_2CO AND ITS DEHYDROGENATED DERIVATIVES:

CH_3CH_2CO and its dehydrogenated derivatives are the products of CH_3CH_2CO—OH bond dissociations and are key intermediates in the DCN mechanism prior to C-C bond cleavage to produce CO and C_2 hydrocarbons. Since these intermediates have one oxygen atom less than propionic acid their interaction with steps is smaller. In comparison to the Pd(111) surface they are on average only more stabilized by 0.24 eV on the Pd(211) surface. The least stabilized adsorbate was CH_3CH_2CO where its binding

energy on the Pd(211) surface is just 0.09 eV larger than on Pd(111). The most stabilized intermediate on step surfaces was CHCHCO were it adsorbs stronger by -0.38 eV.

CH_3CH_3 AND ITS DEHYDROGENATED DERIVATIVES:

CH_3CH_3 and all other C_2 hydrocarbon fragments are the products of C-C bond dissociations of propionic acid. As expected these intermediates are less stabilized in comparison to the oxygenates. On average these intermediates were stabilized by only 0.20 eV with a maximum for CH_2CH_2 by 0.33 eV. According to the result of our previous study,[184] CH_3C is one of the most abundant surface intermediates on Pd(111); however, CH_3C was destabilized by 0.07 eV over the Pd(211) surface. Considering that all other C_2 fragments where stabilized on average by 0.20 eV, we conclude that the HDO will likely proceed via other reaction intermediates on Pd(211) and the coverage of CH_3C is smaller. In Section 6.3.3, we will discuss the surface coverages of the most abundant surface intermediates.

H, CO, OH, CO_2, H_2O, AND COOH:

H and CO have previously[184] been identified as the most abundant surface intermediates on the Pd(111) model surface. Interestingly, H is destabilized on Pd(211) by 0.06 eV while CO is stabilized on Pd(211) by 0.05 eV relative to the (111) surface. These results are in agreement to Ye Xu *et al.[220]* who also found that H adsorbs slightly weaker on a step surface model. In contrast, OH adsorbs significantly stronger on a Pd(211) surface and the binding energy of this intermediate is increased by 0.53 eV. This observation can likely explain why intermediates containing OH groups were stabilized significantly more than other intermediates. Finally, H_2O, CO_2, and COOH (a

reaction product of the CH_3CH_2—COOH bond dissociation) were stabilized by 0.14, 0.20 and 0.35 eV, respectively.

6.3.2 REACTION RATE PARAMETERS

All elementary reactions investigated can be grouped into four different types of bond dissociations: C-C (e.g. $CH_3CH_2CO \rightarrow CH_3CH_2 + CO$), C-OH (e.g. $CH_3CH_2COOH \rightarrow CH_3CHCO + OH$), C-H (e.g. $CH_3CH_2COOH \rightarrow CH_3CHCOOH + H$), and O-H bond dissociations (e.g. $CH_3CH_2COOH \rightarrow CH_3CHCOO + H$). O-H bond dissociations are essential to the decarboxylation mechanism while C-OH bond dissociations are key reactions in the decarbonylation mechanism. According to our sensitivity analysis[184] for the Pd(111) surface, C-H bond cleavages also play an important role in the DCN mechanism and it is unlikely that propionic acid goes through a C-OH bond dissociation prior to dehydrogenation steps of the α-carbon. Finally, C-C bond dissociations are important for both DCX and DCN mechanisms to produce C_2 hydrocarbon fragments from propionate (CH_3CH_2COO), propanoyl (CH_3CH_2CO), and their dehydrogenated derivatives. Dependent on how these elementary reactions are surface structure sensitive will the (211) surface favor the DCN or DCX mechanism relative to the (111) surface.

C-C BOND DISSOCIATIONS:

Elementary activation barriers and reaction energies can often not be considered independent reaction parameters, since at least on transition metal surfaces, linear relationships between activation and reaction energies can be found, i.e., Brønsted-Evans-

Polanyi (BEP) relations.[161, 162] BEP relations for C-C bond dissociations over Pd(211) and Pd(111) are shown in Figure 6.4a. In the BEP plot, the activation barriers of C-C bond cleavages are plotted against their reaction energies. The calculated mean absolute errors (MAE) of the fitted lines for C-C bond dissociations on Pd(211) and Pd(111) are both 0.12 eV. The BEP correlation parameters are similar for both surfaces, although the BEP line of the Pd(211) surface is located slightly below the Pd(111) line which suggests that Pd(211) is generally more active for C-C bond dissociations. Notable exception is reaction 18 (CHCHCO**** ⇌ CHCH*** + CO*) whose barrier is around 0.5 eV larger on Pd(211) than on Pd(111) (See Table 6.3). This observation can be explained by the fact that CHCHCO adsorbs significantly stronger (0.4 eV) on Pd(211) than on Pd(111), and accordingly the reaction energy of this step on Pd(211) is by 0.23 eV less exothermic than on Pd(111) (Table 6.3), and consequently a larger amount of energy is needed to break this C-C bond.

Based on our previous microkinetic modeling study of the Pd(111) surface, the three dominant pathways are:

Pathway1:

$CH_3CH_2COOH \rightarrow CH_3CHCOOH \rightarrow CH_2CHCOOH \rightarrow CH_2CHCO \rightarrow CH_2CH+CO \rightarrow \rightarrow CH_3CH_3+CO$

Pathway2:

$CH_3CH_2COOH \rightarrow CH_3CHCOOH \rightarrow CH_2CHCOOH \rightarrow CHCHCOOH \rightarrow CHCHCO \rightarrow CHCH+CO \rightarrow \rightarrow CH_3CH_3+CO$

Pathway3: $CH_3CH_2COOH \rightarrow CH_3CHCOOH \rightarrow CH_3CHCO \rightarrow CH_3CCO \rightarrow CH_3C+CO \rightarrow \rightarrow CH_3CH_3+CO$

The C-C bond cleavage in the first DCN pathway (reaction15: $CH_2CHCO^{***} + * \rightleftharpoons CH_2CH^{***} + CO^*$) is facilitated on the stepped surfaces, as its barrier is decreased by 0.26 eV (the reaction is also more exothermic by 0.1 eV). In contrast, on the Pd(211) surface, reaction 18 ($CHCHCO^{****} \rightleftharpoons CHCH^{***} + CO^*$), which is the C-C bond dissociation step in pathway 2, has a significantly higher activation barrier and reaction energy on steps ($E_{act\text{-}Pd(211)} - E_{act\text{-}Pd(111)} = 0.55$ eV). Additionally, the reaction energy of reaction 14 ($CH_3CCO^{***} \rightleftharpoons CH_3C^* + CO^* + *$), i.e., the C-C bond dissociation in pathway 3, is more endothermic by 0.25 eV (the corresponding activation barrier is increased by 0.05 eV compared to Pd(111)). Consequently, the C-C bond dissociations in pathway 3 and 2 were inhibited. This suggests that while on Pd(111) there are various competing pathway, on Pd(211) the reaction will probably proceed via the first pathway and the other decarbonylation pathways are of lesser importance.

C-OH BOND DISSOCIATIONS:

C-OH bond cleavages are essential to the DCN mechanism which we previously identified to be the dominant reaction mechanism on Pd(111). Also, our sensitivity analysis of Pd(111) suggested that C-OH bond dissociations are rate-controlling at common hydrogen partial pressures. Figure 6.4b illustrates BEP relations for stepped and flat surfaces for C-OH bond dissociations. This figure suggests that the Pd(211) surface is in general less active for C-OH bond cleavages than the Pd(111) surface. The fitted BEP lines for C-OH bond cleavages on Pd(111) and Pd(211) have MAEs of 0.08 and 0.18 eV, respectively. Almost all of the C-OH bond dissociations have a higher barrier on Pd(211) except reaction 11 ($CH_2CHCOOH^{***} + * \rightleftharpoons CH_2CHCO^{***} + OH^*$) where the

barrier for this step decreased by 0.37 eV due to an "ideal" transition state geometry with interaction of the OH bond with the stepped atoms in the TS configuration (Figure 6.3). Considering furthermore that reaction 11 is also on the first reaction pathway described above, the importance of this pathway for DCN becomes apparent.

C-H BOND DISSOCIATIONS:

The BEP relationships shown in Figure 6.4c suggest that for C-H bond dissociations, stepped surface models are slightly more active than Pd(111) terrace sites. The MAEs of the BEP relations for C-H bond dissociations on Pd(111) were found to be 0.12 eV, while on Pd(211) the MAE was 0.11 eV. Previously, we found for the Pd(111) surface that dehydrogenation steps can at least be partially rate controlling since they facilitate C-C and C-OH bond dissociations.[184] Considering that C-OH bond dissociations are inhibited on Pd(211) surfaces, while C-H cleavages are facilitated, it is difficult to determine the impact of surface structure on the decarbonylation rate and we will discuss this topic in Section 6.3.3 together with our microkinetic modeling results.

Finally, we note that hydrogenation steps are also facilitated on stepped surfaces. These elementary reactions are essential for removing the C_2 hydrocarbon fragments from the surface to close the catalytic cycle. For example, on Pd(111) it is difficult to hydrogenate the CH_3C species and consequently, it is one of the most abundant surface intermediates at low hydrogen partial pressures. The removal of this intermediate from stepped surfaces, reaction 24 ($CH_3C^* + H^* \rightleftharpoons CH_3CH^{**}$), is significantly facilitated, as the activation barrier of this elementary reaction decreases by 0.19 eV and the reaction is less endothermic by 0.43 eV.

O-H BOND DISSOCIATIONS:

O-H bond dissociations are key elementary reactions in the DCX mechanism. BEP relationships of O-H bond dissociations on Pd(111) and Pd(211) have MAEs of 0.09 eV and 0.11 eV, respectively. As shown in Figure 6.4d, the activity of the Pd(211) surface is lower for O-H bond dissociations than the Pd(111) surface, suggesting that the DCN mechanism remains dominant on Pd(211). Finally, we note that while most barriers of O-H bond dissociations were increased by at least 0.1 eV on Pd(211), the activation barrier of reaction 28 ($CH_3CH_2COOH^* + 2^* \rightleftharpoons CH_3CH_2COO^{**} + H^*$) is equivalent to the barrier on Pd(111). Also, reaction 28 is more exothermic by 0.08 eV on Pd(211) such that if the dominant DCX mechanism involves reaction 28, a higher DCX reaction rate will be observed on Pd(211) relative to Pd(111). In the next section, the importance of the DCX and DCN mechanism in the deoxygenation of propionic acid will be investigated by analyzing a mean-field microkinetic model.

6.3.3 MICROKINETIC MODELING

We previously [140, 184] developed mean-field microkinetic models for the reaction mechanism of the DCX and DCN of propanoic acid over Pd(111) model surfaces. Analysis of the models at a temperature of 473 K and partial pressures of propanoic acid, H_2, CO_2, and H_2O of 1 bar and a CO partial pressure in the range of 0.001 to 0.1 bar suggested that the DCN pathway is preferred over the DCX mechanism. The mechanism and turnover frequencies (TOF) were found to be not sensitive to the partial pressures of H_2O, CO_2, and CO (in the range of 10^{-4} to 10^{-1} bar). The most abundant

surface intermediates under gas phase conditions were adsorbed hydrogen, CO, and CH_3C.

In this study, we have developed a mean-field microkinetic model for the HDO of propionic acid over our Pd(211) model surface under reaction conditions equivalent to the conditions of our experimental collaborators[159] and we compare these results to mean-field modeling results on the Pd(111) surface. All calculations were carried out at 473 K and partial pressures of propionic acid and H_2 of 0.01 and 0.2 bar, respectively.[159] The partial pressures of H_2O, CO_2, and CO were set to 0.001 bar which corresponds to approximately 10% conversion. It is noted that our results and conclusions seem to be insensitive to the reaction conditions. Also, we note that since our model does not contain a water-gas shift model, the product partial pressures had to be fixed in the calculation of turnover frequencies.

Next, we note that a method similar to Grabow *et al.[146]* was used for determining coverage dependent adsorption energies of CO and H. More details about the lateral interactions used in the microkinetic model for this study can be found in the supporting information and in our previous study[158]. All DFT-derived rate constants for all elementary reactions considered in the HDO of priopionic acid over Pd(111) and Pd(211) model surfaces are listed in Table 6.4. In the following, we first discuss our results for the (111) surface model, followed by (211) surface model results.

PD(111):

The overall turnover frequency (TOF) on Pd(111) surfaces was calculated to be 1.70×10^{-7} s^{-1} which is by 3 orders of magnitude lower than the experimental TOF of

1.67×10^{-4} s^{-1} over carbon supported palladium catalysts.[159] The sum of the TOFs of the DCN pathways are 1.65×10^{-7} and the sum of the TOFs of the DCX pathways are 4.79×10^{-9}, illustrating that the rate of the DCN is approximately two orders of magnitude higher than the rate of the DCX. Next, we find the dominant mechanism to involve propanoic acid to undergo three dehydrogenation steps of α and β-carbons to form CHCHCOOH, followed by C-OH cleavage, and C-CO bond dissociation to produce C_2 products ($CH_3CH_2COOH \rightarrow CH_3CHCOOH \rightarrow CH_2CHCOOH \rightarrow CHCHCOOH \rightarrow CHCHCO \rightarrow CHCH$, $TOF_{Dominant\text{-}Pathway}=7.18\times10^{-8}$ s^{-1}). 33.9% of the surface was free of adsorbed intermediates and the coverage of the most abundant surface species are adsorbed hydrogen (26.1%), CO (30.9%), and CH_3C (9.0%).

Other competitive pathways are, $CH_3CH_2COOH \rightarrow CH_3CHCOOH \rightarrow CH_2CHCOOH \rightarrow CH_2CHCO \rightarrow CH_2CH+CO \rightarrow\rightarrow CH_3CH_3+CO$, with a TOF of 3.22×10^{-8} s^{-1}, and $CH_3CH_2COOH \rightarrow CH_3CHCOOH \rightarrow CH_3CHCO \rightarrow CH_3CCO \rightarrow CH_3C+CO \rightarrow\rightarrow CH_3CH_3+CO$, with a TOF of 3.43×10^{-8} s^{-1}. All DCN pathways have in common that $\tilde{\alpha}$ and β-carbon dehydrogenation steps precede the C-OH and C-C bond dissociations. The most dominant DCX pathway ($CH_3CH_2COOH \rightarrow CH_3CHCOOH \rightarrow CH_3CHCOO \rightarrow CH_3CCOO \rightarrow CH_3C+CO_2 \rightarrow\rightarrow CH_3CH_3 + CO_2$) possesses a TOF of 1.8×10^{-9} s^{-1}. This reaction pathway also involves α-carbon dehydrogenation steps prior to O-H and C-C bond scissions.

Pd(211):

The overall turnover frequency on Pd(211) was calculated to be 6.20×10^{-8} s^{-1} which is 2.7 times smaller than the TOF over Pd(111). We conclude that within the accuracy of our DFT calculations and the mean-field models the activity of both surface

structures is essentially equivalent. The sum of the TOFs of the DCN pathways are 5.35×10^{-8} s^{-1} which is approximately one order of magnitude larger than the sum of the TOFs of the DCX pathways which is 8.47×10^{-9} s^{-1}. Compared to the (111) surface the DCX pathways become relatively more competitive to the DCN on the (211) surface model. As discussed in Section 6.3.2, reaction 28 ($CH_3CH_2COOH^* + 2^* \rightleftharpoons CH_3CH_2COO^{**} + H^*$) is facilitated on Pd(211) and our microkinetic model confirms our prediction that the DCX follows reaction 28 and direct C-C bond dissociation ($CH_3CH_2COOH \rightarrow CH_3CH_2COO+H \rightarrow CH_3CH_2+CO_2 \rightarrow\rightarrow CH_3CH_3+CO_2$). However, the TOF of the DCN mechanism is still greater than the TOF of the DCX by a factor 6.3.

Next, the microkinetic model of the (211) surface suggests that the dominant DCN pathway is: $CH_3CH_2COOH \rightarrow CH_3CHCOOH \rightarrow CH_2CHCOOH \rightarrow CH_2CHCO \rightarrow CH_2CH+CO \rightarrow \rightarrow CH_3CH_3+CO$, with a TOF of 5.32×10^{-8} s^{-1}, i.e., it again involves dehydrogenation steps prior to C-OH and C-C bond scissions. Finally, the most abundant surface intermediates are CO, H, and free sites with surfaces coverages of 52.1%, 42.9% and 5.0%, respectively. Interestingly, the surface coverage of CH_3C which covered 9.0% of the Pd(111) is essentially not present on Pd(211), $\theta_{CH3C^*} = 4.2\times10^{-8}$.

6.3.4 Apparent Activation Barrier, Reaction Orders, and Sensitivity Analysis

Apparent activation barriers were computed in the temperature range of 423 to 523 K in all reaction environments and hydrogen partial pressures.

$$E_a = RT^2\left(\frac{\partial \ln(r)}{\partial T}\right)_{p_i} \tag{6.9}$$

Next, the reaction order with respect to hydrogen was calculated at 473 K in the range of 0.05 to 0.4 bar. Similarly, the reaction order of propionic acid and CO were calculated at 473 K and a pressure range of 0.005 to 0.1 bar and 0.0001 to 0.1 bar, respectively.

$$\alpha_i = \left(\frac{\partial \ln(r)}{\partial \ln(p_i)} \right)_{T, p_{j \neq i}} \tag{6.10}$$

Finally, Campbell's degrees of rate and thermodynamic control,[147-149] X_{RC} and X_{TRC}, were used to determine the rate controlling steps and intermediates in the mechanism. Rate controlling steps and intermediates are those transition states and intermediates that most strongly influence the reaction rate and are potential activity descriptors.

$$X_{\mathrm{RC},i} = \frac{k_i}{r} \left(\frac{\partial r}{\partial k_i} \right)_{K_i, k_j \neq k_i}, \qquad X_{\mathrm{TRC},n} = \frac{1}{r} \left(\frac{\partial r}{\partial \left(\frac{-G_n^0}{RT} \right)} \right)_{G_{m \neq n}^0, G_i^{0,\mathrm{TS}}} \tag{6.11}$$

where r is the overall rate of reaction, k_i is the forward rate constant for step i, K_i is the equilibrium constant for step i, R is the gas constant, T denotes the reaction temperature, and $G_n^{\,0}$ is the free energy of adsorbate n.

Pd(111):

At a reaction temperature of 473 K, our model predicts an apparent activation energy of 0.85 eV which is in reasonable agreement to the experimental apparent activation energy of ~12-19 kcal/mol (0.52-0.78 eV).[159] The reaction order with

respect to propionic acid, CO and H_2 are +1.0, +0.22, and -0.81, respectively, which is in good agreement to our previous studies[140, 158, 184] at different reaction conditions. Next, Campbell's degree of rate control analysis suggests that the most rate controlling steps on the surface are C-OH bond dissociations. Reaction 17 ($CHCHCOOH^{***} + 2^* \rightleftharpoons CHCHCO^{****} + OH^*$) is the C-OH bond dissociation step in the dominant reaction pathway and has the largest rate control of 0.42. Additionally, C-OH bond dissociation steps of other competing pathways, such as reaction 5 ($CH_3CHCOOH^{**} + * \rightleftharpoons CH_3CHCO^{**} + OH^*$) and reaction 11 ($CH_2CHCOOH^{***} + * \rightleftharpoons CH_2CHCO^{***} + OH^*$) are also rate controlling with X_{RC} values of 0.37, and 0.24 respectively. Finally, dehydrogenation steps of the α- and β-carbons are also found to be partially rate-controlling under the chosen reaction rate conditions. For example, the X_{RC} of the dehydrogenation of the α-carbon of propionic acid (reaction 2) was calculated to be 0.24 and the X_{RC} for the dehydrogenation of the β-carbon of $CH_3CHCOOH$ (reaction 6) and $CH_2CHCOOH$ (reaction 12) were calculated to be 0.07 and 0.05, respectively. We note that the sum of the degree of rate control is larger than one due to numerical inaccuracies of our nonlinear equation solver; however, the trends should not be affected by these numerical issues.

Finally, the thermodynamic rate control analysis suggests that the adsorption free energy of H* and CO* have a significant effect on the overall rate with X_{TRC} = -1.66 and 0.26, respectively, such that destabilizing the adsorbed hydrogen or stabilizing CO slightly improves the overall reaction rate (due to lateral interactions a stabilization of CO leads to a significant destabilization of adsorbed hydrogen).

Pd(211):

For the Pd(211) surface our model predicts an apparent activation energy of 0.86 eV which is essentially equivalent to the (111) surface. Also, the reaction order with respect to propionic acid, CO and H_2 are very similar to the (111) surface with +1.0, 0.0, and -3.2, respectively. The very negative reaction order with respect to hydrogen can be explained by the strong hydrogen adsorption energy on the stepped surface.

Campbell's degree of rate control suggests that the C-OH bond dissociation step in reaction 11 ($CH_2CHCOOH*** + * \rightleftharpoons CH_2CHCO*** + OH*$) is rate controlling with X_{RC} = 0.92. Additionally, the dehydrogenation of the α-carbon of propionic acid (reaction 2) and the β-carbon of $CH_3CHCOOH$ (reaction 6) are partially rate controlling dehydrogenation steps with X_{RC} = 0.12 and 0.15, respectively. Considering that we found that the DCX mechanism is nearly competitive to the DCN mechanism on Pd(211), our sensitivity analysis identified the C-C bond scission in the DCX pathway, reaction 29 ($CH_3CH_2COO** \rightleftharpoons CH_3CH_2* + CO_2*$), to be partially rate controlling with X_{RC} = 0.12.

We note that this reaction is not rate controlling on flat surface sites since the DCX mechanism is significantly slower than the DCN pathway on Pd(111). Finally, the degree of thermodynamic rate control of H* was calculated to be -6.08 implying that adsorbed hydrogen atoms inhibited the reaction significantly. In contrast, the X_{TRC} of CO was calculated to be 0.08 which shows that the impact of CO coverage on the overall rate is very small.

6.3.5 DISPERSION INTERACTIONS

Considering that the predicted turnover frequencies are three orders of magnitude smaller than our experimentally observed turnover frequencies and also that the acid reaction order is systematically too high,[159] we tested if neglect of dispersion interactions in the PW91 functional used in this study could at least partially explain this discrepancy. We used the PBE-D3 method[221] to calculate adsorption/desorption energies of propanoic acid, H_2, CO, CO_2, H_2O, CHCH, CH_2CH_2, and CH_3CH_3 over the Pd(111) and Pd(211) surfaces, and we implemented the obtained reaction parameters in a similar microkinetic model to the one that used the PW91 functional. We note that the PBE and PW91 functional predict very similar adsorption and reaction energies. Also, for surface reactions the PBE and PBE-D3 functional usually predict very similar reaction energies. However, hydrocarbon adsorption energies on metal surfaces computed with PW91 and PBE-D3 functional are quite different. The computational setup for the PBE-D3 calculations is identical to the one for the PW91 calculations. The PBE-D3 and PW91 adsorption energies are listed in Table 6.3. In the following, we show that inclusion of dispersion interactions increases the TOFs for both the Pd(111) and Pd(211) surface models; however, the trend in the activity stays the same and our results suggest that flat surfaces are the active sites for the HDO of propanoic acid. In the following, we call the model that used the PBE-D3 functional for adsorption processes the "dispersion-corrected" model and the model that uses the PW91 functional for adsorption processes the PW91 model.

Pd(111) – PBE-D3:

After including dispersion forces propanoic acid adsorbs stronger on Pd(111) by 0.35 eV. Our "dispersion-corrected" microkinetic model suggests that the dominant reaction mechanism is identical to our previous prediction obtained with PW91 functional (CH_3CH_2COOH → $CH_3CHCOOH$ → $CH_2CHCOOH$ → CHCHCOOH → CHCHCO → CHCH). However, the overall TOF is now higher, $TOF_{Overall\text{-}D3\text{-}Pd(111)}=3.81\times10^{-5}$ s^{-1}, which is more than two orders of magnitude larger than the TOF computed with PW91 functional, 1.70×10^{-7} s^{-1}. We note that the TOF computed in the "dispersion-corrected" model is significantly closer to the experimental TOF over Pd/C under the same reaction conditions (1.67×10^{-4} s^{-1}); although, it is still smaller than the experimental TOF by a factor 4 which we consider to be within the accuracy of DFT and mean-field models. The most abundant surface intermediates are θ_{CO}=34.0%, θ_H=22.2%, θ_{CH3C}=12.0%, and the coverage of free sites, θ_*=31.9%. This is similar to the coverages predicted with the PW91 model (θ_{CO}=30.9%, θ_H=26.1%, θ_{CH3C}=9.0%, and θ_*=33.9%). However, as a result of the stronger adsorption, the propanoic acid reaction order computed with the "dispersion-corrected" model is slightly smaller than in the PW91 model ($n_{PAc\text{-}PW91=}$1.0 vs. $n_{PAc\text{-}PBE\text{-}D3}$=0.95). We note that this is the first time we were able to obtain acid reaction orders smaller than 1 which is in better agreement with the experimental reaction order (~ 0.5 to 0.7).[159] Next, the reaction order of CO decreased from, $n_{CO\text{-}PW91}$= +0.22 to $n_{CO\text{-}PBE\text{-}D3}$=0.19, and finally, the reaction order of H_2 was less negative in the "dispersion-corrected" model ($n_{H2\text{-}PW91}$= -0.81 to $n_{H2\text{-}PBE\text{-}D3}$= -0.67), since the dispersion effect on adsorption of hydrogen is relatively smaller than of the hydrocarbon molecules (Table 6.3). The rate-controlling steps and

species are the same in both models. A schematic of the TOFs of all elementary steps in the HDO of propanoic acid in both models are illustrated in Figure 6.5A and 6.5B.

Pd(211) – PBE-D3:

Similar to the Pd(111) surface the inclusion of dispersion forces does not affect the dominant reaction mechanism over Pd(211) (CH_3CH_2COOH → $CH_3CHCOOH$ → $CH_2CHCOOH$ → CH_2CHCO → CH_2CH → → CH_3CH_3 / CH_2CH_2); however, the "dispersion-corrected" model predicts a TOF that is increased by more than 2 orders of magnitude compared to the previous PW91 model ($TOF_{D3\text{-}PBE\text{-}Pd(211)}=4.69\times10^{-6}$ s^{-1} vs. $TOF_{PW91\text{-}Pd(211)}= 6.20\times10^{-8}$ s^{-1}). We conclude that stepped surface models remain slightly less active than flat surface models independent of the functional used for adsorption processes. The most abundant surface intermediates in the "dispersion-corrected" model are θ_{CO}=58.8%, θ_H=38.1%, and the coverage of free sites, θ_*=2.3%. These results are quite similar to the previous modeling results with PW91 functional (θ_{CO}=52.1%, θ_H=42.9%, and θ_*=5.0%). A key difference between the models is that the coverage of propionate (CH_3CH_2COO) dramatically increased in the "dispersion-corrected" model to 0.4 % (the PW91 model predicts a coverage of only 10^{-5} for propionate).

The reaction order with respect to propionic acid, CO, and H_2 are +0.7, +0.18 and -3.73 in the "dispersion-corrected" model. Similarly to the Pd(111) surface, we observe that the reaction order of the organic acid dropped from 1.0 (PW91 model) to 0.7 (dispersion-corrected model) due to the stronger adsorption. The reaction order of CO slightly increased in the "dispersion-corrected" model relative to the PW91 model where the CO reaction order was essentially zero. The positive CO reaction order can be

explained by our lateral interaction model between H and CO where an increase in the coverage of CO leads to a decrease in the coverage of hydrogen on the surface which results in a slightly higher TOF. Finally, the reaction order of hydrogen is significantly more negative on Pd(211) than on Pd(111) independent of functional and the rate-controlling steps and species are the same in both models.

6.3.6 Active sites for the HDO of propanoic acid over Pd catalysts

We showed that in the PW91 models the TOF of the HDO of propionic acid over Pd(111) is 3 times larger than over Pd(211) ($TOF_{PW91\text{-}Pd(111)} = 1.70\times10^{-7}$ s^{-1} vs. $TOF_{PW91\text{-}Pd(211)} = 6.20\times10^{-8}$ s^{-1}). This trend does not change after inclusion of dispersion forces for adsorption/desorption steps with PBE-D3 functional and the TOF over Pd(111) is 8 times larger than over Pd(211) ($TOF_{PBE\text{-}D3\text{-}Pd(111)} = 3.81\times10^{-5}$ s^{-1} vs. $TOF_{PBE\text{-}D3\text{-}Pd(211)} = 4.69\times10^{-6}$ s^{-1}). Consequently, our result suggests that flat surfaces are slightly more active than stepped surface models for the HDO of propionic acid over palladium catalysts.

In a previous experimental work,[203] the particle size effect on the HDO of propionic acid was investigated over silica supported palladium catalysts at identical reaction conditions to this computational study (473K, partial pressures of propanoic acid and hydrogen of 0.01 and 0.2 bar). The observed activity for the Pd/SiO_2 catalysts over the entire particle size range studied (1.9-12.4 nm) is shown in Figure 6.6.

Smaller particle sized catalysts are slightly less active than the larger ones. Smaller particles have more low-coordinated sites such as steps, edges, and corners. By performing a van Hardeveld and Hartog statistical analysis,[222] we showed[203] that the surface of the largest particles (12.4 nm) consists of 75% Pd (111) facets and 18% Pd

(100) facets, while the smallest one (1.9 nm) has 47% Pd(111) facets and 6% Pd(100) surface sites. The larger particle size catalysts have an activity (TOF) of 0.8 min^{-1}, while the activity of the smallest catalyst (1.9 nm) is reported to be 0.46 min^{-1}.[203] Accordingly, with decreasing particle size and decreasing ratio of Pd(111) sites to low-coordinated sites, the observed activity is decreased. These observations are in very good agreement with our computational results were we found out that the TOF on flat surfaces is by a factor 3 higher than on stepped surface sitess (factor 8 in the "dispersion-corrected" model). Consequently, the computational and experimental results suggest that flat surfaces are the active sites for the HDO of propanoic acid over Pd catalysts.

6.4 CONCLUSIONS

The effect of palladium catalysts surface structure on the hydrodeoxygenation of propionic acid has been investigated by studying both Pd(211) and Pd(111) model surfaces using periodic DFT calculations. We developed a mean-field microkinetic model at a temperature of 473 K and propionic acid and hydrogen partial pressures of 0.01 and 0.2 bar, respectively, which correspond to the experimental reaction conditions investigated by some of us. Activity on stepped surfaces was slightly lower than on flat surface models; however, the difference between the TOFs of flat and stepped surfaces is not remarkable, suggesting that the hydrodeoxygenation of propionic acid over palladium catalyst is nearly insensitive to surface structure. Nevertheless, we predict that Pd(111) surface sites are the main active sites of this reaction. Decarbonylation was the dominant reaction mechanism over Pd(111) model surfaces, while on Pd(211) decarbonylation and decarboxylation are essentially competitive. The most dominant decarbonylation

pathway on Pd(211) involves propionic acid undergoing dehydrogenation of both α- and β-carbons prior to C-OH and C-C bond dissociation, i.e., CH_3CH_2COOH → $CH_3CHCOOH$ → $CH_2CHCOOH$ → CH_2CHCO → CH_2CH → → CH_3CH_3 / CH_2CH_2. In contrast, over Pd(111) an even deeper dehydrogenation is predicted with a reaction sequence of CH_3CH_2COOH → $CH_3CHCOOH$ → $CH_2CHCOOH$ → CHCHCOOH → CHCHCO → CHCH → → CH_3CH_3 / CH_2CH_2.

On flat surface sites, the calculated turnover frequencies of the decarboxylation mechanism are two orders of magnitude smaller than those of the decarbonylation mechanism. In contrast, over Pd(211) model surfaces decarboxylation is facilitated and the turnover frequency of decarboxylation is very close to the turnover frequencies of decarbonylation. While on Pd(111), CH_3C, H, and CO are the most abundant surface intermediates, the formation of CH_3C is not favored on Pd(211) as this intermediate is destabilized on the stepped surface models. Consequently, adsorbed hydrogen and CO are the main intermediates on stepped surface models. The apparent activation energies on Pd(211) and Pd(111) are calculated to be 0.86 and 0.85 eV, respectively. Our sensitivity analysis suggests that on both surfaces C-OH bond dissociations and dehydrogenation steps of both α- and β-carbons are rate-controlling. In addition, on Pd(211) the C-C bond dissociation of propionate to CH_3CH_2 and CO_2—a key step in the decarboxylation mechanism—was also found to be partially rate controlling.

Finally, to improve the accuracy of our models we included dispersion interactions approximately by using the PBE-D3 functional for adsorption/desorption processes. Overall, a very good agreement with the experimental turnover frequencies and reaction orders could be obtained.

6.5 ACKNOWLEDGEMENTS

We gratefully acknowledge the financial support from the National Science Foundation (CHE-1153012). Computational resources have been provided by the National Energy Research Scientific Computing Center (NERSC) which is supported by the Office of Science of the U.S. Department of Energy and in part by XSEDE under grant number TG-CTS090100. Finally, computing resources from the USC NanoCenter and USC's High Performance Computing Group are gratefully acknowledged.

6.6 TABLES

Table 6.1 Binding modes, zero-point energy corrected adsorption energies (E_{ads}, in eV) of reaction intermediates on Pd(211) and Pd(111) model surfaces.

Species	Stoichiometry	Figure 6.3 species	Binding mode On Pd(211)	E_{ads} (eV) Pd(211)	E_{ads} (eV) Pd(111)[119]
Propanoic acid	CH_3CH_2COOH	1	$\eta 1\mu 1$ (O)	-0.57	-0.20
Ethylidene-1-ol-1-olate	$CH_3CHCOOH$	2	$\eta 2\mu 2$ (C,O)	-1.86	-1.40
Ethenyl-1-ol-1-olate	CH_3CCOOH	3	$\eta 2\mu 3$ (C,O)	-3.43	-3.22
Propanoyl	CH_3CH_2CO	4	$\eta 2\mu 3$ (C,O)	-2.57	-2.48
Carbonylethylidene	CH_3CHCO	5	$\eta 2\mu 2$ (C,O)	-1.49	-1.20
Carbonylethenyl	CH_3CCO	6	$\eta 2\mu 3$ (C,C)	-3.21	-2.98
Vinyl-1-ol-1-olate	$CH_2CHCOOH$	7	$\eta 2\mu 2$ (C,C)	-1.16	-0.88
Carbonylvinyl	CH_2CHCO	8	$\eta 2\mu 2$ (C,C)	-2.64	-2.45
Ethyne-1-ol-1-olate	CHCHCOOH	9	$\eta 3\mu 3$ (C,C,O)	-3.20	-2.84
Carbonylethyne	CHCHCO	10	$\eta 3\mu 3$ (C,C,C)	-3.87	-3.49
Propanoate	CH_3CH_2COO	11	$\eta 2\mu 2$ (O,O)	-2.72	-2.21
Carboxylethylidene	CH_3CHCOO	12	$\eta 3\mu 3$ (C,O,O)	-1.66	-1.31
Carboxylethenyl	CH_3CCOO	13	$\eta 2\mu 3$ (C,O)	-2.12	-1.71
Carboxylic	COOH	14	$\eta 2\mu 2$ (C,O)	-2.42	-2.07
Ethyne	CHCH	15	$\eta 2\mu 3$ (C,C)	-2.14	-1.94
ethen-1,1-diyl	CH_2C	16	$\eta 2\mu 4$ (C,C)	-4.21	-3.91
Vinyl	CH_2CH	17	$\eta 2\mu 2$ (C,C)	-2.98	-2.74
Ethene	CH_2CH_2	18	$\eta 2\mu 2$ (C,C)	-1.20	-0.87
Ethenyl	CH_3C	19	$\eta 1\mu 3$ (C)	-5.51	-5.58
Ethylidene	CH_3CH	20	$\eta 1\mu 2$ (C)	-3.95	-3.64
Ethyl	CH_3CH_2	21	$\eta 1\mu 1$ (C)	-1.79	-1.63

Ethane	CH_3CH_3	22	$\eta 1 \mu 1$ (H)	-0.14	-0.05
Hydrogen	H	23	$\eta 1 \mu 3$ (H)	-2.65	-2.71
Hydroxyl	OH	24	$\eta 1 \mu 2$ (O)	-3.12	-2.59
Water	H_2O	25	$\eta 1 \mu 1$ (O)	-0.35	-0.21
Carbon monoxide	CO	26	$\eta 1 \mu 3$ (C)	-2.02	-1.97
Carbon dioxide	CO_2	27	$\eta 2 \mu 2$ (O,C)	-0.21	-0.01

Table 6.2 Zero-point corrected reaction and activation energies in eV for all elementary reaction steps considered in the HDO of propionic acid over Pd(111) and (211). For Pd(211) imaginary transition state frequencies and the bond length of the dissociating fragment are also given.

#	Reaction	Pd(111)[119]		Pd(211)		Pd(211)	Pd(211)
		ΔE_{rxn}	$E^{\ddagger}$	ΔE_{rxn}	$E^{\ddagger}$	ν (cm^{-1})	TS bond (Å)
1	$CH_3CH_2COOH^* + 3^* \rightleftharpoons CH_3CH_2CO^{***} + OH^*$	0.41	0.91	0.17	1.16	318 *i*	2.01
2	$CH_3CH_2COOH^* + 2^* \rightleftharpoons CH_3CHCOOH^{**} + H^*$	-0.11	0.62	-0.14	0.49	730 *i*	1.55
3	$CH_3CH_2CO^{***} \rightleftharpoons CH_3CH_2^* + CO^* + *$	-0.63	1.01	-0.75	0.55	377 *i*	1.95
4	$CH_3CH_2CO^{***} \rightleftharpoons CH_3CHCO^{**} + H^*$	0.01	0.82	-0.14	0.79	756 *i*	1.58
5	$CH_3CHCOOH^{**} + ^* \rightleftharpoons CH_3CHCO^{**} + OH^*$	0.53	0.88	0.17	1.16	246 *i*	2.20
6	$CH_3CHCOOH^{**} + 2^* \rightleftharpoons CH_2CHCOOH^{***} + H^*$	-0.38	0.54	-0.14	0.64	952 *i*	1.54
7	$CH_3CHCOOH^{**} + 2^* \rightleftharpoons CH_3CCOOH^{***} + H^*$	-0.06	1.16	0.24	0.72	772 *i*	1.70
8	$CH_3CHCO^{**} + ^* \rightleftharpoons CH_3CH^{**} + CO^*$	-0.81	1.02	-0.88	0.73	438 *i*	1.94
9	$CH_3CHCO^{**} + 2^* \rightleftharpoons CH_3CCO^{***} + H^*$	-0.38	0.61	-0.26	0.61	790 *i*	1.64
10	$CH_3CHCO^{**} + 2^* \rightleftharpoons CH_2CHCO^{***} + H^*$	-0.32	0.55	-0.16	0.36	771 *i*	1.45
11	$CH_2CHCOOH^{***} + ^* \rightleftharpoons CH_2CHCO^{***} + OH^*$	0.58	1.23	0.86	0.86	259 *i*	2.24
12	$CH_2CHCOOH^{***} + ^* \rightleftharpoons CHCHCOOH^{***} + H^*$	0.03	0.89	0.01	0.58	715 *i*	1.75
13	$CH_3CCOOH^{***} + ^* \rightleftharpoons CH_3CCO^{***} + OH^*$	0.20	0.79	-0.34	0.77	277 *i*	2.00
14	$CH_3CCO^{***} \rightleftharpoons CH_3C^* + CO^* + *$	-1.36	0.47	-1.11	0.51	473 *i*	1.78
15	$CH_2CHCO^{***} + ^* \rightleftharpoons CH_2CH^{***} + CO^*$	-0.76	0.82	-0.86	0.56	409 *i*	1.97
16	$CH_2CHCO^{***} + 2^* \rightleftharpoons CHCHCO^{****} + H^*$	0.01	0.68	-0.13	0.47	739 *i*	1.71
17	$CHCHCOOH^{***} + 2^* \rightleftharpoons CHCHCO^{****} + OH^*$	0.56	1.08	0.02	1.10	281 *i*	1.82
18	$CHCHCO^{****} \rightleftharpoons CHCH^{***} + CO^*$	-1.09	0.38	-0.96	0.93	458 *i*	1.88
19	$CHCH^{***} + H^* \rightleftharpoons CH_2CH^{***} + *$	0.32	0.94	0.23	0.77	638 *i*	1.48
20	$CH_2CH^{***} + H^* \rightleftharpoons CH_2CH_2^{**} + 2^*$	-0.04	0.88	-0.18	0.55	691 *i*	1.78
21	$CH_2CH^{***} \rightleftharpoons CH_2C^{**} + H^*$	-0.43	0.46	-0.43	0.64	936 *i*	1.49
22	$CH_2C^{**} + H^* \rightleftharpoons CH_3C^* + 2^*$	-0.23	0.88	0.08	1.02	995 *i*	1.67
23	$CH_2CH^{***} + H^* \rightleftharpoons CH_3CH^{**} + 2^*$	0.27	0.79	0.14	0.77	983 *i*	1.59
24	$CH_3C^* + H^* \rightleftharpoons CH_3CH^{**}$	0.93	1.09	0.50	0.90	390 *i*	1.36
25	$CH_3CH^{**} + H^* \rightleftharpoons CH_3CH_2^* + 2^*$	0.18	0.88	0.28	0.70	759 *i*	1.70
26	$CH_3CH_2^* + H^* \rightleftharpoons CH_3CH_3^* + *$	0.06	0.65	0.07	0.62	896 *i*	1.61

27	CH_3CH_2* + 2* ⇌ CH_2CH_2** + H*	-0.23	0.52	-0.60	0.18	536 *i*	1.38
28	CH_3CH_2COOH* + 2* ⇌ CH_3CH_2COO** + H*	-0.40	0.35	-0.48	0.35	447 *i*	1.50
29	CH_3CH_2COO** ⇌ CH_3CH_2* + CO_2*	0.24	1.43	0.38	1.51	563 *i*	2.01
30	CH_3CH_2COO** + 2* ⇌ CH_3CHCOO*** + H*	0.38	1.22	0.59	1.05	665 *i*	1.63
31	$CH_3CHCOOH$** + * ⇌ CH_3CHCOO** + H*	0.09	0.78	0.25	0.87	342 *i*	1.57
32	$CH_3CHCOOH$** + * ⇌ CH_3CH ** + COOH*	0.32	1.39	0.11	1.23	409 *i*	1.95
33	CH_3CHCOO*** ⇌ CH_3CH** + CO_2*	-0.32	0.96	-0.48	0.83	442 *i*	1.90
34	CH_3CHCOO*** + * ⇌ CH_3CCOO*** + H*	-0.08	0.85	-0.08	0.69	760 *i*	1.68
35	CH_3CCOOH*** + * ⇌ CH_3CCOO*** + H*	0.06	0.93	-0.07	1.02	411 *i*	1.57
36	CH_3CCOOH*** ⇌ CH_3C* + COOH**	-0.55	0.92	-0.63	0.74	444 *i*	1.89
37	$CH_2CHCOOH$*** + * ⇌ CH_2CH*** + COOH*	0.71	2.07	0.11	0.94	357 *i*	2.00
38	CH_3CCOO*** ⇌ CH_3C* + CO_2* + *	-1.08	0.65	-0.81	0.72	480 *i*	2.08
39	COOH** ⇌ CO_2* + H*	-0.55	0.36	-0.34	0.55	674 *i*	1.49
40	COOH** ⇌ CO* + OH*	-0.60	0.41	-0.82	0.55	259 *i*	1.96
41	OH* + H* ⇌ H_2O* + *	0.17	0.69	0.17	0.97	740 *i*	1.62

Table 6.3 ZPE-corrected adsorption energies (E_{ads}, in eV) in eV of all stable gas phase species in the decarbonylation and decarboxylation of propanoic acid to ethane on Pd(111) and Pd(211) computed using the PW91 functional and the PBE-D3 method.

#	Reaction	Pd(111)-ΔE_{rxn}		Pd(211)-ΔE_{rxn}	
		PW91	PBE-D3	PW91	PBE-D3
42	$CH_3CH_2COOH+* \rightleftharpoons CH_3CH_2COOH*$	-0.20	-0.45	-0.57	-0.85
43	$CH_3CH_3 + * \rightleftharpoons CH_3CH_3*$	-0.05	-0.39	-0.14	-0.41
44	$CH_2CH_2 + 2* \rightleftharpoons CH_2CH_2**$	-0.87	-1.22	-1.20	-1.50
45	$H_2O + * \rightleftharpoons H_2O*$	-0.21	-0.39	-0.35	-0.57
46	$CO_2 + * \rightleftharpoons CO_2*$	-0.01	-0.27	-0.21	-0.43
47	$CHCH + * \rightleftharpoons CHCH*$	-1.94	-2.15	-2.14	-2.40
48	$CO* \rightleftharpoons CO + *$	-1.97	-2.13	-2.02	-2.18
49	$H_2 + 2* \rightleftharpoons 2H*$	-1.13	-1.19	-1.02	-1.08

Table 6.4 Equilibrium and forward reaction rate constants for all elementary steps considered in the HDO of propionic acid over Pd (211) and Pd (111) model surfaces at a temperature of 473 K.

Reaction #	Pd(211)		Pd(111)[158, 184]	
	K_{eq}	$k_{forward}$ (s^{-1})	K_{eq}	$k_{forward}$ (s^{-1})
1	1.56×10^{-2}	2.61	1.77×10^{-5}	4.36×10^{2}
2	1.39×10^{1}	1.36×10^{7}	1.79	3.68×10^{5}
3	3.38×10^{8}	8.07×10^{6}	1.64×10^{7}	1.36×10^{2}
4	2.94×10^{1}	1.60×10^{4}	3.54×10^{-1}	1.01×10^{4}
5	3.31×10^{-2}	2.02	3.51×10^{-6}	5.52×10^{3}
6	1.35×10^{1}	6.04×10^{5}	6.72×10^{3}	9.34×10^{6}
7	7.39×10^{-4}	1.43×10^{5}	2.30	4.56
8	7.79×10^{9}	7.77×10^{4}	8.52×10^{8}	3.25×10^{2}
9	8.20×10^{2}	1.40×10^{6}	8.79×10^{3}	8.08×10^{6}
10	1.99×10^{1}	3.91×10^{8}	6.83×10^{2}	6.77×10^{6}
11	4.88×10^{-2}	7.16×10^{3}	3.57×10^{-7}	9.95×10^{-1}
12	3.91×10^{-1}	3.43×10^{6}	2.37×10^{-1}	2.09×10^{3}
13	3.67×10^{4}	1.28×10^{5}	1.34×10^{-2}	1.75×10^{4}
14	1.92×10^{12}	1.83×10^{7}	5.71×10^{14}	1.01×10^{8}
15	3.40×10^{9}	7.41×10^{6}	2.93×10^{8}	5.11×10^{4}
16	1.14×10^{1}	3.10×10^{7}	9.03×10^{-1}	5.54×10^{5}
17	1.42	1.04×10^{1}	1.36×10^{-6}	2.13×10^{1}
18	5.27×10^{10}	8.52×10^{2}	7.59×10^{11}	4.87×10^{10}
19	5.68×10^{-3}	5.71×10^{4}	4.27×10^{-4}	1.34×10^{3}
20	2.37×10^{2}	1.74×10^{7}	1.13×10^{1}	7.10×10^{3}
21	1.89×10^{4}	1.14×10^{6}	3.07×10^{4}	1.73×10^{8}
22	1.24	1.15×10^{2}	8.27×10^{2}	5.44×10^{3}
23	8.67	7.23×10^{4}	2.34×10^{2}	3.15×10^{4}
24	4.95×10^{-6}	1.00×10^{3}	1.70×10^{-10}	1.61×10^{1}
25	1.48×10^{-3}	3.08×10^{5}	5.06×10^{-2}	8.23×10^{3}
26	1.48	2.92×10^{6}	2.20	1.64×10^{6}
27	1.60×10^{6}	8.66×10^{10}	8.31×10^{2}	2.25×10^{7}
28	6.85×10^{4}	9.69×10^{8}	4.18×10^{3}	2.64×10^{8}
29	1.55×10^{-4}	6.63×10^{-4}	1.75×10^{-2}	2.49×10^{-2}
30	1.91×10^{-7}	9.52	2.14×10^{-5}	2.46×10^{-1}
31	9.46×10^{-4}	1.08×10^{3}	5.00×10^{-2}	1.07×10^{4}
32	9.13×10^{-2}	2.76×10^{-1}	6.41×10^{-4}	1.73×10^{-2}
33	5.48×10^{5}	3.00×10^{4}	1.50×10^{4}	1.41×10^{3}
34	4.64	2.68×10^{5}	8.51	7.97×10^{3}
35	5.94	1.22×10^{2}	2.24×10^{-1}	1.10×10^{3}
36	2.50×10^{7}	1.95×10^{5}	1.65×10^{6}	1.20×10^{3}
37	5.88×10^{-2}	4.65×10^{2}	9.34×10^{-9}	4.43×10^{-10}
38	2.62×10^{9}	4.87×10^{5}	1.14×10^{12}	1.65×10^{6}
39	5.67×10^{3}	1.10×10^{7}	1.09×10^{6}	1.07×10^{9}
40	2.82×10^{9}	2.28×10^{7}	4.66×10^{6}	6.64×10^{8}
41	1.78×10^{-1}	9.05×10^{2}	1.06×10^{3}	9.00×10^{5}

42	4.61×10^{-5}	8.04×10^{7}	1.32×10^{-8}	9.52×10^{7}
43	2.44×10^{8}	3.65×10^{16}	4.54×10^{8}	6.79×10^{16}
44	7.22×10^{-1}	1.12×10^{8}	1.17	1.81×10^{8}
45	1.73×10^{5}	3.35×10^{13}	9.36×10^{3}	1.81×10^{12}
46	2.50×10^{8}	3.24×10^{16}	4.11×10^{8}	5.32×10^{16}
47	1.60×10^{-6}	9.98×10^{-15}	1.30×10^{-6}	8.09×10^{-15}
48	5.33×10^{13}	1.31×10^{8}	5.33×10^{12}	1.39×10^{8}
49	1.20×10^{5}	4.89×10^{8}	1.65×10^{6}	5.18×10^{8}

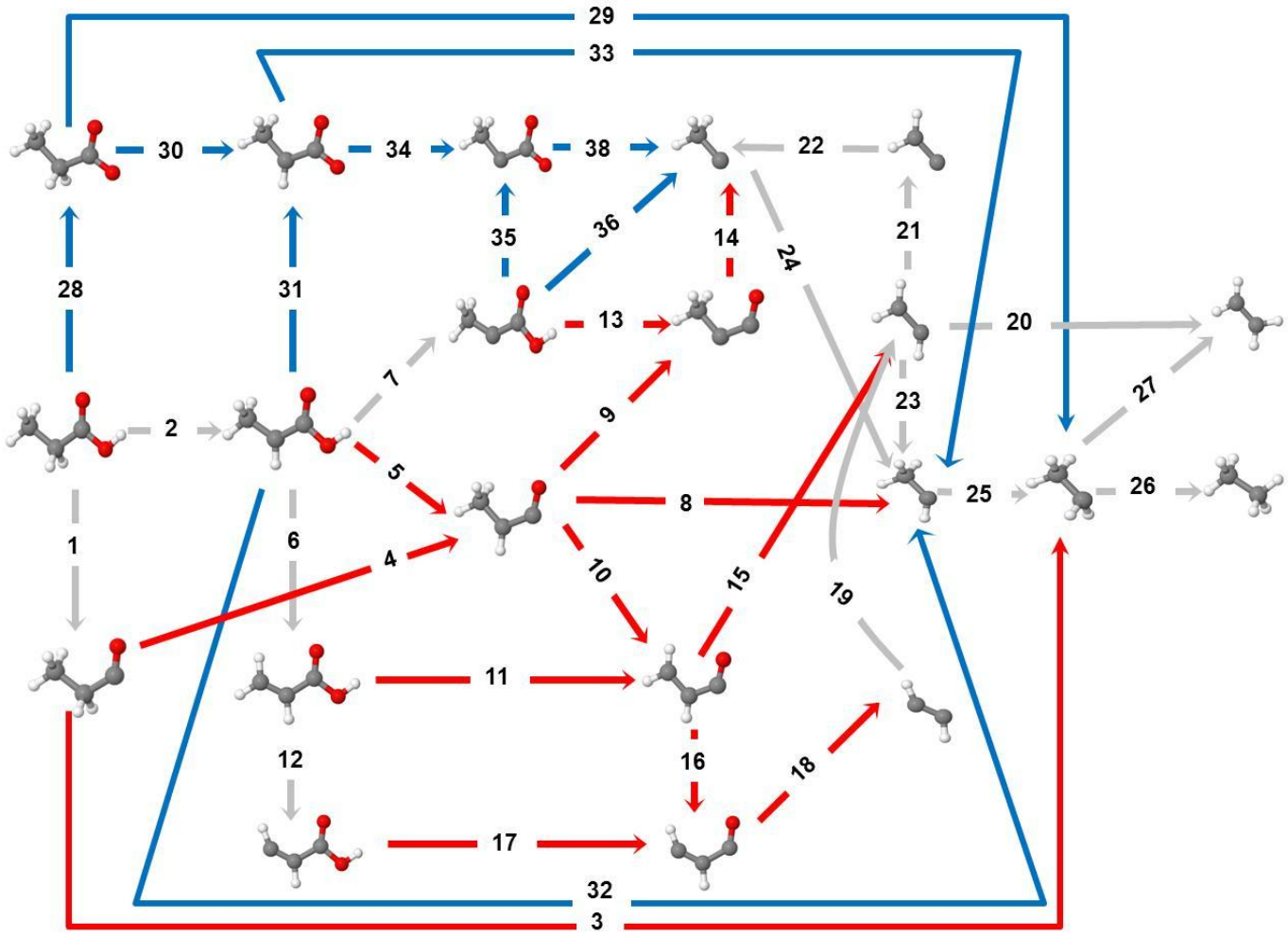
29
33
30
34
38
22
28
31
35
36
14
24
21
13
20
2
7
9
23
27
5
8
25
26
1
6
4
10
15
19
11
12
16
18
17
32
3

Figure 6.1 Network of elementary reaction steps considered in the hydrodeoxygenation of propionic acid over Pd(211). Elementary reactions involved in the DCX mechanism are shown with blue color arrows, DCN reactions are illustrated with red color arrows, and those reaction involved in both mechanisms such as dehydrogenation reactions and removal of the hydrocarbon pool are shown with gray color arrows.

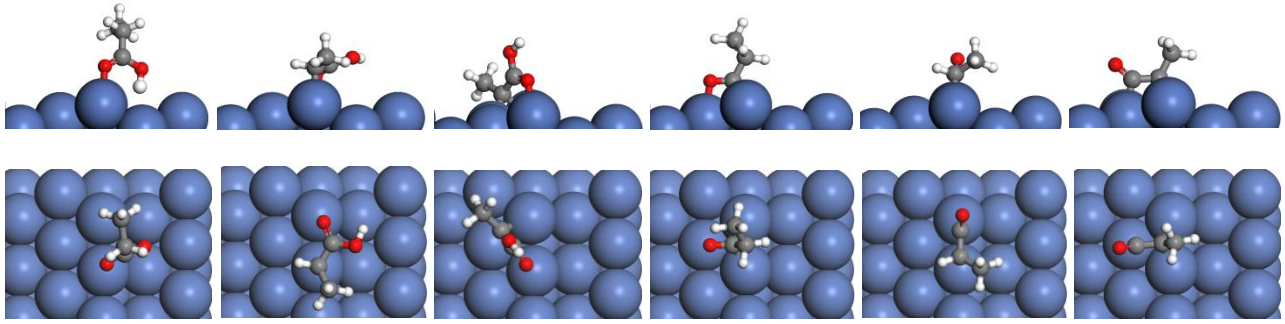

(1) (2) (3) (4) (5) (6)

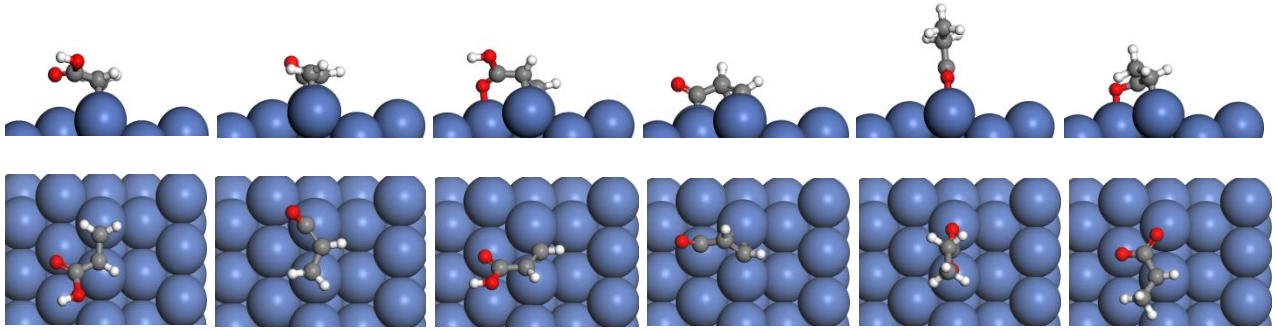

(7) (8) (9) (10) (11) (12)

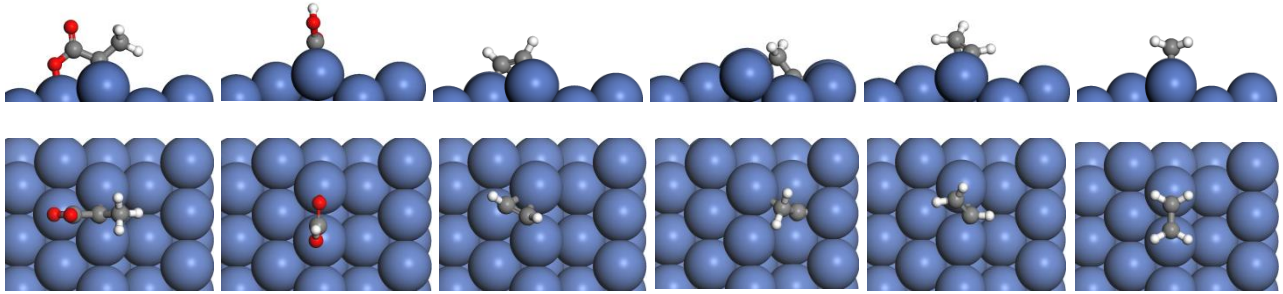

(13) (14) (15) (16) (17) (18)

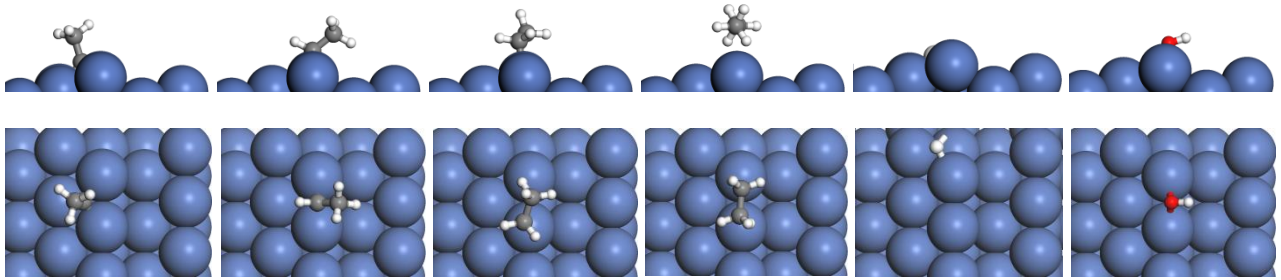

(19) (20) (21) (22) (23) (24)

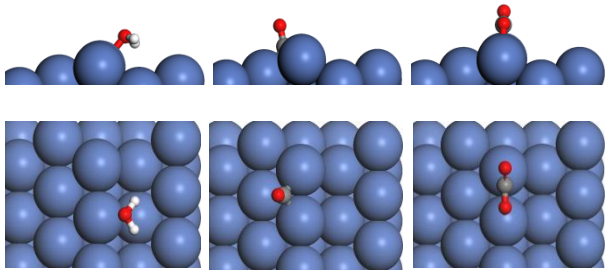

(25) (26) (27)

Figure 6.2 Side (upper panel) and top view (lower panel) of preferred adsorption structure of various intermediates in the reaction networks of the decarbonylation and decarboxylation of propionic acid over Pd(211). (1) propionic acid (CH_3CH_2COOH); (2) ethylidene-1-ol-1-olate ($CH_3CHCOOH$); (3) ethenyl-1-ol-1-olate (CH_3CCOOH); (4) propanoyl (CH_3CH_2CO); (5) carbonylethylidene (CH_3CHCO); (6) carbonylethenyl (CH_3CCO); (7) vinyl-1-ol-1-olate ($CH_2CHCOOH$); (8) carbonylvinyl (CH_2CHCO); (9) ethyne-1-ol-1-olate (CHCHCOOH); (10) carbonylethyne (CHCHCO); (11) propionate (CH_3CH_2COO); (12) carboxylethylidene (CH_3CHCOO); (13) carbonylethenyl (CH_3CCOO); (14) carboxylic (COOH); (15) ethyne (CHCH); (16) ethen-1,1-diyl (CH_2C); (17) vinyl (CH_2CH); (18) ethene (CH_2CH_2); (19) ethenyl (CH_3C); (20) ethylidene (CH_3CH); (21) ethyl (CH_3CH_2); (22) ethane (CH_3CH_3); (23) hydrogen (H); (24) hydroxyl (OH); (25) water (H_2O); (26) carbon monoxide (CO); (27) carbon dioxide (CO_2).

(1) (2) (3) (4) (5) (6)

(7) (8) (9) (10) (11) (12)

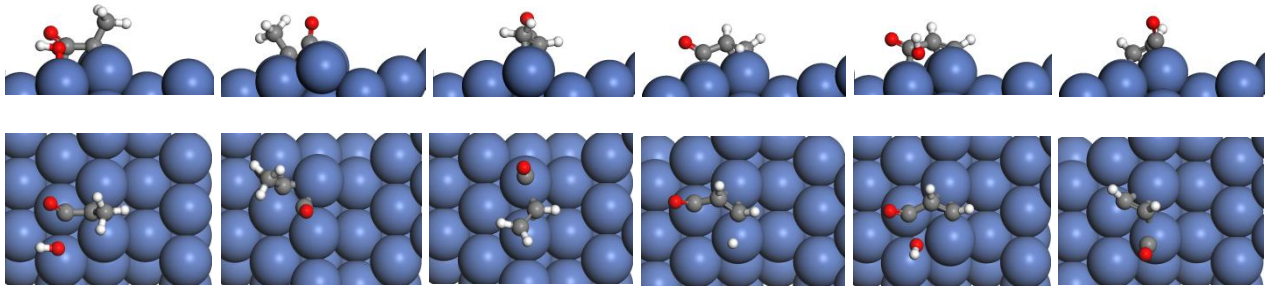

(13) (14) (15) (16) (17) (18)

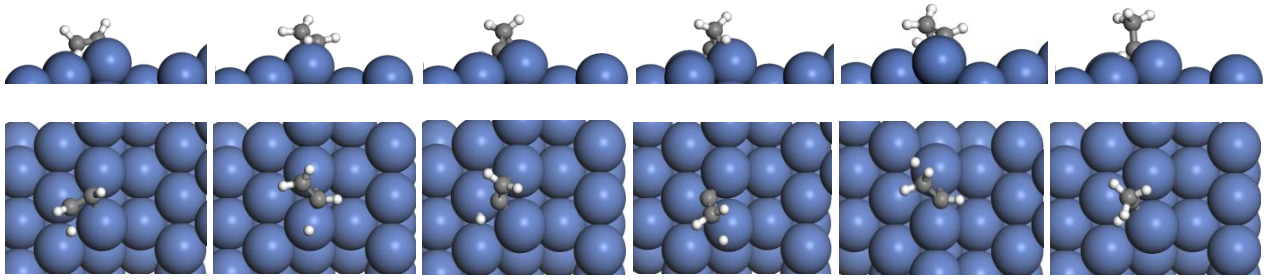

(19) (20) (21) (22) (23) (24)

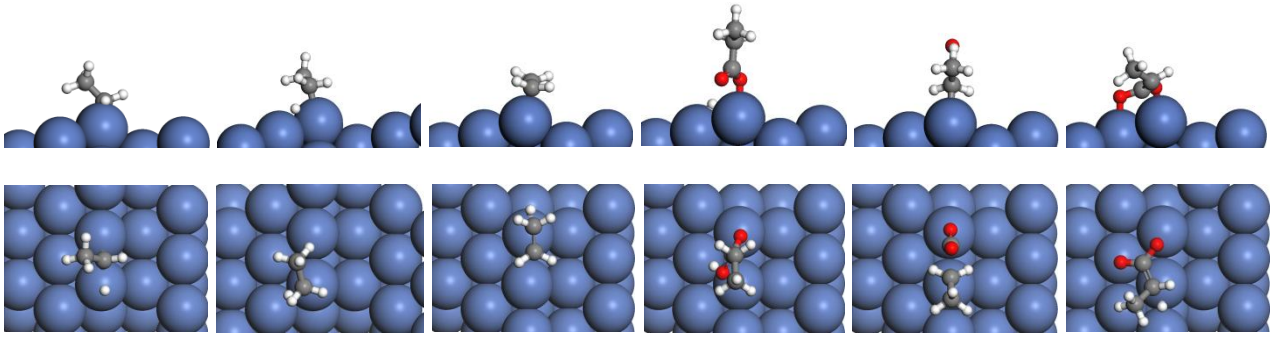

(25) (26) (27) (28) (29) (30)

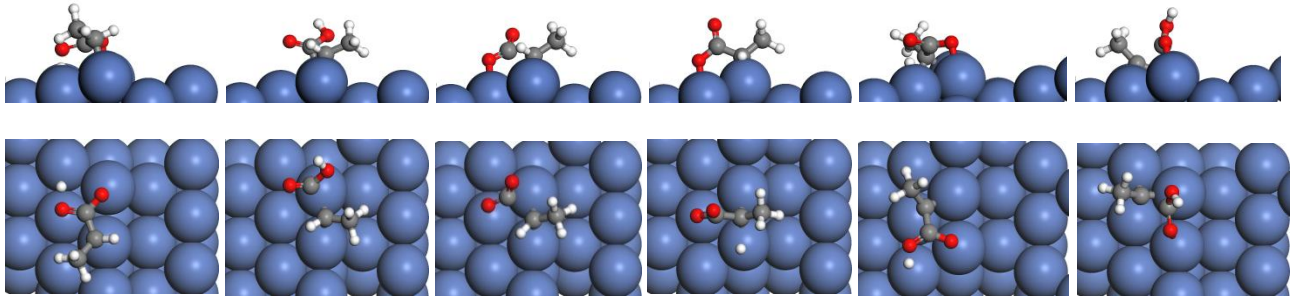

(31) (32) (33) (34) (35) (36)

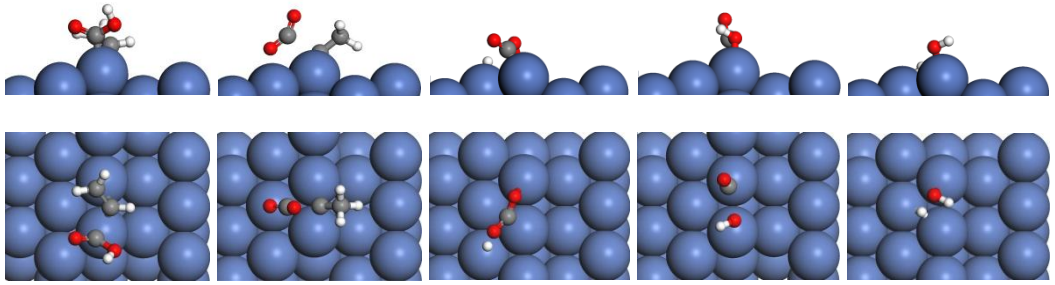

(37) (38) (39) (40) (41)

Figure 6.3 Snapshots of transition states of various elementary reactions involved in hydrodeoxygenation of propionic acid over Pd (211). Upper panels are for side views and lower ones for top views.

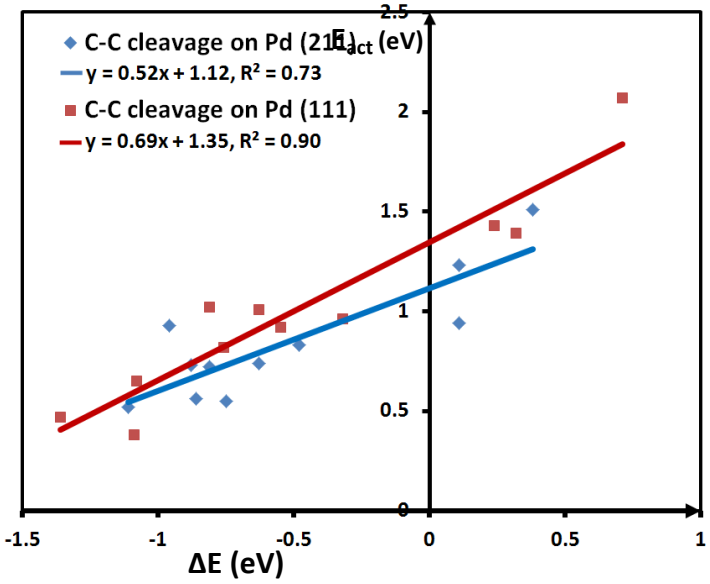
C-C cleavage on Pd (211)
y = 0.52x + 1.12, R² = 0.73
C-C cleavage on Pd (111)
y = 0.69x + 1.35, R² = 0.90
Eact (eV)
ΔE (eV)
2.5
2
1.5
1
0.5
0
-1.5
-1
-0.5
0
0.5
1

(a)

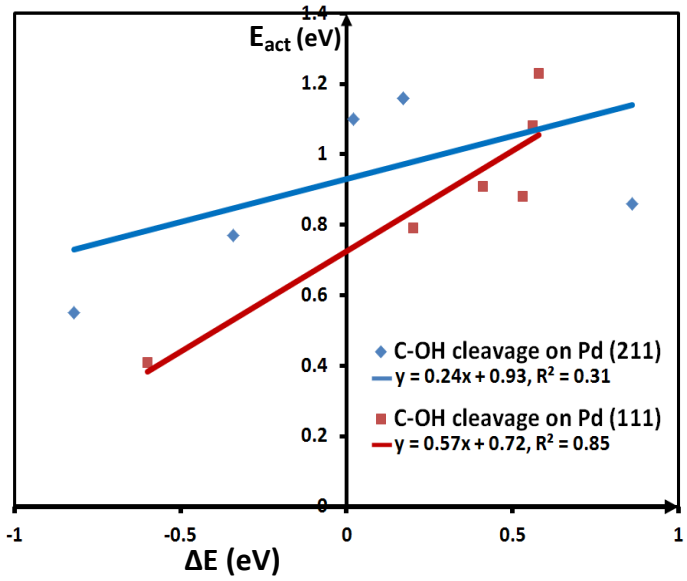
Eact (eV)
C-OH cleavage on Pd (211)
y = 0.24x + 0.93, R² = 0.31
C-OH cleavage on Pd (111)
y = 0.57x + 0.72, R² = 0.85
ΔE (eV)
1.4
1.2
1
0.8
0.6
0.4
0.2
0
-1
-0.5
0
0.5
1

(b)

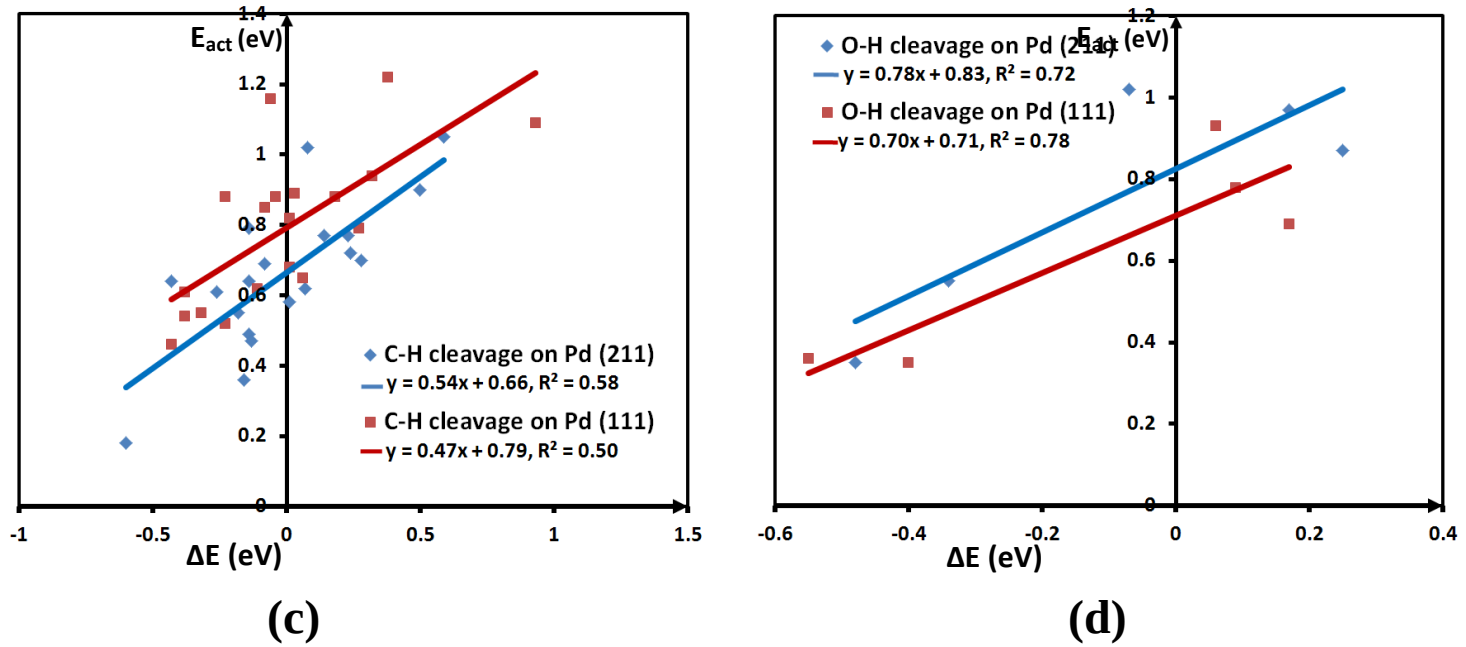

Figure 6.4. Brønsted-Evans-Polanyi (BEP) relations for (a) C-C, (b) C-OH, (c) C-H, and (d) O-H bond cleavage in the HDO of propionic acid over Pd(111) and Pd(211), i.e., zero-point energy corrected activation barriers versus reaction energies.

6.2*10-9 [2.1*10-9]
3.2*10-10 [9.4*10-10]
4.3*10-10
[3.4*10-10]
1.4*10-10
[1.8*10-9]
1.4*10-10
[1.8*10-9]
1.2*10-9
[1.5*10-8]
6.3*10-9
[2.4*10-9]
[2.4*10-9]
2.1*10-11
4.8*10-14
[-4.9*10-13]
1.6*10-9
[2.9*10-12]
3.7*10-9
[3.4*10-8]
[1.5*10-8]
1.2*10-9
5.3*10-11
[1.4*10-11]
6.7*10-9
[5.1*10-9]
4.4*10-8
[1.6*10-7]
5.5*10-8
[1.7*10-7]
1.7*10-9
[1.7*10-11]
3.7*10-9
[3.4*10-8]
5.1*10-11
[-4.3*10-8]
[9.0*10-9]
1.6*10-8
1.9*10-10
[6.0*10-8]
4.0*10-9 [4.1*10-12]
[8.5*10-9]
1.1*10-8
[1.5*10-9]
1.7*10-9
7.7*10-12
[7.6*10-10]
[1.0*10-7]
5.3*10-8
-7.7*10-9
[2.7*10-8]
4.5*10-8
[1.3*10-8]
[1.2*10-7]
7.0*10-12
[7.5*10-10]
-2.4*10-10
5.3*10-8 [3.2*10-8]
[7.2*10-8]
-3.5*10-13
[4.6*10-8]
6.8*10-12
7.0*10-12
[1.2*10-7]
2.5*10-10
[1.4*10-11]
1.8*10-13 [7.2*10-8]
2.6*10-11 [1.9*10-13]

Figure 6.5A TOFs (s^{-1}) for various elementary steps in the HDO of propionic acid at a temperature of 473 K and a propionic acid gas phase pressure of 0.01 bar and a hydrogen partial pressure of 0.2 bar over Pd(211) and Pd(111) model surfaces (numbers inside the square brackets [] are the TOFs over Pd(111)). All other reaction conditions are given in Section 6.3.3. Elementary reactions involved in the DCN mechanism are shown with blue color arrows, DCX reactions are illustrated with red color arrows, and those reactions which are involved in both mechanisms such as dehydrogenation of propionic acid and its derivatives and removal of the hydrocarbon pool are shown with the gray color arrows. Elementary reactions involved in the most dominant pathway on Pd(211) are illustrated with a double-line arrow.

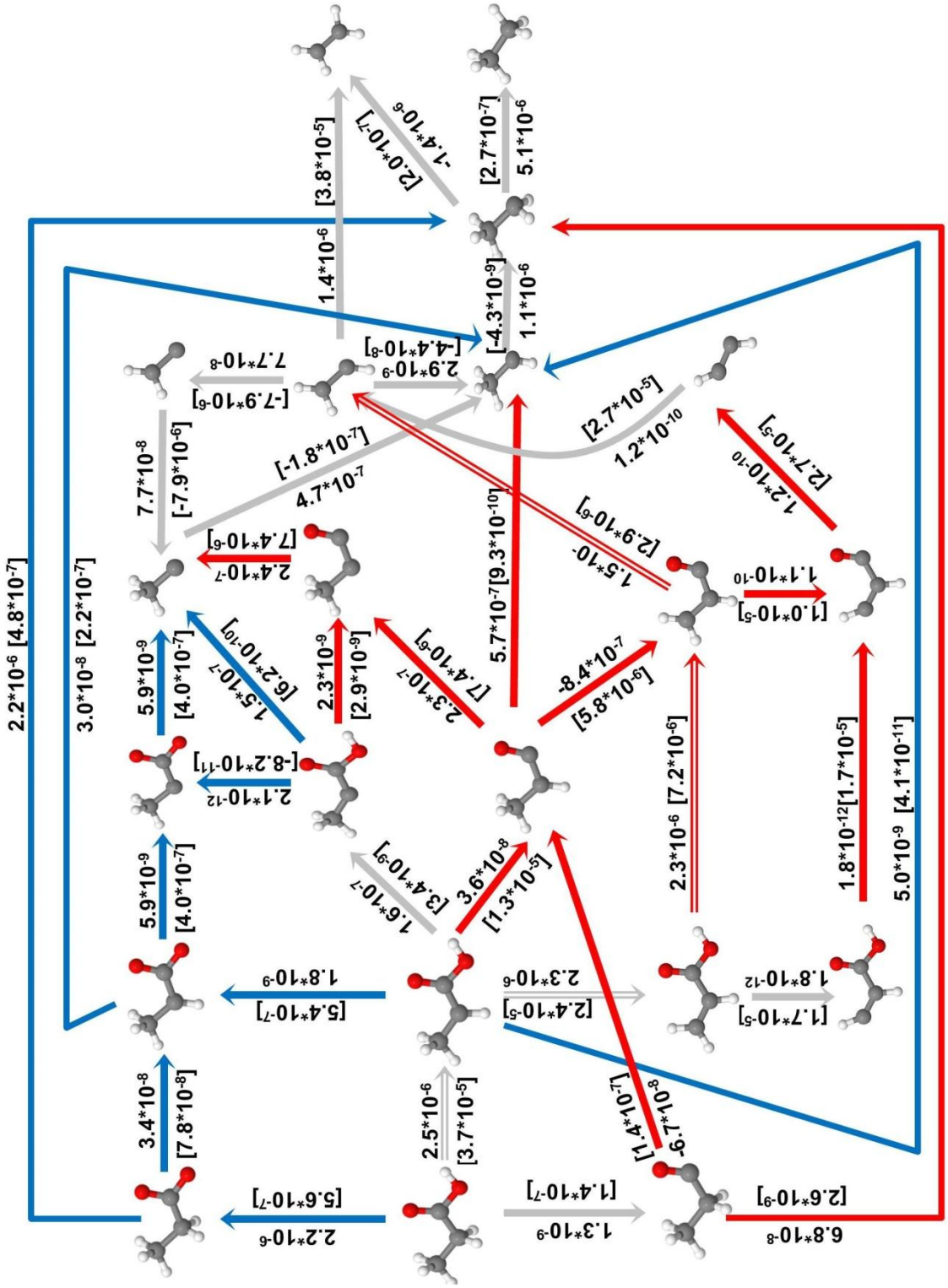
2.2*10-6 [4.8*10-7]
3.0*10-8 [2.2*10-7]
3.4*10-8 [7.8*10-8]
5.9*10-9 [4.0*10-7]
5.9*10-9 [4.0*10-7]
2.5*10-6 [3.7*10-5]
2.2*10-6 [5.6*10-7]
1.3*10-9 [1.4*10-7]
6.8*10-8 [2.6*10-9]
1.4*10-6 [3.8*10-5]
[2.0*10-7] -1.4*10-6
[2.7*10-7] 5.1*10-6
[-4.3*10-9] 1.1*10-6
2.9*10-9 [-4.4*10-8]
7.7*10-8 [-7.9*10-6]
[-7.9*10-6] 7.7*10-8
[-1.8*10-7] 4.7*10-7
[2.7*10-5] 1.2*10-10
1.2*10-10 [2.7*10-5]
1.5*10- [2.9*10-6]
5.7*10-7[9.3*10-10]
2.4*10-7 [7.4*10-6]
1.1*10-10 [1.0*10-5]
2.3*10-9 [2.9*10-6]
2.3*10-7 [7.4*10-6]
-8.4*10-7 [5.8*10-6]
1.5*10-7 [6.2*10-10]
2.1*10-12 [-8.2*10-11]
1.6*10-7 [3.4*10-9]
3.6*10-8 [1.3*10-5]
2.3*10-6 [7.2*10-6]
1.8*10-12[1.7*10-5]
5.0*10-9 [4.1*10-11]
[5.4*10-7] 1.8*10-9
2.3*10-6 [2.4*10-5]
1.8*10-12 [1.7*10-5]
-6.7*10-8 [1.4*10-7]

Figure 6.5B "Dispersion-corrected" model TOFs (s^{-1}) for various elementary steps in the HDO of propionic acid at a temperature of 473 K and a propionic acid gas phase pressure of 0.01 bar and a hydrogen partial pressure of 0.2 bar over Pd(211) and Pd(111) model surfaces (numbers inside the square brackets [] are the TOFs over Pd(111)). To include dispersion interaction for adsorption/desorption processes, the PBE-D3 functional was used to compute the adsorption energetics of CH_3CH_2COOH, H_2, CO, CO_2, H_2O, CH_2CH_2, CH_3CH_3.

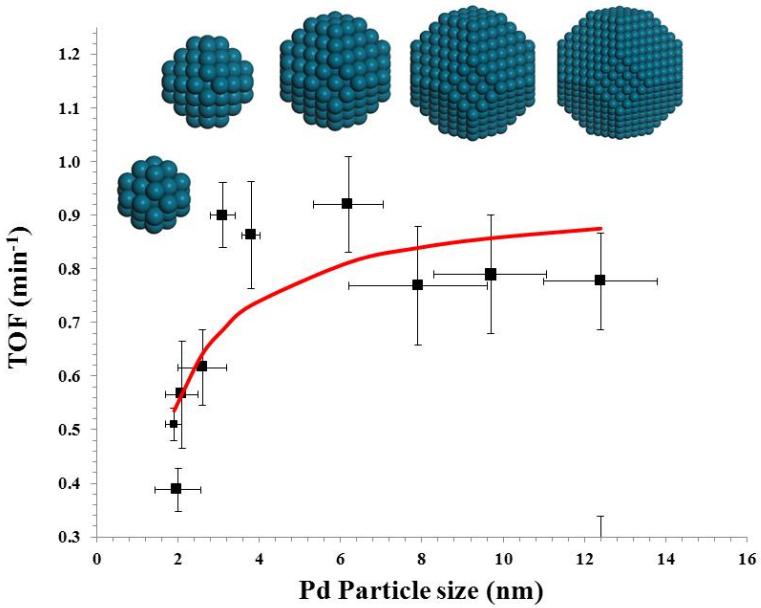

Figure 6.6 Experimental TOF of C_2 formation as a function of particle size of Pd/SiO_2 catalysts for the HDO of propionic acid. Reactor conditions: T = 473 K; P = 1 atm; ~1% propanoic acid, 20% H_2 balanced with He; catalyst mass =200 mg; total flow rate = 200 sccm. Adapted from ref. [203].

CHAPTER 7

EFFECTS OF SOLVENTS ON CATALYTIC HYDRODEOXYGENATION OF PROPANOIC ACID[1]

[1] Behtash, S.; Lu, J. M.; Faheem, M.; Heyden, A. *Green Chemistry* 2014, *16*, 4427.
[1] Behtash, S.; Lu, J. M.; Faheem, M.; Heyden, A. *Green Chemistry* 2014, *16*, 605.
This article was featured inside the front cover of the Journal of Green Chemistry and reprinted with the permission of publisher.

ABSTRACT

The effects of liquid water, n-octane, and n-butanol on the hydrodeoxygenation of propanoic acid over Pd (111) model surfaces have been studied from first principles. We developed a microkinetic model for the hydrodeoxygenation and studied the reaction mechanism at a temperature of 473 K. Our model predicts that for all reaction media, decarbonylation pathways are favored over decarboxylation pathways. However, in the presence of polar solvents like water, decarboxylation routes become competitive to decarbonylation routes. The activity of the Pd surface various as a function of environment as follows: water > n-butanol > octane ≈ gas phase. Finally, a sensitivity analysis of our models suggests that both C-OH and C-H bond cleavages control the overall rate of the catalyst in all environments and are likely activity descriptors for the hydrodeoxygenation of organic acids.

KEYWORDS:

Solvent effects; organic acids; palladium; density functional theory; COSMO; decarbonylation; decarboxylation; microkinetic modeling

7.1 INTRODUCTION

In the past two centuries, fossil fuels have been overused and currently, most countries are extremely dependent on combustion of fossil fuels.[151, 223] Considering the environmental impact of fossil fuel utilization, there is a substantial need for the development of renewable resources such as solar, wind, geothermal, hydropower and biomass for meeting the world's growing energy demand. Biomass is one of the most promising renewable resources and first generation biofuels such as bioethanol and biodiesel have been successfully implemented in the energy system. However, the energy efficiency of 1^{st} generation biofuels is low and there are substantial infrastructure compatibility issues.[2, 16, 127, 128, 224] Therefore, there is a need for the development of second-generation biofuels that are identical to current liquid fuels and that can be produced at low cost and high energy conversion efficiency.[22]

Lipid-rich biomass feedstocks, such as vegetable oils, waste fats, and algal lipids are one potential class of raw materials for the production of green fuels. Recently, research efforts[47, 54, 59] have been directed to convert these fatty esters and acids into liquid hydrocarbons with the help of a hydroprocess, i.e., the hydrodeoxygenation (HDO) of the feeds over conventional hydrotreating catalysts such as sulfided $NiMo/Al_2O_3$ and $CoMo/Al_2O_3$. However, considering the low level of sulfur in biomass and the higher activity of oxygenated feeds versus sulfide feeds conventional hydrotreating catalysts display a short catalyst life time. Also, humin formation and difficulties in separation of carbon oxides from the recycle gas have been reported.[54, 59, 225, 226] Consequently, there is an apparent need for new catalysts for the HDO of organic acids and esters. In

this context, we note that the HDO of lipids and triglyceride feedstocks is also relevant to upgrading of the bio-oils obtained from pyrolysis of lignocellulosic biomass.[2, 47, 58]

To rationally design a metal catalyst for the HDO of these feeds, it is necessary to obtain a fundamental understanding of the reaction mechanism for the HDO of organic acids and esters on the catalyst surface.

In our previous studies[119, 140], two major mechanisms for the HDO, decarbonylation (DCN) and decarboxylation (DCX), of propanoic acids, our model molecule for organic acids, were investigated over Pd (111) model surfaces. The elementary reaction steps involved in the DCN and DCX were identified from first principles and a microkinetic model was developed to determine the dominant pathway and rate-controlling steps under realistic gas phase reaction conditions of 473 K and low, medium, and high partial pressures of hydrogen (0.01, 1 and 30 bar). Our results suggest that the DCN is favored over the DCX and the C-OH bond dissociation of the acid functionality is rate controlling in the DCN mechanism.

Previously, Murzin *et al.* reported[62, 141, 143] that for long chain fatty acids over Pd/C catalysts the DCN is favored over the DCX in the presence of hydrogen and only in the absence of hydrogen is the DCX pathway dominant.[145] These results agree with observations from Boda et al.[227] who identified the DCN as the most dominant pathway for the HDO of caprylic acid in a hydrogen atmosphere. However, recently Ford *et al[228]*. reported that even in the presence of hydrogen, the deoxygenation of stearic, lauric, and capric acids follows a decarboxylation mechanism over Pd/C. In this context, it is noted that the experimental studies used different solvents as reaction medium and the effect of solvents on the preferred reaction pathway of the HDO of organic acids

remains unknown. For example, Murzin *et al.* mostly used dodecane as solvent in their studies;[62, 67, 141, 143, 144, 229] however, in one of their studies[62], the effect of two different solvents, dodecane and mesitylene, was studied on the decarboxylation of ethyl stearate. According to their results, in dodecane the formation of n-heptadecane was favored while in mesitylene the intermediate product stearic acid was not further reacting to n-heptadecane. Also, it was reported that the initial rates of the decarboxylation are slightly higher in dedocane than in mesitylene. Finally, Hoelderich et al.[230] reported for the catalytic deoxygenation of oleic acid (C18) over Pd/C that the presence of water can change the selectivity towards C17 hydrocarbons by up to 20%.

Considering the lack of fundamental understanding of the effects of solvents on heterogeneous metal catalysts, we investigated in this study the reaction mechanism of the HDO of propanoic acid over Pd (111) from first principles with our novel implicit solvation model for solid surfaces (iSMS).

Since industrial hydrotreatment processing often occurs in a complex liquid environment, we have purposefully selected water, octane and n-butanol as solvents that might mimic this complex environment. In many experimental studies of the HDO of fatty acids, remarkable amounts of water have been produced during the deoxygenation process[145, 224, 228, 229] and also pyrolysis bio-oils contain 25-50 wt% water[231], justifying the study of water effects on the HDO of organic acids. Similarly, the study of nonpolar octane is justified considering that the chemically similar dedocane is used in most experimental studies of the HDO of fatty acids. Finally, n-butanol has been selected for this study as a solvent with a moderate polarity that might mimic the reaction environments in some bio-oils that contain various alcohols.[231]

7.2 METHODS

7.2.1 SOLVATION MODEL

In this study, the approximate effect of a solvent is investigated with the help of the iSMS method.[232] iSMS is a new approach for modeling reactions at metal-liquid interfaces with implicit solvation models. More information about iSMS and a validation of this method has recently been published by some of us.[232] Basically, the free energy of an adsorbed intermediate on a periodic metal slab at the solid-liquid interface, $G^{liquid}_{surface+intermediate}$, is defined using a subtraction scheme

$$G^{liquid}_{surface+intermediate} = G^{vacuum}_{surface+intermediate} + (G^{liquid}_{cluster+intermediate} - E^{vacuum}_{cluster+intermediate}) \quad (7.1)$$

where, $G^{vacuum}_{surface+intermediate}$, is the free energy in the absence of a solvent (plane-wave DFT energy of the periodic slab model including vibrational contributions to the free energy), $G^{liquid}_{cluster+intermediate}$ is the free energy of a metal cluster in the liquid (without explicitly considering vibrational contributions) constructed by removing selected metal atoms from the periodic-slab model and removing the periodic boundary conditions, and $E^{vacuum}_{cluster+intermediate}$ is the DFT energy of the same cluster in the absence of the solvent. Combinations of COSMO and COSMO-RS[233, 234] implicit solvation models have been used to calculate $G^{liquid}_{cluster+intermediate}$. COSMO-RS calculations have been performed using COSMOtherm.[235] Thermodynamic properties of the solvents are obtained from the COSMOtherm database, based on the results of quantum chemical COSMO calculations at the BP-TZVP level of theory. For all other structures, COSMO-RS input files have been generated from COSMO calculations at the same level of theory. We note

that as a first approximation we did not include the solvent degrees of freedom in the reaction coordinate.

7.2.2 DFT CALCULATIONS

Cluster model DFT calculations were carried out using TURBOMOLE 6.0.[116-118] The Pd (111) cluster model surfaces have been modeled by a two layered cluster with a 5×5 surface. These structures were constructed by removal of the periodic boundaries from the periodic slabs that were obtained from our previous plane-wave (VASP)[107, 108] calculations.[119] All adsorbates were represented by all-electron TZVP[120-122] basis sets while for Pd we used a relativistic small core potential (ECP) together with a basis set of same quality as the adsorbates for the valence electrons. The Coulomb potential was approximated with the RI-J approximation with auxiliary basis sets[123-125]. Single point energy calculations were performed with a self-consistent field energy convergence criterion of 1.0×10^{-6}. Finally, for each cluster model energy calculations on various spin surfaces were performed to identify the lowest energy spin state for further calculations.

For cluster models in the liquid phase, COSMO calculations were performed on the same spin surface as for the vacuum cluster calculations. The dielectric constant was set to infinity to provide the input for the COSMO-RS calculations. For cavity construction, the default radii-based cavities were used.

7.2.3 MICROKINETIC MODELING

For surface reactions, the forward rate constant (k_{for}) of each reaction is calculated as,

$$k_{\text{for}} = \frac{k_{\text{B}}T}{h} e^{-\frac{\Delta G^{\ddagger}}{k_{\text{B}}T}} \tag{7.2}$$

where k_B is the Boltzmann constant, T denotes the reaction temperature, h is the Planck constant, and $\Delta G^{\ddagger}$ represents the free energy of activation for a specific temperature and reaction environment. I.e., in the presence of solvents, the free energy of activation ($\Delta G^{\ddagger}_{\text{solvent}}$) and free energy of reaction ($\Delta G_{\text{rxn-solvent}}$) were calculated as,

$$\Delta G^{\ddagger}_{\text{Solvent}} = \Delta G^{\ddagger}_{\text{Gas}} + G_{TS}(solv) - G_{IS}(solv), \tag{7.3}$$

and

$$\Delta G_{\text{rxn-solvent}} = \Delta G_{\text{Gas}} + G_{FS}(solv) - G_{IS}(solv) \tag{7.4}$$

where, $G_{IS}(solv)$, $G_{FS}(solv)$, and $G_{TS}(solv)$ are the solvation energies of the initial, final, and transition states, respectively, that were obtained from the difference in energy of the COSMO-RS and gas-phase cluster calculations, and $\Delta G^{\ddagger}_{\text{Gas}}$ and ΔG_{Gas} are the free energy of activation and reaction under gas phase conditions, respectively. The reverse rate constant (k_{rev}) is calculated similarly from the thermodynamic equilibrium constant K is given as

$$k_{\text{rev}} = \frac{k_{\text{for}}}{K} \tag{7.5}$$

For an adsorption reaction A(g)+*→A*the rate of adsorption is given by collision theory with a sticking probability of 1 independent of solvent.

$$k_{\text{for}} = \frac{1}{N_0 \sqrt{2\pi m_A k_B T}} \tag{7.6}$$

where N_0 is the number of sites per area (1.478×10^{19} m^{-2}) and m_A denotes the molecular weight of A. The desorption rate constant is again given by the equilibrium constant, i.e., equation 7.5.

In the presence of a solvent, the free energy of adsorption for A(g)+*→A* is calculated as,

$$\Delta G_{ads-solvent} = \Delta G_{ads-gas} + G_{A*}(solv) - G_{Pd}(solv) \tag{7.7}$$

where $\Delta G_{ads-gas}$ is the free energy of adsorption under gas phase conditions and $G_{A*}(solv)$ and $G_{Pd}(solv)$ are as before the solvation energies of the adsorbed molecule A and Pd surface immersed in the solvent, respectively.

With the forward and reverse rate constants defined, rates of the elementary reactions can be expressed by mean-field rate laws. Considering that some of the adsorbed intermediates occupy multiple active sites (the number of occupied sites by each adsorbate is shown in Table 7.1), the rate expressions and steady state molecular balance equations are highly nonlinear. To solve the set of steady state differential reactor equations and to obtain the surface coverages of the intermediates, we used the BzzMath library[115] developed by Buzzi-Ferraris. No assumptions were made regarding rate-limiting steps.

7.3 Result and Discussion

The reaction network investigated in this study was obtained from our previous study on the mechanism of the DCN and DCX of propanoic acid.[119, 140] All of the elementary steps and intermediates involved in DCN and DCX of propanoic acid are

shown in Figure 7.1. The DFT-derived parameters for the reactions are listed in Table 7.1. Although the DCN and DCX mechanisms are interconnected, key steps in each mechanism are distinguishable. For example, C-OH bond dissociations in propanoic acid and its derivatives (CH_xCH_yCOOH, x=[1,2,3], y=[0,1,2]) form CH_xCH_yCO intermediates which produce CO and C_2 hydrocarbons after a C-C bond dissociation and are therefore key steps in the DCN mechanism. Similarly, key steps unique to the DCX mechanism are O-H bond dissociations to form CH_xCH_yCOO intermediates followed by C-C cleavage to form CO_2. Also, we grouped C-C bond dissociations to form CH_xCH_y and COOH on the surface in the DCX mechanism considering that COOH dissociates on Pd (111) easier to CO_2 and hydrogen than to CO and OH.

Table 7.1 illustrates the effect of solvents on the free energy of reactions and activation barriers of all elementary steps. Solvents can stabilize or destabilize the reactant, product, and transition states.

For the DCX mechanism, the presence of water affects the following elementary reaction steps most significantly: C-H cleavage in

reaction 30 ($CH_3CH_2COO^{**} + 2^* \rightarrow CH_3CHCOO^{***} + H^*$, $\Delta G_{rxn\text{-}water}$-$\Delta G_{rxn\text{-}gas}$ = -0.17 eV and $\Delta G^{\ddagger\text{-}water}$-$\Delta G^{\ddagger\text{-}Gas}$=-0.24 eV), and

reaction 34 ($CH_3CHCOO^{***} + ^* \rightarrow CH_3CCOO^{***} + H^*$, $\Delta G_{rxn\text{-}water}$-$\Delta G_{rxn\text{-}gas}$ = -0.08 eV and $\Delta G^{\ddagger\text{-}water}$-$\Delta G^{\ddagger\text{-}Gas}$=-0.10 eV), C-$CO_2$ cleavage in

reaction 33 ($CH_3CHCOO^{***} \rightarrow CH_3CH^{**} + CO_2^*$, $\Delta G_{rxn\text{-}water}$-$\Delta G_{rxn\text{-}gas}$ = +0.17 eV and $\Delta G^{\ddagger\text{-}water}$-$\Delta G^{\ddagger\text{-}Gas}$= +0.05 eV) and

reaction 38 ($CH_3CCOO^{***} \rightarrow CH_3C^* + CO_2^* + ^*$, $\Delta G_{rxn\text{-}water}$-$\Delta G_{rxn\text{-}gas}$ = +0.23 eV and $\Delta G^{\ddagger\text{-}water}$-$\Delta G^{\ddagger\text{-}Gas}$=+0.19 eV), and O-H bond cleavage in

reaction 35 ($CH_3CCOOH^{***} + * \rightarrow CH_3CCOO^{***} + H^*$, $\Delta G_{rxn\text{-}water}$-$\Delta G_{rxn\text{-}gas}$ = -0.11 eV and $\Delta G^{\ddagger\text{-}water}$-$\Delta G^{\ddagger\text{-}Gas}$=-0.03 eV).

Clearly, in the presence of water, the formation of a (negatively charged) CH_3CCOO species is facilitated and further C-C bond cleavage is inhibited.

For the DCN mechanism, the presence of water affects the following elementary steps most significantly: C-OH bond dissociations become slightly more difficult, e.g., reaction 5 ($CH_3CHCOOH^{**} + * \rightarrow CH_3CHCO^{**} + OH^*$, $\Delta G_{rxn\text{-}water}$-$\Delta G_{rxn\text{-}gas}$ = +0.08 eV, and $\Delta G^{\ddagger\text{-}water}$-$\Delta G^{\ddagger\text{-}Gas}$=+0.07) and C-CO bond cleavages become more exergonic, e.g., reaction 3 ($CH_3CH_2CO^{***} \rightarrow CH_3CH_2^* + CO^* + *$, $\Delta G_{rxn\text{-}water}$-$\Delta G_{rxn\text{-}gas}$ = -0.09 eV) and reaction 8 ($CH_3CHCO^{**} + * \rightarrow CH_3CH^{**} + CO^*$, $\Delta G_{rxn\text{-}water}$-$\Delta G_{rxn\text{-}gas}$ = -0.07 eV). Also, we observe that C-H dissociates relevant for both DCN and DCX pathways become generally more exergonic, while the corresponding removal of the hydrocarbon pool from the surface, e.g. $CHCH + 4H \rightarrow CH_3CH_3(g)$, $\Delta G_{rxn\text{-}water}$-$\Delta G_{rxn\text{-}gas}$ = +0.12 eV, becomes more endergonic.

Overall, the effect of water is more pronounced for the DCX mechanism than the DCN pathways and while the effect on elementary reaction rates seems to be small, we will show in section 7.3.1 that the overall effect is quite significant.

Next, the effect of the presence of n-butanol on DCX reactions follows a similar trend to the effect of water with diminished intensity. E.g., C-H bond cleavage in reaction 30 and 34 become more exergonic by -0.06 and -0.07 eV, respectively, while C-CO_2 bond cleavages in e.g. reaction 38 become more endergonic by 0.13 eV (the activation barrier increases by 0.16 eV). So again, production of CH_xCH_yCOO intermediates is facilitated. Also, activation barriers for C-OH bond dissociations such as in reaction 5

($CH_3CHCOOH^{***} + {*} \rightarrow CH_3CHCO^{***} + OH^{*}$) and reaction 13 ($CH_3CCOOH^{***} + {*} \rightarrow CH_3CCO^{***} + OH^{*}$) are increased by 0.11 eV and 0.10 eV, respectively.

Finally, in the presence of n-octane reaction free energies are not significantly affected by the solvent. The most remarkable change occurs in the C-CO bond cleavage of reaction 15 ($CH_2CHCO^{***} + {*} \rightarrow CH_2CH^{***} + CO^{*}$) with $\Delta G_{rxn\text{-}octane} - \Delta G_{rxn\text{-}gas}$ = -0.06 eV and C-CO_2 bond cleavage of reaction 38 ($CH_3CCOO^{***} \rightarrow CH_3C^{*} + CO_2^{*} + {*}$) with $\Delta G_{rxn\text{-}Octane} - \Delta G_{rxn\text{-}gas}$ = +0.08 eV and $\Delta G^{\ddagger\text{-}water} - \Delta G^{\ddagger\text{-}Gas}$=+0.12 eV.

In the following sections the effect of solvents on the turnover frequency (TOF) and the coverage of the most dominant surface species will be studied by mean-field microkinetic modeling.

7.3.1 MICROKINETIC MODELING

We previously[140] developed mean-field microkinetic models for the reaction mechanism of the DCX and DCN of propanoic acid over Pd (111) surfaces under experimental gas phase conditions. Analysis of the models at a temperature of 473 K and partial pressures of propanoic acid, H_2, CO_2, and H_2O of 1 bar and a CO partial pressure of 0.001 bar (the C_2 product partial pressures were set to zero) suggested that the DCN is slightly preferred over the DCX. Also, the mechanism and turnover frequencies (TOF) were found to be not sensitive to the partial pressures of H_2O and CO_2, as well as CO (in the range of 10^{-4} to 10^{-1} bar). The most abundant surface intermediates under gas phase conditions were adsorbed hydrogen atom, CO, and CH_3C. We note that we used a method similar to Grabow *et al.[146]* for determining coverage dependent adsorption energies of CO, H, and CH_3C.

In this study, we developed a microkinetic model for all elementary steps involved in both the DCX and DCN networks (previously the networks were studied independently) with forward and reverse rate parameters shown in Table 7.2.

Again, all calculations were carried out at 473K which is a typical experimental temperature[62, 67, 141-145] and we selected partial pressures of propanoic acid, water, and CO_2 of 1 bar and a CO partial pressure of 0.1 bar which is larger than in our previous study and corresponds to a condition of about 10% conversion. Additionally, all simulations were carried out under low (0.001 bar) and medium (1 bar) hydrogen partial pressures to investigate the effect of hydrogen partial pressure on the reaction mechanism in the presence of various solvents. For simplicity, all results corresponding to the low partial pressure of hydrogen environment are displayed in this paper in [ ] bracket next to the results of the medium hydrogen partial pressure. Finally, for all simulations in all solvents we employed the same coverage dependent adsorption energies of CO, H, and CH_3C as in our previous study.[140]

Figure 7.2 illustrates the turnover frequencies of all elementary steps under gas-phase conditions. The overall TOF was calculated to be 1.30×10^{-6} s^{-1} at medium hydrogen partial pressure [2.13×10^{-5} s^{-1} at low hydrogen partial pressure]. The TOF of the DCN pathways are 1.28×10^{-6} s^{-1} [2.11×10^{-5} s^{-1}] and the TOF of DCX pathways are 2.26×10^{-8} s^{-1} [1.43×10^{-7} s^{-1}], illustrating that the rate of the DCN is two orders of magnitude higher than the DCX. Next, we find the dominant reaction mechanism to be independent of the partial pressure of hydrogen to involve propanoic acid to undergo three dehydrogenation steps of α and β-carbons to form CHCHCOOH, followed by C-OH cleavage, and C-CO bond dissociation to produce C_2 products (CH_3CH_2COOH → $CH_3CHCOOH$ →

$CH_2CHCOOH \rightarrow CHCHCOOH \rightarrow CHCHCO \rightarrow CHCH$). 31% [43% in the low hydrogen scenario] of the surface was free of adsorbed intermediates and the coverages of the most abundant surface species are adsorbed hydrogen, CO, and CH_3C were calculated to be 23% [7%], 34% [35%], and 12% [14%], respectively.

In the following, the effects of various solvent on reaction mechanism and TOF of the DCN and DCX mechanism will be discussed.

7.3.1.1 *LIQUID WATER EFFECTS*

Water itself is one of the products of our reaction network as well as a relevant reaction environment. In the presence of water, calculations were again carried out at 473 K and chemical potentials corresponding to the same gas phase partial pressures of the gas-phase study described above (except for water). For the water chemical potential we assumed gas-liquid equilibrium, i.e., the water partial pressure is computed as,

$$x_{water} f^{L}_{water} = y_{water} P_{total} = P_{water} \tag{7.8}$$

where x_{water} is the mole fraction of water in the solvent mixture, f^{L}_{water} is the fugacity of pure water at 473 K, y_{water} is the mole fraction of water in the vapor, P_{tot} is the total pressure of the system, and P_{water} denotes the partial pressure of water. Assuming the solution is dilute, the mole fraction of water in solution (x_{water}) is 1. Also, the fugacity of pure water at 473 K can be obtained from a steam table[236] and is f^{L}_{water}=14.17 bar. Finally, the partial pressure of water is calculated to be 14.17 bar and this value was used for all further microkinetic simulations. However, for the other solvents, the partial pressure of water was set to 1 bar.

In liquid water, we find again that the most abundant surface species are H, CO, CH_3C and free (water covered) sites with coverages of 22% [7%], 35% [38%], 13% [14%], and 30% [41%], respectively. The overall TOF increased by a factor of 28 [31 in the low hydrogen partial pressure scenario] from $TOF_{overall\text{-}gas}=1.30\times10^{-6}$ s^{-1} [2.13×10^{-5} s^{-1}] to $TOF_{overall\text{-}water}=3.62\times10^{-5}$ s^{-1} [6.61×10^{-4} s^{-1}]. The calculated TOFs for all elementary steps are shown in Figure 7.3.

As we expected, the DCX is significantly more affected by liquid water than the DCN. TOFs of DCX pathways increased by more than two orders of magnitude from $TOF_{DCX\text{-}gas}= 2.26\times10^{-8}$ s^{-1} [1.43×10^{-7} s^{-1}] to $TOF_{DCX\text{-}water}= 6.21\times10^{-6}$ s^{-1} [7.86×10^{-5} s^{-1}] while the TOFs of DCN pathways only increased by one order of magnitude from $TOF_{DCN\text{-}gas}= 1.28\times10^{-6}$ s^{-1} [2.11×10^{-5} s^{-1}] to $TOF_{DCN\text{-}water}= 3.00\times10^{-5}$ s^{-1} [2.94×10^{-4} s^{-1}]. Clearly, in liquid water DCX and DCN pathways are very competitive and our calculations suggest that the DCN is dominant with a TOF_{DCN} to TOF_{DCX} ratio of only 4.8 [3.7] which is most likely within the accuracy of our calculations and models. As a result of the dominance of the DCN, the predicted most favorable pathway does not change in the presence of water from our previous gas phase results. The dominant DCX pathway starts with a dehydrogenation step of the α-carbon to form $CH_3CHCOOH$, followed by O-H bond cleavage and further α-carbon dehydrogenation prior to C-CO_2 bond cleavage and hydrogenation to C_2 products (CH_3CH_2COOH → $CH_3CHCOOH$ → CH_3CHCOO → CH_3CCOO → CH_3C → → CH_3CH_3 / CH_2CH_2).

7.3.1.2 *LIQUID OCTANE EFFECTS*

Simulations in liquid octane were performed at reaction conditions similar to the gas-phase simulations. The results of our DFT calculations in liquid octane already

suggested that octane has only a minor effect on the reaction parameters and consequently, we did not expect any significant effect on the reaction mechanism and overall TOF in comparison to our gas-phase results. Indeed, Figure 7.4 illustrates that the DCX and DCN mechanisms are hardly affected and the dominant pathway remains under all studied hydrogen environments: CH_3CH_2COOH → $CH_3CHCOOH$ → $CH_2CHCOOH$ → CHCHCOOH → CHCHCO → CHCH. Also, the overall TOF values in the presence and absence of Octane are almost the same ($TOF_{overall\text{-}Octane}=1.77\times10^{-6}$ s^{-1} [2.23×10^{-5} s^{-1}] vs. $TOF_{overall\text{-}gas}=1.30\times10^{-6}$ s^{-1}[2.13×10^{-5} s^{-1}]). The most abundant species were free sites, CO, H, and CH_3C with surface coverages of 30% [42%], 35% [37%], 23% [7%], and 13% [13%], respectively.

7.3.1.3 *LIQUID N-BUTANOL EFFECTS*

Simulations in liquid n-butanol were performed at reaction conditions similar to the gas-phase simulations. The overall TOF was calculated to be $5.75\times10^{-6}s^{-1}$ [1.23×10^{-4} s^{-1}] which is relatively larger than the gas phase and octane TOFs and smaller than the water TOFs. The dominant mechanism at both low and medium hydrogen partial pressures is again the DCN with the most favorable pathways staying the same as under gas-phase conditions. However, in the presence of n-butanol, the TOF of the DCX increased by a factor of 28 [47] from $TOF_{DCX\text{-}gas}=2.26\times10^{-8}$ s^{-1} [1.43×10^{-7} s^{-1}] to $TOF_{DCX\text{-}Butanol}=6.26\times10^{-7}$ s^{-1} [6.76×10^{-6} s^{-1}]. Figure 7.5 illustrates that the dominant pathway of the DCX is similar to the pathway in liquid water (CH_3CH_2COOH → $CH_3CHCOOH$ → CH_3CHCOO → CH_3CCOO → CH_3C → → CH_3CH_3 / CH_2CH_2). The most abundant

surface species are free sites, CO, H, and CH_3C with the coverages of 30% [42%], 35% [37%], 22% [7%], and 13% [13%], respectively.

As already predicted from the solvation free energies, in the presence of n-butanol the TOFs are similar but lower than the TOFs in liquid water. We observe that as the polarity of the solvents increases from octane to n-butanol to water, the DCX and to a lower degree the DCN are facilitated such that the overall TOF in the presence of liquid octane is about the same as in the gas-phase, increases for butanol by a factor of 4.4 [5.8] and finally increases for water by a factor of 27.9 [31.1].

7.3.2 Apparent Activation Barrier, Reaction Orders, and Sensitivity Analysis

Apparent activation barriers were computed in the temperature range of 423 to 523 K in all reaction environments and hydrogen partial pressures.

$$E_a = RT^2\left(\frac{\partial \ln(r)}{\partial T}\right)_{p_i} \tag{7.9}$$

Next, the reaction order with respect to hydrogen was calculated at 473 K for the low hydrogen partial pressure in the range of 0.0005 to 0.002 bar and for the medium hydrogen partial pressure in the range of 0.5 to 2 bar using equation 7.10. Similarly, the reaction order of propanoic acid and CO were calculated at 473 K and a pressure range of 0.5 to 2 bar and 0.0001 to 1 bar, respectively.

$$\alpha_i = \left(\frac{\partial \ln(r)}{\partial \ln(p_i)}\right)_{T, p_{j\neq i}} \tag{7.10}$$

Finally, Campbell's degrees of rate and thermodynamic control [147-149], X_{RC} and X_{TRC}, were used to determine the rate controlling steps and intermediates in the mechanism.

Rate controlling steps and intermediates are those transition states and intermediates that most strongly influence the reaction rate and are potential activity descriptors.

$$X_{\mathrm{RC},i} = \frac{k_i}{r}\left(\frac{\partial r}{\partial k_i}\right)_{K_i, k_j \neq k_i}, \qquad X_{\mathrm{TRC},n} = \frac{1}{r}\left(\frac{\partial r}{\partial\left(\frac{-G_n^0}{RT}\right)}\right)_{G^0_{m\neq n}, G_i^{0,\mathrm{TS}}} \quad (11)$$

where r is the overall rate of reaction, k_i is the forward rate constant for step i, K_i equilibrium constant for step i, R is the gas constant, T denotes the reaction temperature, and G_n^0 is the free energy of adsorbate n.

7.3.2.1 *GAS PHASE*

Medium partial pressure of hydrogen (p_{H2} = 1 bar)

At a reaction temperature of 473 K and a hydrogen partial pressure of 1 bar, our model predicts an apparent activation energy of 0.84 eV in a gas phase environment. The reaction order with respect to propanoic acid is +1.0, with respect to CO it is +0.31, and finally with respect to H_2 it is -0.80. These results are in good agreement to our previous study[140]. Next, the C-OH bond dissociation as well as α- and β-carbon dehydrogenation steps are found to be rate-controlling. For example, the X_{RC} values for the C-OH cleavage reactions 17 (CHCHCOOH*** + 2*→ CHCHCO**** + OH*), reaction 5 ($CH_3CHCOOH$** + *→ CH_3CHCO** + OH*), and reaction 11 ($CH_2CHCOOH$*** + *→ CH_2CHCO*** + OH*) were calculated to be 0.49, 0.23, and 0.17, respectively. The X_{RC} value of the dehydrogenation of the α-carbon in propanoic acid (reaction 2) is rate controlling with X_{RC} = 0.32 and the first and second dehydrogenation steps of the β-carbon in $CH_3CHCOOH$ are rate controlling with X_{RC} =

0.09 (reaction 6) and X_{RC} = 0.06 (reaction 12), respectively. We note that the sum of the degree of rate control is larger one due to numerical inaccuracies of our nonlinear equation solver; however, the trends should not be affected by these numerical issues. Also, these results are in agreement with previous calculations[82, 150] from Pallassana and Neurock and Olcay et al. who found that the C-OH bond cleavage is rate controlling for the HDO of acetic acid. Our model in addition highlights the importance of dehydrogenation steps. Finally, the thermodynamic rate control analysis suggests that the adsorption free energy of H* and CO* have a significant effect on the overall rate with X_{TRC} = -1.52 and 0.21, respectively, such that destabilizing the adsorbed hydrogen or stabilizing CO improves the overall reaction rate. CO is generally known to be a surface poison; however, due to repulsive lateral interactions with adsorbed H* and the negative reaction order with respect to hydrogen we observe that destabilizing adsorbed H* is more important than stabilizing CO*.

Low partial pressure of hydrogen (p_{H2} = 0.001bar)

At a low partial pressure of hydrogen, the coverage of hydrogen drops from 23% (p_{H2} = 1 bar) to 7%. Also, the available free sites increased from 31% to 42%. However, the coverage of CO is not significantly affected and in fact, slightly increases from 34% to 35%. Now, the thermodynamic rate control analysis suggests that destabilizing both CO* and H* improves the overall rate with X_{TRC} = -0.03 and -0.33, respectively. Also, the dehydrogenation of the α-carbon in propanoic acid is clearly the most rate controlling step with X_{RC} = 1.0 and C-OH bond dissociation becoming less important with X_{RC} = 0.05 for reaction 17.

Finally, our model predicts an apparent activation barrier of 0.62 eV (which is lower than at higher hydrogen partial pressures) and orders of reaction for CO and H_2 that are close to zero (i.e., -0.02 and -0.13, respectively). The calculated propanoic acid reaction order is again 1.

7.3.2.2 *LIQUID WATER*

Water - Medium partial pressure of hydrogen (P_{H2} = 1 bar)

In the presence of liquid water and at a hydrogen partial pressure of 1 bar, C-OH bond dissociations are in agreement with our gas-phase simulations the most rate controlling steps (e.g., X_{RC} = 0.43 for reaction 17, X_{RC} = 0.28 for reaction 11, and X_{RC} = 0.09 for reaction 5). Next, α and β-carbon dehydrogenation steps have some influence on the net reaction rate (X_{RC} = 0.25 for reaction 2, X_{RC} = 0.09 for reaction 6, and X_{RC} = 0.05 for reaction 12). As discussed above, in the presence of water the DCX becomes competitive with the DCN. As a result, our sensitivity analysis finds that O-H and C-H cleavage steps involved in the DCX become rate controlling, e.g., reaction 31 ($CH_3CHCOOH^{**} + * \rightarrow CH_3CHCOO^{**} + H^*$) with X_{RC} = 0.03, reaction 34 ($CH_3CHCOO^{***} + * \rightarrow CH_3CCOO^{***} + H^*$) with X_{RC} = 0.06, and reaction 30 ($CH_3CH_2COO^{**} + 2* \rightarrow CH_3CHCOO^{***} + H^*$) with X_{RC} = 0.05. Thermodynamic rate control analysis suggests again that destabilizing H* and stabilizing CO* improves the reaction rate with X_{TRC} = -1.55 and +0.18, respectively. Finally, the reaction orders with respect to CO, hydrogen, and propanoic acid are -0.77, 0.28 and 1.0, respectively, and the apparent activation energy is calculated as 0.68 eV which is 0.16 eV smaller than the gas-phase activation barrier.

Water - Low partial pressure of hydrogen (P_{H2} = 0.001 bar)

At a hydrogen partial pressure of 0.001 bar, dehydrogenation steps of the α-carbon of propanoic acid are the most rate controlling steps, e.g., for reaction 2 X_{RC} = 0.79 and for reaction 30 X_{RC} = 0.11, while the C-OH bond dissociation in reaction 17 becomes less influential with X_{RC} = 0.08. Again, in agreement with the gas-phase simulations thermodynamic rate control analysis suggests that destabilizing both CO* and H* improves the reaction rate with X_{TRC} = -0.03 and X_{TRC} = -0.39. Finally, the reaction orders of propanoic acid, CO and H_2 are calculated to be 1.0, -0.02, and -0.17 respectively, and the apparent activation barrier is predicted as 0.48 eV.

7.3.2.3 *LIQUID OCTANE*

Octane - Medium partial pressure of hydrogen (P_{H2} = 1 bar)

In the presence of liquid octane changes in the reaction parameters, TOF, and surface coverages are negligible in comparison to our gas-phase results. As a result, our model predicts an activation barrier of 0.84 eV and reaction orders of propanoic acid, H_2 and CO of 1.0, -0.74, and 0.28, respectively, that are very similar to our gas-phase simulations. Finally, C-OH bond dissociations in reaction 17, 11, and 5 are most rate controlling with X_{RC}'s of 0.48, 0.20 and 0.20, respectively. Next, dehydrogenation steps in reaction 2, 6, and 12 (X_{RC} = 0.34, X_{RC} = 0.09, and X_{RC} = 0.06, respectively) and the stability of adsorbed CO* and H* (X_{TRC} = +0.19 and X_{TRC} = -1.44, respectively) have some influence on the overall reaction rate.

Octane – Low partial pressure of hydrogen (P_{H2}=0.001 bar)

At a hydrogen partial pressure of 0.001 bar, the dehydrogenation of the α-carbon of propanoic acid (reaction 2) is most rate controlling (X_{RC}=0.89) and the C-OH bond dissociation in reaction 17 is less influential (X_{RC}=0.05). The thermodynamic degree of rate control for CO* and H* are calculated as -0.03 and -0.34, respectively. Finally, very similar to our gas-phase simulations our model predicts an apparent activation barrier of 0.63 eV and propanoic acid, hydrogen and CO reaction orders of 1.0, -0.15, and -0.02 respectively.

7.3.2.4 *LIQUID N-BUTANOL*

Butanol – Medium partial pressure of hydrogen (P_{H2} =1 bar)

The presence of liquid n-butanol leads to qualitatively similar changes to the reaction mechanism and TOF as the presence of liquid water. C-OH bond dissociations are still the most rate controlling steps, i.e., reaction 17 (X_{RC} = 0.48), reaction 11 (X_{RC} =0.27), and reaction 5 (X_{RC} =0.15), followed by α and β-carbon dehydrogenations (reaction 2 with X_{RC} = 0.25, reaction 6 with X_{RC} = 0.10, reaction 12 with X_{RC} = 0.06, and reaction 34 with $X_{RC\text{-}R34}$=0.06) and O-H bond dissociations relevant for the DCX (reaction 31 with X_{RC} = 0.02 and reaction 30 with X_{RC} = 0.01). Thermodynamic rate control analysis suggests again that destabilizing H* and stabilizing CO* improves the reaction rate with X_{TRC} = -1.61 and +0.21, respectively. Finally, the reaction orders with respect to propanoic acid, H_2 and CO are 1.0, -0.82, and +0.31, respectively, and the apparent activation energy is calculated as 0.76 eV which is 0.1 eV smaller than the gas-phase activation barrier and 0.08 eV larger than the activation barrier in liquid water.

Butanol – Low partial pressure of hydrogen (P_{H2} = 0.001 bar)

At a hydrogen partial pressure of 0.001 bar, dehydrogenation steps of the α-carbon in propanoic acid are the most rate controlling steps, e.g., for reaction 2 X_{RC}= 0.80 and for reaction 30 X_{RC} = 0.06, while the C-OH bond dissociation in reaction 17 becomes less influential with X_{RC} = 0.10. Again, in agreement with both water and gas-phase simulations thermodynamic rate control analysis suggests that destabilizing both CO* and H* improves the reaction rate with X_{TRC} = -0.03 and X_{TRC} = -0.41. Finally, the reaction orders of propanoic acid, CO and H_2 are calculated to be 1.0, -0.01, and -0.18, respectively, and the apparent activation barrier is predicted to be 0.47 eV which is essentially equivalent to the activation barrier in liquid water.

7.4 *CONCLUSION*

The effect of three different solvents, liquid water, n-octane, and n-butanol has been investigated on the decarbonylation and decarboxylation of propanoic acid over Pd (111) model surfaces with the help of periodic DFT calculations, COSMO-RS implicit solvation with iSMS scheme and microkinetic modeling. We developed mean-field microkinetic models for each solvent at a temperature of 473 K and low (0.001 bar) and medium (1 bar) hydrogen partial pressures. Under all conditions is the decarbonylation the dominant HDO mechanism with the most favored pathway following dehydrogenation steps prior to C-OH and C-CO bond cleavages, i.e., CH_3CH_2COOH → $CH_3CHCOOH$ → $CH_2CHCOOH$ → CHCHCOOH → CHCHCO → CHCH → → CH_3CH_3 / CH_2CH_2. In nonpolar solvents such as octane, we do not observe any significant solvent effects on the elementary surface reactions and overall turnover

frequency. However, with increasing polarity of the solvent, e.g., n-butanol and protic water, does the overall turnover frequency increase by up to a factor 30 from the gas-phase turnover frequency. Also, the apparent activation barrier decreases in the presence of liquid water by up to 0.16 eV. Another significant effect of a polar solvent such as water is that it stabilizes key intermediates in the decarboxylation mechanism such that the decarboxylation rate increases by two orders of magnitude and the decarbonylation and decarboxylation pathways become essentially competitive. Finally, a sensitivity analysis suggests that in all reaction environments and at a low hydrogen partial pressure is the dehydrogenation of α-carbon in propanoic acid most rate controlling. With increasing hydrogen partial pressure, the C-OH bond dissociation becomes most rate controlling and the importance of C-H bond cleavages is diminished. As a result, both C-H and C-OH bond dissociations are likely activity descriptors for a future computational catalyst discovery and design study.

7.5 *ACKNOWLEDGEMENTS*

We gratefully acknowledge the financial support from the National Science Foundation (CHE-1153012) and in part from the U.S. Department of Energy, Office of Basic Energy Sciences, Chemical Sciences Division under Contract DE-SC0007167. Computational resources have been provided by the National Energy Research Scientific Computing Center (NERSC) which is supported by the Office of Science of the U.S. Department of Energy and in part by XSEDE under grant number TG-CTS090100. Finally, computing resources from the USC NanoCenter and USC's High Performance Computing Group are gratefully acknowledged.

7.6 *TABLES*

Table 7.1. Reaction free energies in eV for all elementary reaction steps in the hydro-deoxygenation of propanoic acid over Pd (111) model surfaces at a temperature of 473 K.

#	Reaction	Gas		Water		Octane		Butanol	
		ΔG_{rxn}	$\Delta G^{\ddagger}$	ΔG_{rxn}	$\Delta G^{\ddagger}$	ΔG_{rxn}	$\Delta G^{\ddagger}$	ΔG_{rxn}	$\Delta G^{\ddagger}$
0	$CH_3CH_2COOH+*\rightarrow CH_3CH_2COOH*$	0.94	N/A	0.88	N/A	0.95	N/A	0.89	N/A
1	$CH_3CH_2COOH* + 3*\rightarrow CH_3CH_2CO*** + OH*$	0.35	0.89	0.40	0.86	0.36	0.88	0.39	0.90
2	$CH_3CH_2COOH* + 2*\rightarrow CH_3CHCOOH** + H*$	-0.11	0.61	-0.20	0.53	-0.13	0.60	-0.13	0.59
3	$CH_3CH_2CO*** \rightarrow CH_3CH_2* + CO* + *$	-0.66	1.01	-0.75	1.00	-0.70	1.03	-0.71	1.03
	$CH_3CH_2CO*** \rightarrow CH_3CHCO** + H*$	0.02	0.83	-0.04	0.77	0.01	0.85	0.00	0.83
5	$CH_3CHCOOH** + *\rightarrow CH_3CHCO** + OH*$	0.47	0.86	0.56	0.94	0.50	0.87	0.52	0.92
6	$CH_3CHCOOH** + 2*\rightarrow CH_2CHCOOH*** + H*$	-0.35	0.57	-0.31	0.57	-0.35	0.60	-0.34	0.60
7	$CH_3CHCOOH** + 2*\rightarrow CH_3CCOOH*** + H*$	-0.06	1.14	-0.05	1.15	-0.08	1.15	-0.09	1.15
8	$CH_3CHCO** + *\rightarrow CH_3CH** + CO*$	-0.84	1.00	-0.91	1.01	-0.88	1.00	-0.89	1.00
9	$CH_3CHCO** + 2*\rightarrow CH_3CCO*** + H*$	-0.39	0.61	-0.41	0.58	-0.40	0.60	-0.41	0.60
10	$CH_3CHCO** + 2*\rightarrow CH_2CHCO*** + H*$	-0.29	0.57	-0.32	0.51	-0.29	0.58	-0.29	0.56
11	$CH_2CHCOOH*** + *\rightarrow CH_2CHCO*** + OH*$	0.53	1.20	0.54	1.14	0.56	1.17	0.56	1.18

12	$CH_2CHCOOH^{***} + *\rightarrow CHCHCOOH^{***} + H^*$	0.04	0.89	-0.03	0.83	0.03	0.89	0.01	0.87
13	$CH_3CCOOH^{***} + *\rightarrow CH_3CCO^{***} + OH^*$	0.14	0.77	0.19	0.77	0.18	0.78	0.20	0.81
14	$CH_3CCO^{***}\rightarrow CH_3C^* + CO^* + *$	-1.37	0.47	-1.43	0.46	-1.41	0.48	-1.42	0.48
15	$CH_2CHCO^{***} + *\rightarrow CH_2CH^{***} + CO^*$	-0.80	0.80	-0.86	0.79	-0.86	0.80	-0.87	0.80
16	$CH_2CHCO^{***} + 2*\rightarrow CHCHCO^{****} + H^*$	0.02	0.68	-0.01	0.67	0.00	0.67	0.00	0.67
17	$CHCHCOOH^{***} + 2*\rightarrow CHCHCO^{****} + OH^*$	0.51	1.07	0.57	1.11	0.53	1.06	0.55	1.10
18	$CHCHCO^{****} \rightarrow CHCH^{***} + CO^*$	-1.13	0.19	-1.19	0.24	-1.18	0.20	-1.18	0.21
19	$CHCH^{***} + H^*\rightarrow CH_2CH^{***} + *$	0.31	0.95	0.34	0.97	0.31	0.96	0.32	0.96
20	$CH_2CH^{***} + H^* \rightarrow CH_2CH_2^{**} + 2*$	-0.03	0.87	0.00	0.87	-0.02	0.88	-0.01	0.88
21	$CH_2CH^{***}\rightarrow CH_2C^{**} + H^*$	-0.43	0.45	-0.45	0.44	-0.43	0.44	-0.44	0.44
22	$CH_2C^{**} + H^*\rightarrow CH_3C^* + 2*$	-0.24	0.87	-0.21	0.86	-0.23	0.88	-0.22	0.87
23	$CH_2CH^{***} + H^* \rightarrow CH_3CH^{**} + 2*$	-0.26	0.79	-0.27	0.78	-0.27	0.79	-0.27	0.79
24	$CH_3C^* + H^* \rightarrow CH_3CH^{**}$	0.92	1.09	0.93	1.09	0.93	1.10	0.94	1.10
25	$CH_3CH^{**} + H^* \rightarrow CH_3CH_2^* + 2*$	0.16	0.87	0.20	0.88	0.17	0.88	0.18	0.88
26	$CH_3CH_2^* + H^* \rightarrow CH_3CH_3^* + *$	0.05	0.64	0.05	0.65	0.04	0.64	0.04	0.64
27	$CH_3CH_2^* + 2* \rightarrow CH_2CH_2^{**} + H^*$	-0.45	0.42	-0.43	0.40	-0.44	0.41	-0.44	0.41
28	$CH_3CH_2COOH^* + 2* \rightarrow CH_3CH_2COO^{**} + H^*$	-0.40	0.35	-0.34	0.38	-0.44	0.32	-0.39	0.37
29	$CH_3CH_2COO^{**} \rightarrow CH_3CH_2^* + CO_2^*$	0.18	1.40	0.22	1.34	0.22	1.40	0.23	1.39

30	$CH_3CH_2COO^{**} + 2^* \rightarrow CH_3CHCOO^{***} + H^*$	0.39	1.22	0.22	0.98	0.37	1.18	0.34	1.12
31	$CH_3CHCOOH^{**} + ^* \rightarrow CH_3CHCOO^{**} + H^*$	0.10	0.79	0.08	0.84	0.06	0.78	0.09	0.82
32	$CH_3CHCOOH^{**} + ^* \rightarrow CH_3CH^{**} + COOH^*$	0.28	1.37	0.29	1.40	0.30	1.38	0.29	1.38
33	$CH_3CHCOO^{***} \rightarrow CH_3CH^{**} + CO_2^*$	-0.37	0.94	-0.20	0.99	-0.32	0.95	-0.29	0.96
34	$CH_3CHCOO^{***} + ^* \rightarrow CH_3CCOO^{***} + H^*$	-0.07	0.85	-0.15	0.75	-0.12	0.81	-0.14	0.78
35	$CH_3CCOOH^{***} + ^* \rightarrow CH_3CCOO^{***} + H^*$	0.04	0.89	-0.06	0.86	-0.01	0.88	0.00	0.90
36	$CH_3CCOOH^{***} \rightarrow CH_3C^* + COOH^{**}$	-0.58	0.90	-0.60	0.88	-0.55	0.92	-0.56	0.92
37	$CH_2CHCOOH^{***} + ^* \rightarrow CH_2CH^{***} + COOH^*$	0.70	2.07	0.65	2.02	0.70	2.07	0.68	2.06
38	$CH_3CCOO^{***} \rightarrow CH_3C^* + CO_2^* + ^*$	-1.12	0.63	-0.89	0.82	-1.05	0.70	-1.00	0.74
39	$COOH^{**} \rightarrow CO_2^* + H^*$	-0.55	0.35	-0.41	0.33	-0.56	0.27	-0.49	0.31
40	$COOH^{**} \rightarrow CO^* + OH^*$	-0.65	0.40	-0.64	0.40	-0.68	0.37	-0.66	0.40
41	$OH^* + H^* \rightarrow H_2O^* + ^*$	-0.20	0.69	-0.15	0.68	-0.20	0.67	-0.18	0.69
42	$CH_3CH_3^* \rightarrow CH_3CH_3 + ^*$	-0.79	N/A	-0.81	N/A	-0.78	N/A	-0.78	N/A
43	$CH_2CH_2^{**} \rightarrow CH_2CH_2 + 2^*$	0.01	N/A	-0.01	N/A	0.00	N/A	0.00	N/A
44	$H_2O^* \rightarrow H_2O + ^*$	-0.49	N/A	-0.37	N/A	-0.50	N/A	-0.44	N/A
45	$CO_2^* \rightarrow CO_2 + ^*$	-0.81	N/A	-0.83	N/A	-0.81	N/A	-0.81	N/A
46	$CHCH^* \rightarrow CHCH + ^*$	1.16	N/A	1.17	N/A	1.14	N/A	1.15	N/A
47	$CO^* \rightarrow CO + ^*$	-1.19	N/A	-1.27	N/A	-1.24	N/A	-1.25	N/A
48	$H_2 + 2^* \rightarrow 2H^*$	-0.58	N/A	-0.61	N/A	-0.60	N/A	-0.61	N/A

Table 7.2 Equilibrium and forward rate constants for the elementary steps in the HDO of propanoic acid over Pd (111) model surfaces at a temperature of 473 K.

Reaction #	Gas		Water		Octane		Butanol	
	K_{eq}	$k_{forward}$ (s^{-1})	K_{eq}	$k_{forward}$ (s^{-1})	K_{eq}	$k_{forward}$ (s^{-1})	K_{eq}	$k_{forward}$ (s^{-1})
0	8.98×10^{-11}	9.52×10^{7}	4.45×10^{-10}	9.52×10^{7}	8.46×10^{-11}	9.52×10^{7}	3.68×10^{-10}	9.52×10^{7}
1	2.10×10^{-4}	3.14×10^{3}	5.18×10^{-5}	6.36×10^{3}	1.45×10^{-4}	4.66×10^{3}	7.83×10^{-5}	2.37×10^{3}
2	1.39×10^{1}	3.04×10^{6}	1.30×10^{2}	2.08×10^{7}	2.17×10^{1}	3.75×10^{6}	2.59×10^{1}	4.87×10^{6}
3	1.01×10^{7}	1.76×10^{2}	9.71×10^{7}	1.99×10^{2}	2.54×10^{7}	1.07×10^{2}	3.37×10^{7}	1.17×10^{2}
4	6.05×10^{-1}	1.34×10^{4}	2.76	6.66×10^{4}	7.41×10^{-1}	9.57×10^{3}	9.90×10^{-1}	1.35×10^{4}
5	9.14×10^{-6}	6.16×10^{3}	1.10×10^{-6}	1.02×10^{3}	4.94×10^{-6}	5.78×10^{3}	2.99×10^{-6}	1.70×10^{3}
6	5.81×10^{3}	8.43×10^{6}	1.87×10^{3}	8.74×10^{6}	4.96×10^{3}	3.70×10^{6}	3.87×10^{3}	4.41×10^{6}
7	4.06	6.85	3.03	6.08	7.88	5.21	8.24	5.86
8	8.58×10^{8}	2.03×10^{2}	5.22×10^{9}	1.66×10^{2}	2.28×10^{9}	2.04×10^{2}	2.75×10^{9}	1.98×10^{2}
9	1.32×10^{4}	3.51×10^{6}	2.52×10^{4}	5.78×10^{6}	2.00×10^{4}	4.17×10^{6}	2.17×10^{4}	4.39×10^{6}
10	1.33×10^{3}	8.80×10^{6}	2.68×10^{3}	3.82×10^{7}	1.11×10^{3}	6.29×10^{6}	1.33×10^{3}	1.05×10^{7}
11	2.09×10^{-6}	1.68	1.57×10^{-6}	6.52	1.11×10^{-6}	3.20	1.03×10^{-6}	2.55
12	4.16×10^{-1}	3.31×10^{3}	2.15	1.57×10^{4}	4.58×10^{-1}	3.40×10^{3}	7.55×10^{-1}	5.52×10^{3}
13	2.98×10^{-2}	6.70×10^{4}	9.13×10^{-3}	6.96×10^{4}	1.26×10^{-2}	4.53×10^{4}	7.88×10^{-3}	2.18×10^{4}
14	3.95×10^{14}	9.98×10^{7}	1.71×10^{15}	1.15×10^{8}	1.03×10^{15}	7.62×10^{7}	1.23×10^{15}	8.07×10^{7}

15	3.52×10^{8}	2.91×10^{4}	1.57×10^{9}	3.59×10^{4}	1.61×10^{9}	3.08×10^{4}	1.74×10^{9}	3.22×10^{4}
16	6.61×10^{-1}	5.57×10^{5}	1.28	7.05×10^{5}	9.61×10^{-1}	6.46×10^{5}	1.09	6.96×10^{5}
17	3.32×10^{-6}	4.33×10^{1}	9.37×10^{-7}	1.35×10^{1}	2.33×10^{-6}	4.77×10^{1}	1.48×10^{-6}	1.95×10^{1}
18	1.12×10^{12}	8.65×10^{10}	4.63×10^{12}	3.07×10^{10}	3.38×10^{12}	7.58×10^{10}	3.86×10^{12}	6.36×10^{10}
19	4.76×10^{-4}	8.33×10^{2}	2.65×10^{-4}	4.63×10^{2}	4.96×10^{-4}	6.37×10^{2}	4.14×10^{-4}	6.02×10^{2}
20	2.28	4.99×10^{3}	9.49×10^{-1}	4.97×10^{3}	1.48	3.86×10^{3}	1.26	3.96×10^{3}
21	3.39×10^{4}	1.73×10^{8}	6.28×10^{4}	2.10×10^{8}	4.21×10^{4}	1.99×10^{8}	4.72×10^{4}	2.05×10^{8}
22	3.30×10^{2}	5.89×10^{3}	1.63×10^{2}	6.28×10^{3}	2.74×10^{2}	4.46×10^{3}	2.45×10^{2}	5.09×10^{3}
23	5.46×10^{2}	1.94×10^{7}	8.06×10^{2}	3.68×10^{7}	7.86×10^{2}	2.73×10^{7}	8.41×10^{2}	3.19×10^{7}
24	1.64×10^{-10}	2.51×10^{1}	1.21×10^{-10}	2.31×10^{1}	1.10×10^{-10}	1.87×10^{1}	1.03×10^{-10}	1.81×10^{1}
25	1.95×10^{-2}	5.46×10^{3}	6.75×10^{-3}	3.93×10^{3}	1.50×10^{-2}	4.65×10^{3}	1.24×10^{-2}	4.62×10^{3}
26	3.17×10^{-1}	1.46×10^{6}	2.65×10^{-1}	1.29×10^{6}	4.01×10^{-1}	1.37×10^{6}	3.62×10^{-1}	1.36×10^{6}
27	6.40×10^{4}	3.26×10^{8}	3.61×10^{4}	5.39×10^{8}	5.30×10^{4}	3.74×10^{8}	4.80×10^{4}	4.10×10^{8}
28	1.92×10^{4}	1.99×10^{9}	3.83×10^{3}	8.79×10^{8}	4.64×10^{4}	3.62×10^{9}	1.33×10^{4}	1.25×10^{9}
29	1.08×10^{-2}	1.13×10^{-2}	4.28×10^{-3}	5.41×10^{-2}	4.29×10^{-3}	1.25×10^{-2}	3.88×10^{-3}	1.57×10^{-2}
30	6.55×10^{-5}	9.39×10^{-1}	4.50×10^{-3}	3.29×10^{2}	1.07×10^{-4}	2.84	2.38×10^{-4}	1.04×10^{1}
31	9.04×10^{-2}	3.95×10^{4}	1.33×10^{-1}	1.11×10^{4}	2.29×10^{-1}	5.08×10^{4}	1.22×10^{-1}	1.89×10^{4}
32	9.80×10^{-4}	2.33×10^{-2}	8.03×10^{-4}	1.22×10^{-2}	5.97×10^{-4}	1.90×10^{-2}	8.03×10^{-4}	1.96×10^{-2}
33	8.49×10^{3}	1.05×10^{3}	1.41×10^{2}	3.13×10^{2}	2.66×10^{3}	7.34×10^{2}	1.32×10^{3}	5.81×10^{2}

34	6.23	8.87×10^{3}	4.27×10^{1}	1.11×10^{5}	1.89×10^{1}	2.40×10^{4}	3.02×10^{1}	4.54×10^{4}
35	3.43×10^{-1}	3.29×10^{3}	4.60	7.30×10^{3}	1.36	3.96×10^{3}	1.10	2.27×10^{3}
36	1.47×10^{6}	2.84×10^{3}	2.19×10^{6}	4.52×10^{3}	6.88×10^{5}	1.58×10^{3}	9.46×10^{5}	1.72×10^{3}
37	3.33×10^{-8}	7.99×10^{-10}	1.25×10^{-7}	2.79×10^{-9}	3.42×10^{-8}	9.18×10^{-10}	6.30×10^{-8}	1.20×10^{-9}
38	9.13×10^{11}	1.76×10^{6}	3.01×10^{9}	1.68×10^{4}	1.40×10^{11}	3.60×10^{5}	4.66×10^{10}	1.32×10^{5}
39	7.28×10^{5}	1.63×10^{9}	2.16×10^{4}	3.18×10^{9}	9.49×10^{5}	1.45×10^{10}	1.86×10^{5}	4.57×10^{9}
40	8.00×10^{6}	4.84×10^{8}	7.13×10^{6}	5.36×10^{8}	1.89×10^{7}	1.23×10^{9}	1.02×10^{7}	5.54×10^{8}
41	1.48×10^{2}	4.20×10^{5}	3.75×10^{1}	5.44×10^{5}	1.53×10^{2}	7.96×10^{5}	8.07×10^{1}	4.23×10^{5}
42	2.44×10^{8}	3.65×10^{16}	4.54×10^{8}	6.79×10^{16}	1.94×10^{8}	2.91×10^{16}	2.12×10^{8}	3.17×10^{16}
43	7.22×10^{-1}	1.12×10^{8}	1.17	1.81×10^{8}	9.66×10^{-1}	1.50×10^{8}	9.53×10^{-1}	1.48×10^{8}
44	1.73×10^{5}	3.35×10^{13}	9.36×10^{3}	1.81×10^{12}	2.12×10^{5}	4.10×10^{13}	4.54×10^{4}	9.45×10^{12}
45	2.50×10^{8}	3.24×10^{16}	4.11×10^{8}	5.32×10^{16}	2.75×10^{8}	3.56×10^{16}	2.48×10^{8}	3.21×10^{16}
46	1.60×10^{-6}	9.98×10^{-15}	1.30×10^{-6}	8.09×10^{-15}	2.73×10^{-6}	1.70×10^{-14}	2.10×10^{-6}	1.31×10^{-14}

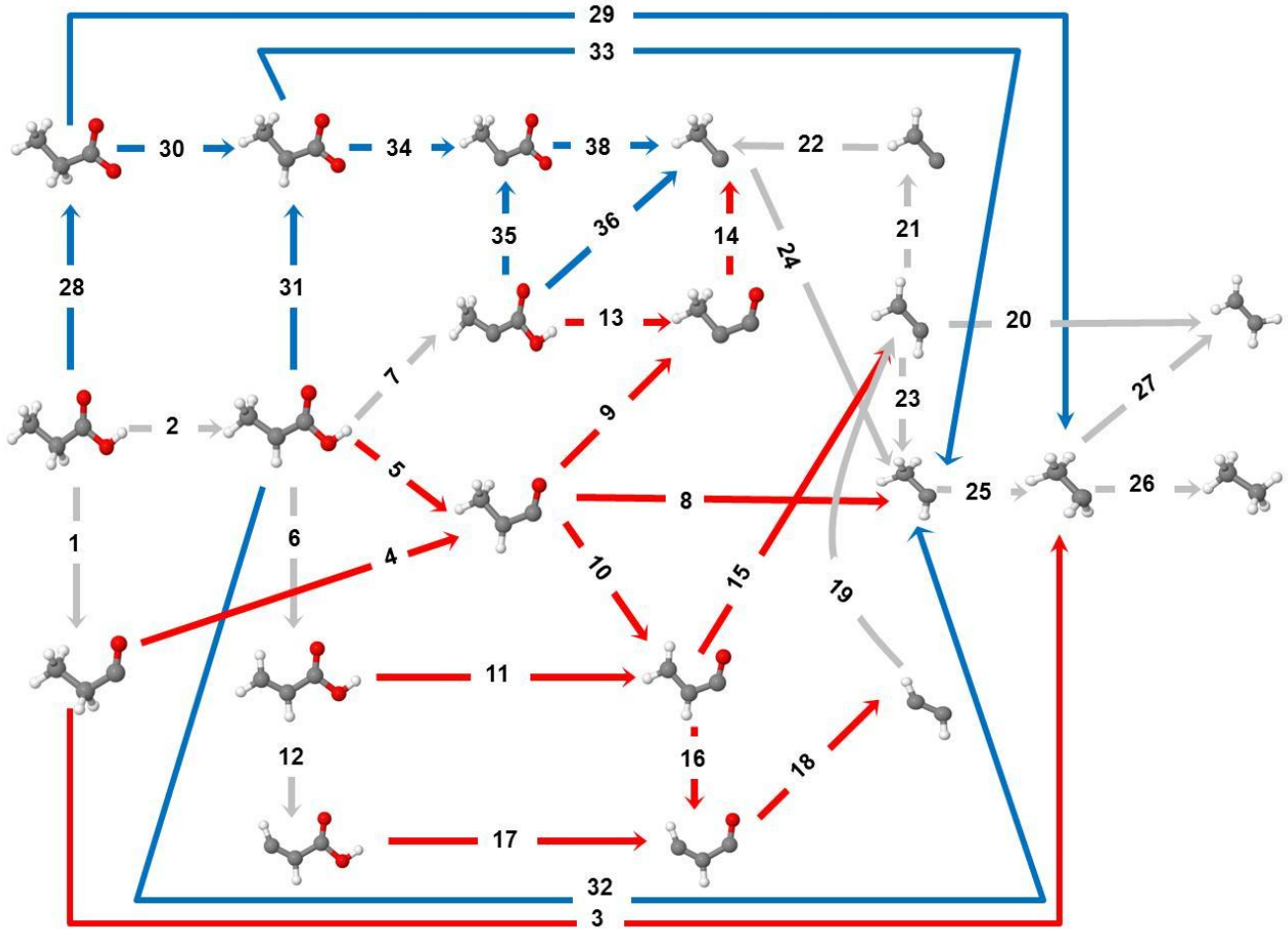
29
33
30
34
38
22
35
36
14
21
28
31
24
13
20
7
9
23
27
2
5
8
25
26
1
6
4
10
15
19
11
12
16
18
17
32
3

Figure 7.1. Network of elementary reaction steps considered in the hydrodeoxygenation of propanoic acid over Pd (111). The elementary reactions which are involved in DCN mechanism are shown with the blue color arrows, DCX reactions are illustrated with the red color arrows, and those reaction which are involved in both of the mechanisms such as, dehydrogenation of propionaic acid and its derivatives, and removal of hydrocarbon pool are shown with the gray color arrows.

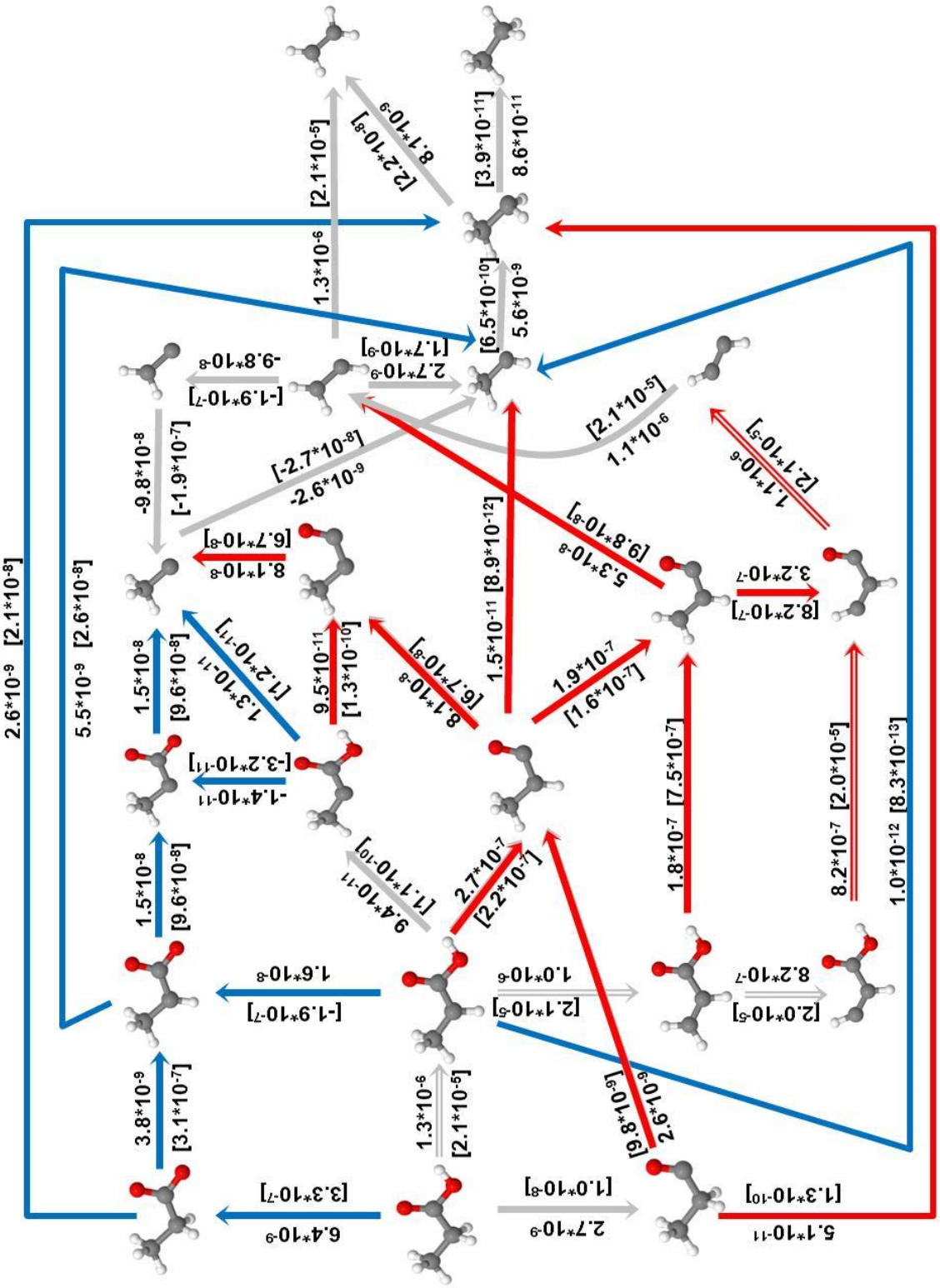
2.6*10-9 [2.1*10-8]
5.5*10-9 [2.6*10-8]
1.3*10-6 [2.1*10-5]
[2.2*10-8] 8.1*10-9
[3.9*10-11] 8.6*10-11
[6.5*10-10] 5.6*10-9
2.7*10-9 [1.7*10-9]
[-1.9*10-7] -9.8*10-8
-9.8*10-8 [-1.9*10-7]
[-2.7*10-8] -2.6*10-9
[2.1*10-5] 1.1*10-6
1.1*10-6 [2.1*10-5]
8.1*10-8 [6.7*10-8]
5.3*10-8 [9.8*10-8]
[8.2*10-7] 3.2*10-7
1.5*10-8 [9.6*10-8]
9.5*10-11 [1.3*10-10]
[1.2*10-11] 1.3*10-11
8.1*10-8 [6.7*10-8]
1.5*10-11 [8.9*10-12]
1.9*10-7 [1.6*10-7]
-1.4*10-11 [-3.2*10-11]
1.5*10-8 [9.6*10-8]
9.4*10-11 [1.1*10-10]
2.7*10-7 [2.2*10-7]
1.8*10-7 [7.5*10-7]
8.2*10-7 [2.0*10-5]
1.0*10-12 [8.3*10-13]
[-1.9*10-7] 1.6*10-8
1.0*10-6 [2.1*10-5]
[2.0*10-5] 8.2*10-7
3.8*10-9 [3.1*10-7]
1.3*10-6 [2.1*10-5]
2.9*10-9 [9.8*10-9]
6.4*10-9 [3.3*10-7]
2.7*10-9 [1.0*10-8]
5.1*10-11 [1.3*10-10]

Figure 7.2. TOFs (s^{-1}) for various elementary steps in the HDO of propanoic acid in absence of any solvents at a temperature of 473 K and a propanoic acid gas phase pressure of 1 bar and a hydrogen partial pressure of 1 bar or 0.001 bar (numbers inside the square brackets []). All other reaction conditions are given in section 7.3.1. The elementary reactions which are involved in DCN mechanism are shown with the blue color arrows, DCX reactions are illustrated with the red color arrows, and those reactions which are involved in both of the mechanisms such as, dehydrogenation of propionaic acid and its derivatives, and removal of hydrocarbon pool are shown with the gray color arrows. The reactions that are involved in the most dominant pathway are illustrated with a double-line arrow. The TOF_{DCN} was calculated to be 1.28×10^{-6} s^{-1} [2.11×10^{-5} s^{-1}] while the TOF_{DCX} was 2.26×10^{-8} s^{-1} [1.43×10^{-7} s^{-1}] (TOF_{DCN}/TOF_{DCX} = 56.4 [148])

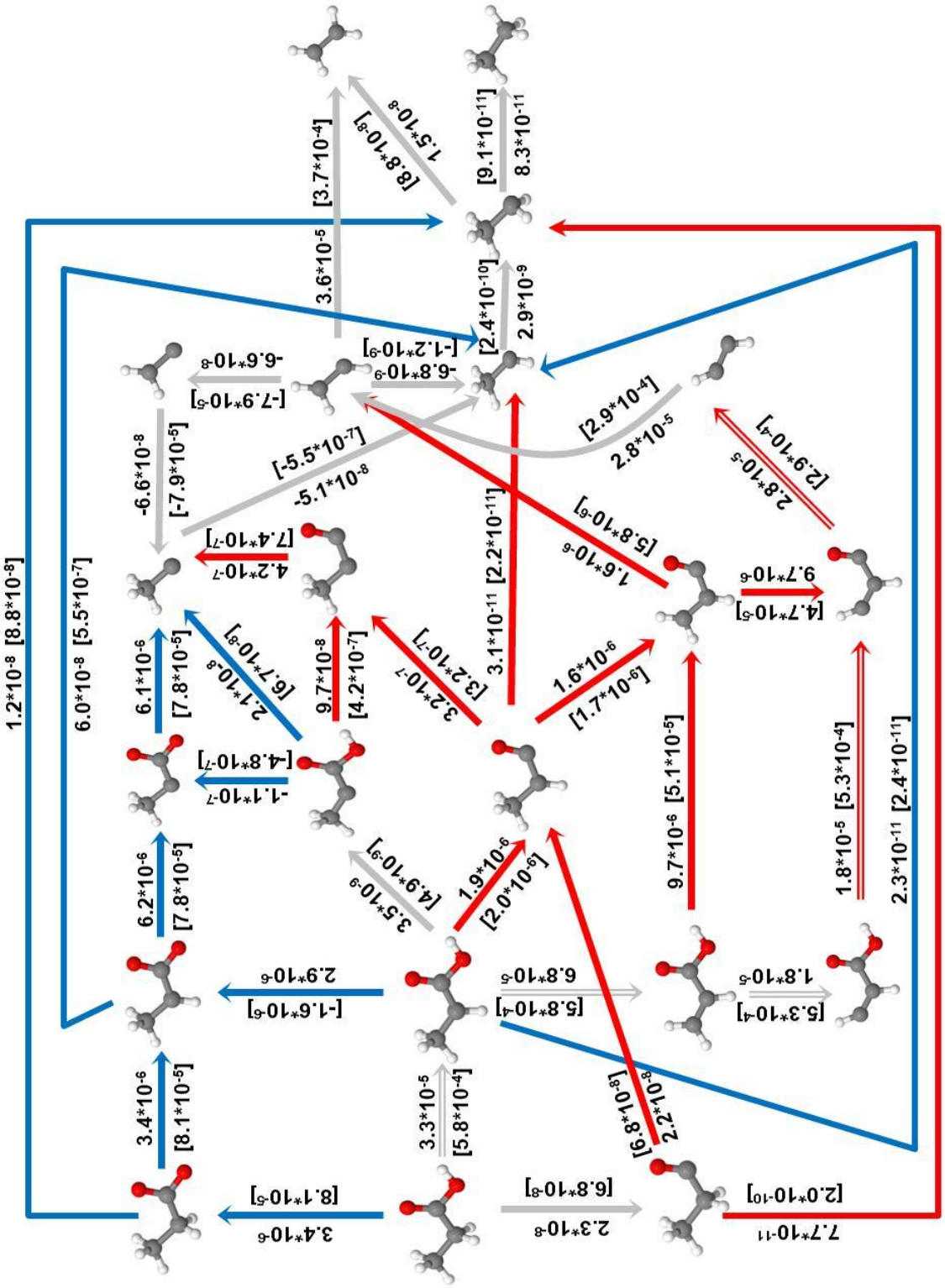
1.2*10-8 [8.8*10-8]
6.0*10-8 [5.5*10-7]
3.4*10-6 [8.1*10-5]
6.2*10-6 [7.8*10-5]
6.1*10-6 [7.8*10-5]
-6.6*10-8 [-7.9*10-5]
3.6*10-5 [3.7*10-4]
2.9*10-9 [2.4*10-10]
8.3*10-11 [9.1*10-11]
1.5*10-8 [8.8*10-9]
-6.8*10-9 [-1.2*10-9]
-6.6*10-8 [-7.9*10-5]
-5.1*10-8 [-5.5*10-7]
2.8*10-5 [2.9*10-4]
2.8*10-5 [2.9*10-4]
1.6*10-6 [5.8*10-6]
9.7*10-6 [4.7*10-5]
1.8*10-5 [5.3*10-4]
2.3*10-11 [2.4*10-11]
3.1*10-11 [2.2*10-11]
1.6*10-6 [1.7*10-6]
9.7*10-6 [5.1*10-5]
1.9*10-6 [2.0*10-6]
3.5*10-9 [4.9*10-9]
9.7*10-8 [4.2*10-7]
3.2*10-7 [3.2*10-7]
2.1*10-8 [6.7*10-8]
-1.1*10-7 [-4.8*10-7]
4.2*10-7 [7.4*10-7]
3.3*10-5 [5.8*10-4]
2.2*10-8 [6.8*10-8]
-1.6*10-6 2.9*10-6
6.8*10-5 [5.8*10-4]
1.8*10-5 [5.3*10-4]
3.4*10-6 [8.1*10-5]
2.3*10-8 [6.8*10-8]
7.7*10-11 [2.0*10-10]

Figure 7.3. TOFs (s^{-1}) for various elementary steps in the HDO of propanoic acid in the presence of liquid water at a temperature of 473 K and a chemical potential corresponding to a propanoic acid gas phase pressure of 1 bar and a hydrogen partial pressure of 1 bar or 0.001 bar (numbers inside the square brackets []). All other reaction conditions are given in section 7.3.1. The elementary reactions which are involved in DCN mechanism are shown with the blue color arrows, DCX reactions are illustrated with the red color arrows, and those reactions which are involved in both of the mechanisms such as, dehydrogenation of propionaic acid and its derivatives, and removal of hydrocarbon pool are shown with the gray color arrows. The reactions that are involved in the most dominant pathway are illustrated with a double-line arrow. The TOF_{DCN} was calculated to be 3.00×10^{-5} s^{-1} [2.94×10^{-4} s^{-1}] while the TOF_{DCX} was = 6.21×10^{-6} s^{-1} [7.86×10^{-5} s^{-1}] (TOF_{DCN}/TOF_{DCX} = 4.8 [3.7])

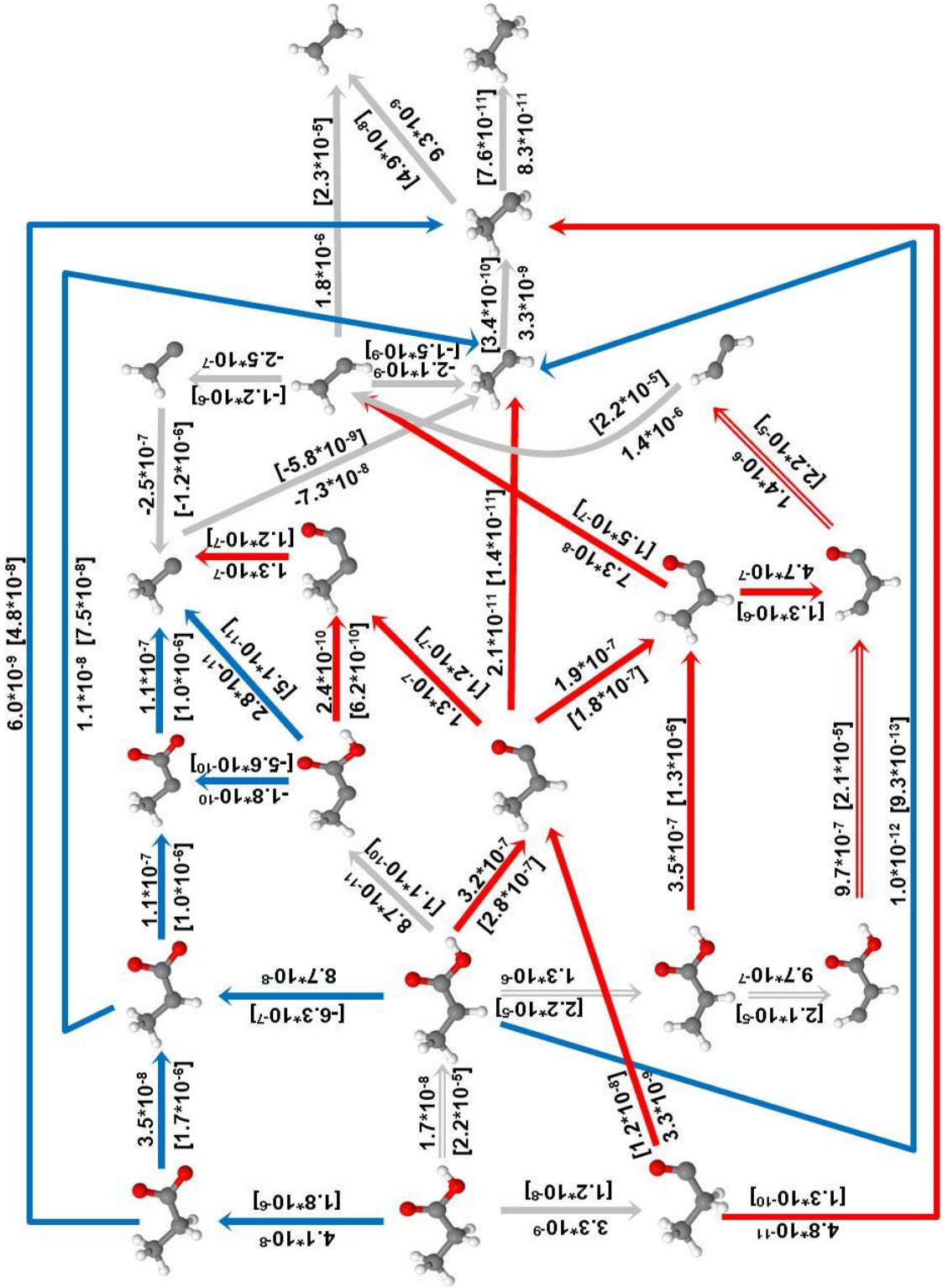
6.0*10-9 [4.8*10-8]
1.1*10-8 [7.5*10-8]
1.1*10-7 [1.0*10-6]
3.5*10-8 [1.7*10-6]
1.8*10-6 [2.3*10-5]
9.3*10-9 [4.9*10-8]
8.3*10-11 [7.6*10-11]
3.3*10-9 [3.4*10-10]
-2.5*10-7 [-1.2*10-6]
-7.3*10-8 [-5.8*10-9]
1.4*10-6 [2.2*10-5]
1.4*10-6 [2.2*10-5]
-2.1*10-9 [-1.5*10-9]
-2.5*10-7 [-1.2*10-6]
1.3*10-7 [1.2*10-7]
7.3*10-8 [1.5*10-7]
4.7*10-7 [1.3*10-6]
2.1*10-11 [1.4*10-11]
1.9*10-7 [1.8*10-7]
1.3*10-7 [1.2*10-7]
2.4*10-10 [6.2*10-10]
2.8*10-11 [5.1*10-11]
1.1*10-7 [1.0*10-6]
-1.8*10-10 [-5.6*10-10]
3.5*10-7 [1.3*10-6]
9.7*10-7 [2.1*10-5]
1.0*10-12 [9.3*10-13]
8.7*10-11 [1.1*10-10]
3.2*10-7 [2.8*10-7]
1.1*10-7 [1.0*10-6]
8.7*10-8 [-6.3*10-7]
1.3*10-6 [2.2*10-5]
9.7*10-7 [2.1*10-5]
1.7*10-8 [2.2*10-5]
3.3*10-8 [1.2*10-8]
4.1*10-8 [1.8*10-6]
3.3*10-9 [1.2*10-8]
4.8*10-11 [1.3*10-10]

Figure 7.4. TOFs (s^{-1}) for various elementary steps in the HDO of propanoic acid in the presence of n-octane at a temperature of 473 K and a chemical potential corresponding to a propanoic acid gas phase pressure of 1 bar and a hydrogen partial pressure of 1 bar or 0.001 bar (numbers inside the square brackets []). All other reaction conditions are given in section 7.3.1. The elementary reactions which are involved in DCN mechanism are shown with the blue color arrows, DCX reactions are illustrated with the red color arrows, and those reactions which are involved in both of the mechanisms such as, dehydrogenation of propionaic acid and its derivatives, and removal of hydrocarbon pool are shown with the gray color arrows. The reactions that are involved in the most dominant pathway are illustrated with a double-line arrow. The TOF_{DCN} was calculated to be 1.64×10^{-6} s^{-1} [2.23×10^{-5} s^{-1}] while the TOF_{DCX} was 1.28×10^{-7} s^{-1} [1.14×10^{-6} s^{-1}] (TOF_{DCN}/TOF_{DCX} = 12.8 [19.6])

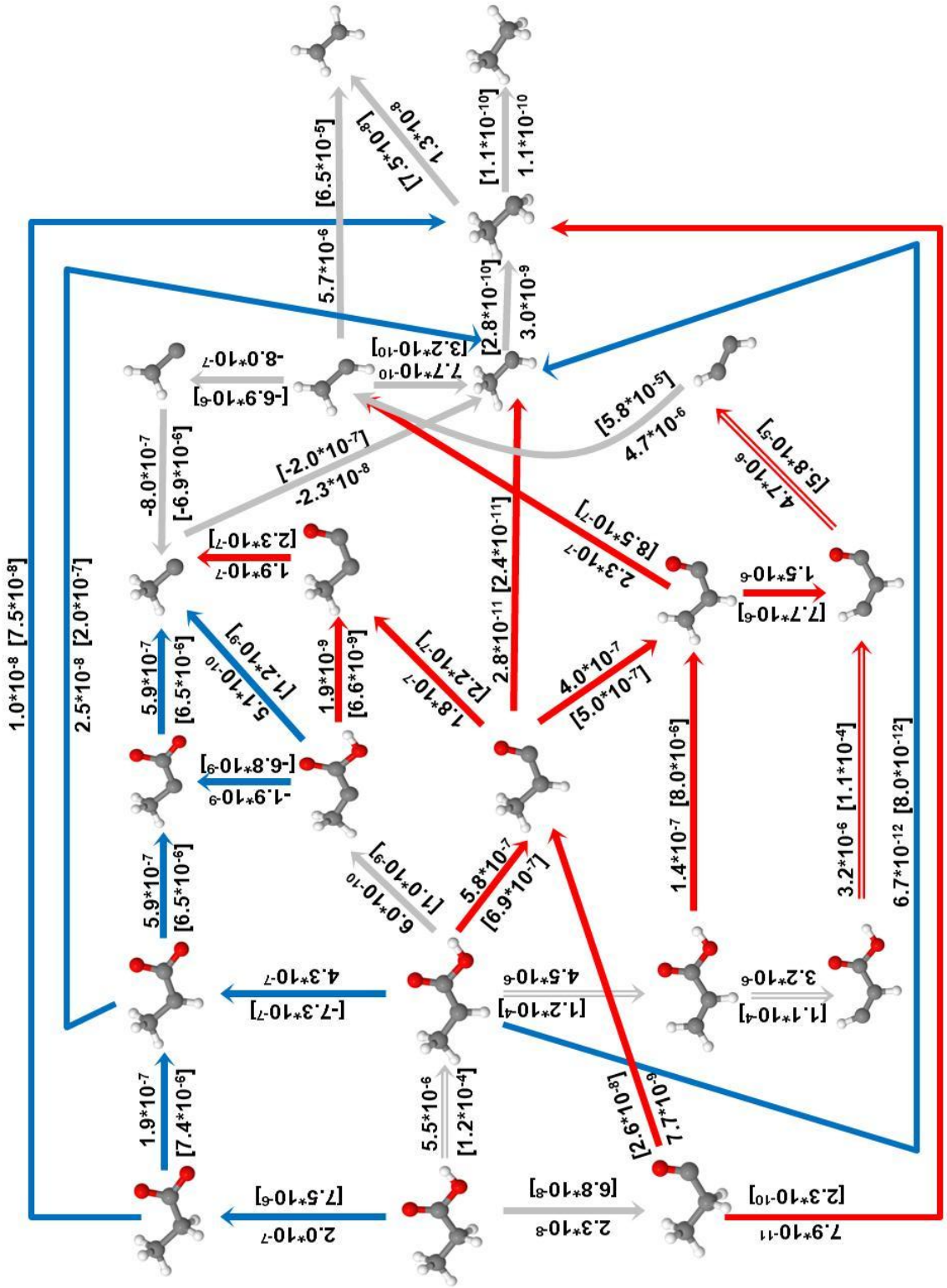
1.0*10-8 [7.5*10-8]
2.5*10-8 [2.0*10-7]
5.7*10-6 [6.5*10-5]
1.3*10-8 [7.5*10-8]
[1.1*10-10] 1.1*10-10
3.0*10-9 [2.8*10-10]
[3.2*10-10] 7.7*10-10
-8.0*10-7 [-6.9*10-6]
-8.0*10-7 [-6.9*10-6]
[-2.0*10-7] -2.3*10-8
[5.8*10-5] 4.7*10-6
4.7*10-6 [5.8*10-5]
2.8*10-11 [2.4*10-11]
[8.5*10-7] 2.3*10-7
1.9*10-7 [2.3*10-7]
1.5*10-6 [7.7*10-6]
5.9*10-7 [6.5*10-6]
5.1*10-10 [1.2*10-9]
1.9*10-9 [6.6*10-9]
1.8*10-7 [2.2*10-7]
4.0*10-7 [5.0*10-7]
-1.9*10-9 [-6.8*10-9]
6.0*10-10 [1.0*10-9]
5.8*10-7 [6.9*10-7]
1.4*10-7 [8.0*10-6]
3.2*10-6 [1.1*10-4]
6.7*10-12 [8.0*10-12]
5.9*10-7 [6.5*10-6]
[-7.3*10-7] 4.3*10-7
[1.2*10-4] 4.5*10-6
[1.1*10-4] 3.2*10-6
1.9*10-7 [7.4*10-6]
5.5*10-6 [1.2*10-4]
[2.6*10-8] 7.7*10-9
2.0*10-7 [7.5*10-6]
2.3*10-8 [6.8*10-8]
7.9*10-11 [2.3*10-10]

Figure 7.5. TOFs (s^{-1}) for various elementary steps in the HDO of propanoic acid in the presence of n-butanol at a temperature of 473 K, a chemical potential corresponding to a propanoic acid gas phase pressure of 1 bar and a hydrogen partial pressure of 1 bar or 0.001 bar (numbers inside the square brackets []). All other reaction conditions are given in section 7.3.1. The elementary reactions which are involved in DCN mechanism are shown with the blue color arrows, DCX reactions are illustrated with the red color arrows, and those reactions which are involved in both of the mechanisms such as, dehydrogenation of propionaic acid and its derivatives, and removal of hydrocarbon pool are shown with the gray color arrows. The reactions that are involved in the most dominant pathway are illustrated with a double-line arrow. The TOF_{DCN} was calculated to be 5.12×10^{-6} s^{-1} [5.86×10^{-5} s^{-1}] while the TOF_{DCX} was 6.26×10^{-7} s^{-1} [6.76×10^{-6} s^{-1}] (TOF_{DCN}/TOF_{DCX} = 8.2 [8.7])

CHAPTER 8

EFFECTS OF SOLVENTS ON CATALYTIC HYDRODEOXYGENATION OF METHYL PROPIONATE [1]

[1]S. Behtash, J. Lu, E. Walker, O. Mamun, and A. Heyden.
To be submitted to Journal of Physical Chemistry C.

ABSTRACT

The effects of liquid water and 1,4-dioxane on the hydrodeoxygenation of methyl propionate over Pd (111) model surfaces have been studied from first principles. We developed a microkinetic model and studied the effects of solvents on the reaction mechanism in different reaction media. Our model predicts that for all reaction media, decarbonylation pathways are favored over decarboxylation pathways. However, in the presence of water, the decarboxylation mechanism was slightly facilitated due to the stabilizing effects of water on propionate and its dehydrogenated derivatives. The overall activity of 1,4-dioxane was higher than water. The kinetic parameters in the presence of 1,4-dioxane are quite similar to gas-phase conditions, while in the presence of water they deviated. Finally, a sensitivity analysis of our models suggests that both propanoyl-methoxy type dissociations and dehydrogenation steps control the overall rate of the catalyst in all environments and are likely activity descriptors for the hydrodeoxygenation of organic esters.

KEYWORDS:

Solvent effects; organic esters; methyl propionate; palladium; density functional theory; COSMO; decarbonylation; decarboxylation; microkinetic modeling

8.1 INTRODUCTION

Lipid-rich biomass feedstocks, such as vegetable oils, waste fats, and algal lipids are one potential class of raw materials for the production of green fuels. The content of lipid feedstock's are oxygenates such as: triglyceride, fatty acid, and esters. The conversion of these molecules to liquid hydrocarbons, have been greatly investigated using hydrotreatment processes and conventional hydrodesulphurization catalysts such as sulfided $NiMo/Al_2O_3$ and $CoMo/Al_2O_3$.[47, 54, 59] However, considering the low level of sulfur in biomass and the higher activity of oxygenated feeds versus sulfide feeds, conventional hydrotreating catalysts display a short catalyst lifetime. Also, difficulties in the separation of carbon oxides from the recycle gas have been reported.[54, 59] In order to rationally design a catalyst for hydrodeoxygenation of fatty acids and esters, we previously investigated the kinetic and reaction mechanism of propionic acid[119, 158] and methyl propionate[202] under gas-phase conditions; however, as the industrial hydrotreatment processes often occurs in a complex liquid environment, our understanding of the mechanism cannot be completed without studying the solvent effects, as it can influence the kinetic of hydrodeoxygenation of organic acids and esters.

Solvent effects in heterogeneous catalysis have been rationalized by correlating reaction rates and product distribution with polarity or dielectric constant and activity coefficient[237-240]. It has been observed that a polar solvent enhances the adsorption of the non-polar reactant, while a non-polar solvent enhances the adsorption of a polar reactant.[240-243] For example in competitive hydrogenation of acetone and cyclohexene, polar solvents enhanced the reaction rate of conversion of cyclohexene to cyclohexane while, presumably strong interaction between polar solvent and acetone in

the bulk reduced the adsorption of acetone.[241, 242] Similar behavior has been also reported for hydrogenation of 1-hexene and 2-methyl-3buten-2-ol over silica supported Pt[243] or hydrogenation of *o*-nitrotolene where the authors[244] were also able to correlate their reaction rates with the activity coefficients.

While solvent properties can qualitatively explain the changes in the kinetic of reactions or products distribution, much more work remains to be done to explain and characterize the solvent effects quantitatively. With recent developments in the application of density functional theory for characterization of the properties of molecules at heterogeneous interfaces, a better understanding of the interactions of solvent, intermediates, and catalyst surface is obtainable. The effects of solvent on the reaction parameters of the elementary reactions in a chemical process can be quantified using solvation models. We previously[232] developed a solvation scheme (iSMS) to implicitly investigate the properties of liquid/solid interfaces, and we utilized[157, 200] our solvation scheme to investigate the solvent effects on HDO of propionic acid over Pd catalysts. We found that while non-polar solvents such as octane do not change the kinetic of the HDO of propionic acid, polar solvents such as water can influence the mechanism to some level. For example, in water the overall activity was enhanced, and the turn over frequency of the decarboxylation pathway, which is not favored under gas-phase condition, was significantly increased in the presence of water, and essentially become as competitive as decarbonylation pathway, the dominant mechanism.[157, 200] Considering that solvents can influence the activity and the mechanism of the reactions, to further investigate the catalytic HDO of organic esters, in this study, we investigated the solvent effect on HDO of methyl propionate over Pd (111) surfaces in the presence of

water and 1,4-dioxane. In our studies[119, 157, 158, 200, 202] on HDO of methyl propionate and propanoic acid over Pd(111) under gas-phase condition, we found quite similar results where decarbonylation was the dominant mechanism, and H, CO, CH_3C were the most abundant surface intermediates. Additionally, many of the reaction intermediates involved in the HDO of methyl priopionate are identical to intermediates involved in HDO of priopionic acid, and since we previously[157, 200] found that the polar solvents have more effects on these intermediates and the overall mechanism, in this study, we focused on investigation of a polar protic solvent, water, and a polar aprotic solvent, 1,4-dioxane. We investigated the effect of solvents on the adsorption/desorption energies, activation barriers, and reaction energies of elementary steps. We implemented the reaction parameters into a microkinetic model to study the effects of solvent, reaction conditions on the kinetics, and reaction mechanism of HDO of methyl propionate.

8.2 METHODS

8.2.1 SOLVATION MODEL

In this study, the approximate effect of a solvent is investigated with the help of the iSMS method.[232] iSMS is a new approach for modeling reactions at metal-liquid interfaces with implicit solvation models. More information about iSMS and a validation of this method has recently been published .[232] Basically, the free energy of an adsorbed intermediate on a periodic metal slab at the solid-liquid interface, $G^{liquid}_{surface+intermediate}$, is defined using a subtraction scheme

$$G^{liquid}_{surface+\mathrm{int}ermediate} = G^{vacuum}_{surface+\mathrm{int}ermediate} + (G^{liquid}_{cluster+\mathrm{int}ermediate} - E^{vacuum}_{cluster+\mathrm{int}ermediate}) \quad (8.1)$$

where, $G^{vacuum}_{surface+\mathrm{int}ermediate}$, is the free energy in the absence of a solvent (plane-wave DFT energy of the periodic slab model including vibrational contributions to the free energy), $G^{liquid}_{cluster+\mathrm{int}ermediate}$ is the free energy of a metal cluster in the liquid (without explicitly considering vibrational contributions) constructed by removing selected metal atoms from the periodic-slab model and removing the periodic boundary conditions, and $E^{vacuum}_{cluster+\mathrm{int}ermediate}$ is the DFT energy of the same cluster in the absence of the solvent. Combinations of COSMO and COSMO-RS[233, 234] implicit solvation models have been used to calculate $G^{liquid}_{cluster+\mathrm{int}ermediate}$. COSMO-RS calculations have been performed using COSMOtherm.[235] Thermodynamic properties of the solvents are obtained from the COSMOtherm database, based on the results of quantum chemical COSMO calculations at the BP-TZVP level of theory. For all other structures, COSMO-RS input files have been generated from COSMO calculations at the same level of theory. We note that as a first approximation we did not include the solvent degrees of freedom in the reaction coordinate.

8.2.2 DFT CALCULATIONS

Cluster model DFT calculations were carried out using TURBOMOLE 6.0.[116-118] The Pd (111) cluster model surfaces have been modeled by a two layered cluster with a 5×5 surface. These structures were constructed by removal of the periodic boundaries from the periodic slabs that were obtained from our previous plane-wave (VASP)[107, 108] calculations.[119] All adsorbates were represented by all-electron

TZVP[120-122] basis sets while for Pd we used a relativistic small core potential (ECP) together with a basis set of same quality as the adsorbates for the valence electrons. The Coulomb potential was approximated with the RI-J approximation with auxiliary basis sets[123-125]. Single point energy calculations were performed with a self-consistent field energy convergence criterion of 1.0×10^{-6}. Finally, for each cluster model energy calculations on various spin surfaces were performed to identify the lowest energy spin state for further calculations.

For cluster models in the liquid phase, COSMO calculations were performed on the same spin surface as for the vacuum cluster calculations. The dielectric constant was set to infinity to provide the input for the COSMO-RS calculations. For cavity construction, the default radii-based cavities were used.

8.2.3 MICROKINETIC MODELING

For surface reactions, the forward rate constant (k_{for}) of each reaction is calculated as

$$k_{for} = \frac{k_B T}{h} e^{-\frac{\Delta G^{\ddagger}}{k_B T}} \tag{8.2}$$

where k_B is the Boltzmann constant, T denotes the reaction temperature, h is the Planck constant, and $\Delta G^{\ddagger}$ represents the free energy of activation for a specific temperature and reaction environment. I.e., in the presence of solvents, the free energy of activation ($\Delta G^{\ddagger}_{solvent}$) and free energy of reaction ($\Delta G_{rxn\text{-}solvent}$) were calculated as,

$$\Delta G^{\ddagger}_{Solvent} = \Delta G^{\ddagger}_{Gas} + G_{TS}(solv) - G_{IS}(solv), \tag{8.3}$$

and

$$\Delta G_{\text{rxn-solvent}} = \Delta G_{\text{Gas}} + G_{FS}(solv) - G_{IS}(solv) \tag{8.4}$$

where, G_{IS}(solv), G_{FS}(solv), and G_{TS}(solv) are the solvation energies of the initial, final, and transition states, respectively, that were obtained from the difference in energy of the COSMO-RS and gas-phase cluster calculations, and $\Delta G^{\ddagger}_{\text{Gas}}$ and ΔG_{Gas} are the free energy of activation and reaction under gas phase conditions, respectively. The reverse rate constant (k_{rev}) is calculated similarly from the thermodynamic equilibrium constant K is given as

$$k_{\text{rev}} = \frac{k_{\text{for}}}{K} \tag{8.5}$$

For an adsorption reaction A(g)+*→A*the rate of adsorption is given by collision theory with a sticking probability of 1 independent of solvent.

$$k_{\text{for}} = \frac{1}{N_0\sqrt{2\pi m_A k_B T}} \tag{8.6}$$

where N_0 is the number of sites per area (1.478×10^{19} m^{-2}) and m_A denotes the molecular weight of A. The desorption rate constant is again given by the equilibrium constant, i.e., equation 8.5.

In the presence of a solvent, the free energy of adsorption for A(g)+*→A* is calculated as,

$$\Delta G_{ads-solvent} = \Delta G_{ads-gas} + G_{A^*}(solv) - G_{Pd}(solv) \tag{8.7}$$

where $\Delta G_{ads-gas}$ is the free energy of adsorption under gas phase conditions and $G_{A^*}(solv)$ and $G_{Pd}(solv)$ are as before the solvation energies of the adsorbed molecule A and Pd surface immersed in the solvent, respectively.

With the forward and reverse rate constants defined, rates of the elementary reactions can be expressed by mean-field rate laws. Considering that some of the adsorbed intermediates occupy multiple active sites (the number of occupied sites by each adsorbate is shown in Table1), the rate expressions and steady state molecular balance equations are highly nonlinear. To solve the set of steady state differential reactor equations and to obtain the surface coverages of the intermediates, we used the BzzMath library[115] developed by Buzzi-Ferraris. No assumptions were made regarding rate-limiting steps.

8.3 Results and discussions

8.3.1 Solvent Effects on Intermediates Adsorption Strength

The investigated intermediates in the network of reaction for HDO of methyl propionate are listed in Table 8.1. The 41 intermediates in Table 8.1 can be classified as 7 different structural classes: Methyl propionate and its hydrogenated derivatives are $CH_3CH_2COOCH_3$ such as, $CH_3CHCOOCH_3$, etc.; Propanoyl (CH_3CH_2CO) and its dehydrogenated intermediates such as CH_3CHCO, etc. which are the product of propanoyl-methoxy type dissociations ($CH_3CH_2CO—OCH_3$); Propionate (CH_3CH_2COO) and its intermediates such as, CH_3CHCOO, etc.; Methanol (CH_3OH) and its intermediates such as, methoxy, etc.; Ethane (CH_3CH_3) and its dehydrogenated derivatives such as, CH_3CH_2, etc. which are the products of C-C bond cleavages in the propanoyl (CH_3CH_2CO) class; Methane (CH_4) and its dehydrogenated intermediates such as methyl (CH_3) which are the product of propionate-methyl bond cleavages; $COOCH_3$ and $COOCH_2$ which are the products of C-C bond cleavages in methyl propionate

(CH_3CH_2—$COOCH_3$) or CH_3CH_2—$COOCH_2$. We will later show that the two latter groups do not participate in the dominant reaction mechanism, since C-C bond dissociation in methyl propionate, as well as propionate-methyl bond dissociations are less favored both thermodynamically and kinetically. Finally, there are small molecules or atoms such as, CO_2, CO, and H.

The presence of solvent may vary the strength of the adsorption of all classes of intermediates due to adsorbate-solvent interactions or solvent-metal interactions. To investigate the effects of the presence of water and 1,4-dioxane on the adsorption strength of the intermediates involved in the HDO of methyl propionate, for all intermediates, we assumed adsorption processes in the absence and presence of solvents as,

$$A(g) + *\,(g) \leftrightarrow A^*(g) \tag{8.8}$$

$$A(g) + *\,(l) \leftrightarrow A^*(l) \tag{8.9}$$

and to measure the changes in the strength of adsorption in different reaction media, we calculated the effects of solvent on the free energy of adsorption of intermediates,

$$\Delta(G_{ads,A}) = G_{ads,A}(l) - G_{ads,A}(g) = [G^{A*}(l) - G^{A*}(g)] - [G^*(l) - G^*(g)] \tag{8.10}$$

where, $G_{ads,A}(l)$ and $G_{ads,A}(g)$ are the free energy of adsorption of a gas molecule of intermediate A in the presence and absence of solvent. $G^{A*}(l)$ and $G^{A*}(g)$ are the free energy of adsorbed A in the presence and absence of solvent, and similarly $G^*(l)$ and $G^*(g)$ are the free energy of the free active sites of the catalyst in the presence and absence of solvent.

We note that while the above adsorption/desorption process does take place for the stable reactants and products such as methyl propionate, ethane, methanol, CO, CO_2, and H_2, perhaps for unstable and unsaturated intermediates, this process does not occur,

because unstable intermediates may not exist in the gas-phase. However, with calculating the changes in the adsorption energy of all intermediates in the presence of solvents, we can gain an insight on the effects of solvent on the adsorbed intermediates and clean surface of the Pd.

We calculated changes in the free energy of adsorption in the presence of water and 1,4-Dioxane for all the intermediates in the HDO of methyl propionate (Table 8.1). As shown in Table 8.1, Methyl propionate adsorbs stronger in the presence of water and 1,4-dioxane by 0.09 and 0.14 eV respectively. Similarly, the adsorption strength of other dehydrogenated species is enhanced in the presence of solvents. For example, in water, $CH_2CH_2COOCH_2$, $CH_3CHCOOCH_2$, and $CH_3CH_2COOCH_2$ adsorbs stronger by 0.17, 0.13, and 0.12 eV respectively. Likewise, in the presence of 1,4-dioxane, adsorbed $CH_2CH_2COOCH_2$, $CH_2CHCOOCH_2$, $CH_3CHCOOCH_3$ interacts stronger with the Pd surface by 0.10, 0.09 and 0.06 eV.

Propanoyl and its dehydrogenated derivatives such as CH_3CHCO, CH_2CH_2CO are not affected remarkably in the presence of both water and 1,4-dioxane. Similarly, non-polar hydrocarbons such as ethane, ethene, acethylene, methane, methyl and their dehydrogenated fragments are not affected by the presence of polar solvents.

However, propionate type species, such as, CH_3CHCOO , and CH_3CCOO , are the most affected species in both water and 1,4-dioxane. Propionate (CH_3CH_2COO) itself, is not significantly affected by solvents; however, for example CH_3CHCOO , and CH_3CCOO adsorbs stronger by 0.15 and 0.21 eV in water, and 0.07 and 0.12 in 1,4-dioxane. Propionate type intermediates later go through C-C bond dissociation and form CO_2 and consequently, are the important intermediates in the decarboxylation

mechanism. Considering that these intermediates were stabilized significantly, an increase in the activity of decarboxylation mechanism is expected.

Finally, CO adsorbs quite stronger in water by 0.08 eV and 0.07 eV in 1,4-dioxane, and our model predicts that adsorbed H atoms adsorb stronger by just 0.01 eV in both water and 1,4-dioxane.

The overall effects of the changes in the stability of adsorbed intermediates on the kinetic of the HDO of methyl propionate, can be understood better by calculating the changes in the reaction parameters such as reaction energy and activation barrier. In the following section, we will explain the effects of solvents on elementary processes.

8.3.2 Solvent Effects on Reactions

Uneven effects of solvent on the free energy of reactant and product states of an elementary reaction can change the free energy of reaction (ΔG_{rxn}) of that elementary step. Similarly, for reactions with reactant-like transition states we do not expect to see a change in the activation barriers; however, uneven changes in the free energy of reactant and transition states results in an alteration of the activation barrier.

The solvent effects on the free energy of activation and free energy of reaction for all elementary steps involved in the HDO of methyl propionate, at temperature of 473 K are presented in Table 8.2.

We previously[202] studied the network of reactions, shown in Table 8.2, under gas-phase conditions, where with the help of sensitivity analysis, we found out that the rate-controlling step are dehydrogenation steps such as, dehydrogenation of α-, β-, and methoxy-end carbons in methyl propionate (Step 3, 4, and 5 respectively), as well as

propanoyl-methoxy type dissociations such as, Step2 ($CH_3CH_2COOCH_3$** + 2*↔ CH_3CH_2CO*** + CH_3O*) and Step 12 ($CH_2CHCOOCH_3$*** + 1* ↔ CH_2CHCO*** +CH_3O*).

In the previous section, we showed that some of the intermediates involved in the rate-controlling steps have been affected in the presence of water and 1,4-dioxane, and we expect some changes in the free energy of activation and reaction of rate-controlling steps that perhaps will affect the overall kinetic of the reaction. Additionally, it is possible that in water or 1,4-dioxane, some reactions that are not kinetically important in the absence of solvent, become competitive and consequently, influential in the overall kinetic.

The free energy reaction and activation in methyl propionate dehydrogenation steps (Step 3-5), were not affected in the presence of water, since methyl propionate (reactant state), the dehydrogenated products, and transition states for these steps, are stabilized uniformly. However, in 1,4-dioxane, we showed that methyl propionate adsorbs stronger by 0.14 eV (Table 8.1), while the adsorption strength of its dehydrogenated intermediates such as $CH_3CHCOOCH_3$, $CH_2CH_2COOCH_3$, and $CH_3CH_2COOCH_2$ were enhanced by 0.06, 0.06, and 0.05 eV respectively. The unalike changes in the free energy of methyl propionate and its dehydrogenated derivatives resulted in an increase in the free energy of reaction for the dehydrogenation steps. For example, the ΔG_{rxn} of the dehydrogenation of α-carbon (Step 3) increased by 0.07 eV , and the activation barrier of this step became greater by 0.08 eV. Dehydrogenation of β-carbon (Step4) in the presence of 1,4-dioxane, is also less exothermic by 0.06 eV, and has a higher barrier by 0.05 eV. Similarly, the ΔG_{rxn} and activation barrier of

dehydrogenation of the methoxy-end carbon (Step 5) have increased by 0.08 and 0.06 eV respectively.

Propanoyl-methoxy type dissociations are also rate-controlling, and in these reactions, methyl propionate type reactants decompose to propanoyl-type reactants and methoxy (E.g. Step 2: $CH_3CH_2COOCH_3$** + 2*↔ CH_3CH_2CO*** + CH_3O*) . We showed that methyl propionate and its derivative were stabilized in the presence of both water and 1,4-dioxane, while propanoyl type intermediates were rarely affected by the presence of solvents. Additionally, methoxy is destabilized (adsorbs weaker on Pd surface) in the presence of water and 1,4-dioxane by 0.04 and 0.01 eV respectively. The overall changes show that the reactant states of Propanoyl-methoxy type dissociations is stabilized while the product states are destabilized which leads to an increase of the ΔG_{rxn} of these reactions. For example in water, the endergonicity of Step2 ($CH_3CH_2COOCH_3$** + 2*↔ CH_3CH_2CO*** + CH_3O*) was increased by 0.17 eV , and its barrier became greater by 0.01 eV.

Similarly, in 1,4-dioxane, this step has become more endergonic by 0.16 eV and the its activation barrier has increased by 0.10 eV.

The ΔG_{rxn} of Step 12 ($CH_2CHCOOCH_3$*** + 1* ↔ CH_2CHCO*** +CH_3O*) in water, has increased by 0.09 eV, and its barrier became greater by just 0.01 eV. However, in 1,4-dioxane the ΔG_{rxn} was increased by just 0.04 eV, because, $CH_2CHCOOCH_3$ in water was more stabilized than 1,4-dioxane and additionally, methoxy of the product states is more destabilized in water. Overall, we can see in Table 8.2 that this trend stays the same for all propanoyl-methoxy type dissociation such as, Step 2, Step12, Step 17, Step 21, that are more affected in water than1,4-dioxane.

The increase in the endergonicity and activation barriers of the rate-controlling steps, such dehydrogenation steps and propanoyl-methoxy type dissociations can lower the overall activity; while, in contrast, the stronger adsorption of methyl propionate in water and 1,4-dioxane can improve the activity. With the aim of a microkinetic model, the overall effects of these opposite changes on the turnover frequencies and reaction mechanism are discussed in the section 8.3.3.

Finally, we see that dehydrogenation of propionate to CH_3CHCOO and eventually CH_3CCOO (Step 61 and Step 63) are facilitated significantly both in water and 1,4-dioxane. For example, The activation barrier of Step 61 is decreased by 0.24 eV, and its exergonicity increased by 0.17 eV. Similarly, the ΔG_{rxn} of this step decreased by 0.05 eV and its barrier was lowered by 0.09 eV in 1,4-dioxane. These steps play an important role in the decarboxylation mechanism, as propionate and its dehydrogenated derivatives will finally go through C-C bond cleavage to form CO_2. However, our previous results suggests that decarboxylation mechanism are not the dominant mechanism, since the propionate-methyl type bond dissociations which are the most important step in the DCX mechanism, are very difficult and have a remarkably higher barrier than propanoyl-methoxy bond dissociations which are the essential reaction for decarbonylations. Consequently, even though further activation of propionate is facilitated on the Pd surface, probably reaction will not proceed via production of propionate, and consequently, we do not expect that Step 61 or 63 become influential in the kinetic.

8.3.3 MICROKINETIC MODEL

We previously[202] developed a mean-field microkinetic model for the reaction mechanism of HDO of methyl propionate over Pd (111) model surface under gas-phase conditions. In this study, we have developed a similar mean-field microkinetic model for the HDO of methyl propionate over Pd (111) model surfaces in the presence of 1,4-dioxane and water and under the reaction conditions equivalent to the conditions of our previous study. All calculations were carried out at 473 K and partial pressures of propionic acid and H_2 of 0.01 and 0.2 bar, respectively.[159] The partial pressures of CO_2, and CO were set to 0.001 bar which corresponds to approximately 10% conversion. It is noted that our results and conclusions seem to be insensitive to the reaction conditions. Next, we note that a method similar to Grabow *et al.[146]* was used for determining coverage dependent adsorption energies of CO, H, and CH_3C. More details about the lateral interactions used in the microkinetic model for this study can be found in the supporting information of our previously published paper.

In the absence of solvent, we found out that the most abundant surface intermediates were adsorbed hydrogen, CO, and CH_3C with surface coverages of 67%, 20%, and 7% respectively (the free site coverage is 6%). The overall TOF was calculated to be 3.42×10^{-7} s^{-1}. Decarbonylation was identified to be the dominant mechanism (dominant pathway: $CH_3CH_2COOCH_3 \rightarrow CH_3CHCOOCH_3 \rightarrow CH_2CHCOOCH_3 \rightarrow CH_2CHCO+OCH_3 \rightarrow \ldots \rightarrow CH_3CH_3+CO+CH_3OH$), and the TOF of decarboxylation pathways were at least 3 orders of magnitude smaller than decarbonylation pathways. A schematic of our previous result is

shown in Figure 8.1, and TOFs of all elementary steps in the presence and absence of solvents are presented in Table 8.3.

The calculated rate constants and turnover frequency of all elementary steps in the HDO of methyl propionate over Pd (111) model surfaces, in the absence and presence of solvents are presented in Table 8.3 and 8.4.

LIQUID WATER EFFECTS:

The overall turnover frequency was calculated to be 1.64×10^{-8} s^{-1} which is an order of magnitude smaller than the gas-phase TOF (3.42×10^{-7} s^{-1}). In the most dominant pathway, methyl propionate goes through dehydrogenation of α-, and β-carbon to form $CH_2CHCOOCH_3$. $CH_2CHOOCH_3$ will go through C-O bond dissociation to form CH_2CHO and methoxy (CH_3O). Next, methoxy gets hydrogenated to methanol and CH_2CHO goes through hydrogenation and finally C-C cleavage to form C_2 hydrocarbons and CO ($CH_3CH_2COOCH_3 \rightarrow CH_3CHCOOCH_3 \rightarrow CH_2CHCOOCH_3 \rightarrow CH_2CHCO+OCH_3 \rightarrow \ldots \rightarrow CH_3CH_3+CO+CH_3OH$). This pathway is identical to the dominant pathway in the absence of water. A schematic of the TOFs of the important reaction pathways in the presence of water is shown in Figure 8.1.

The most abundant surface intermediates were hydrogen, CO, and CH_3C with surface coverages of 70%, 19%, and 10% respectively.

The decrease in the rate of the reaction in the presence of water can be explained by not only the fact that some of the rate-controlling steps are inhibited in water, but also the decrease in the availability of free sites. We saw that adsorption strength of single

hydrogen atom was barely affected in the presence of water, while according to Table 8.1, CO is stabilized by 0.07 eV. One at first might expect an increase in the coverage of CO and decrease in the coverage of H. In contrast, our results show that the coverage of H is increased by 3% and the coverage of CO slightly decreased to 19% (from 20% in the absence of solvent). Additionally, the coverage of CH_3C is increased to 10% (from 7% in the absence of water). The increase in the coverage of CH_3C was expected, since the formation of CH_3C was enhanced due to increase in the exergonicity of Step 37 ($CH_3CCO^{***} \leftrightarrow CH_3C^* + CO^* + 1^*$) by 0.06 eV in water . The opposite behavior of H and CO can be explained by the fact that adsorption energy of these intermediates is dependent on the coverage of these intermediates and other surface abundant intermediates. We note that Table 8.1 shows the adsorption energy of single atoms/molecules; however, the adsorption energy of surface abundant intermediates is different than single adsorbates due to lateral interactions between adsorbed molecules. Our previous adsorption energy analysis for coverage dependent intermediates shows that there are attractive interactions between CH_3C and H while there are repulsive forces between CH_3C and CO. As the result of attractive forces between H and CH_3C, an increase in the coverage of CH_3C, makes the adsorption of hydrogen more favored thermodynamically and that's why the coverage of H was increased. However, due to repulsive interactions between CO and CH_3C the coverage of CO molecules was not increased.

Finally, in the presence of water, DCN mechanism is the dominant mechanism. In the absence of water the ratio of the TOF of the dominant decarboxylation pathway ($CH_3CH_2COOCH_3 \rightarrow CH_3CH_2COOCH_2 \rightarrow$

$CH_3CH_2COO+CH_2 \rightarrow \ldots \rightarrow CH_3CH_3+CO_2+CH_4$) to the overall TOF was 0.001, but as we expected due to facilitation of dehydrogenation of propionate and its derivative, decarboxylation pathway are now more competitive and this ratio in the presence of water was increased to 0.013. However, it shows that the TOF of decarboxylation mechanisms are still 2 orders of magnitude smaller than decarbonylation pathways.

LIQUID 1,4-DIOXANE EFFECTS:

The overall turnover frequency of the HDO of methyl propionate over Pd (111) in the presence of 1,4-dioxane was calculated to be 2.86×10^{-7} s^{-1}. The most abundant surface intermediates were hydrogen, CO, and CH_3C with surface coverages of 66%, 21%, and 8% respectively, and the coverage of free sites was 4%.

A schematic of the TOFs of the important reaction mechanisms in the presence of 1,4-dioxane is shown in Figure 8.2. The dominant reaction mechanism is the same as gas-phase and water ($CH_3CH_2COOCH_3 \rightarrow CH_3CHCOOCH_3 \rightarrow CH_2CHCOOCH_3 \rightarrow CH_2CHCO+OCH_3 \rightarrow \ldots \rightarrow CH_3CH_3+CO+CH_3OH$). The TOF in 1,4-Dioxane is an order of magnitude larger than water which emphasizes that, perhaps stronger adsorption of methyl propionate in dioxane, as well as a lesser increase in the endergonicity and activation barriers of propanoyl-methoxy bond dissociation led to a higher activity in dioxane. The solvent effects on the elementary reactions were more significant in water which led to a remarkable deviation from the gas-phase.

Finally, as we explained in section, in 1,4-dioxane , influential reactions in the DCX mechanism, such as dehydrogenation of propionate or CH_3CHCOO (Step 61and

63) were less facilitated thermodynamically; hence, in contrast to water, the TOF of DCX mechanism was not increased remarkably, and the ratio of the TOF of the most dominant DCX mechanism to the overall TOF in 1,4-dioxane was calculated to be 0.004. This ratio in the presence of water and absence of solvent was 0.013 and 0.004 respectively.

8.3.4 Apparent Activation Barrier, Reaction Orders, and Sensitivity Analysis

Absence of solvent:

The following information for the apparent activation barrier, reaction orders and sensitivity analysis of the HDO of methyl propionate over Pd (111) in the absence of water and 1,4-dioxane, have been thoroughly discussed in our previous work. However, in order to investigate the effects of solvents on these kinetic parameters, we briefly present the gas-phase information and compare them with the results of water, and 1,4-dioxane.

The apparent activation barrier was computed in the temperature range of 423 to 523 K.

$$E_a = RT^2\left(\frac{\partial \ln(r)}{\partial T}\right)_{p_i} \tag{8.11}$$

In the absence of solvent, our model predicts an apparent activation energy of 1.01 eV.

The reaction order with respect to hydrogen was calculated at 473 K in the range of 0.05 to 0.4 bar. Similarly, the reaction order of methyl propionate and CO were

calculated at 473 K and a pressure range of 0.005 to 0.1 bar and 0.0001 to 0.1 bar, respectively.

$$\alpha_i = \left(\frac{\partial \ln(r)}{\partial \ln(p_i)} \right)_{T, p_{j \neq i}} \tag{8.12}$$

Reaction order with respect to methyl propionate was calculated to be +1.0, which can be explained by the small methyl propionate coverage in our model. The reaction order with respect to CO is -0.49. Finally, the reaction order of H_2 is -0.07, which indicates that under the investigated reaction conditions the hydrogen coverage is balanced with the free site coverage such that the dehydrogenation rates prior to decarbonylation are balanced with the hydrogenation processes required for desorption of the reaction products.

To understand the sensitivity of our model and to determine rate controlling steps and intermediates in the mechanism, we computed Campbell's degrees of rate and thermodynamic control,[147-149, 245] X_{RC} and X_{TRC}.

$$X_{\mathrm{RC},i} = \frac{k_i}{r} \left(\frac{\partial r}{\partial k_i} \right)_{K_i, k_{j \neq i} k_i}, \qquad X_{\mathrm{TRC},n} = \frac{1}{r} \left(\frac{\partial r}{\partial \left(\frac{-G_n^0}{RT} \right)} \right)_{G_{m \neq n}^0, G_i^{0,\mathrm{TS}}} \tag{8.13}$$

where r is the overall rate of reaction, k_i is the forward rate constant for step i, K_i equilibrium constant for step i, R is the gas constant, T denotes the reaction temperature, and $G_n{}^0$ is the free energy of adsorbate n. We note that that the degree of rate control for a single rate-determining step in a reaction mechanism is one; and, for transition and intermediate states that do not influence the overall activity, the degrees of thermodynamic and rate control are zero. The most controlling steps were identified to be

propanoyl-methoxy type bond dissociation and dehydrogenation of α-, β-, and methoxy-end carbons of methyl propionate. Reaction 2 ($CH_3CH_2COOCH_3$** + 2*↔ CH_3CH_2CO*** + CH_3O*), propanoyl-methoxy dissociation, is the most rate-controlling C-O bond dissociation step with the X_{RC} of 0.17. Additionally, Reaction 12 ($CH_2CHCOOCH_3$*** + 1* ↔ CH_2CHCO*** +CH_3O*) and Reaction 28 ($CH_3CH_2COOCH_2$*** + 3* ↔ CH_3CH_2CO*** + OCH_2***) are also rate-controlling with the X_{RC} of 0.09 and 0.02 respectively, such that the sum of C-O rate-control is 0.28. Dehydrogenation of the α-carbon of methyl propionate (Reaction 2) is the most rate-controlling dehydrogenation step with an X_{RC} of 0.35. Dehydrogenation of the methoxy-end carbon of methyl propionate (Reaction 5) has an X_{RC} of 0.19, and finally, dehydrogenation of the β-carbon of methyl propionate (Reaction 4) and also dehydrogenation of the β-carbon of $CH_3CHCOOCH_3$*** (Reaction 8: $CH_3CHCOOCH_3$*** + 1* ↔ $CH_2CHCOOCH_3$*** + H*) have a X_{RC} of 0.05 and 0.03 respectively.

LIQUID WATER

In the presence of water, our model predicts an apparent activation energy of 2.40 eV for the HDO of methyl propionate over Pd (111) model surfaces. In the absence of water, the apparent activation barrier was calculated to be 1.01 eV. In both the presence and absence of water, the apparent activation barrier is higher than the activation barrier of the rate-controlling steps which are in the range of 0.8 to 0.9 eV. This can be explained with a crowded surface that becomes less crowded at higher temperatures, leading to a further increase in the reaction rate. Considering that in the presence of water, surface is

even more crowded with hydrogen and CH_3C, the apparent activation energy is significantly higher than gas-phase condition.

In the presence of water our model still predicts a reaction order of +1.0 with respect to methyl propionate. This can be expected due to endergonicity of adsorption of methyl propionate, ($\Delta G_{ads\text{-}water}$= 0.36) and consequently, week adsorption and low coverage of methyl propionate on Pd. Reaction order with respect to CO was calculated to be -0.19. This value in the absence of water was -0.49 which emphasizes that in water, the poisoning effects of CO was reduced. We also previously showed that in the presence of water, the coverage of CO slightly decreased. In the absence of water, the reaction order with respect to hydrogen was -0.07. Due to an increase in the errors/noises in our model at very small values of TOFs in water (~10^{-20}- 10^{-8} s^{-1}), we were not able to obtain a converged value for the reaction order of H_2. However, we expect that the reaction order of hydrogen in water to be even more negative than the gas-phase value, -0.07, because, in the presence of water, the coverage of hydrogen was increased to 70%, and due to abundance of hydrogen, a smaller reaction order of hydrogen is expected.

The rate-controlling steps in the presence of water are still dehydrogenation steps, as well as, propanoyl-methoxy type dissociation. However, the values of the degree of rate control of these steps, which indicates the importance of a step in the overall kinetic, were altered in water.

For the convenience in comparison with gas-phase values, in the following the degrees of rate control of controlling steps in gas-phase are shown in [ ] next to the water values.

The rate-controlling dehydrogenation steps in water are Step 3 ($CH_3CH_2COOCH_3$** + 2* ↔ $CH_3CHCOOCH_3$*** + H*) with X_{RC} of 0.14 [0.35], Step 4 ($CH_3CH_2COOCH_3$** + 2* ↔ $CH_2CH_2COOCH_3$*** + H*) with X_{RC} of 0.04 [0.05], and Step5 ($CH_3CH_2COOCH_3$** + 2* ↔ $CH_3CH_2COOCH_2$*** + H*) with X_{RC} of 0.07 [0.19]. Clearly, in the presence of water, the importance of the dehydrogenation steps in the kinetic and activity of HDO of methyl propionate was decreased significantly. This can be explained by the fact that the propanoyl-methoxy type dissociations were inhibited in water, and the activity of methyl propionate in water is more limited by activation of propanoyl-methoxy type C-O bond dissociation than dehydrogenation steps.

Degree of rate-control analysis also confirms that propanoyl-methoxy type dissociations are more influential in water. Step 2 ($CH_3CH_2COOCH_3$** + 2*↔ CH_3CH_2CO*** + CH_3O*) has an X_{RC} of 0.21 [0.17]. The X_{RC} of Step12 ($CH_2CHCOOCH_3$*** + 1* ↔ CH_2CHCO*** +CH_3O*) was calculated to be 0.23 [0.09], and finally Step 28 ($CH_3CH_2COOCH_2$*** + 3* ↔ CH_3CH_2CO*** + OCH_2***) has the X_{RC} of 0.13 [0.02].

Finally, the degree of thermodynamic rate-control for CO was calculated to be -0.20 [-0.57] which indicates that the CO is less important in the overall activity and perhaps, hydrogen, is limiting the activity due to higher coverage on the surface. However, due to the same reason explained for calculation of hydrogen reaction order, we were not able to calculate the degree of thermodynamic rate-control of H.

LIQUID WATER

In contrast to water, 1,4-dioxane shows a very similar activity to gas-phase condition. In the presence of 1,4-dioxane, dehydrogenation steps were inhibited (Section 8.3.3) and the propanoyl-methoxy type dissociations were not affected as significant as water. Consequently, the overall kinetic is limited by the dehydrogenation step. For example, dehydrogenation steps such Step 3 ($CH_3CH_2COOCH_3$** + 2* ↔ $CH_3CHCOOCH_3$*** + H*), Step 4 ($CH_3CH_2COOCH_3$** + 2* ↔ $CH_2CH_2COOCH_3$*** + H*), and Step5 ($CH_3CH_2COOCH_3$** + 2* ↔ $CH_3CH_2COOCH_2$*** + H*) have the X_{RC} of 0.29 [0.34], 0.07 [0.05], and 0.18 [0.19] respectively (the numbers in the [ ] are the X_{RC} values in the absence of solvent).

Additionally, propanoyl-methoxy type dissociations such as Step 2 ($CH_3CH_2COOCH_3$** + 2*↔ CH_3CH_2CO*** + CH_3O*) , Step12 ($CH_2CHCOOCH_3$*** + 1* ↔ CH_2CHCO*** +CH_3O*), and Step 28 ($CH_3CH_2COOCH_2$*** + 3* ↔ CH_3CH_2CO*** + OCH_2***) have the X_{RC} of 0.10 [17], 0.09 [0.12], and 0.04[0.02] respectively.

We see that in the presence of 1,4-dioxane, similar to gas-phase condition, dehydrogenation steps are more kinetically influential than C-O bond dissociations, and overall, the important parameters in the kinetic are very similar in presence and absence of 1,4-dioxane.

Similar to gas-phase and water results, the reaction order with respect to methyl propionate was calculated to be +1.0, while the reaction orders of CO and H_2 were predicted to be -0.48 [-0.49], and -0.11 [0.07] which are very similar to the results for the

absence of solvent. Additionally, an apparent activation energy of 1.49 eV was obtained in the presence of 1,4-dioxane.

Finally, the X_{TRC} of CO and H shows also a similar trend to the gas-phase, where CO with X_{RC} of -0.75 is one of the influential intermediates in the activity while stabilizing or destabilizing adsorbed H atoms does not change the overall TOF remarkably as the X_{RC} of this intermediate is -0.05. We note that while the trend of the thermodynamic degrees of rate-control in1,4-dioxane is very similar to gas-phase results, it is in contrast with water results where adsorbed H plays a more important role in the activity and CO is less influential.

8.4. *CONCLUSION*

The effects of water and 1,4-dioxane on the hydrodeoxygenation of methyl propionate was investigated over Pd (111) model surfaces. The effects of solvent on the adsorption strength of intermediates, and also reaction parameters of elementary steps were quantified by using an implicit solvation scheme, and a microkinetic model was developed to study the reaction mechanism in different reaction media. The overall activity of 1,4-Dioxane was higher than water. Decarbonylation mechanism was identified to be the most dominant mechanism in all reaction media; however, in the presence of water, propionate and its hydrogenated derivatives that are the key intermediates of decarboxylation mechanism were stabilized and consequently, decarboxylation mechanism was slightly facilitated. CH_3C, H, and CO were the most abundant surface intermediates in all reaction environments. In water, the coverage of hydrogen was increased which resulted in a decrease in the coverage of free sites and

consequently, a lower turnover frequency. In both the presence and absence of solvents, dehydrogenation steps, as well as propanoyl-methoxy type dissociations were identified as the rate-controlling steps. In water, propanoyl-methoxy type dissociations have become more endergonic and their activation barriers were increased, and as a result, the overall activity was more limited by propanoyl-methoxy dissociations, and the importance of the dehydrogenation steps was diminished. In contrast, in 1,4-dioxane, and under gas-phase condition, dehydrogenation steps were more rate-controlling than propanoyl-methoxy type dissociations.

8.5. *ACKNOWLEDGEMENT*

This work has been supported by the National Science Foundation under Grant No. CBET-1159863 and in part by the USC future fuels program and USC NanoCenter. Computational resources have been provided by the National Energy Research Scientific Computing Center (NERSC) which is supported by the Office of Science of the U.S. Department of Energy and in part by XSEDE resources provided by the National Institute for Computational Sciences (NICS), Texas advanced Computing Center (TACC), and the Purdue University under grant number TG-CTS090100. Finally, computing resources from the USC NanoCenter and USC's High Performance Computing Group are gratefully acknowledged.

8.6. *TABLES*

Table 8.1. Effects of water and 1,4-dioxane on the adsorption strength of intermediates in the HDO of methyl propionate over Pd (111) model surfaces at a temperature of 473 K. Δ(ΔG) is the difference in the adsorption free energy of intermediate A, in the presence ($A(g) + * (g) \leftrightarrow A^*(g)$)and absence of solvents ($A(g) + * (l) \leftrightarrow A^*(l)$).

Reaction	Water	1,4-Dioxane
	Δ(ΔG)	Δ(ΔG)
$CH_3CH_2COOCH_3$**	-0.09	-0.14
$CH_3CHCOOCH_3$***	-0.08	-0.06
$CH_3CH_2COOCH_2$***	-0.12	-0.05
$CH_2CH_2COOCH_3$***	-0.09	-0.06
$CH_2CHCOOCH_3$***	-0.09	-0.05
$CH_3CHCOOCH_2$***	-0.13	-0.06
$CH_2CH_2COOCH_2$***	-0.17	-0.10
$CH_2CHCOOCH_2$****	-0.17	-0.09
$CHCHCOOCH_3$****	-0.11	-0.06
CH_3CH_2CO***	0.04	0.00
CH_3CHCO***	-0.01	-0.01
CH_2CH_2CO***	0.00	0.00
CH_3CCO***	-0.02	-0.02
CH_2CHCO***	-0.03	-0.02
$CHCHCO$****	-0.04	-0.01
CH_3CH_2COO**	0.01	-0.03
CH_3CHCOO***	-0.15	-0.07
CH_3CCOO***	-0.21	-0.12
CH_3OH*	-0.07	-0.06
CH_3O*	0.04	0.01
CH_2O***	-0.03	-0.02

CHO^{***}	0.01	0.01
$COOCH_3^{***}$	-0.05	-0.03
$COOCH_2^{****}$	-0.02	-0.02
$CH_3CH_3^{*}$	0.03	0.00
$CH_3CH_2^{*}$	0.03	0.01
CH_3CH^{**}	0.00	0.00
$CH_2CH_2^{**}$	0.02	0.01
CH_2CH^{***}	0.00	0.00
CH_3C^{***}	0.00	-0.01
CH_2C^{**}	-0.02	-0.01
$CHCH^{***}$	-0.02	0.00
CH_4^{*}	0.04	0.02
CH_3^{*}	0.03	0.02
CH_2^{**}	0.02	0.02
CO^{*}	-0.08	-0.07
CO_2^{*}	0.02	0.00
H^{*}	-0.01	-0.01
OH^{*}	-0.05	-0.03
H_2O^{*}	-0.12	-0.07

Table 8.2. Reaction free energies in eV for all elementary reaction steps in the hydro-deoxygenation of methyl propionate over Pd (111) model surfaces at a temperature of 473 K, in the presence and absence of water and 1,4-dioxane.

	Reaction	Gas		Water		1,4-Dioxane	
		ΔG_{rxn}	$\Delta G^{\ddagger}$	ΔG_{rxn}	$\Delta G^{\ddagger}$	ΔG_{rxn}	$\Delta G^{\ddagger}$
1	$CH_3CH_2COOCH_3$** + 1* ↔ CH_3CH_2COO** + CH_3*	-0.47	1.57	-0.35	1.55	-0.35	1.61
2	$CH_3CH_2COOCH_3$** + 2*↔ CH_3CH_2CO*** + CH_3O*	0.20	0.79	0.37	0.80	0.35	0.89
3	$CH_3CH_2COOCH_3$** + 2* ↔ $CH_3CHCOOCH_3$*** + H*	-0.02	0.74	-0.02	0.74	0.05	0.82
4	$CH_3CH_2COOCH_3$** + 2* ↔ $CH_2CH_2COOCH_3$*** + H*	0.16	0.84	0.14	0.80	0.22	0.89
5	$CH_3CH_2COOCH_3$** + 2* ↔ $CH_3CH_2COOCH_2$*** + H*	0.09	0.78	0.05	0.75	0.17	0.84
6	$CH_3CHCOOCH_3$*** + 1* ↔ CH_3CHCOO*** + CH_3*	-0.04	1.63	-0.08	1.58	-0.03	1.61
7	$CH_3CHCOOCH_3$*** + 1* ↔ CH_3CHCO*** + CH_3O*	0.24	0.74	0.35	0.80	0.30	0.78
8	$CH_3CHCOOCH_3$*** + 1* ↔ $CH_2CHCOOCH_3$*** + H*	-0.43	0.50	-0.46	0.46	-0.44	0.49
9	$CH_3CHCOOCH_3$*** + 1* ↔ $CH_3CHCOOCH_2$*** + H*	0.03	0.80	-0.04	0.75	0.01	0.79
10	$CH_2CHCOOCH_3$*** + 2* ↔ $CH_2CHCOOCH_2$**** + H*	0.18	0.99	0.08	0.91	0.13	0.97
11	$CH_2CHCOOCH_3$*** + 2* ↔ $CHCHCOOCH_3$**** + H*	0.07	0.87	0.03	0.82	0.05	0.84

12	$CH_2CHCOOCH_3$*** + 1* ↔ CH_2CHCO*** +CH_3O*	0.37	0.91	0.46	0.92	0.41	0.92
13	$CH_3CHCOOCH_2$*** + 2* ↔ $CH_2CHCOOCH_2$**** + H*	-0.28	0.43	-0.33	0.42	-0.32	0.44
14	$CH_3CHCOOCH_2$*** + 3* ↔ CH_3CHCO*** + OCH_2***	-0.24	0.46	-0.15	0.52	-0.21	0.49
15	$CHCHCOOCH_3$**** + 2* ↔ CHCH*** + $COOCH_3$***	-0.10	0.90	-0.02	0.89	-0.06	0.88
16	$CH_2CHCOOCH_2$**** + 3* ↔ CH_2CH*** + $COOCH_2$****	-0.04	0.95	0.07	0.99	0.02	0.97
17	$CH_2CHCOOCH_2$**** + 2* ↔ CH_2CHCO*** + OCH_2***	-0.27	0.41	-0.16	0.44	-0.22	0.43
18	$CH_2CH_2COOCH_3$*** + 1* ↔ $CH_2CHCOOCH_3$*** + H*	-0.61	0.38	-0.62	0.36	-0.61	0.38
19	$CH_2CH_2COOCH_3$*** + 1* ↔ $CH_2CH_2COOCH_2$*** + H*	0.09	0.91	0.00	0.86	0.04	0.90
20	$CH_2CH_2COOCH_3$*** + 2* ↔ CH_2CH_2** + $COOCH_3$***	-0.43	1.03	-0.34	1.04	-0.37	1.04
21	$CH_2CH_2COOCH_3$*** + 1* ↔ CH_2CH_2CO*** + CH_3O*	0.20	0.62	0.33	0.67	0.27	0.66
22	$CH_2CH_2COOCH_2$*** + 1* ↔ $CH_2CHCOOCH_2$**** + H*	-0.52	0.66	-0.54	0.65	-0.52	0.66
23	$CH_2CH_2COOCH_2$*** + 3* ↔ CH_2CH_2** +$COOCH_2$****	-0.63	0.89	-0.50	0.96	-0.55	0.94
24	$CH_2CH_2COOCH_2$*** + 3* ↔ CH_2CH_2CO*** + OCH_2***	-0.37	0.27	-0.24	0.33	-0.29	0.32
25	$CH_3CH_2COOCH_2$*** + 1* ↔ $CH_3CHCOOCH_2$*** + H*	-0.08	0.60	-0.11	0.62	-0.11	0.60

26	$CH_3CH_2COOCH_2$*** + 1* ↔ $CH_2CH_2COOCH_2$*** + H*	0.16	0.96	0.09	0.92	0.09	0.94
27	$CH_3CH_2COOCH_2$*** + 1* ↔ CH_3CH_2COO** + CH_2**	-0.60	0.67	-0.46	0.70	-0.57	0.67
28	$CH_3CH_2COOCH_2$*** + 3* ↔ CH_3CH_2CO*** + OCH_2***	-0.37	0.21	-0.24	0.26	-0.34	0.23
29	CH_3CH_2CO*** + 1* ↔ CH_3CHCO*** + H*	0.05	0.86	-0.01	0.79	0.02	0.85
30	CH_3CH_2CO*** ↔ CH_3CH_2* + CO* + 1*	-0.63	1.02	-0.72	1.01	-0.68	1.03
31	CH_3CHCO*** + 1* ↔ CH_2CHCO*** + H*	-0.31	0.49	-0.35	0.43	-0.33	0.48
32	CH_3CHCO*** ↔ CH_3CH** + CO*	-0.83	0.98	-0.90	0.99	-0.88	0.98
33	CH_3CHCO*** + 1* ↔ CH_3CCO*** + H*	-0.38	0.54	-0.40	0.52	-0.40	0.53
34	CH_2CHCO*** + 1* ↔ CH_2CH*** + CO*	-0.73	0.80	-0.79	0.80	-0.78	0.80
35	CH_2CHCO*** + 2* ↔ $CHCHCO$**** + H*	0.00	0.68	-0.01	0.68	0.00	0.69
36	$CHCHCO$**** ↔ $CHCH$*** + CO*	-1.11	0.59	-1.16	0.63	-1.16	0.60
37	CH_3CCO*** ↔ CH_3C* + CO* + 1*	-1.41	0.45	-1.47	0.44	-1.46	0.45
38	CH_2CH_2CO*** ↔ CH_2CH_2** + CO*	-1.25	0.73	-1.31	0.72	-1.30	0.71
39	CH_2CH_2CO*** + 1* ↔ CH_2CHCO *** + H*	-0.44	0.69	-0.48	0.66	-0.47	0.68

40	$COOCH_3*** + 2* \leftrightarrow COOCH_2*** + H*$	-0.12	0.64	-0.16	0.61	-0.13	0.64
41	$COOCH_3*** \leftrightarrow CO* + CH_3O* + 1*$	-0.62	0.54	-0.65	0.57	-0.65	0.55
42	$COOCH_3*** \leftrightarrow CO_2* + CH_3* + 1*$	-0.48	1.48	-0.41	1.40	-0.44	1.46
43	$COOCH_2**** \leftrightarrow CO* + OCH_2***$	-0.96	0.26	-1.02	0.24	-1.02	0.25
44	$COOCH_2**** \leftrightarrow CO_2* + CH_2** + 1*$	-0.38	0.89	-0.29	0.86	-0.34	0.87
45	$CHCH*** + H* \leftrightarrow CH_2CH*** + 1*$	0.29	0.82	0.31	0.84	0.30	0.83
46	$CH_2CH*** \leftrightarrow CH_2C** + H*$	-0.42	0.45	-0.45	0.44	-0.44	0.44
47	$CH_2C**+H* \leftrightarrow CH_3C** + 2*$	-0.27	0.87	-0.24	0.87	-0.26	0.87
48	$CH_2CH*** + H* \leftrightarrow CH_2CH_2** + 2*$	-0.07	0.87	-0.04	0.87	-0.05	0.88
49	$CH_2CH*** + H* \leftrightarrow CH_3CH** + 2*$	0.22	0.79	0.23	0.78	0.24	0.79
50	$CH_3C*** + H* \leftrightarrow CH_3CH** + 2*$	0.96	1.17	0.97	1.17	0.98	1.18
51	$CH_3CH** + H* \leftrightarrow CH_3CH_2* + 2*$	0.15	0.82	0.20	0.84	0.18	0.83
52	$CH_2CH_2** + H* \leftrightarrow CH_3CH_2* + 2*$	-0.44	0.45	-0.42	0.43	-0.43	0.43
53	$CH_3CH_2* + H* \leftrightarrow CH_3CH_3* + 1*$	-0.03	0.60	-0.02	0.61	-0.03	0.61

54	$CH_3O^* + 3^* \leftrightarrow CH_2O^{***} + H^*$	-0.46	0.47	-0.54	0.43	-0.50	0.46
55	$CH_2O^{***} + 1^* \leftrightarrow CHO^{***} + H^*$	-0.85	0.56	-0.83	0.58	-0.83	0.58
56	$CHO^{***} \leftrightarrow CO^* + H^* + 1^*$	-1.41	0.08	-1.50	0.09	-1.50	0.08
57	$CH_3O^* + H^* \leftrightarrow CH_3OH^* + 1^*$	0.12	0.69	0.02	0.65	0.06	0.68
58	$CH_2^{**} + H^* \leftrightarrow CH_3^* + 2^*$	0.02	0.75	0.04	0.76	0.03	0.76
59	$CH_3^* + H^* \leftrightarrow CH_4^* + 1^*$	-0.15	0.55	-0.12	0.56	-0.13	0.56
60	$CH_3CH_2COO^{**} \leftrightarrow CH_3CH_2^* + CO_2^*$	0.16	1.37	0.20	1.31	0.21	1.35
61	$CH_3CH_2COO^{**} + 2^* \leftrightarrow CH_3CHCOO^{***} + H^*$	0.44	1.28	0.26	1.04	0.39	1.19
62	$CH_3CHCOO^{***} + \leftrightarrow CH_3CH^{**} + CO_2^*$	-0.39	0.92	-0.22	0.97	-0.32	0.94
63	$CH_3CHCOO^{***} + 1^* \leftrightarrow CH_3CCOO^{***} + H^*$	-0.09	0.85	-0.17	0.75	-0.15	0.79
64	$CH_3CCOO^{***} \leftrightarrow CH_3C^* + CO_2^* + 1^*$	-1.22	0.64	-0.99	0.83	-1.11	0.73
65	$CH_3CH_2COOCH_3 + 2^* \leftrightarrow CH_3CH_2COOCH_3^{**}$	0.45	N/A	0.36	N/A	0.31	N/A
66	$CH_3CH_3 + 1^* \leftrightarrow CH_3CH_3^*$	0.62	N/A	0.64	N/A	0.61	N/A
67	$CH_2CH_2 + 2^* \leftrightarrow CH_2CH_2^{**}$	-0.14	N/A	-0.12	N/A	-0.13	N/A

68	CHCH + 3* ↔ CHCH***	-1.17	N/A	-1.18	N/A	-1.17	N/A
69	CH_4 + 1* ↔ CH_4*	0.48	N/A	0.52	N/A	0.50	N/A
70	CH_3OH + 1* ↔ CH_3OH*	0.40	N/A	0.33	N/A	0.34	N/A
71	CO + 1* ↔ CO*	-1.19	N/A	-1.27	N/A	-1.25	N/A
72	CO_2 + 1* ↔ CO_2*	0.52	N/A	0.54	N/A	0.52	N/A
73	H_2 + 2* → 2H*	-0.58	N/A	-0.61	N/A	-0.61	N/A

Table 8.3. Equilibrium and forward rate constants for the elementary steps in the HDO of methyl propionate over Pd (111) model surfaces at a temperature of 473 K, in the presence and absence of water and 1,4-dioxane.

#	Reaction	Gas		Water		1,4-Dioxane	
		K_{eq}	k_f (s^{-1})	K_{eq}	k_f (s^{-1})	K_{eq}	k_f (s^{-1})
1	$CH_3CH_2COOCH_3$** + 1* ↔ CH_3CH_2COO** + CH_3*	1.08×10^{5}	2.08×10^{-4}	4.95×10^{3}	3.03×10^{-4}	4.91×10^{3}	6.46×10^{-5}
2	$CH_3CH_2COOCH_3$** + 2*↔ CH_3CH_2CO*** + CH_3O*	7.63×10^{-3}	3.96×10^{4}	1.20×10^{-4}	2.77×10^{4}	1.69×10^{-4}	3.14×10^{3}
3	$CH_3CH_2COOCH_3$** + 2* ↔ $CH_3CHCOOCH_3$*** + H*	1.52	1.37×10^{5}	1.58	1.31×10^{5}	2.66×10^{-1}	2.04×10^{4}
4	$CH_3CH_2COOCH_3$** + 2* ↔ $CH_2CH_2COOCH_3$*** + H*	1.91×10^{-2}	1.01×10^{4}	2.89×10^{-2}	2.80×10^{4}	4.06×10^{-3}	2.95×10^{3}
5	$CH_3CH_2COOCH_3$** + 2* ↔ $CH_3CH_2COOCH_2$*** + H*	9.81×10^{-2}	5.02×10^{4}	2.77×10^{-1}	1.03×10^{5}	1.50×10^{-2}	1.11×10^{4}
6	$CH_3CHCOOCH_3$*** + 1* ↔ CH_3CHCOO*** + CH_3*	2.41	4.00×10^{-5}	7.54	1.61×10^{-4}	2.16	6.64×10^{-5}
7	$CH_3CHCOOCH_3$*** + 1* ↔ CH_3CHCO*** + CH_3O*	2.49×10^{-3}	1.30×10^{5}	1.73×10^{-4}	3.00×10^{4}	5.82×10^{-4}	5.10×10^{4}
8	$CH_3CHCOOCH_3$*** + 1* ↔ $CH_2CHCOOCH_3$*** + H*	3.98×10^{4}	4.64×10^{7}	7.06×10^{4}	1.11×10^{8}	4.66×10^{4}	6.20×10^{7}
9	$CH_3CHCOOCH_3$*** + 1* ↔ $CH_3CHCOOCH_2$*** + H*	4.89×10^{-1}	3.04×10^{4}	2.55	1.07×10^{5}	7.52×10^{-1}	3.45×10^{4}
10	$CH_2CHCOOCH_3$*** + 2* ↔ $CH_2CHCOOCH_2$**** + H*	1.27×10^{-2}	2.69×10^{2}	1.31×10^{-1}	1.84×10^{3}	4.48×10^{-2}	5.09×10^{2}
11	$CH_2CHCOOCH_3$*** + 2* ↔ $CHCHCOOCH_3$**** + H*	1.90×10^{-1}	5.29×10^{3}	4.75×10^{-1}	1.99×10^{4}	3.26×10^{-1}	1.07×10^{4}
12	$CH_2CHCOOCH_3$*** + 1* ↔ CH_2CHCO*** +CH_3O*	1.28×10^{-4}	1.98×10^{3}	1.25×10^{-5}	1.44×10^{3}	4.38×10^{-5}	1.46×10^{3}
13	$CH_3CHCOOCH_2$*** + 2* ↔ $CH_2CHCOOCH_2$**** + H*	1.03×10^{3}	2.69×10^{8}	3.62×10^{3}	3.52×10^{8}	2.77×10^{3}	2.20×10^{8}
14	$CH_3CHCOOCH_2$*** + 3* ↔ CH_3CHCO*** + OCH_2***	3.77×10^{2}	1.10×10^{8}	3.75×10^{1}	3.19×10^{7}	1.84×10^{2}	6.58×10^{7}
15	$CHCHCOOCH_3$**** + 2* ↔ CHCH*** + $COOCH_3$***	1.24×10^{1}	2.77×10^{3}	1.75	2.89×10^{3}	4.92	3.98×10^{3}
16	$CH_2CHCOOCH_2$**** + 3* ↔ CH_2CH*** + $COOCH_2$****	2.59	6.95×10^{2}	1.61×10^{-1}	2.95×10^{2}	6.20×10^{-1}	4.66×10^{2}

17	$CH_2CHCOOCH_2$**** + 2* ↔ CH_2CHCO*** + OCH_2***	7.51×10^{2}	3.84×10^{8}	5.29×10^{1}	2.08×10^{8}	2.33×10^{2}	2.78×10^{8}
18	$CH_2CH_2COOCH_3$*** + 1* ↔ $CH_2CHCOOCH_3$*** + H*	3.17×10^{6}	8.55×10^{8}	3.85×10^{6}	1.59×10^{9}	3.06×10^{6}	8.40×10^{8}
19	$CH_2CH_2COOCH_3$*** + 1* ↔ $CH_2CH_2COOCH_2$*** + H*	1.14×10^{-1}	1.93×10^{3}	9.67×10^{-1}	6.45×10^{3}	3.62×10^{-1}	2.83×10^{3}
20	$CH_2CH_2COOCH_3$*** + 2* ↔ CH_2CH_2** + $COOCH_3$***	3.87×10^{4}	9.87×10^{1}	3.80×10^{3}	8.60×10^{1}	9.87×10^{3}	7.51×10^{1}
21	$CH_2CH_2COOCH_3$*** + 1* ↔ CH_2CH_2CO*** + CH_3O*	7.44×10^{-3}	2.41×10^{6}	3.30×10^{-4}	6.42×10^{5}	1.18×10^{-3}	1.03×10^{6}
22	$CH_2CH_2COOCH_2$*** + 1* ↔ $CH_2CHCOOCH_2$**** + H*	3.52×10^{5}	8.95×10^{5}	5.22×10^{5}	1.07×10^{6}	3.78×10^{5}	9.89×10^{5}
23	$CH_2CH_2COOCH_2$*** + 3* ↔ CH_2CH_2** +$COOCH_2$****	5.74×10^{6}	3.30×10^{3}	2.18×10^{5}	5.81×10^{2}	7.25×10^{5}	1.07×10^{3}
24	$CH_2CH_2COOCH_2$*** + 3* ↔ CH_2CH_2CO*** + OCH_2***	8.44×10^{3}	1.18×10^{10}	3.30×10^{2}	2.90×10^{9}	1.35×10^{3}	4.01×10^{9}
25	$CH_3CH_2COOCH_2$*** + 1* ↔ $CH_3CHCOOCH_2$*** + H*	7.56	3.86×10^{6}	1.46×10^{1}	2.29×10^{6}	1.33×10^{1}	3.58×10^{6}
26	$CH_3CH_2COOCH_2$*** + 1* ↔ $CH_2CH_2COOCH_2$*** + H*	2.22×10^{-2}	5.89×10^{2}	1.01×10^{-1}	1.66×10^{3}	9.78×10^{-2}	1.03×10^{3}
27	$CH_3CH_2COOCH_2$*** + 1* ↔ CH_3CH_2COO** + CH_2**	2.74×10^{6}	7.28×10^{5}	7.46×10^{4}	3.13×10^{5}	1.16×10^{6}	7.94×10^{5}
28	$CH_3CH_2COOCH_2$*** + 3* ↔ CH_3CH_2CO*** + OCH_2***	8.01×10^{3}	5.37×10^{10}	3.32×10^{2}	1.81×10^{10}	3.72×10^{3}	3.49×10^{10}
29	CH_3CH_2CO*** + 1* ↔ CH_3CHCO*** + H*	3.08×10^{-1}	7.47×10^{3}	1.42	3.77×10^{4}	5.72×10^{-1}	8.50×10^{3}
30	CH_3CH_2CO*** ↔ CH_3CH_2* + CO* + 1*	4.73×10^{6}	1.36×10^{2}	4.63×10^{7}	1.54×10^{2}	1.75×10^{7}	9.26×10^{1}
31	CH_3CHCO*** + 1* ↔ CH_2CHCO*** + H*	2.06×10^{3}	5.51×10^{7}	5.10×10^{3}	2.42×10^{8}	3.50×10^{3}	8.45×10^{7}
32	CH_3CHCO*** ↔ CH_3CH** + CO*	6.68×10^{8}	3.55×10^{2}	4.13×10^{9}	2.89×10^{2}	2.35×10^{9}	3.52×10^{2}
33	CH_3CHCO*** + 1* ↔ CH_3CCO*** + H*	1.05×10^{4}	1.68×10^{7}	2.02×10^{4}	2.77×10^{7}	1.79×10^{4}	2.08×10^{7}
34	CH_2CHCO*** + 1* ↔ CH_2CH*** + CO*	6.37×10^{7}	3.06×10^{4}	2.35×10^{8}	3.17×10^{4}	2.15×10^{8}	2.91×10^{4}
35	CH_2CHCO*** + 2* ↔ $CHCHCO$**** + H*	9.03×10^{-1}	5.54×10^{5}	1.44	5.74×10^{5}	1.03	4.66×10^{5}
36	$CHCHCO$**** ↔ $CHCH$*** + CO*	7.59×10^{11}	5.57×10^{6}	2.52×10^{12}	1.96×10^{6}	2.27×10^{12}	3.92×10^{6}

37	$CH_3CCO^{***} \leftrightarrow CH_3C^* + CO^* + 1^*$	1.00×10^{15}	1.76×10^{8}	4.40×10^{15}	2.03×10^{8}	3.53×10^{15}	1.48×10^{8}
38	$CH_2CH_2CO^{***} \leftrightarrow CH_2CH_2^{**} + CO^*$	2.19×10^{13}	1.81×10^{5}	8.90×10^{13}	1.95×10^{5}	7.55×10^{13}	2.41×10^{5}
39	$CH_2CH_2CO^{***} + 1^* \leftrightarrow CH_2CHCO^{***} + H^*$	5.46×10^{4}	3.89×10^{5}	1.46×10^{5}	9.30×10^{5}	1.14×10^{5}	5.46×10^{5}
40	$COOCH_3^{***} + 2^* \leftrightarrow COOCH_2^{***} + H^*$	1.69×10^{1}	1.42×10^{6}	5.55×10^{1}	3.06×10^{6}	2.66×10^{1}	1.49×10^{6}
41	$COOCH_3^{***} \leftrightarrow CO^* + CH_3O^* + 1^*$	4.20×10^{6}	1.77×10^{7}	7.73×10^{6}	9.10×10^{6}	9.02×10^{6}	1.29×10^{7}
42	$COOCH_3^{***} \leftrightarrow CO_2^* + CH_3^* + 1^*$	1.21×10^{5}	1.87×10^{-3}	2.60×10^{4}	1.24×10^{-2}	5.35×10^{4}	2.83×10^{-3}
43	$COOCH_2^{****} \leftrightarrow CO^* + OCH_2^{***}$	1.85×10^{10}	1.75×10^{10}	7.71×10^{10}	2.58×10^{10}	8.07×10^{10}	2.33×10^{10}
44	$COOCH_2^{****} \leftrightarrow CO_2^* + CH_2^{**} + 1^*$	1.11×10^{4}	3.62×10^{3}	1.22×10^{3}	6.98×10^{3}	4.46×10^{3}	5.87×10^{3}
45	$CHCH^{***} + H^* \leftrightarrow CH_2CH^{***} + 1^*$	8.26×10^{-4}	2.03×10^{4}	4.58×10^{-4}	1.12×10^{4}	6.51×10^{-4}	1.42×10^{4}
46	$CH_2CH^{***} \leftrightarrow CH_2C^{**} + H^*$	3.07×10^{4}	1.73×10^{8}	5.72×10^{4}	2.11×10^{8}	4.55×10^{4}	2.09×10^{8}
47	$CH_2C^{**}+H^* \leftrightarrow CH_3C^{**} + 2^*$	8.27×10^{2}	5.44×10^{3}	4.07×10^{2}	5.81×10^{3}	1.23×10^{3}	6.58×10^{3}
48	$CH_2CH^{***} + H^* \leftrightarrow CH_2CH_2^{**} + 2^*$	6.28	5.64×10^{3}	2.59	5.62×10^{3}	3.09	4.43×10^{3}
49	$CH_2CH^{***} + H^* \leftrightarrow CH_3CH^{**} + 2^*$	5.10×10^{-3}	3.71×10^{4}	3.44×10^{-3}	4.77×10^{4}	3.12×10^{-3}	4.16×10^{4}
50	$CH_3C^{***} + H^* \leftrightarrow CH_3CH^{**} + 2^*$	6.32×10^{-11}	3.50	4.64×10^{-11}	3.22	3.70×10^{-11}	2.41
51	$CH_3CH^{**} + H^* \leftrightarrow CH_3CH_2^* + 2^*$	2.30×10^{-2}	1.74×10^{4}	7.89×10^{-3}	1.25×10^{4}	1.30×10^{-2}	1.48×10^{4}
52	$CH_2CH_2^{**} + H^* \leftrightarrow CH_3CH_2^* + 2^*$	2.05×10^{-5}	3.54×10^{3}	3.65×10^{-5}	1.05×10^{4}	2.91×10^{-5}	6.67×10^{3}
53	$CH_3CH_2^* + H^* \leftrightarrow CH_3CH_3^* + 1^*$	2.18	3.67×10^{6}	1.82	3.24×10^{6}	2.34	3.40×10^{6}
54	$CH_3O^* + 3^* \leftrightarrow CH_2O^{***} + H^*$	7.42×10^{4}	1.02×10^{8}	5.54×10^{5}	2.55×10^{8}	2.38×10^{5}	1.10×10^{8}
55	$CH_2O^{***} + 1^* \leftrightarrow CHO^{***} + H^*$	1.20×10^{9}	9.66×10^{6}	6.98×10^{8}	6.93×10^{6}	7.44×10^{8}	6.03×10^{6}

56	$CHO^{***} \leftrightarrow CO^{*} + H^{*} + 1^{*}$	9.35×10^{14}	1.24×10^{12}	1.05×10^{16}	1.01×10^{12}	8.78×10^{15}	1.33×10^{12}
57	$CH_3O^{*} + H^{*} \leftrightarrow CH_3OH^{*} + 1^{*}$	5.74×10^{-2}	4.23×10^{5}	6.35×10^{-1}	1.06×10^{6}	2.38×10^{-1}	5.54×10^{5}
58	$CH_2^{**} + H^{*} \leftrightarrow CH_3^{*} + 2^{*}$	6.45×10^{-1}	1.12×10^{5}	3.84×10^{-1}	8.14×10^{4}	4.51×10^{-1}	8.29×10^{4}
59	$CH_3^{*} + H^{*} \leftrightarrow CH_4^{*} + 1^{*}$	4.38×10^{1}	1.50×10^{7}	2.07×10^{1}	9.54×10^{6}	2.74×10^{1}	9.98×10^{6}
60	$CH_3CH_2COO^{**} \leftrightarrow CH_3CH_2^{*} + CO_2^{*}$	1.75×10^{-2}	2.49×10^{-2}	6.83×10^{-3}	1.21×10^{-1}	6.49×10^{-3}	3.82×10^{-2}
61	$CH_3CH_2COO^{**} + 2^{*} \leftrightarrow CH_3CHCOO^{***} + H^{*}$	2.14×10^{-5}	2.46×10^{-1}	1.52×10^{-3}	9.06×10^{1}	7.41×10^{-5}	2.12
62	$CH_3CHCOO^{***} + \leftrightarrow CH_3CH^{**} + CO_2^{*}$	1.50×10^{4}	1.41×10^{3}	2.40×10^{2}	4.14×10^{2}	2.84×10^{3}	9.04×10^{2}
63	$CH_3CHCOO^{***} + 1^{*} \leftrightarrow CH_3CCOO^{***} + H^{*}$	8.51	7.97×10^{3}	5.93×10^{1}	1.02×10^{5}	3.94×10^{1}	3.67×10^{4}
64	$CH_3CCOO^{***} \leftrightarrow CH_3C^{*} + CO_2^{*} + 1^{*}$	1.04×10^{13}	1.65×10^{6}	3.24×10^{10}	1.51×10^{4}	7.24×10^{11}	1.65×10^{5}
65	$CH_3CH_2COOCH_3 + 2^{*} \leftrightarrow CH_3CH_2COOCH_3^{**}$	1.81×10^{-5}	8.73×10^{7}	1.50×10^{-4}	8.73×10^{7}	5.61×10^{-4}	8.73×10^{7}
66	$CH_3CH_3 + 1^{*} \leftrightarrow CH_3CH_3^{*}$	2.79×10^{-7}	1.50×10^{8}	1.49×10^{-7}	1.50×10^{8}	3.03×10^{-7}	1.50×10^{8}
67	$CH_2CH_2 + 2^{*} \leftrightarrow CH_2CH_2^{**}$	2.79×10^{1}	1.55×10^{8}	2.01×10^{1}	1.55×10^{8}	2.47×10^{1}	1.55×10^{8}
68	$CHCH + 3^{*} \leftrightarrow CHCH^{***}$	2.59×10^{12}	1.61×10^{8}	3.76×10^{12}	1.61×10^{8}	2.65×10^{12}	1.61×10^{8}
69	$CH_4 + 1^{*} \leftrightarrow CH_4^{*}$	8.51×10^{-6}	2.05×10^{8}	2.88×10^{-6}	2.05×10^{8}	4.82×10^{-6}	2.05×10^{8}
70	$CH_3OH + 1^{*} \leftrightarrow CH_3OH^{*}$	5.89×10^{-5}	1.45×10^{8}	3.36×10^{-4}	1.45×10^{8}	2.38×10^{-4}	1.45×10^{8}
71	$CO + 1^{*} \leftrightarrow CO^{*}$	5.33×10^{12}	1.55×10^{8}	3.87×10^{13}	1.55×10^{8}	2.64×10^{13}	1.55×10^{8}
72	$CO_2 + 1^{*} \leftrightarrow CO_2^{*}$	2.79×10^{-6}	1.24×10^{8}	1.69×10^{-6}	1.24×10^{8}	3.04×10^{-6}	1.24×10^{8}
73	$H_2 + 2^{*} \rightarrow 2H^{*}$	1.65×10^{6}	5.80×10^{8}	3.05×10^{6}	5.80×10^{8}	3.14×10^{6}	5.80×10^{8}

Table 8.4. Calculated net rate (turnover frequency) for the elementary steps in the HDO of methyl propionate over Pd (111) model surfaces at a temperature of 473 K, in the presence and absence of water and 1,4-dioxane.

#	Reaction	Gas	Water	1,4-Dioxane
		TOF (s^{-1})	TOF (s^{-1})	TOF (s^{-1})
1	$CH_3CH_2COOCH_3$** + 1* ↔ CH_3CH_2COO** + CH_3*	6.16×10^{-15}	2.39×10^{-15}	1.39×10^{-14}
2	$CH_3CH_2COOCH_3$** + 2*↔ CH_3CH_2CO*** + CH_3O*	6.43×10^{-8}	3.79×10^{-9}	2.94×10^{-8}
3	$CH_3CH_2COOCH_3$** + 2* ↔ $CH_3CHCOOCH_3$*** + H*	1.85×10^{-7}	6.94×10^{-9}	1.46×10^{-7}
4	$CH_3CH_2COOCH_3$** + 2* ↔ $CH_2CH_2COOCH_3$*** + H*	1.39×10^{-8}	1.50×10^{-9}	2.12×10^{-8}
5	$CH_3CH_2COOCH_3$** + 2* ↔ $CH_3CH_2COOCH_2$*** + H*	7.84×10^{-8}	4.21×10^{-9}	8.93×10^{-8}
6	$CH_3CHCOOCH_3$*** + 1* ↔ CH_3CHCOO*** + CH_3*	1.34×10^{-18}	5.31×10^{-19}	2.55×10^{-18}
7	$CH_3CHCOOCH_3$*** + 1* ↔ CH_3CHCO*** + CH_3O*	4.35×10^{-9}	9.90×10^{-11}	1.96×10^{-9}
8	$CH_3CHCOOCH_3$*** + 1* ↔ $CH_2CHCOOCH_3$*** + H*	1.80×10^{-7}	6.79×10^{-9}	1.43×10^{-7}
9	$CH_3CHCOOCH_3$*** + 1* ↔ $CH_3CHCOOCH_2$*** + H*	9.01×10^{-10}	5.91×10^{-11}	1.01×10^{-9}
10	$CH_2CHCOOCH_3$*** + 2* ↔ $CH_2CHCOOCH_2$**** + H*	1.39×10^{-9}	9.37×10^{-11}	2.36×10^{-9}
11	$CH_2CHCOOCH_3$*** + 2* ↔ $CHCHCOOCH_3$**** + H*	1.25×10^{-11}	5.84×10^{-14}	1.77×10^{-11}
12	$CH_2CHCOOCH_3$*** + 1* ↔ CH_2CHCO*** +CH_3O*	1.91×10^{-7}	8.15×10^{-9}	1.61×10^{-7}
13	$CH_3CHCOOCH_2$*** + 2* ↔ $CH_2CHCOOCH_2$**** + H*	1.76×10^{-9}	4.62×10^{-10}	3.73×10^{-9}
14	$CH_3CHCOOCH_2$*** + 3* ↔ CH_3CHCO*** + OCH_2***	4.99×10^{-11}	1.67×10^{-12}	5.64×10^{-11}
15	$CHCHCOOCH_3$**** + 2* ↔ CHCH*** + $COOCH_3$***	1.25×10^{-11}	5.84×10^{-14}	1.77×10^{-11}
16	$CH_2CHCOOCH_2$**** + 3* ↔ CH_2CH*** + $COOCH_2$****	3.12×10^{-16}	1.37×10^{-17}	4.44×10^{-16}
17	$CH_2CHCOOCH_2$**** + 2* ↔ CH_2CHCO*** + OCH_2***	3.14×10^{-9}	5.56×10^{-10}	6.08×10^{-9}
18	$CH_2CH_2COOCH_3$*** + 1* ↔ $CH_2CHCOOCH_3$*** + H*	1.30×10^{-8}	1.46×10^{-9}	2.06×10^{-8}
19	$CH_2CH_2COOCH_3$*** + 1* ↔ $CH_2CH_2COOCH_2$*** + H*	7.41×10^{-13}	1.66×10^{-13}	1.58×10^{-12}
20	$CH_2CH_2COOCH_3$*** + 2* ↔ CH_2CH_2** + $COOCH_3$***	2.09×10^{-15}	8.92×10^{-17}	1.88×10^{-15}
21	$CH_2CH_2COOCH_3$*** + 1* ↔ CH_2CH_2CO*** + CH_3O*	9.33×10^{-10}	3.84×10^{-11}	5.93×10^{-10}
22	$CH_2CH_2COOCH_2$*** + 1* ↔ $CH_2CHCOOCH_2$**** + H*	-3.22×10^{-15}	2.53×10^{-15}	-3.88×10^{-15}
23	$CH_2CH_2COOCH_2$*** + 3* ↔ CH_2CH_2** +$COOCH_2$****	2.85×10^{-19}	1.43×10^{-19}	7.63×10^{-19}
24	$CH_2CH_2COOCH_2$*** + 3* ↔ CH_2CH_2CO*** + OCH_2***	1.02×10^{-12}	7.16×10^{-13}	2.86×10^{-12}
25	$CH_3CH_2COOCH_2$*** + 1* ↔ $CH_3CHCOOCH_2$*** + H*	9.07×10^{-10}	4.05×10^{-10}	2.78×10^{-9}
26	$CH_3CH_2COOCH_2$*** + 1* ↔ $CH_2CH_2COOCH_2$*** + H*	2.73×10^{-13}	5.52×10^{-13}	1.27×10^{-12}

27	$CH_3CH_2COOCH_2$*** + 1* ↔ CH_3CH_2COO** + CH_2**	3.49×10^{-10}	2.07×10^{-10}	1.03×10^{-9}
28	$CH_3CH_2COOCH_2$*** + 3* ↔ CH_3CH_2CO*** + OCH_2***	7.71×10^{-8}	3.60×10^{-9}	8.54×10^{-8}
29	CH_3CH_2CO*** + 1* ↔ CH_3CHCO*** + H*	1.05×10^{-7}	5.88×10^{-9}	9.15×10^{-8}
30	CH_3CH_2CO*** ↔ CH_3CH_2* + CO* + 1*	3.60×10^{-8}	1.50×10^{-9}	2.33×10^{-8}
31	CH_3CHCO*** + 1* ↔ CH_2CHCO*** + H*	-6.40×10^{-8}	-6.98×10^{-9}	-6.09×10^{-8}
32	CH_3CHCO*** ↔ CH_3CH** + CO*	6.71×10^{-11}	7.78×10^{-12}	6.00×10^{-11}
33	CH_3CHCO*** + 1* ↔ CH_3CCO*** + H*	1.74×10^{-7}	1.30×10^{-8}	1.54×10^{-7}
34	CH_2CHCO*** + 1* ↔ CH_2CH*** + CO*	5.95×10^{-8}	1.99×10^{-9}	5.45×10^{-8}
35	CH_2CHCO*** + 2* ↔ $CHCHCO$**** + H*	5.89×10^{-8}	-2.76×10^{-10}	3.79×10^{-8}
36	$CHCHCO$**** ↔ $CHCH$*** + CO*	5.89×10^{-8}	-2.76×10^{-10}	3.79×10^{-8}
37	CH_3CCO*** ↔ CH_3C* + CO* + 1*	1.74×10^{-7}	1.30×10^{-8}	1.54×10^{-7}
38	CH_2CH_2CO*** ↔ CH_2CH_2** + CO*	9.86×10^{-10}	5.09×10^{-11}	6.67×10^{-10}
39	CH_2CH_2CO*** + 1* ↔ CH_2CHCO*** + H*	-5.23×10^{-11}	-1.19×10^{-11}	-7.15×10^{-11}
40	$COOCH_3$*** + 2* ↔ $COOCH_2$*** + H*	3.02×10^{-15}	9.22×10^{-18}	3.87×10^{-15}
41	$COOCH_3$*** ↔ CO* + CH_3O* + 1*	1.25×10^{-11}	9.09×10^{-14}	1.77×10^{-11}
42	$COOCH_3$*** ↔ CO_2* + CH_3* + 1*	1.33×10^{-21}	1.24×10^{-22}	3.89×10^{-21}
43	$COOCH_2$**** ↔ CO* + OCH_2***	3.31×10^{-15}	-9.49×10^{-17}	4.32×10^{-15}
44	$COOCH_2$**** ↔ CO_2* + CH_2** + 1*	7.88×10^{-21}	5.55×10^{-22}	6.81×10^{-21}
45	$CHCH$*** + H* ↔ CH_2CH*** + 1*	5.90×10^{-8}	-2.76×10^{-10}	3.79×10^{-8}
46	CH_2CH*** ↔ CH_2C** + H*	-2.98×10^{-7}	-1.42×10^{-8}	-1.99×10^{-7}
47	CH_2C**+H* ↔ CH_3C** + 2*	-2.98×10^{-7}	-1.42×10^{-8}	-1.99×10^{-7}
48	CH_2CH*** + H* ↔ CH_2CH_2** + 2*	3.28×10^{-8}	5.03×10^{-9}	3.27×10^{-8}
49	CH_2CH*** + H* ↔ CH_3CH** + 2*	3.83×10^{-7}	1.09×10^{-8}	2.59×10^{-7}
50	CH_3C*** + H* ↔ CH_3CH** + 2*	-1.12×10^{-7}	-1.26×10^{-9}	-6.17×10^{-9}
51	CH_3CH** + H* ↔ CH_3CH_2* + 2*	2.72×10^{-7}	9.65×10^{-9}	2.53×10^{-7}
52	CH_2CH_2** + H* ↔ CH_3CH_2* + 2*	3.22×10^{-8}	4.89×10^{-9}	8.20×10^{-9}
53	CH_3CH_2* + H* ↔ CH_3CH_3* + 1*	3.40×10^{-7}	1.63×10^{-8}	2.85×10^{-7}
54	CH_3O* + 3* ↔ CH_2O*** + H*	1.44×10^{-8}	1.06×10^{-11}	4.53×10^{-9}
55	CH_2O*** + 1* ↔ CHO*** + H*	9.47×10^{-8}	4.17×10^{-9}	9.61×10^{-8}
56	CHO*** ↔ CO* + H* + 1*`	9.47×10^{-8}	4.17×10^{-9}	9.61×10^{-8}

57	$CH_3O^* + H^* \leftrightarrow CH_3OH^* + 1^*$	2.47×10^{-7}	1.21×10^{-8}	1.89×10^{-7}
58	$CH_2^{**} + H^* \leftrightarrow CH_3^* + 2^*$	3.49×10^{-10}	2.07×10^{-10}	1.03×10^{-9}
59	$CH_3^* + H^* \leftrightarrow CH_4^* + 1^*$	3.49×10^{-10}	2.07×10^{-10}	1.03×10^{-9}
60	$CH_3CH_2COO^{**} \leftrightarrow CH_3CH_2^* + CO_2^*$	3.47×10^{-10}	2.04×10^{-10}	1.02×10^{-9}
61	$CH_3CH_2COO^{**} + 2^* \leftrightarrow CH_3CHCOO^{***} + H^*$	1.99×10^{-12}	2.18×10^{-12}	1.24×10^{-11}
62	$CH_3CHCOO^{***} + \leftrightarrow CH_3CH^{**} + CO_2^*$	1.52×10^{-12}	4.39×10^{-13}	4.49×10^{-12}
63	$CH_3CHCOO^{***} + 1^* \leftrightarrow CH_3CCOO^{***} + H^*$	4.71×10^{-13}	1.74×10^{-12}	7.90×10^{-12}
64	$CH_3CCOO^{***} \leftrightarrow CH_3C^* + CO_2^* + 1^*$	4.71×10^{-13}	1.74×10^{-12}	7.90×10^{-12}
65	$CH_3CH_2COOCH_3 + 2^* \leftrightarrow CH_3CH_2COOCH_3^{**}$	3.42×10^{-7}	1.64×10^{-8}	2.86×10^{-7}
66	$CH_3CH_3 + 1^* \leftrightarrow CH_3CH_3^*$	3.40×10^{-7}	1.63×10^{-8}	2.85×10^{-7}
67	$CH_2CH_2 + 2^* \leftrightarrow CH_2CH_2^{**}$	1.56×10^{-9}	1.89×10^{-10}	3.39×10^{-10}
68	$CHCH + 3^* \leftrightarrow CHCH^{***}$	5.29×10^{-14}	3.08×10^{-15}	1.53×10^{-15}
69	$CH_4 + 1^* \leftrightarrow CH_4^*$	3.49×10^{-10}	2.07×10^{-10}	1.03×10^{-9}
70	$CH_3OH + 1^* \leftrightarrow CH_3OH^*$	2.47×10^{-7}	1.21×10^{-8}	1.89×10^{-7}
71	$CO + 1^* \leftrightarrow CO^*$	Equilibrium	Equilibrium	Equilibrium
72	$CO_2 + 1^* \leftrightarrow CO_2^*$	3.49×10^{-10}	2.07×10^{-10}	1.03×10^{-9}
73	$H_2 + 2^* \rightarrow 2H^*$	Equilibrium	Equilibrium	Equilibrium

8.7. *FIGURES*

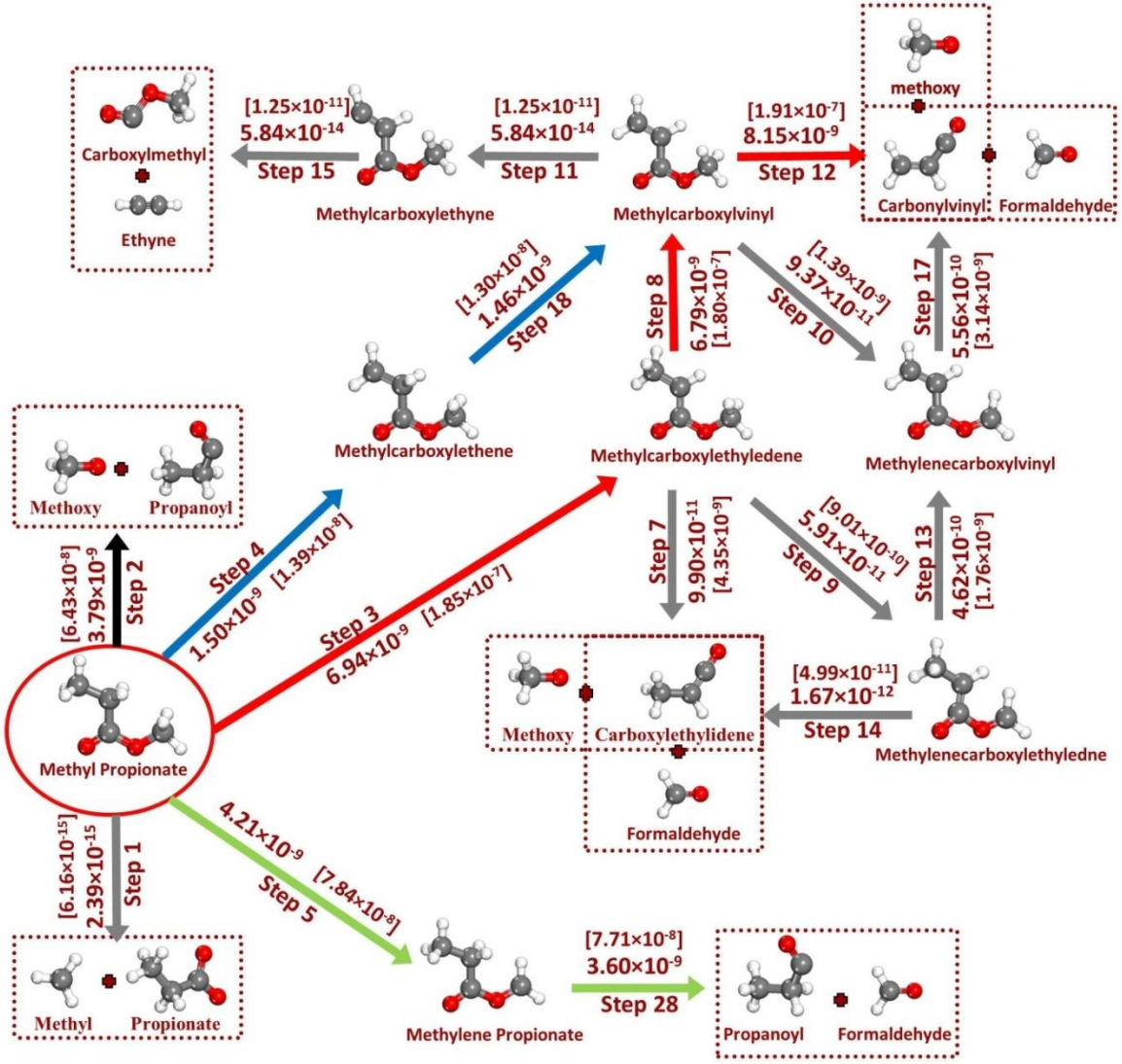
Carboxylmethyl
Ethyne
[1.25×10-11]
5.84×10-14
Step 15
Methylcarboxylethyne
[1.25×10-11]
5.84×10-14
Step 11
Methylcarboxylvinyl
[1.91×10-7]
8.15×10-9
Step 12
methoxy
Carbonylvinyl
Formaldehyde
[1.30×10-8]
1.46×10-9
Step 18
Methylcarboxylethene
Step 8
6.79×10-9
[1.80×10-7]
Methylcarboxylethyledene
[1.39×10-9]
9.37×10-11
Step 10
Step 17
5.56×10-10
[3.14×10-9]
Methylenecarboxylvinyl
Methoxy
Propanoyl
[6.43×10-8]
3.79×10-9
Step 2
Step 4
1.50×10-9 [1.39×10-8]
Step 3
6.94×10-9 [1.85×10-7]
Step 7
9.90×10-11
[4.35×10-9]
[9.01×10-10]
5.91×10-11
Step 9
Step 13
4.62×10-10
[1.76×10-9]
Methoxy
Carboxylethylidene
Formaldehyde
[4.99×10-11]
1.67×10-12
Step 14
Methylenecarboxylethyledne
Methyl Propionate
[6.16×10-15]
2.39×10-15
Step 1
4.21×10-9 [7.84×10-8]
Step 5
Methyl
Propionate
Methylene Propionate
[7.71×10-8]
3.60×10-9
Step 28
Propanoyl
Formaldehyde

Figure 8.1. Schematic representation of the most important reaction pathways in the network considered in the HDO of methyl propionate over Pd (111) in the presence of water. We note that in our microkinetic calculations, we included all the elementary steps illustrated in Table 8.2; however, this Figure is a schematic of elementary steps involved in the dominant pathways of the HDO of methyl propionate. TOFs (s^{-1}) shown for various elementary steps are computed at a temperature of 473 K, a methyl propionate gas phase pressure of 0.01 bar and a hydrogen partial pressure of 0.2 bar. For convenience in comparison, the calculated values of TOFs (s^{-1}) in the absence of solvent are shown in [ ] next to the obtained values of TOFs(s^{-1}) in the presence of water. TOFs (s^{-1}) for elementary reactions not shown in this figure are illustrated in Table 8.4. The most dominant pathway is shown in red color ($CH_3CH_2COOCH3 \rightarrow CH_3CHCOOCH_3 \rightarrow CH_2CHCOOCH_3 \rightarrow CH_2CHCO+OCH_3 \rightarrow \ldots \rightarrow CH_3CH_3+CO+CH_3OH$). Other competitive pathways are shown in black, blue, and green.

Methyl Propionate
Step 1
[6.16×10-15]
1.39×10-14
Methyl
Propionate
Step 2
[6.43×10-8]
2.94×10-8
Methoxy
Propanoyl
Step 3
1.46×10-7
[1.85×10-7]
Step 4
2.12×10-8
[1.39×10-8]
Step 5
8.93×10-8
[7.84×10-8]
Methylene Propionate
[7.71×10-8]
8.54×10-8
Step 28
Propanoyl
Formaldehyde
Methylcarboxylethene
Step 18
[1.30×10-8]
2.06×10-8
Methylcarboxylethyledene
Step 7
1.96×10-9
[4.35×10-9]
Step 8
1.43×10-7
[1.80×10-7]
Methylcarboxylethyne
Step 15
[1.25×10-11]
1.77×10-11
Carboxylmethyl
Ethyne
Methylcarboxylvinyl
Step 11
[1.25×10-11]
1.77×10-11
Step 12
[1.91×10-7]
1.61×10-7
methoxy
Carbonylvinyl
Formaldehyde
Methylenecarboxylvinyl
Step 10
[1.39×10-9]
2.36×10-9
Step 17
6.08×10-9
[3.14×10-9]
Step 9
[9.01×10-10]
1.01×10-9
Step 13
3.73×10-9
[1.76×10-9]
Methoxy
Carboxylethylidene
Formaldehyde
Step 14
[4.99×10-11]
5.64×10-11
Methylenecarboxylethyledne

Figure 8.2. Schematic representation of the most important reaction pathways in the network considered in the HDO of methyl propionate over Pd (111) in the presence of 1,4-dioxane. We note that in our microkinetic calculations, we included all the elementary steps illustrated in Table 8.1; however, this Figure is a schematic of elementary steps involved in the dominant pathways of the HDO of methyl propionate. TOFs (s^{-1}) shown for various elementary steps are computed at a temperature of 473 K, a methyl propionate gas phase pressure of 0.01 bar and a hydrogen partial pressure of 0.2 bar. For convenience in comparison, the calculated values of TOFs (s^{-1}) in the absence of solvent are shown in [ ] next to the obtained values of TOFs(s^{-1}) in the presence of 1,4-dioxane. TOFs (s^{-1}) for elementary reactions not shown in this figure are illustrated in Table 8.4. The most dominant pathway is shown in red color ($CH_3CH_2COOCH3 \rightarrow CH_3CHCOOCH_3 \rightarrow CH_2CHCOOCH_3 \rightarrow CH_2CHCO+OCH_3 \rightarrow \ldots \rightarrow CH_3CH_3+CO+CH_3OH$). Other competitive pathways are shown in black, blue, and green.

CHAPTER 9

EFFECTS OF ADSORBATE-ADSORBATE INTERACTIONS ON THE KINETICS AND DEGREES OF RATE AND THERMODYNAMIC CONTROL OF SURFACE CATALYZED REACTIONS: A NEW THERMODYNAMIC MODEL[1]

[1] S. Behtash, O. Mamun, and A. Heyden. To be submitted to Journal of Catalysis.

ABSTRACT

Heterogeneous catalytic reactions take palace on the surface of solid particles, where the adsorbed molecules are in close proximity of each other. The repulsive and attractive forces between the adsorbed molecules (direct and indirect interaction, e.g., by changing the electronic structure of the metal particle) can stabilize or destabilize the relative free energies of adsorbed species. If the lateral interactions between adsorbed species change the relative free energies of transition or intermediate states that are kinetically relevant, the overall rate of a reaction can decrease or increase remarkably. Important kinetic parameters can be identified by the degrees of rate and thermodynamic control that are powerful tools for quantifying the extent to which a differential change in the standard-state free energy of any given transition or intermediate state influences the net reaction rate. We show in this paper how lateral interactions between adsorbed species can change the degrees of rate and thermodynamic control such that e.g. the influence of an intermediate species that plays an important role on a thermodynamically ideal surface disappears when lateral interactions between intermediates at higher surface coverage become important. Overall, we aim at developing conceptual analogies between the thermodynamics of molecules in mixtures and the behavior of surface intermediates. We propose a thermodynamic model that can take the interaction between surface intermediates into account by using surface activity coefficients of intermediates that are conceptually equivalent to the activity coefficients of molecules in solutions. By implementing such a model in microkinetic simulations based on parameters obtained from first principles, it can provide a reliable transition from the quantum molecular to the reactor scale.

KEYWORDS: Degree of rate control; Lateral interactions; Kinetics; Heterogeneous catalysis; Thermodynamic model

9.1 INTRODUCTION

Catalytic processes typically involve a multistep reaction mechanism. The aim of chemical kinetics studies is to understand the complex relation of the overall rate of a process with the rate constants of all of the elementary steps involved in its reaction mechanism. However, all of the reaction parameters are not independent of each other, and often, the overall rate can be described by few kinetic parameters. The overall rate expression can get as simple as the rate of an elementary step, when under specific reaction conditions, the net rate of a reaction mechanism is controlled by one elementary step which is known as rate determining steps (RDS). However, a single rate determining step only exists under limited conditions and perhaps several steps usually control the net rate. Identifying the rate-controlling elementary steps and kinetic parameters not only provides a simplified description of the net rate, but also information of the intermediates and transition state which can possibly be adjusted to improve the overall rate. Ideally, with modification of the reactant structure, or using a catalyst or a solvent that can target and stabilize or destabilize specific rate-controlling intermediates and transition states, we can achieve a higher rate of desired and lower rate of undesired products. Therefore, finding those rate-controlling steps and intermediates is of great interest. Identifying the rate-controling steps in a mechanism has been a long standing problem in the catalysis community. However, with the rapid advances in the application of quantum chemical calculations in catalysis, and growing use of microkinetic models, a greater

understanding of the kinetic of complex reaction mechanisms is achievable. Now that all the reaction rate constants are obtainable, the challenge is to determine rate-controlling kinetic parameters. Various methods have been suggested for assessing which step in a reaction scheme limit the overall rate. Christiansen[246], Boudart[247] and Dumesic[248] made great efforts by simplifying the description of the net rate, and identifying the important kinetic parameters for simple reaction schemes by using De Donder relations. However, it was shown that situations exist for which the proposed methods lack universality and may fail in prediction of the RDS and important parameters[148]. To our knowledge, the most powerful tool that has been introduced is the degree of rate control which quantifies the extent to which a differential change in the standard-state free energy of any given transition state or intermediates influences the net reaction rate. Campbell[147-149] defined the degree of the rate control for elementary reaction step *i* ($X_{RC,i}$) to be the dimensionless partial derivatives of the overall rate with respect to the forward rate constant of the step *i* while all other rate constants but the backward rate constants of step *i* are held constant. Considering that the forward and backward rate constant of any elementary reaction can be correlated to the free energy of the transition state by transition state theory[197], the definition of the $X_{RC,i}$ is then equivalent to taking the dimensionless partial derivative of the overall rate with respect to the free energy of the transition state of the step *i*, while the free energy of all other intermediates and transition states are kept constant. Similarly, the degree of the thermodynamic rate-control for intermediate *n* ($X_{RC,n}$), was defined[149, 245] as the partial derivative of the overall rate with respect to the free energy of the intermediate *n*, while the free energy of all other intermediates and transition states are hold constant.

Although we found the concept of degree of rate-control to be unrestricted and universal, we have noticed that a great understanding and interpretation of the quantities of the degrees of the rate controls X_{RC} and X_{TRC} is not available in the literature. Since the degrees of rate controls have been used in analysis of simple reaction networks under idealistic reaction conditions where the description of the overall rate is simple and predictable. However, in our previous density functional theory and microkinetic modeling studies[157, 158], we used the degree of rate-control analysis for more complex reaction networks and under more realistic reaction conditions without any simplifying assumptions, where our results were in contradiction to some not scientifically proved relationships in the literature[149] that link the thermodynamic degree of rate control to the surface coverage. The proposed relationship by Campbell—the authors note[149] that there is no mathematical proof for their relationship—suggested that X_{TRC} of an intermediate is proportionate with the coverage of that intermediate by a negative constant which typically varies between -2 and -1 depending on the required number of sites in the rate-controling process. Accordingly, the X_{TRC} values are suggested to be always negative and that means if we destabilize the most abundant surface intermediates to decrease their adsorption strength, the overall rate will increase. This statement at first, sounded logical, and unrestricted so, we tried to find the source of errors in our results were we found zero or positive thermodynamic degrees of rate control for some of the most abundant surface intermediates, which means that with increasing the poisoning effects of some intermediates we will be able to improve the overall rate. As we failed to find any errors in our simulations we tried to conceptually investigate the possibility of such phenomenon that stabilizing a surface poisoning intermediate yields a higher net

rate that can possibly be of great interest. This led us to find some universal and unrestricted mathematical proofs for the relationships between the degrees of the rate control that we call conservations of the degrees of rate control. While, previously, Dumesic[249], Baranski[250], Shaik[251], and Campbell[149] have shown for specific and simple reaction schemes, the sum over the rate-control degrees of elementary steps is one. In this article we present a solid mathematical proof, without any assumption for the overall rate expression, that the summation of the rate control of all intermediates and transition states is equal to zero. More specifically, we will prove that the sum over the degrees of the rate control of all elementary steps in a mechanism should be one, while the summation of the thermodynamic degrees of rate-control for all intermediates is equal to minus one. We will show that under realistic reaction conditions where there are lateral interactions between surface intermediates, it is possible to stabilize an abundant surface intermediate and as a result increase the net rate. With the understanding of the importance of non-ideal thermodynamic behavior of the surface intermediates in the kinetic of the reaction mechanisms and overall rate, it is necessary to develop a thermodynamic model that can predict and take into account the interaction and real behavior of surface intermediates. With the aim of the conceptual analogies between the thermodynamics of molecules in a mixture, and behaviors of the surface intermediates, we propose a thermodynamic mean-field model that can take the interaction between surface intermediates into account by using catalytic activity coefficients of an intermediate that is conceptually equivalent to the activity coefficients of molecules in solutions. The impact of such a model can be enormous in understanding the kinetic of chemical processes. This can be the transition from the idealistic surface intermediates

behavior to the more realistic conditions where the microkinetic models will be able to predict the turnover frequencies, dominant pathways, and surface coverages, and provide the understanding of the kinetics of reaction mechanisms under real conditions that are quantitatively more compatible with real conditions and experimental results.

9.2 CONSERVATION OF X_{RC} AND X_{TRC}

i) Summation over all degrees of rate-controls is zero:

The total differential of a function, f, of several variables (e.g. x_i) is defined by the following expression:

$$df = \sum_i \left(\frac{\partial f}{\partial x_i}\right)_{x_{j\neq i}} \times dx_i \tag{9.1}$$

where, $\left(\frac{\partial f}{\partial x_i}\right)_{X_{j\neq i}}$ is the partial derivatives of the function, *f*, with respect to x_i while other arguments are constant.

At constant temperature and partial pressures, the net rate of a network of surface reactions is a function of the free energies of all intermediates and transition states. If we assume our function is the natural logarithm of the overall rate (ln *r*), and our variables are the dimensionless free energies of the intermediate and transition states (e.g. for intermediate i: $\frac{-G_i}{RT}$), according to equation 9.1, the following expression holds for any reaction:

$$d(\ln r) = \sum_i \left(\frac{\partial \ln r}{\partial \frac{-G_i}{RT}}\right)_{G_{j\neq i}} \times \left(-\frac{dG_i}{RT}\right) \tag{9.2}$$

Re-arranging the equation 9.2 and separating all free energies of transitions states and stable intermediates we can re-write equation as,

$$d(\ln r) = \left[\sum_i \left(\frac{\partial \ln r}{\partial \frac{-G_i^{0\,TS}}{RT}}\right)_{G_{j\neq i}^{0\,TS}, G_m} \times \left(-\frac{dG_i^{0\,TS}}{RT}\right)\right] + \left[\sum_n \left(\frac{\partial \ln r}{\partial \frac{-G_n^0}{RT}}\right)_{G_{m\neq n}^0, G_i^{0\,TS}} \times \left(-\frac{dG_n^0}{RT}\right)\right] \quad (9.3)$$

where $\left(\frac{\partial \ln r}{\partial \frac{-G_i^{0\,TS}}{RT}}\right)_{G_{j\neq i}^{0\,TS}, G_m}$ is the partial derivative of ln *r* with respect to the dimensionless free energy of the transition state of elementary step *i*, while the free energy of all other transition states and intermediates are constant, and similarly, $\left(\frac{\partial \ln r}{\partial \frac{-G_n^0}{RT}}\right)_{G_{m\neq n}^0, G_i^{0\,TS}}$ is the partial derivative of ln *r* with respect to the dimensionless free energy of intermediate *n*, while the free energy of all other transition states and intermediates are constant. Now, assuming we stabilize or destabilize all intermediate and transition states uniformly by a constant d*G*. The elementary reaction free energies and barriers, and consequently elementary forward, backward and equilibrium rate constants, as well as TOF, remain unchanged. A schematic of this is shown in Figure 9.1a for the Langmuir-Hinshelwood mechanism). Therefore, d(ln *r*) is equal to zero or,

$$\frac{d(\ln r)}{-\frac{dG}{RT}} = \left[\sum_i \left(\frac{\partial \ln r}{\partial \frac{-G_i^{0\,TS}}{RT}}\right)_{G_{j\neq i}^{0\,TS}, G_m}\right] + \left[\sum_n \left(\frac{\partial \ln r}{\partial \frac{-G_n^0}{RT}}\right)_{G_{m\neq n}^0, G_i^{0\,TS}}\right] = 0 \quad (9.4)$$

The degrees of rate and thermodynamic control of elementary step *i*, and intermediates *n* are defined as,

$$X_{RC,i} = \left(\frac{\partial \ln r}{\partial \frac{-G_i^{0\,TS}}{RT}} \right)_{G_{j\neq i}^{0\,TS}, G_m} \tag{9.5}$$

$$X_{TRC,n} = \left(\frac{\partial \ln r}{\partial \frac{-G_n^0}{RT}} \right)_{G_{m\neq n}^0, G_i^{0\,TS}} \tag{9.6}$$

and equation 9.4 actually states that the summation of the both degrees of rate and thermodynamic controls is conserved and equal to zero.

$$\sum_i X_{RC,i} + \sum_n X_{TRC,n} = 0 \tag{9.7}$$

ii) $\sum_i X_{RC,i} = 1$

Campbell's insightful definition for the rate-determining step states that an elementary step in a reaction mechanism is the RDS when it has a degree of the rate-control of 1, while the degrees of rate-control for all other elementary steps are zero, implying that the summation of the degrees of rate-control in a mechanism with a single RDS is equal to one. Dumesic[249], Baranski[250], and Shaik[251] also showed that the summation of the degrees of the rate control of all of the elementary steps is equal to one for some simple reaction schemes where an expression for the TOF of the overall rate is available; however, there is no mathematical proof in the literature for conservation of the X_{RC} for more general reaction mechanisms with multiple rate-controlling steps where an expression for the overall rate is not available.

Let's assume that in a reaction mechanism, we uniformly stabilize all the transition states by d*G* (Figure 9.1b), while the free energies of all intermediates are held constant. Then, equation 9.4 can be simplified as,

$$\frac{d(\ln r)}{\frac{dG}{RT}} = \left[\sum_i \left(\frac{\partial \ln r}{\partial \frac{-G_i^{0\,TS}}{RT}}\right)_{G_{j\neq i}^{0\,TS},G\ m}\right] = \sum_i X_{RC,i} \qquad (9.8)$$

If we can show that $\frac{d(\ln r)}{\frac{dG}{RT}}$ is equal to one then we proved that the summation of the degrees of rate-control for all the elementary steps are equal to 1.

The overall rate for an elementary step (r_j) is a product of rate-constants and coverages and can generally be expressed in mean-field models as,

$$r_j = k_{f,j}\prod_n \theta_n^{\alpha_{n,j}} - k_{b,j}\prod_n \theta_n^{\beta_{n,j}} \qquad (9.9)$$

where $k_{f,j}$, and $k_{b,j}$ are forward and backward rate-constants of elementary reaction *j*, and $\theta_n^{\alpha_{n,j}}$ and $\theta_n^{\beta_{n,j}}$ are the coverages of the intermediates (or the partial pressures for adsorption/desorption processes) involved in the forward and backward rates of the reaction *j*.

Under steady-state condition, the mole balance for any given intermediate (e.g. intermediate *n*) can be written as the linear combination of the elementary reactions which produce or consume intermediate *n*,

$$\frac{d\theta_n}{dt} = \sum_j \vartheta_{n,j}\, r_j = \sum_j \left(k_{f,j}\prod_n \theta_n^{\alpha_{n,j}} - k_{b,j}\prod_n \theta_n^{\beta_{n,j}}\right)\vartheta_{n,j} = 0 \qquad (9.10)$$

where $\vartheta_{n,j}$ is the stoichiometric coefficient of the reactions for production of intermediate *n*. Solving the nonlinear algebraic mole-balance equations for all intermediates on the surface, we can calculate the surface coverages and rate of every elementary reaction.

Now let's go back to our first assumption that we uniformly stabilized all the transition states by d*G* while the free energies of all intermediates are held constant. Similarly, we can write the mole-balance equations for the new condition as (rates, rate-constant and coverages for the new condition are shown with prime symbols),

$$\frac{d\theta_n'}{dt} = \sum_j \vartheta_{n,j}\, r_j' = \sum_j \left(k_{f,j}' \prod_n {\theta_n'}^{\alpha_{n,j}} - k_{b,j}' \prod_n {\theta_n'}^{\beta_{n,j}} \right) \vartheta_{n,j} = 0 \qquad (9.11)$$

where,

$$k_{f,j}' = e^{\frac{dG}{RT}}.\ k_{f,j} \quad \text{and} \quad k_{b,j}' = e^{\frac{dG}{RT}}.\ k_{b,j} \qquad (9.12)$$

Now, if replace all the $k_{f,j}'$ and $k_{b,j}'$ by equation 9.12 we can re-write the equation 9.11 as,

$$\frac{d\theta_n'}{dt} = \sum_j \vartheta_{n,j}\, r_j' = e^{\frac{dG}{RT}} . \sum_j \left(k_{f,j} \prod_n {\theta_n'}^{\alpha_{n,j}} - k_{b,j} \prod_n {\theta_n'}^{\beta_{n,j}} \right) \vartheta_{n,j} = 0 \qquad (9.13)$$

By dividing both sides of the equation 9.13 by $e^{\frac{dG}{RT}}$ we see that the governing equation for θ_n and θ_n' are exactly the same which result in,

$$\theta_n = \theta_n' \qquad (9.14)$$

Now, that coverages stay the same, we can show that, $r_j' = e^{\frac{dG}{RT}} . r_j$,

$$r_j' = k_{f,j}' \prod_n \theta_n^{\alpha_{n,j}} - k_{b,j}' \prod_n \theta_n^{\beta_{n,j}} = e^{\frac{dG}{RT}} . \left[k_{f,j} \prod_n \theta_n^{\alpha_{n,j}} - k_{b,j} \prod_n \theta_n^{\beta_{n,j}} \right] =$$

$$e^{\frac{dG}{RT}} . r_j \qquad (9.15)$$

Additionally, the overall rate of a network of elementary reactions is equal to the summation of all the elementary reactions which consume the reactant or the summation of those steps which produce the products. Generally the overall rate can be expressed as a linear combination of the reaction rate of the elementary steps,

$$r = \sum_j \lambda_j r_j \qquad (9.16)$$

where λ_j is a stoichiometric constant. Considering that all the rates of the elementary steps were increased by a factor $e^{\frac{dG}{RT}}$ ($r_j' = e^{\frac{dG}{RT}} . r_j$), then a linear combination of the rate of the elementary steps will also increase by a factor $e^{\frac{dG}{RT}}$. As a result, the overall rate will increase by a factor $e^{\frac{dG}{RT}}$,

$$r' = e^{\frac{dG}{RT}}.r \qquad (9.17)$$

Consequently the infinitesimal change in the free energy of the transition state, will change ln r by $\frac{dG}{RT}$,

$$d(\ln r) = \ln r_j' - \ln r_j = \frac{dG}{RT} \text{ or } \qquad \frac{d(\ln r)}{\frac{dG}{RT}} = 1 \qquad (9.18)$$

and consequently, the summation of the degrees of rate control of all the elementary step in a reaction mechanism is exactly equal to 1. We again note that we did not use any expression for the overall rate of the reaction mechanism and this rule is valid for any reaction mechanism under any reaction conditions.

iii) $\sum_n X_{TRC,n} = -1$

We proved that the summation of all degrees of rate control of elementary steps and surface intermediates is zero, and the sum over the degrees of rate control of elementary steps is equal to 1. Consequently, the thermodynamic degrees of the rate control are also conserved and add up to -1,

$$\sum_n X_{TRC,n} = -1 \qquad (9.19)$$

We again note that the above equation is independent of the reaction mechanism and the overall rate-expression, and no assumptions have been made regarding to reaction conditions.

9.3 IS IT POSSIBLE TO STABILIZE AN ABUNDANT SURFACE INTERMEDIATE AND INCREASE THE NET RATE?

To demonstrate the effects of non-ideal thermodynamic behavior of adsorbed intermediates on the reaction rate in a reaction mechanism, we used a simple Langmuir-Hinshelwood (L-H) mechanism for solid-catalyzed reactions, with one irreversible RDS and all other steps quasi equilibrated. We note that Campbell[149] also used L-H mechanism for explanation of the concept of the degrees of rate-control, and our aim is to show how under realistic thermodynamic conditions, degrees of rate-control deviate from ideal values in this simple reaction mechanism.

$$(\mathbf{1}: \boldsymbol{EQ}) \quad \boldsymbol{A} + * \rightleftharpoons \boldsymbol{A}^*$$

$$(\mathbf{2}: \boldsymbol{EQ}) \quad \boldsymbol{B} + * \rightleftharpoons \boldsymbol{B}^*$$

$$(\mathbf{3}: \boldsymbol{RDS}) \quad \boldsymbol{A}^* + \boldsymbol{B}^* \rightleftharpoons \boldsymbol{AB} + \mathbf{2} *$$

In the above L-H scheme, the asterisk (*) denotes a free site, intermediates with an asterisk are adsorbed on the surface, and those without asterisk are gas-phase species. The overall rate of the mechanism above can be obtained by applying the RDS and quasi-equilibrium approximations,

$$r = \frac{k_3 K_1 K_2 P_A P_B}{(1 + K_1 P_A + K_2 P_B)^2} \tag{9.20}$$

where k_3 is the forward rate constant of step 3, K_i is the equilibrium constant of step *i*, and p_i is dimensionless partial pressure of species i (partial pressure of species i divided by the reference pressure of 1 bar).

i) No lateral interaction: Thermodynamically ideal adsorbates

Now if we assume that there is no lateral interaction between the adsorbed intermediates one can show that,

$$X_{RC,\ r3} = \left(\frac{\partial \ln r}{\partial \frac{-G_3^{0\,TS}}{RT}} \right)_{G_{j\neq 3}^{0\,TS}, G_m} = 1 \tag{9.21}$$

$$X_{TRC,A} = \left(\frac{\partial \ln r}{\partial \frac{-G_{A*}^{0}}{RT}} \right)_{G_{m\neq A}^{0}, G_i^{0\,TS}} = \frac{-2K_1P_A}{(1+K_1P_A+K_2P_B)} = -2\theta_A \tag{9.22}$$

$$X_{TRC,B} = \left(\frac{\partial \ln r}{\partial \frac{-G_{B*}^{0}}{RT}} \right)_{G_{m\neq B}^{0}, G_i^{0\,TS}} = \frac{-2K_2P_B}{(1+K_1P_A+K_2P_B)} = -2\theta_B \tag{9.23}$$

We see that the degree of rate-control for the step 3 is one and for other steps it is 0, which verifies our assumption that step 3 is RDS. Also, the thermodynamic degree of rate-control for A, and B are equal to $-2\theta_A$, and $-2\theta_B$ respectively. By investigating simple catalytic reaction mechanisms Campbell suggested[149] that there is a simple link between the degree of thermodynamic rate-control for any intermediate *n* and its coverage θ_n as,

$$X_{TRC,n} = -\sigma.\theta_n \tag{9.24}$$

where σ is the average number of sites required in the rate-limiting steps that typically varies between 1 and 2. We see that for L-H mechanism, at ideal thermodynamic conditions, Campbell's proposed relationship is valid. At limiting cases where the surface is mostly covered by A or B and the coverages of θ_A or θ_B are 1, we can see that the degrees of rate-control, for the most abundant surface intermediate, becomes -2. While at first, it sounds like a violation of the conservation of the thermodynamic degrees of rate-control that states the summation over all X_{RTC} should be -1, we note that the

conservation of X_{RTC} is held over all energy states in the reaction mechanism including the energies of reactant and product states. The reactant energy state in L-H mechanism is the energy of the gas-phase A and B molecules, and the clean surface of the catalyst. Similarly, the product energy state is the energy of the gas-phase AB molecule and clean surface. Now we have to also take into account the degree which the rate will change if we infinitesimally stabilize or destabilize the free energies of reactant and product states.

We can change the energy of the gas-phase molecules by modification in their molecular structures or using a solvent. However, let's assume that the energies of our gas-phase molecules are constant and we want to just try different catalysts. Consequently, just the energy of the clean surface (free sites) is changing. Now if we calculate the degree of rate control for the energy of the clean surface, $X_{TRC,*}$ can be calculated as,

$$X_{TRC,*} = \left(\frac{\partial \ln r}{\partial \frac{-G_*^0}{RT}}\right)_{G_{m\neq *}^0, G_i^{0\,TS}} = 2\theta_B + 2\theta_A - 1 \qquad (9.25)$$

where we see that the sum over the degrees of rate control is exactly -1.

ii) Effects of the presence of lateral interactions between the adsorbed intermediates

If we assume that there are lateral interactions between adsorbed A and B molecules, using the rate-expression in equation 9.20, the degrees of rate and thermodynamic control are,

$$X_{RC,\ r3} = \left(\frac{\partial \ln r}{\partial \frac{-G_3^{0\,TS}}{RT}}\right)_{G_{j\neq 3}^{0\,TS}, G_m} = 1 \qquad (9.26)$$

$$X_{TRC,A} = \left(\frac{\partial \ln r}{\partial \frac{-G^0_{A*}}{RT}}\right)_{G^0_{m\neq A}, G_i^{0\,TS}} = \frac{-2K_1P_A}{(1+K_1P_A+K_2P_B)} - \frac{2K_2P_B}{(1+K_1P_A+K_2P_B)} \times \frac{\partial \frac{-G^0_{B*}}{RT}}{\partial \frac{-G^0_{A*}}{RT}} = -2\theta_A -$$

$$2\theta_B \frac{\partial \frac{-G^0_{B*}}{RT}}{\partial \frac{-G^0_{A*}}{RT}} \qquad (9.27)$$

$$X_{TRC,B} = \left(\frac{\partial \ln r}{\partial \frac{-G^0_{B*}}{RT}}\right)_{G^0_{m\neq B}, G_i^{0\,TS}} = -2\theta_B - 2\theta_A \frac{\partial \frac{-G^0_{A*}}{RT}}{\partial \frac{-G^0_{B*}}{RT}} \qquad (9.28)$$

$$X_{TRC,*}\left(\frac{\partial \ln r}{\partial \frac{-G^0_{*}}{RT}}\right)_{G^0_{m\neq *}, G_i^{0\,TS}} = 2\theta_B + 2\theta_B \frac{\partial \frac{-G^0_{B*}}{RT}}{\partial \frac{-G^0_{A*}}{RT}} + 2\theta_A + 2\theta_A \frac{\partial \frac{-G^0_{A*}}{RT}}{\partial \frac{-G^0_{B*}}{RT}} - 1 \qquad (9.29)$$

Because, there are lateral interactions between the adsorbed A and B molecules, the free energies of adsorbed A and B molecules are dependent of each other, and in the above expressions for the degree of rate controls**,** $\frac{\partial \frac{-G^0_{B*}}{RT}}{\partial \frac{-G^0_{A*}}{RT}}$ is the partial derivative of the free energy of adsorbed B molecules with respect the free energy of adsorbed A molecules, while the free energy of other intermediates are held constant. When there is no lateral interaction this term will disappear and then the above equations are equivalent to those expressions (equation 9.21-9.25) that we derived for the L-H mechanism in the absence of lateral interaction.

Now if we re-arrange equations 9.28 and 9.29 one can show that the below inequalities are held,

If $-\frac{\theta_A}{\theta_B} \geq \frac{\partial \frac{-G^0_{B*}}{RT}}{\partial \frac{-G^0_{A*}}{RT}}$, then $X_{TRC,A} \geq 0$ (9.30)

If $-\frac{\theta_A}{\theta_B} \leq \frac{\partial \frac{-G^0_{B*}}{RT}}{\partial \frac{-G^0_{A*}}{RT}}$, then $X_{TRC,B} \geq 0$ (9.31)

So, we could show that for L-H mechanism under the above condition, an adsorbed intermediate can have positive degree of rate control. But what is the physical meaning of this? To provide a better understanding of the above equations, in the following paragraphs we will discuss two example cases where we have interaction and repulsion between the adsorbed A and B intermediates.

If there is attraction between adsorbed A and B molecules, then $\frac{\partial \frac{-G^0_{B*}}{RT}}{\partial \frac{-G^0_{A*}}{RT}}$ is greater than zero. Consequently, equation 9.31 is then true, and the thermodynamic degree of rate control of intermediate B is positive while the thermodynamic degree of rate-control for A is negative. Now if we assume there are repulsive forces between A and B, then $\frac{\partial \frac{-G^0_{B*}}{RT}}{\partial \frac{-G^0_{A*}}{RT}}$ is smaller than zero. Now both of $\frac{\partial \frac{-G^0_{B*}}{RT}}{\partial \frac{-G^0_{A*}}{RT}}$ and $-\frac{\theta_A}{\theta_B}$ have negative values, and without the exact values of the partial derivatives and the ratio of the coverages, it is difficult to determine the sign of the degrees of rate control and under specific conditions, either A or B can have positive or negative degrees of rate control.

Apparently, if lateral interactions between the adsorbed molecules are not negligible then Campbell's proposed relation ($X_{TRC,n} = -\sigma.\theta_n$) is not valid anymore. However, we note that the conservation of the degrees of rate-control is universal and still holds regardless of the thermodynamics of the adsorbed intermediates, and the degrees of thermodynamic control (equation 9.27-9.29) add up to -1 and the sum of the degree of kinetic rate control add to 1 (equation 9.26).

We saw that the kinetics of the reactions can be strongly dependent on the thermodynamics of the adsorbed intermediates. The degree of the thermodynamic rate-control can be used as a tool to quantify the extent to which the lateral-interaction

between molecules can affect the overall kinetic of the reactions; however, it is not trivial to obtain the complex relations of the free energies of the adsorbed intermediates without a thermodynamic model that take the interaction between molecules into account.

9.4 MODEL FOR THERMODYNAMICALLY NON-IDEAL SURFACES

The Gibbs free energy for substance *i* and its variation with pressure, temperature, and number of molecules of substance *i* is given as,

$$dG_i = V_i dP - S_i dT + \mu_i dN_i \tag{9.32}$$

Often, the molar partial derivatives of G_i , V_i , S_i are assumed to be constant and equal to molar values of these parameters, $\widetilde{G}_i$, $\widetilde{V}_i$, $\widetilde{S}_i$. If we suppose for a system this assumption is true, then by taking the molar partial derivatives of equations 9.32 and applying this assumption we can write,

$$d\mu_i = d\widetilde{G}_i = \widetilde{V}_i dP - \widetilde{S}_i dT \tag{9.33}$$

The above equation is extensively used in thermodynamic studies of gas-phase molecules. Now what if under specific condition the chemical potential itself is a function of the quantity of the substance *i*? E.g. when the molecules of substance *i* are adsorbed on a surface of a catalyst and in close proximity of each other and therefore, there are lateral interactions between the molecules. Then, $\frac{\partial \mu_i}{\partial N_i}$ is not zero anymore, and should be taken into account in the derivation as,

$$d\mu_i = \widetilde{V}_i dP - \widetilde{S}_i dT + \widetilde{X}_i dN_i \tag{9.34}$$

where, $\widetilde{X}_i$ is molar partial derivative of chemical potential ($\frac{\partial \mu_i}{\partial N_i}$).

Chemical potential can be also expressed in terms of activity as,

$$\mu_i = \mu_0 + RT \ln a_i \quad (9.35)$$

where a_i is the activity of substance *i*. Now, for a catalytic reaction, we define the catalytic activity of substance *i*, a_i to be,

$$a_i \equiv \frac{f_i}{f_0} \quad (9.36)$$

Where we name f_i , the surface fugacity of the substance *i*, and f_0 is a reference fugacity and constant.

Now at constant temperature and pressure we can say,

$$d\mu_i = RT\, d(ln\, a_i) = RT\, d(ln\, f_i) = \tilde{X}_i dN_i \quad (9.37)$$

Now, if we define a surface fugacity coefficient as,

$$\emptyset_i \equiv \frac{f_i}{N_i} \quad (9.38)$$

Then, one can show that,

$$d(ln\, \emptyset) = \left\{\frac{\tilde{X}_i}{RT} - \frac{1}{N_i}\right\} dN_i, \quad \text{and} \quad ln\, \emptyset = \int_{N_0}^{N} \left\{\frac{\tilde{X}_i}{RT} - \frac{1}{N_i}\right\} dN_i \quad (9.39)$$

Now we define a surface thermodynamically ideal for the adsorption of substance i, when the chemical potential of the adsorbed molecules of i can be expressed as,

$$\mu_i = \mu_0 + RT \ln \frac{N_i}{N_0} \quad (9.40)$$

where N_i is the number of moles of adsorbed i per surface area , and N_0 is a reference number. Then on the ideal surface, $\tilde{X}_i$ for substance *i*, is equal to partial derivation of the chemical potential which is $\frac{1}{N_i}$. Consequently, according to equation 9.39 the surface fugacity coefficient for substance *i* on an ideal surface is one.

Similar to ideal-gas or solution mixtures, we can define the chemical potential of substance i in an ideal and regular mixture of adsorbed molecules as,

$$\mu_i \equiv G_i^0 + RT \ln \frac{\hat{f}_i}{f_i} \quad (9.41)$$

$$\mu_i^{id} \equiv G_i^0 + RT \ln \theta_i = G_i^0 + RT \ln \frac{\hat{f}_i^{id}}{f_i} \quad (9.42)$$

where, θ_i is the coverage of intermediate i on the surface of the catalyst, $\hat{f}_i$ is the fugacity of substance *i* in the mixture, and $f_i$is the surface fugacity of pure substance *i*. One can show that the Lewis/Randall rule[252] for solutions is also hold in our model for the fugacity of an ideal mixture as,

$$\hat{f}_i^{id} = \theta_i f_i \quad (9.43)$$

Now let's define the catalytic activity coefficient for adsorbate *i* as,

$$\gamma_i \equiv \frac{\hat{f}_i}{\hat{f}_i^{id}} \quad (9.44)$$

then the chemical potential of adsorbed intermediate *i* in a mixture of adsorbed molecules can be written as,

$$\mu_i = G_i^0 + RT \ln \gamma_i \theta_i \quad (9.45)$$

Comparing equation 35 and the above equation, the activity of the adsorbed intermediate *i*, can be expressed as,

$$a_i = \gamma_i \theta_i \quad (9.46)$$

Now we have all the tools that we need to calculate the equilibrium, forward, and backward rate-constant, and consequently obtain an expression for the rate of an elementary reaction.

The chemical potential of a reaction can be written as,

$$\mu = \sum_i \vartheta_i \mu_i \equiv \sum_i \vartheta_i (G_i^0 + RT \ln \gamma_i \theta_i) \quad (9.47)$$

where ϑ_i is the stoichiometry coefficient of intermediate i. At equilibrium the chemical potential is equal to zero, and the equilibrium constant can be obtained as,

$$K_{eq} = e^{\frac{-\Delta G^0}{RT}} = \prod_i (a_i)^{\vartheta_i} = \prod_i (\gamma_i \theta_i)^{\vartheta_i} \quad (9.48)$$

According to transition state theory, the reactant state and the transition-state complex are in an equilibrium for any given elementary reaction such as, $R^* \leftrightarrow TS^{\ddagger} \rightarrow P^*$, and the forward reaction rate and turnover frequency(TOF) of the reaction can be written as,

$$Rate = \frac{k_B T}{h} N^{\ddagger} \quad , \quad \text{and} \quad TOF = \frac{k_B T}{h} \theta^{\ddagger} \quad (9.49)$$

where, k_B is the Boltzmann constant, h is the Planck constant, T denotes the temperature, $N^{\ddagger}$ is the number of the transition-state molecules on the surface, and $\theta^{\ddagger}$ is the coverage of transition-state adsorbates. Because there is equilibrium between the reactant and transition-state, we can calculate $\theta^{\ddagger}$ as,

$$\theta^{\ddagger} = K^{\ddagger} \frac{\gamma_R}{\gamma^{\ddagger}} \theta_R \quad (9.50)$$

where $K^{\ddagger}$ is the equilibrium constant between the reactant and transition-state and calculated by $K^{\ddagger} = e^{\frac{-\Delta G^{\ddagger,0}}{RT}}$, $\gamma^{\ddagger}$, and γ_R are the activity coefficient for transition-state and reactant, and θ_R is the coverage of the reactant molecules.

By replacing the $\theta^{\ddagger}$ in the TOF expression for the forward reaction, and similarly calculating the backward TOF, we can show that the turnover frequency of a reversible elementary reaction $R^* \leftrightarrow P^*$, can be expressed as,

$$r = r_f - r_b = k_f \theta_R - k_b \theta_P = k_f^0 \left(\frac{\gamma_R}{\gamma^{\ddagger}} \right) \theta_R - k_b^0 \left(\frac{\gamma_P}{\gamma^{\ddagger}} \right) \theta_P \quad (9.51)$$

where $k_f^0 = \frac{k_B T}{h} e^{\frac{-\Delta G_{forward}^{\ddagger,0}}{RT}}$, and $k_b^0 = \frac{k_B T}{h} e^{\frac{-\Delta G_{backward}^{\ddagger,0}}{RT}}$ are the ideal forward and backward rate-constants, and k_f, and k_b are non-ideal rate-constants where the relationship of these rates can be shown as,

$$\frac{k_f}{k_f^0} = \left(\frac{\gamma_R}{\gamma^{\ddagger}}\right), \quad \text{and} \quad \frac{k_b}{k_b^0} = \left(\frac{\gamma_b}{\gamma^{\ddagger}}\right) \tag{9.52}$$

Finally, we want to show how De Donder relation, will change when using the definition of the activities of our thermodynamic model. According to the De Donder formulation, the rate of the elementary reaction step *i*, is expressed in terms of forward rate, r_f, and the affinity of step *i*, A_i,

$$r = r_f \left[1 - \exp\left(\frac{-A_i}{RT}\right)\right] \tag{9.53}$$

where affinity is given as,

$$A_i = -\sum_i \vartheta_i (G_i^0 + RT \ln a_i) = -\sum_i \vartheta_i (G_i^0 + RT \ln \gamma_i \theta_i) \tag{9.54}$$

Consequently, the De Donder relation can be expressed in terms of coverages and activity coefficient,

$$r = r_f \left[1 - \frac{\prod_i a_i^{\vartheta_i}}{K_{ieq}}\right] = \left[1 - \frac{\prod_i (\gamma_i \theta_i)^{\vartheta_i}}{K_{ieq}}\right]$$

where, at equilibrium the, $\frac{\prod_i (\gamma_i \theta_i)^{\vartheta_i}}{K_{ieq}}$ is one and consequently the net rate is zero. Also, by using the definition of the forward rate, and replacing it in the De Donder relation one can show that a similar expression to equation 9.51 for the reaction rate of an elementary step can be obtained.

MICROKINETIC MODELS:

By implementing the more thermodynamically realistic definition of elementary rate-reactions, more realistic results are expected to be obtained, and this model can be a more accurate bridge between the molecular scale calculations and reactor-scale. The turnover frequencies, coverages, and the predicted dominant pathways that are obtained

by this model are more reliable, and finally, the degrees of rate-control analysis can assist to identify the realistically important kinetic parameters.

Admittedly, while our model sheds light on the thermodynamic of the adsorbed intermediate, the main remaining challenge in extensive application and implementation of our proposed model in microkinetic simulations, is finding the values or expressions for the catalytic fugacity and activity coefficient. More often in the catalytic reactions, just few or one surface intermediate poison the surface, and consequently the γ_i for many of the intermediates is expected to be 1. But how can we obtain these few needed coefficients?

Fugacity and activity coefficient have been extensively studied in solutions. Various relationships have been derived/proposed for predicting the activity coefficients, and correlations of these parameters. We note that, by analogy, the scientifically proved correlations between the activity parameters in solutions are also applicable to our model for catalyst surface. E.g. by using correlations such as Gibbs/Duhem equations[253], the activity coefficients can be correlated. Also, by using power series expansion, such as Redlich/Kister[254] expansion for excess properties, modules similar to Margules equation[253] or even more complicated modules such as Van Laar[253], and Wilson[255] equations can be obtained for systems with binary abundant intermediates or UNIFAC[253, 256, 257] or UNIQUAC[253, 258] methods for greater complexity for systems with multiple abundant surface intermediates. Also, in the catalysis community, various efforts have been made for quantifying the self-interaction and cross interaction between the adsorbed molecules. By using the analogy, comparison, and learning, from the already developed modules for the calculations of activity in solution, new efforts can

be more focused on developing analogous modules for the calculations of the catalytic activity coefficients of adsorbed intermediates. A combination of DFT calculations and experimental studies can ideally provide an extensive data base/software for the fugacity and activity coefficient of different intermediates on different surfaces, similar to what is currently available for various substances in different solvents and solutions.

9.5. *CONCLUSION*

The degree of rate control analysis is a powerful tool for identifying the rate limiting elementary steps and intermediates. By applying the rate-degree of control analysis in our studies for more complex reaction schemes, we faced positive values for rate-controlling intermediates, which means with stabilizing the poisoning intermediates we can improve the net rate. Since, at first, it sounds irrational to us, we conceptually and mathematically investigated the possibility of such phenomenon which led us to find some universal and unrestricted correlations for degrees of rate-control. We presented a solid mathematical proof that the degrees of rate-control, regardless of the reaction mechanism and conditions, are conserved through all elementary steps and intermediates such that, the summation of the degrees of rate-controls for all the elementary steps is equal to 1, and the sum over the degrees of rate-control of all the intermediates, is equal to -1, and consequently the degrees of rate-control for all the energy states in a reaction scheme is equal to zero. Next, we showed that the thermodynamic of adsorbed intermediates on the surface plays an important role in the kinetic of reaction mechanisms. The presence of the lateral interaction between the intermediates on the surface of the catalyst, can significantly impact the kinetic of the reaction process. E.g.

for Langmuir-Hinshelwood mechanism we showed that the importance of the abundant surface intermediates that we identified to be the rate-controlling on ideal surfaces (In the absence of lateral interaction), under specific conditions, can fade when there are lateral interactions between adsorbed molecules. Finally, with the aim of the conceptual analogies between the thermodynamics of molecules in a mixtures, and behaviors of the surface adsorbates, we proposed a thermodynamic model that can take the interaction between surface intermediates into account by using catalytic activity coefficients of intermediate that is conceptually equivalent to the activity coefficients of molecules in solutions. The impact of such model can be enormous in understanding of the kinetic of chemical processes. By providing an extensive data base/software for the fugacity and activity coefficient of different intermediates on various catalysts, similar to what is currently available for various substances in different solvents and solutions, the proposed model can provide a reliable and accurate transition from the molecular scale calculations to macro-scale reactors.

9.6. *ACKNOWLEDGEMENT*

This work was funded by the United States Department of Energy, Office of Basic Energy Sciences under contract DE-SC0007167 (DE-FG02-11ER16268).

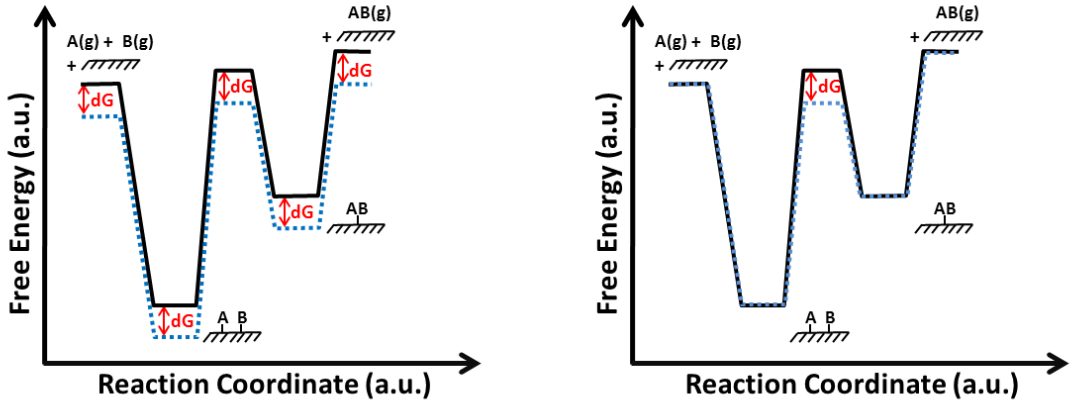

(a) **(b)**

Figure 9.1 A schematic of a mechanism, where in (a) all intermediates are stabilized by d*G* , and in (b) just the transition state is stabilized by d*G* while the free energy of all other states remains the same.

CHAPTER 10

SUMMARY

Lipid feedstocks and pyrolysis oils from woody biomass can be utilized for the production of second-generation biofuels via a catalytic hydrodeoxygenation (HDO) process. The conversion of fatty acids and esters plays an important role in the activity and selectivity of these processes. Understanding the HDO reaction mechanism of organic acids and esters on metal surfaces is a prerequisite for the rational design of new HDO catalysts specifically designed for upgrading pyrolysis oils or lipid feedstocks.

The aim of this thesis is to provide insight into the reaction mechanism and kinetic of catalytic hydrodeoxygenation of organic acids and esters.

Heterogenity is the essential challenge in the field of catalysis where the reactions take place at interfaces of gas, solid, and liquid phases. So, rational design of a catalyst for a chemical process such as hydrodeoxyegnation of acids and esters requires identifying the active interfaces, and understanding the reaction mechanism, activity, and selectivity descriptors at relevant interfaces.

In this thesis, we addressed these challenges, and identified the active sites, reaction mechanism, and activity descriptors of the hydrodeoxygenation of propionic acid and methyl propionate which are model ester and acid molecules. Additionally, since industrial hydodeoxygenation of acids and esters usually takes place in complex liquid environments, we thoroughly investigated the effects of solvents on activity descriptors of the hydrodeoxygenation of organic acids and esters.

We performed a systematic investigation of the elementary reactions involved in the hydrodeoxygenation of propanoic acid and methyl propionate over Pd catalysts and developed a microkinetic model with parameters derived from DFT calculations and transition state theory. Under all conditions, we found that decarbonylation mechanism is the dominant mechanism in hydrodeoxygenation of acids and esters. With the help of a sensitivity analysis, we identified both dehydrogenation steps and C-O bond dissociations, such as propanoyl-hydroxyl in propionic acid, and propanoyl-methoxy in methyl propionate to be the activity descriptors. C-O bond dissociations were previously also identified as the rate-determining step for the hydrodeoxygenation of acetic acid.[82, 150] However, the importance of dehydrogenation steps such as dehydrogenation of α-carbon in both methyl propionate and propionic acid was not clearly addressed in the literature. Consequently, we designed an experiment and performed a kinetic isotope study on deuteriated propionic acid, where we were able to verify the importance of the dehydrogenation steps on the overall activity and obtained a very good agreement between computational and experimental results.

To identify the active sites, we investigated the effect of palladium catalysts surface structures on the hydrodeoxygenation of propionic acid over Pd (211) and Pd (111) model surfaces with the help of periodic DFT calculations. We found that the activity on stepped surfaces was slightly lower than on flat surfaces; however, the difference between the TOFs of flat and stepped surfaces was not remarkable, suggesting that the hydrodeoxygenation of propionic acid over palladium catalyst is nearly insensitive to surface structure.

Finally, the effect of different solvents on hydrodeoxyegnation of propanoic acid and methyl propionate over Pd catalyst was investigated by using an implicit solvation scheme. We saw that in the presence of a polar solvent such as water that it stabilizes key intermediates in the decarboxylation mechanism, the decarboxylation rate increases by two orders of magnitude and the decarbonylation and decarboxylation pathways become essentially competitive. Furthermore in the presence of solvents, C-H and C-O bond dissociations were still the rate-determining steps and are likely activity descriptors for a future computational catalyst discovery and design study.

Additionally, during the sensitivity analyses for the reaction mechanisms of hydrodeoxygenation of acids and esters, we faced amazing mathematical relationships between the degrees of rate-controls. We were able to theoretically prove the conservation relationships between the degrees of rate-controls which led us to a better understanding of the thermodynamics of the adsorbates on the surface of the catalyst. While we are still developing our ideas, the last chapter of this thesis was dedicated to this new way of looking at thermodynamics of adsorbate-catalyst interfaces.

REFERENCES

1. Centi, G. and R.A. Santen, *Catalysis for renewables: from feedstock to energy production*. 2007: Wiley-VCH.
2. Serrano-Ruiz, J.C. and J.A. Dumesic, *Catalytic routes for the conversion of biomass into liquid hydrocarbon transportation fuels.* Energy & Environmental Science, 2011. 4(1): p. 83-99.
3. *Annual Energy review 2009*. 2010, EIA/DOE.
4. *Statistical Aspect of the Energy Economy*. 2008, Eurostat.
5. *Annual Energy Review 2011*. 2011, EIA.
6. *BP Statistical Review of World Energy* 2011, BP.
7. Steve Sorrel, J.S., Roger Bentley, Adam Brandft and Richard Miller, *Global Oil Depletion, An assesment of the evidence for a near-term peak in global oil production*. 2009, UKERC (UK Energy Research Centre).
8. *IPCC Fourth Assessment Report:Climate Change 2007*. 2007.
9. *Climate Change 2007: Synthesis Report*. 2007, IPCC.
10. *A Deadly Toll: The Gulf Oil Spill and the Unfolding Wildlife Disaster*. 2011, Center For Biological Diversity.
11. *Renewable Energy*. Available from: http://www.eere.energy.gov/topics/renewable_energy.html.
12. *Biomass*. Available from: http://www.eere.energy.gov/topics/biomass.html.
13. Chheda, J.N., G.W. Huber, and J.A. Dumesic, *Liquid-phase catalytic processing of biomass-derived oxygenated hydrocarbons to fuels and chemicals.* Angewandte Chemie-International Edition, 2007. 46(38): p. 7164-7183.
14. Ragauskas, A.J., et al., *The path forward for biofuels and biomaterials.* Science, 2006. 311(5760): p. 484-489.
15. Andersin, J. and K. Honkala, *DFT study on complete ethylene decomposition on flat and stepped Pd.* Surface Science, 2010. 604(9-10): p. 762-769.
16. Nykanen, L., J. Andersin, and K. Honkala, *First-principles calculations of the initial incorporation of carbon into flat and stepped Pd surfaces.* Physical Review B, 2010. 81(7).
17. *Standard Specification for Denatured Fuel Ethanol for Blending with Gasoline for Use as Automotive Spark Ignition Engine Fuel*. 2010, ASTM International.
18. Almas, J.B.a.R., *Increasing Food and Energy Prices in 2008: What Were the Causes and Who Was the Blame.*

International Journal of Sociology of Agriculture and Food, 2011. 18(3): p. 236-259.

19. Perrin, R.K., *Ethanol and Food Prices - Preliminary Assessment.* Faculty Publication: Agricultural Economics Paper 49, 2008.
20. *Chemical Potential Energy, http://physics.info/energy-chemical*.
21. Regalbuto, J.R., *Cellulosic Biofuels-Got Gasoline?* Science, 2009. 325(5942): p. 822-824.

22. Regalbuto, J., *An NSF perspective on next generation hydrocarbon biorefineries.* Computers & Chemical Engineering, 2010. 34(9): p. 1393-1396.
23. Fahy, E., et al., *Update of the LIPID MAPS comprehensive classification system for lipids.* Journal of Lipid Research, 2009. 50: p. S9-S14.
24. Savage, N., *The ideal biofuel.* Nature, 2011. 474(7352): p. S9-S11.
25. Banerji, R., G. Misra, and S.K. Nigam, *Non-Edible Oilseeds - Potential Raw-Material for Industry.* Journal of Scientific & Industrial Research, 1983. 42(12): p. 686-693.
26. Demirbas, A., *Potential Resources of Non-edible Oils for Biodiesel.* Energy Sources Part B-Economics Planning and Policy, 2009. 4(3): p. 310-314.
27. Gui, M.M., K.T. Lee, and S. Bhatia, *Feasibility of edible oil vs. non-edible oil vs. waste edible oil as biodiesel feedstock.* Energy, 2008. 33(11): p. 1646-1653.
28. Kumar, A. and S. Sharma, *Potential non-edible oil resources as biodiesel feedstock: An Indian perspective.* Renewable & Sustainable Energy Reviews, 2011. 15(4): p. 1791-1800.
29. Haag, A.L., *Algae bloom again.* Nature, 2007. 447(7144): p. 520-521.
30. Huo, S.H., et al., *Available Resources for Algal Biofuel Development in China.* Energies, 2011. 4(9): p. 1321-1335.
31. Luque, R., *Algal biofuels: the eternal promise?* Energy & Environmental Science, 2010. 3(3): p. 254-257.
32. Pittman, J.K., A.P. Dean, and O. Osundeko, *The potential of sustainable algal biofuel production using wastewater resources.* Bioresource Technology, 2011. 102(1): p. 17-25.
33. Subhadra, B.G., *Sustainability of algal biofuel production using integrated renewable energy park (IREP) and algal biorefinery approach.* Energy Policy, 2010. 38(10): p. 5892-5901.
34. Kirubakaran, V., et al., *A review on gasification of biomass.* Renewable & Sustainable Energy Reviews, 2009. 13(1): p. 168-175.
35. Elliott, D.C., et al., *Developments in Direct Thermochemical Liquefaction of Biomass - 1983-1990.* Energy & Fuels, 1991. 5(3): p. 399-410.
36. Mohan, D., C.U. Pittman, and P.H. Steele, *Pyrolysis of wood/biomass for bio-oil: A critical review.* Energy & Fuels, 2006. 20(3): p. 848-889.
37. Lange, J.P., *Lignocellulose conversion: an introduction to chemistry, process and economics.* Biofuels Bioproducts & Biorefining-Biofpr, 2007. 1(1): p. 39-48.
38. *Preliminary Screening-Technical and Economic Assessment of Synthesis Gas to Fuels and Chemicals with Emphasis on the Potential for Biomass-Derived Syngas*, P.L.S.a. D.C.Dayton, Editor. 2003, NREL National Renewable Energy Labratory: Golden Colorado.
39. Steynberg, A.P., *Introduction to Fischer-Tropsch technology.* Fischer-Tropsch Technology, 2004. 152: p. 1-63.
40. Manzer, L.E., *Catalytic synthesis of alpha-methylene-gamma-valerolactone: a biomass-derived acrylic monomer.* Applied Catalysis a-General, 2004. 272(1-2): p. 249-256.

41. Bozell, J.J., et al., *Production of levulinic acid and use as a platform chemical for derived products.* Resources Conservation and Recycling, 2000. 28(3-4): p. 227-239.
42. Deng, L., et al., *Catalytic Conversion of Biomass-Derived Carbohydrates into gamma-Valerolactone without Using an External H(2) Supply.* Angewandte Chemie-International Edition, 2009. 48(35): p. 6529-6532.
43. Heeres, H., et al., *Combined dehydration/(transfer)-hydrogenation of C6-sugars (D-glucose and D-fructose) to gamma-valerolactone using ruthenium catalysts.* Green Chemistry, 2009. 11(8): p. 1247-1255.
44. Horvath, I.T., et al., *gamma-Valerolactone - a sustainable liquid for energy and carbon-based chemicals.* Green Chemistry, 2008. 10(2): p. 238-242.
45. Lange, J.P., J.Z. Vestering, and R.J. Haan, *Towards 'bio-based' Nylon: conversion of gamma-valerolactone to methyl pentenoate under catalytic distillation conditions.* Chemical Communications, 2007(33): p. 3488-3490.
46. Serrano-Ruiz, J.C., et al., *Conversion of cellulose to hydrocarbon fuels by progressive removal of oxygen.* Applied Catalysis B-Environmental, 2010. 100(1-2): p. 184-189.
47. Donnis, B., et al., *Hydroprocessing of Bio-Oils and Oxygenates to Hydrocarbons. Understanding the Reaction Routes.* Topics in Catalysis, 2009. 52(3): p. 229-240.
48. Mikkonen, S., *Second-generation renewable diesel offers advantages.* Hydrocarbon Processing, 2008. 87(2): p. 63-66.
49. Helwani, Z., et al., *Solid heterogeneous catalysts for transesterification of triglycerides with methanol: A review.* Applied Catalysis a-General, 2009. 363(1-2): p. 1-10.
50. Tran, N.H., et al., *Catalytic upgrading of biorefinery oil from micro-algae.* Fuel, 2010. 89(2): p. 265-274.
51. Melero, J.A., J. Iglesias, and G. Morales, *Heterogeneous acid catalysts for biodiesel production: current status and future challenges.* Green Chemistry, 2009. 11(9): p. 1285-1308.
52. Soares, R.R., D.A. Simonetti, and J.A. Dumesic, *Glycerol as a source for fuels and chemicals by low-temperature catalytic processing.* Angewandte Chemie-International Edition, 2006. 45(24): p. 3982-3985.
53. Furimsky, E., *Catalytic hydrodeoxygenation.* Applied Catalysis a-General, 2000. 199(2): p. 147-190.
54. Huber, G.W., P. O'Connor, and A. Corma, *Processing biomass in conventional oil refineries: Production of high quality diesel by hydrotreating vegetable oils in heavy vacuum oil mixtures.* Applied Catalysis a-General, 2007. 329: p. 120-129.
55. Choudhary, T.V. and C.B. Phillips, *Renewable fuels via catalytic hydrodeoxygenation.* Applied Catalysis a-General, 2011. 397(1-2): p. 1-12.
56. Smith, B., H.C. Greenwell, and A. Whiting, *Catalytic upgrading of tri-glycerides and fatty acids to transport biofuels.* Energy & Environmental Science, 2009. 2(3): p. 262-271.
57. Kalnes, T., T. Marker, and D.R. Shonnard, *Green diesel: A second generation biofuel.* International Journal of Chemical Reactor Engineering, 2007. 5.

58. Stocker, M., *Biofuels and Biomass-To-Liquid Fuels in the Biorefinery: Catalytic Conversion of Lignocellulosic Biomass using Porous Materials.* Angewandte Chemie-International Edition, 2008. 47(48): p. 9200-9211.
59. Kubicka, D., P. Simacek, and N. Zilkova, *Transformation of Vegetable Oils into Hydrocarbons over Mesoporous-Alumina-Supported CoMo Catalysts.* Topics in Catalysis, 2009. 52(1-2): p. 161-168.
60. Jenner, G., *Homogeneous Catalytic Reactions Involving Methyl Formate.* Applied Catalysis a-General, 1995. 121(1): p. 25-44.
61. Pruett, R.L. and R.T. Kacmarcik, *Reactions of Formic-Acid .1. The Iridium-Catalyzed Synthesis of Acetic-Acid from Methyl Formate.* Organometallics, 1982. 1(12): p. 1693-1699.
62. Maki-Arvela, P., et al., *Catalytic deoxygenation of fatty acids and their derivatives.* Energy & Fuels, 2007. 21(1): p. 30-41.
63. Madsen, A.T., et al., *Step Changes and Deactivation Behavior in the Continuous Decarboxylation of Stearic Acid.* Industrial & Engineering Chemistry Research, 2011. 50(19): p. 11049-11058.
64. Murzin, D.Y. and I.L. Simakova, *Kinetic aspects of stereoselectivity in hydrogenation of fatty acids.* Journal of Molecular Catalysis a-Chemical, 2008. 286(1-2): p. 156-161.
65. Snare, M., et al., *Catalytic deoxygenation of unsaturated renewable feedstocks for production of diesel fuel hydrocarbons.* Fuel, 2008. 87(6): p. 933-945.
66. Simakova, I.L., et al., *Hydrogenation of vegetable oils over Pd on nanocomposite carbon catalysts.* Industrial & Engineering Chemistry Research, 2008. 47(19): p. 7219-7225.
67. Lestari, S., et al., *Catalytic Deoxygenation of Stearic Acid and Palmitic Acid in Semibatch Mode.* Catalysis Letters, 2009. 130(1-2): p. 48-51.
68. Do, P.T., et al., *Catalytic Deoxygenation of Methyl-Octanoate and Methyl-Stearate on Pt/Al(2)O(3).* Catalysis Letters, 2009. 130(1-2): p. 9-18.
69. Pestman, R., et al., *Reactions of carboxylic acids on oxides .2. Bimolecular reaction of aliphatic acids to ketones.* Journal of Catalysis, 1997. 168(2): p. 265-272.
70. Idriss, H., et al., *Reactions of Acetaldehyde on Ceo2 and Ceo2-Supported Catalysts.* Journal of Catalysis, 1995. 155(2): p. 219-237.
71. Pham, T.T., et al., *Hydrogenation and Hydrodeoxygenation of 2-methyl-2-pentenal on supported metal catalysts.* Journal of Catalysis, 2009. 266(1): p. 9-14.
72. Kubicka, D. and L. Kaluza, *Deoxygenation of vegetable oils over sulfided Ni, Mo and NiMo catalysts.* Applied Catalysis a-General, 2010. 372(2): p. 199-208.
73. Simacek, P., et al., *Premium quality renewable diesel fuel by hydroprocessing of sunflower oil.* Fuel, 2011. 90(7): p. 2473-2479.
74. Priecel, P., et al., *The role of alumina support in the deoxygenation of rapeseed oil over NiMo-alumina catalysts.* Catalysis Today, 2011. 176(1): p. 409-412.
75. Kubicka, D., M. Bejblova, and J. Vlk, *Conversion of Vegetable Oils into Hydrocarbons over CoMo/MCM-41 Catalysts.* Topics in Catalysis, 2010. 53(3-4): p. 168-178.
76. Simacek, P., et al., *Hydroprocessed rapeseed oil as a source of hydrocarbon-based biodiesel.* Fuel, 2009. 88(3): p. 456-460.

77. *A process for the preparation of aldehydes by hydrogen reduction of carboxylic acids, esters or anhydrides*. 1995
Rhone-Poulenc Chimie

78. Tahara, K., et al., *Liquid-phase hydrogenation of carboxylic acid on supported bimetallic Ru-Sn-alumina catalysts.* Applied Catalysis a-General, 1997. 154(1-2): p. 75-86.
79. Tahara, K., et al., *Liquid phase hydrogenation of carboxylic acid catalyzed by supported bimetallic Ru-Sn-alumina catalyst: Effects of tin compounds in impregnation method.* Journal of Molecular Catalysis a-Chemical, 1996. 110(1): p. L5-L6.
80. Tahara, K., et al., *Liquid-phase hydrogenation of dicarboxylates catalyzed by supported Ru-Sn catalysts.* Catalysis Today, 1996. 28(3): p. 267-272.
81. Miyake, T., et al., *Alcohol synthesis by hydrogenation of fatty acid methyl esters on supported Ru-Sn and Rh-Sn catalysts.* Applied Catalysis a-General, 2009. 364(1-2): p. 108-112.
82. Pallassana, V. and M. Neurock, *Reaction paths in the hydrogenolysis of acetic acid to ethanol over Pd(111), Re(0001), and PdRe alloys.* Journal of Catalysis, 2002. 209(2): p. 289-305.
83. Calaza, F., et al., *Structure and decomposition pathways of vinyl acetate on Pd(111).* Surface Science, 2005. 598(1-3): p. 263-275.
84. Santiago, M.A.N., et al., *Catalytic reduction of acetic acid, methyl acetate, and ethyl acetate over silica-supported copper.* Journal of Catalysis, 2000. 193(1): p. 16-28.
85. Gursahani, K.I., et al., *Reaction kinetics measurements and analysis of reaction pathways for conversions of acetic acid, ethanol, and ethyl acetate over silica-supported Pt.* Applied Catalysis a-General, 2001. 222(1-2): p. 369-392.
86. Xu, L.J. and Y. Xu, *Activation of methyl acetate on Pd(111).* Surface Science, 2010. 604(11-12): p. 887-892.
87. *Oil spill in Gulf Mexico*. 2010.
88. Jensen, F., *Introduction to computational chemistry*. 1999: Wiley.
89. Hohenberg, P. and P.C. Martin, *Superfluid Dynamics in Hydrodynamic (Omegatau Less Than 1) + Collisionless)Omegatau More Than 1) Domains.* Physical Review Letters, 1964. 12(3): p. 69-&.
90. Ratner, M.A. and G.C. Schatz, *An introduction to quantum mechanics in chemistry*. 2001: Prentice Hall.
91. Kohn, W. and L.J. Sham, *Self-Consistent Equations Including Exchange and Correlation Effects.* Physical Review, 1965. 140(4A): p. 1133-&.
92. Cramer, C.J., *Essentials of computational chemistry: theories and models*. 2004: Wiley.
93. Maragakis, P., et al., *Adaptive nudged elastic band approach for transition state calculation.* Journal of Chemical Physics, 2002. 117(10): p. 4651-4658.
94. Sheppard, D., R. Terrell, and G. Henkelman, *Optimization methods for finding minimum energy paths.* Journal of Chemical Physics, 2008. 128(13).
95. Pratt, L.R., *A Statistical-Method for Identifying Transition-States in High Dimensional Problems.* Journal of Chemical Physics, 1986. 85(9): p. 5045-5048.

96. Elber, R. and M. Karplus, *A Method for Determining Reaction Paths in Large Molecules - Application to Myoglobin.* Chemical Physics Letters, 1987. 139(5): p. 375-380.
97. Henkelman, G. and H. Jonsson, *Improved tangent estimate in the nudged elastic band method for finding minimum energy paths and saddle points.* Journal of Chemical Physics, 2000. 113(22): p. 9978-9985.
98. Henkelman, G. and H. Jonsson, *A dimer method for finding saddle points on high dimensional potential surfaces using only first derivatives.* Journal of Chemical Physics, 1999. 111(15): p. 7010-7022.
99. Sholl, D. and J.A. Steckel, *Density Functional Theory: A Practical Introduction*: John Wiley & Sons.
100. Klamt, A., *Cosmo-rs: From Quantum Chemistry to Fluid Phase Thermodynamics And Drug Design*. 2005: Elsevier.
101. Rostof, D.I., *Continuum Solvation Models in Guassian03*. 2008, Australian National University Canberra.
102. Born, M., *Volumes and hydration warmth of ions.* Zeitschrift Fur Physik, 1920. 1: p. 45-48.
103. Kirkwood, J.G., *On the Theory of Strong Electrolyte Solutions.* Journal of Chemical Physics, 1934. 2(11).
104. Kirkwood, J.G., *Theory of Solutions of Molecules Containing Widely Separated Charges with Special Application to Zwitterions.* Journal of Chemical Physics, 1934. 2(7).
105. Onsager, L., *Electric moments of molecules in liquids.* Journal of the American Chemical Society, 1936. 58: p. 1486-1493.
106. Kresse, G. and J. Hafner, *Ab-Initio Molecular-Dynamics for Open-Shell Transition-Metals.* Physical Review B, 1993. 48(17): p. 13115-13118.
107. Kresse, G. and J. Furthmuller, *Efficiency of ab-initio total energy calculations for metals and semiconductors using a plane-wave basis set.* Computational Materials Science, 1996. 6(1): p. 15-50.
108. Kresse, G. and J. Hafner, *Abinitio Molecular-Dynamics for Liquid-Metals.* Physical Review B, 1993. 47(1): p. 558-561.
109. Kresse, G. and D. Joubert, *From ultrasoft pseudopotentials to the projector augmented-wave method.* Physical Review B, 1999. 59(3): p. 1758-1775.
110. Perdew, J.P. and W. Yue, *Accurate and Simple Density Functional for the Electronic Exchange Energy - Generalized Gradient Approximation.* Physical Review B, 1986. 33(12): p. 8800-8802.
111. Perdew, J.P. and Y. Wang, *Accurate and Simple Analytic Representation of the Electron-Gas Correlation-Energy.* Physical Review B, 1992. 45(23): p. 13244-13249.
112. Henkelman, G., B.P. Uberuaga, and H. Jonsson, *A climbing image nudged elastic band method for finding saddle points and minimum energy paths.* Journal of Chemical Physics, 2000. 113(22): p. 9901-9904.
113. Heyden, A., A.T. Bell, and F.J. Keil, *Efficient methods for finding transition states in chemical reactions: Comparison of improved dimer method and partitioned rational function optimization method.* Journal of Chemical Physics, 2005. 123(22).

114. Truhlar, D.G., B.C. Garrett, and S.J. Klippenstein, *Current status of transition-state theory.* Journal of Physical Chemistry, 1996. 100(31): p. 12771-12800.
115. Buzzi-Ferraris, G., "BzzMath: Numerical libraries in C++", Politecnico di Milano: www.chem.polimi.it/homes/gbuzzi.
116. Ahlrichs, R., et al., *Electronic-Structure Calculations on Workstation Computers - the Program System Turbomole.* Chemical Physics Letters, 1989. 162(3): p. 165-169.
117. Treutler, O. and R. Ahlrichs, *Efficient Molecular Numerical-Integration Schemes.* Journal of Chemical Physics, 1995. 102(1): p. 346-354.
118. *TURBOMOLE V6.0 2009, a development of University of Karlsruhe and Forschungszentrum Karlsruhe GmbH, 1989–2007, TURBOMOLE GmbH, since 2007.*
119. Lu, J.M., S. Behtash, and A. Heyden, *Theoretical Investigation of the Reaction Mechanism of the Decarboxylation and Decarbonylation of Propanoic Acid on Pd(111) Model Surfaces.* Journal of Physical Chemistry C, 2012. 116(27): p. 14328-14341.
120. Weigend, F., et al., *RI-MP2: optimized auxiliary basis sets and demonstration of efficiency.* Chemical Physics Letters, 1998. 294(1-3): p. 143-152.
121. Weigend, F. and R. Ahlrichs, *Balanced basis sets of split valence, triple zeta valence and quadruple zeta valence quality for H to Rn: Design and assessment of accuracy.* Physical Chemistry Chemical Physics, 2005. 7(18): p. 3297-3305.
122. Weigend, F., *Accurate Coulomb-fitting basis sets for H to Rn.* Physical Chemistry Chemical Physics, 2006. 8(9): p. 1057-1065.
123. Eichkorn, K., et al., *Auxiliary Basis-Sets to Approximate Coulomb Potentials (Vol 240, Pg 283, 1995).* Chemical Physics Letters, 1995. 242(6): p. 652-660.
124. Eichkorn, K., et al., *Auxiliary basis sets for main row atoms and transition metals and their use to approximate Coulomb potentials.* Theoretical Chemistry Accounts, 1997. 97(1-4): p. 119-124.
125. Von Arnim, M. and R. Ahlrichs, *Performance of parallel TURBOMOLE for density functional calculations.* Journal of Computational Chemistry, 1998. 19(15): p. 1746-1757.
126. Georg Kresse, M.M.a.J.F. *Vienna Ab initio Simulation Package (VASP) user manual*. 2011; Available from: http://cms.mpi.univie.ac.at/vasp/vasp/vasp.html.
127. Knothe, G., *Dependence of biodiesel fuel properties on the structure of fatty acid alkyl esters.* Fuel Processing Technology, 2005. 86(10): p. 1059-1070.
128. Ramos, M.J., et al., *Influence of fatty acid composition of raw materials on biodiesel properties.* Bioresource Technology, 2009. 100(1): p. 261-268.
129. Maier, W.F., et al., *Gas-phase decarboxylation of carboxylic acids.* Chemische Berichte, 1982. 115: p. 808-812.
130. Maki-Arvela, P., et al., *Continuous decarboxylation of lauric acid over Pd/C catalyst.* Fuel, 2008. 87(17-18): p. 3543-3549.
131. Lestari, S., et al., *Catalytic deoxygenation of stearic acid and palmitic acid in semibatch mode.* Catalysis Letters, 2009. 130(1-2): p. 48-51.
132. Simakova, I.L., et al., *Deoxygenation of palmitic and stearic acid over supported Pd catalysts: Effect of metal dispersion.* Applied Catalysis A: General, 2009. 355: p. 100-108.

133. Ford, J.P., J.G. Immer, and H.H. Lamb, *Palladium catalysts for fatty acid deoxygenation: Influence of the support and fatty acid chain length on decarboxylation kinetics.* Topics in Catalysis, 2012. 55: p. 175-184.
134. Boda, L., et al., *Catalytic hydroconversion of tricaprylin and caprylic acid as model reaction for biofuel production from triglycerides* Applied Catalysis A: General, 2010. 374(1-2): p. 158-169.
135. Waugh, K.C., *Prediction of global reaction kinetics by solution of the Arrhenius parameterised component elementary reactions: microkinetic analysis.* Catalysis Today, 1999. 53(2): p. 161-176.
136. Callaghan, C., et al., *An improved microkinetic model for the water gas shift reaction on copper.* Surface Science, 2003. 541(1-3): p. 21-30.
137. Grabow, L.C., et al., *Mechanism of the water gas shift reaction on Pt: First principles, experiments, and microkinetic modeling.* Journal of Physical Chemistry C, 2008. 112: p. 4608-4617.
138. Dahl, S., et al., *Surface science based microkinetic analysis of ammonia synthesis over ruthenium catalysts* Journal of Catalysis, 2000. 192(2): p. 391-399.
139. Kandoi, S., et al., *Prediction of experimental methanol decomposition rates on platinum from first principles.* Topics in Catalysis, 2006. 37: p. 17-28.
140. Lu, J., et al., *Microkinetic modeling of the decarboxylation and decarbonylation of propanoic acid over Pd(1 1 1) model surfaces based on parameters obtained from first principles.* Journal of Catalysis, 2013. 305(0): p. 56-66.
141. Simakova, I., et al., *Catalytic Deoxygenation of C18 Fatty Acids Over Mesoporous Pd/C Catalyst for Synthesis of Biofuels.* Topics in Catalysis, 2011. 54(8-9): p. 460-466.
142. Maki-Arvela, P., et al., *Catalytic Deoxygenation of Tall Oil Fatty Acid over Palladium Supported on Mesoporous Carbon.* Energy & Fuels, 2011. 25(7): p. 2815-2825.
143. Simakova, I., et al., *Decarboxylation of fatty acids over Pd supported on mesoporous carbon.* Catalysis Today, 2010. 150(1-2): p. 28-31.
144. Lestari, S., et al., *Diesel-like Hydrocarbons from Catalytic Deoxygenation of Stearic Acid over Supported Pd Nanoparticles on SBA-15 Catalysts.* Catalysis Letters, 2010. 134(3-4): p. 250-257.
145. Rozmyslowicz, B., et al., *Influence of Hydrogen in Catalytic Deoxygenation of Fatty Acids and Their Derivatives over Pd/C.* Industrial & Engineering Chemistry Research, 2012. 51(26): p. 8922-8927.
146. Grabow, L.C., B. Hvolbaek, and J.K. Norskov, *Understanding Trends in Catalytic Activity: The Effect of Adsorbate-Adsorbate Interactions for CO Oxidation Over Transition Metals.* Topics in Catalysis, 2010. 53(5-6): p. 298-310.
147. Campbell, C.T., *Micro- and macro-kinetics: their relationship in heterogeneous catalysis.* Topics in Catalysis, 1994. 1(3-4): p. 353-366.
148. Campbell, C.T., *Finding the rate-determining step in a mechanism - Comparing DeDonder relations with the "degree of rate control".* Journal of Catalysis, 2001. 204(2): p. 520-524.

149. Stegelmann, C., A. Andreasen, and C.T. Campbell, *Degree of Rate Control: How Much the Energies of Intermediates and Transition States Control Rates.* Journal of the American Chemical Society, 2009. 131(23): p. 8077-8082.
150. Olcay, H., et al., *Aqueous-Phase Hydrogenation of Acetic Acid over Transition Metal Catalysts.* Chemcatchem, 2010. 2(11): p. 1420-1424.
151. *EIA Annual Energy review 2010*. October 2011, URL: http://www.eia.gov/totalenergy/data/annual/pdf/aer.pdf, U.S. Energy Information Administration.
152. *BP Statistical Review of World Energy, URL:http://www.bp.com/content/dam/bp/pdf/statistical-review/statistical_review_of_world_energy_2013.pdf*. 2013, 8, . p. 8.
153. Martin, M.A., *First generation biofuels compete.* New Biotechnology, 2010. 27(5): p. 596-608.
154. *Biomass as Feedstock for a Bioenergy and Bioproducts Industry: The Technical Feasibility of a Billion-Ton Annual Supply* 2005, URL: http://www1.eere.energy.gov/biomass/pdfs/final_billionton_vision_report2.pdf, U.S. Department of Energy.
155. Hummelshoj, J.S., et al., *Density functional theory based screening of ternary alkali-transition metal borohydrides: A computational material design project.* Journal of Chemical Physics, 2009. 131(1).
156. Bertero, M., G. de la Puente, and U. Sedran, *Fuels from bio-oils: Bio-oil production from different residual sources, characterization and thermal conditioning.* Fuel, 2012. 95(1): p. 263-271.
157. Behtash, S., et al., *Solvent effects on the hydrodeoxygenation of propanoic acid over Pd(111) model surfaces.* Green Chemistry, 2014. 16(2): p. 605-616.
158. Lu, J.M., et al., *Microkinetic modeling of the decarboxylation and decarbonylation of propanoic acid over Pd(111) model surfaces based on parameters obtained from first principles.* Journal of Catalysis, 2013. 305: p. 56-66.
159. Lugo-Jose, Y.K., J.R. Monnier, and C.T. Williams, *Gas-phase, catalytic hydrodeoxygenation of propanoic acid, over supported group VIII noble metals: Metal and support effects.* Applied Catalysis a-General, 2014. 469: p. 410-418.
160. Grabow, L.C., B. Hovlbak, and J.K. Norskov, *Understanding trends in catalytic activity: The effect of adsorbate-adsorbate interactions for CO oxidation over transition metals.* Topics in Catalysis, 2010. 53: p. 298-310.
161. Logadottir, A., et al., *The Bronsted-Evans-Polanyi relation and the volcano plot for ammonia synthesis over transition metal catalysts.* Journal of Catalysis, 2001. 197(2): p. 229-231.
162. Wang, S.G., et al., *Universal Bronsted-Evans-Polanyi Relations for C-C, C-O, C-N, N-O, N-N, and O-O Dissociation Reactions.* Catalysis Letters, 2011. 141(3): p. 370-373.
163. Zhong, H. and W. Xianqin, *Hydrocarbon Production from Carboxylic Acids via Catalytic Deoxygenation: Required Catalytic Properties*, in *Novel Materials for Catalysis and Fuels Processing*. 2013, American Chemical Society. p. 301-329.

164. Carpenter, D., et al., *Biomass feedstocks for renewable fuel production: a review of the impacts of feedstock and pretreatment on the yield and product distribution of fast pyrolysis bio-oils and vapors.* Green Chemistry, 2014. 16(2): p. 384-406.
165. O'Neill, B.J., E.I. Gürbüz, and J.A. Dumesic, *Reaction kinetics studies of the conversions of formic acid and butyl formate over carbon-supported palladium in the liquid phase.* Journal of Catalysis, 2012. 290(0): p. 193-201.
166. Ping, E.W., et al., *On the nature of the deactivation of supported palladium nanoparticle catalysts in the decarboxylation of fatty acids.* Applied Catalysis A: General, 2011. 396(1-2): p. 85-90.
167. Simakova, I., et al., *Deoxygenation of palmitic and stearic acid over supported Pd catalysts: Effect of metal dispersion.* Applied Catalysis A: General, 2009. 355(1-2): p. 100-108.
168. Bernas, H., et al., *Deoxygenation of dodecanoic acid under inert atmosphere.* Fuel, 2010. 89(8): p. 2033-2039.
169. Murzin, D.Y., et al., *Production of diesel fuel from renewable feeds: Kinetics of ethyl stearate decarboxylation.* Chemical Engineering Journal, 2007. 134(1-3): p. 29-34.
170. Lestari, S., et al., *Synthesis of Biodiesel via Deoxygenation of Stearic Acid over Supported Pd/C Catalyst.* Catalysis Letters, 2008. 122(3): p. 247-251.
171. Lestari, S., et al., *Catalytic Deoxygenation of Stearic Acid and Palmitic Acid in Semibatch Mode.* Catalysis Letters, 2009. 130(1): p. 48-51.
172. Chia, M. and J.A. Dumesic, *Liquid-phase catalytic transfer hydrogenation and cyclization of levulinic acid and its esters to g-valerolactone over metal oxide catalysts.* Chemical Communications, 2011. 47(44): p. 12233-12235.
173. Jacobson, K., K.C. Maheria, and A. Kumar Dalai, *Bio-oil valorization: A review.* Renewable and Sustainable Energy Reviews, 2013. 23(0): p. 91-106.
174. Mohammad, M., et al., *Overview on the production of paraffin based-biofuels via catalytic hydrodeoxygenation.* Renewable and Sustainable Energy Reviews, 2013. 22(0): p. 121-132.
175. Furimsky, E., *Hydroprocessing challenges in biofuels production.* Catalysis Today, 2013. 217(0): p. 13-56.
176. Pham, T.N., D. Shi, and D.E. Resasco, *Evaluating strategies for catalytic upgrading of pyrolysis oil in liquid phase.* Applied Catalysis B: Environmental, 2014. 145(0): p. 10-23.
177. Mäki-Arvela, P.i., et al., *Catalytic Deoxygenation of Tall Oil Fatty Acid over Palladium Supported on Mesoporous Carbon.* Energy & Fuels, 2011. 25(7): p. 2815-2825.
178. Lugo-José, Y.K., J.R. Monnier, and C.T. Williams, *Gas-phase, catalytic hydrodeoxygenation of propanoic acid, over supported group VIII noble metals: Metal and support effects.* Applied Catalysis A: General, 2014. 469(0): p. 410-418.
179. Lestari, S., et al., *Catalytic Deoxygenation of Stearic Acid in a Continuous Reactor over a Mesoporous Carbon-Supported Pd Catalyst.* Energy & Fuels, 2009. 23(8): p. 3842-3845.

180. Ping, E.W., et al., *Highly dispersed palladium nanoparticles on ultra-porous silica mesocellular foam for the catalytic decarboxylation of stearic acid.* Microporous and Mesoporous Materials, 2010. 132(1–2): p. 174-180.
181. Snåre, M., et al., *Heterogeneous Catalytic Deoxygenation of Stearic Acid for Production of Biodiesel.* Industrial & Engineering Chemistry Research, 2006. 45(16): p. 5708-5715.
182. Carr, R.W., *Chapter 3 Elements of Chemical Kinetics*, in *Comprehensive Chemical Kinetics*, W.C. Robert, Editor. 2007, Elsevier. p. 43-99.
183. Marin, G.B. and G.S. Yablonsky, *Kinetics of chemical reactions : decoding complexity*. 2011, Weinheim, Germany: Wiley-VCH. xvii, 428 p.
184. Behtash, S., et al., *Solvent effects on the hydrodeoxygenation of propanoic acid over Pd(111) model surfaces.* Green Chemistry, 2014. 16(2): p. 605-616.
185. Davis, J.L. and M.A. Barteau, *Reactions of carboxylic acids on the Pd(111)-(2 × 2)O surface: multiple roles of surface oxygen atoms.* Surface Science, 1991. 256(1–2): p. 50-66.
186. Davis, J.L. and M.A. Barteau, *Hydrogen bonding in carboxylic acid adlayers on Pd(111): evidence for catemer formation.* Langmuir, 1989. 5(6): p. 1299-1309.
187. Tamaru, K., *Dynamic Relaxation Methods in Heterogeneous Catalysis*, in *Catalysis*, J.R. Anderson and M. Boudart, Editors. 1991, Springer Berlin Heidelberg. p. 87-129.
188. Neurock, M., *The microkinetics of heterogeneous catalysis. By J. A. Dumesic, D. F. Rudd, L. M. Aparicio, J. E. Rekoske, and A. A. Treviño, ACS Professional Reference Book, American Chemical Society, Washington, DC, 1993, 315 pp.* AIChE Journal, 1994. 40(6): p. 1085-1087.
189. Happel, J., *Isotopic assessment of heterogeneous catalysis*. 1986: Academic Press.
190. Sommer, J. and S. Walspurger, *Deuterium-Labelling in Mechanistic Studies on Heterogeneous Acid—Base Catalysts.* ChemInform, 2007. 38(4): p. 1-29.
191. Bond, G.C., et al., *Hydrogenation of olefins. Part 3.-Reaction of ethylene and of propylene with deuterium over alumina-supported palladium and rhodium.* Transactions of the Faraday Society, 1966. 62(0): p. 443-454.
192. Eyring, H. and M. Polanyi, *Concerning simple gas reactions.* Zeitschrift Fur Physikalische Chemie-Abteilung B-Chemie Der Elementarprozesse Aufbau Der Materie, 1931. 12(4): p. 279-311.
193. Bigeleisen, J. and M.G. Mayer, *Calculation of Equilibrium Constants for Isotopic Exchange Reactions.* The Journal of Chemical Physics, 1947. 15(5): p. 261-267.
194. Winkler, F.J., *Reaction Rates of Isotopic Molecules. Von L. Melander und W. H. Saunders, Jr. Wiley, New York 1980. XIV, 391 S., geb. £ 16.30.* Angewandte Chemie, 1981. 93(2): p. 220-220.
195. Kresse, G. and J. Hafner, *Abinitio Molecular-Dynamics for Liquid-Metals*, in *Physical Review B*. 1993. p. 558-561.
196. Stegelmann, C., A. Andreasen, and C.T. Campbell, *Degree of Rate Control: How Much the Energies of Intermediates and Transition States Control Rates (vol 131, pg 8077, 2009).* Journal of the American Chemical Society, 2009. 131(37): p. 13563-13563.
197. Truhlar, D.G., W.L. Hase, and J.T. Hynes, *Current Status of Transition-State Theory*. Journal of Physical Chemistry, 1983. 87(15): p. 2664-2682.

198. Eyring, H., *The activated complex in chemical reactions.* Journal of Chemical Physics, 1935. 3(2): p. 107-115.
199. Tomasi, R.A., *A Spectrum of Spectral Problems: Supplement*. 1994: Sunbelt R & T, Incorporated.
200. Behtash, S., et al., *Solvent effects on the hydrodeoxygenation of propanoic acid over Pd(111) model surfaces (vol 16, pg 605, 2014).* Green Chemistry, 2014. 16(9): p. 4427-4428.
201. *BP Statistical Review of World Energy*. June 2012, URL: http://www.bp.com/assets/bp_internet/globalbp/globalbp_uk_english/reports_and_publications/statistical_energy_review_2011/STAGING/local_assets/pdf/statistical_review_of_world_energy_full_report_2012.pdf.
202. Behtash, S., J. Lu, and A. Heyden, *Theoretical investigation of the hydrodeoxygenation of methyl propionate over Pd (111) model surfaces.* Catalysis Science & Technology, 2014. 4: p. 3981.
203. Lugo-Jose, Y.K., et al., *Hydrodeoxygenation of propanoic acid over silica-supported palladium: effect of metal particle size.* Catalysis Science & Technology, 2014, . Advance article, DOI: 10.1039/c4cy00605d, URL: http://dx.doi.org/10.1039/C4CY00605D.
204. Ahmed, F., et al., *Comparison of reactivity on step and terrace sites of Pd(3 3 2) surface for the dissociative adsorption of hydrogen: A quantum chemical molecular dynamics study.* Applied Surface Science, 2011. 257(24): p. 10503-10513.
205. Yang, B., et al., *Influence of surface structures, subsurface carbon and hydrogen, and surface alloying on the activity and selectivity of acetylene hydrogenation on Pd surfaces: A density functional theory study.* Journal of Catalysis, 2013. 305: p. 264-276.
206. Bengaard, H.S., et al., *Steam reforming and graphite formation on Ni catalysts.* Journal of Catalysis, 2002. 209(2): p. 365-384.
207. Kratzer, P., et al., *Highly site-specific H-2 adsorption on vicinal Si(001) surfaces.* Physical Review Letters, 1998. 81(25): p. 5596-5599.
208. Dahl, S., et al., *Role of steps in N-2 activation on Ru(0001).* Physical Review Letters, 1999. 83(9): p. 1814-1817.
209. Hammer, B., *Reactivity of a stepped surface - NO dissociation on Pd(211).* Faraday Discussions, 1998. 110: p. 323-333.
210. Hammer, B. and J.K. Norskov, *Why Gold Is the Noblest of All the Metals.* Nature, 1995. 376(6537): p. 238-240.
211. Wang, S., et al., *Universal transition state scaling relations for (de)hydrogenation over transition metals.* Physical Chemistry Chemical Physics, 2011. 13(46): p. 20760-20765.
212. Somorjai, G.A., *Introduction to surface chemistry and catalysis*. 1994, New York: Wiley. xxiv, 667 p.
213. Abild-Pedersen, F., et al., *Methane activation on Ni(111): Effects of poisons and step defects.* Surface Science, 2005. 590(2-3): p. 127-137.
214. Belelli, P.G., R.M. Ferullo, and N.J. Castellani, *Unsaturated hydrocarbons adsorbed on low coordinated Pd surface: A periodic DFT study.* Surface Science, 2010. 604(3-4): p. 386-395.

215. Tian, P.F., et al., *Density functional theory study of direct synthesis of H2O2 from H-2 and O-2 on Pd(111), Pd(100), and Pd(110) surfaces.* Chinese Journal of Catalysis, 2013. 34(5): p. 1002-1012.
216. Henkelman, G. and H. Jonsson, *A dimer method for finding saddle points on high dimensional potential surfaces using only first derivatives.* Journal of Chemical Physics, 1999. 111: p. 7010-7022.
217. Olsen, R.A., et al., *Comparison of methods for finding saddle points without knowledge of the final states.* Journal of Chemical Physics, 2004. 121: p. 9776-9792.
218. Heyden, A., A.T. Bell, and F.J. Keil, *Efficient Methods for Finding Transition States in Chemical Reactions Comparison of modified dimer method and partitioned rational function optimization method.* Journal of Chemical Physics, 2005. 123: p. 224101-14.
219. Lu, J.M., et al., *Microkinetic modeling of the decarboxylation and decarbonylation of propanoic acid over Pd(111) model surfaces based on parameters obtained from first principles.* Journal of Catalysis, 2013. 305: p. 56-66.
220. Xu, L.J. and Y. Xu, *Effect of Pd surface structure on the activation of methyl acetate.* Catalysis Today, 2011. 165(1): p. 96-105.
221. Grimme, S., et al., *A consistent and accurate ab initio parametrization of density functional dispersion correction (DFT-D) for the 94 elements H-Pu.* Journal of Chemical Physics, 2010. 132: p. 154104.
222. Vanhardeveld.R and F. Hartog, *Statistics of Surface Atoms and Surface Sites on Metal Crystals.* Surface Science, 1969. 15(2): p. 189-230.
223. *BP Statistical Review of World Energy* June 2012, URL: http://www.bp.com/assets/bp_internet/globalbp/globalbp_uk_english/reports_and_publications/statistical_energy_review_2011/STAGING/local_assets/pdf/statistical_review_of_world_energy_full_report_2012.pdf.
224. Monnier, J., et al., *Hydrodeoxygenation of oleic acid and canola oil over alumina-supported metal nitrides.* Applied Catalysis A-General, 2010. 382(2): p. 176-180.
225. Weingarten, R., et al., *Design of solid acid catalysts for aqueous-phase dehydration of carbohydrates: The role of Lewis and Bronsted acid sites.* Journal of Catalysis, 2011. 279(1): p. 174-182.
226. Wettstein, S.G., et al., *Production of levulinic acid and gamma-valerolactone (GVL) from cellulose using GVL as a solvent in biphasic systems.* Energy & Environmental Science, 2012. 5(8): p. 8199-8203.
227. Boda, L., et al., *Catalytic hydroconversion of tricaprylin and caprylic acid as model reaction for biofuel production from triglycerides.* Applied Catalysis A-General, 2010. 374(1-2): p. 158-169.
228. Ford, J.P., J.G. Immer, and H.H. Lamb, *Palladium Catalysts for Fatty Acid Deoxygenation: Influence of the Support and Fatty Acid Chain Length on Decarboxylation Kinetics.* Topics in Catalysis, 2012. 55(3-4): p. 175-184.
229. Immer, J.G., M.J. Kelly, and H.H. Lamb, *Catalytic reaction pathways in liquid-phase deoxygenation of C18 free fatty acids.* Applied Catalysis A-General, 2010. 375(1): p. 134-139.

230. Arend, M., et al., *Catalytic deoxygenation of oleic acid in continuous gas flow for the production of diesel-like hydrocarbons.* Applied Catalysis A-General, 2011. 399(1-2): p. 198-204.
231. Vispute, T.P., et al., *Renewable Chemical Commodity Feedstocks from Integrated Catalytic Processing of Pyrolysis Oils.* Science, 2010. 330(6008): p. 1222-1227.
232. Faheem, M., S. Suthirakun, and A. Heyden, *New Implicit Solvation Scheme for Solid Surfaces.* Journal of Physical Chemistry C, 2012. 116(42): p. 22458-22462.
233. Klamt, A., *Conductor-Like Screening Model for Real Solvents - a New Approach to the Quantitative Calculation of Solvation Phenomena.* Journal of Physical Chemistry, 1995. 99(7): p. 2224-2235.
234. Klamt, A., et al., *Refinement and parametrization of COSMO-RS.* Journal of Physical Chemistry A, 1998. 102(26): p. 5074-5085.
235. Klamt, A., *COSMO-RS: From Quantum Chemistry to Fluid PhaseThermodynamics and Drug Design*. 2005: Elsevier Science.
236. Smith, J.M., H.C. Van Ness, and M.M. Abbott, *Introduction to chemical engineering thermodynamics*. 2005: McGraw-Hill.
237. Blaser, H.U., H.P. Jalett, and J. Wiehl, *Enantioselective Hydrogenation of Alpha-Ketoesters with Cinchona-Modified Platinum Catalysts - Effect of Acidic and Basic Solvents and Additives.* Journal of Molecular Catalysis, 1991. 68(2): p. 215-222.
238. Wehrli, J.T., et al., *Enantioselective Hydrogenation of Alpha-Ketoesters - Influence of Reaction Medium and Conversion.* Journal of Molecular Catalysis, 1989. 57(2): p. 245-257.
239. Gilbert, L. and C. Mercier, *Solvent Effects in Heterogeneous Catalysis - Application to the Synthesis of Fine Chemicals.* Heterogeneous Catalysis and Fine Chemicals Iii, 1993. 78: p. 51-66.
240. Singh, U.K. and M.A. Vannice, *Kinetics of liquid-phase hydrogenation reactions over supported metal catalysts - a review.* Applied Catalysis a-General, 2001. 213(1): p. 1-24.
241. Koopman, P.G.J., et al., *Solvent-Reactant-Support Interactions in Liquid-Phase Hydrogenation.* Recueil Des Travaux Chimiques Des Pays-Bas-Journal of the Royal Netherlands Chemical Society, 1981. 100(4): p. 156-161.
242. Wauquier, J.P. and J.C. Jungers, *La Cinetique Quantitative En Catalyse Heterogene - Linfluence Du Milieu Sur Lactivite Et La Selectivite Du Catalyseur.* Bulletin De La Societe Chimique De France, 1957(8-9): p. 1280-1288.
243. Cerveny, L., M. Kuncova, and V. Ruzicka, *Effect of Composition of the Solvent on the Selectivity of Competitive Hydrogenation of 2-Methyl-3-Butene-2-Ol and 1-Hexene.* Reaction Kinetics and Catalysis Letters, 1982. 19(1-2): p. 219-222.
244. Rajadhyaksha, R.A. and S.L. Karwa, *Solvent Effects in Catalytic-Hydrogenation.* Chemical Engineering Science, 1986. 41(7): p. 1765-1770.
245. Kozuch, S. and S. Shaik, *A combined kinetic-quantum mechanical model for assessment of catalytic cycles: Application to cross-coupling and Heck reactions.* Journal of the American Chemical Society, 2006. 128(10): p. 3355-3365.
246. Christiansen, J.A., *The Elucidation of Reaction Mechanisms by the Method of Intermediates in Quasi-Stationary Concentrations.* Advances in Catalysis, 1953. 5: p. 311-353.

247. Boudart, M., *Kinetics of chemical processes*. Prentice-Hall international series in the physical and chemical engineering sciences. 1968, Englewood Cliffs, N.J.,: Prentice-Hall. 67-71.
248. Dumesic, J.A., *Analyses of reaction schemes using De Donder relations.* Journal of Catalysis, 1999. 185(2): p. 496-505.
249. Dumesic, J.A., *Reply to finding the rate-determining step in a mechanism: Comparing DeDonder relations with the "degree of rate control"*. Journal of Catalysis, 2001. 204(2): p. 525-529.
250. Baranski, A., *On the usefulness of Campbell's concept of the rate-determining step.* Solid State Ionics, 1999. 117(1-2): p. 123-128.
251. Kozuch, S. and S. Shaik, *Kinetic-quantum chemical model for catalytic cycles: The Haber-Bosch process and the effect of reagent concentration.* Journal of Physical Chemistry A, 2008. 112(26): p. 6032-6041.
252. Lewis, G.N. and M. Randall, *Thermodynamics and the free energy of chemical substances*. 1st ed. 1923, New York: McGraw-Hill. xxiii, 653 p.
253. Smith, J.M., H.C. Van Ness, and M.M. Abbott, *Introduction to chemical engineering thermodynamics*. 7th ed. McGraw-Hill chemical engineering series. 2005, Boston: McGraw-Hill. xviii, 817 p.
254. Redlich, O., A.T. Kister, and C.E. Turnquist, *Thermodynamics of Solutions - Analysis of Vapor-Liquid Equilibria.* Chemical Engineering Progress Symposium Series, 1952. 48(2): p. 49-61.
255. Wilson, G.M., *Vapor-Liquid Equilibrium .11. New Expression for Excess Free Energy of Mixing.* Journal of the American Chemical Society, 1964. 86(2): p. 127-130.
256. Fredenslund, A. and P. Rasmussen, *Correlation of Pure Component Gibbs Energy Using Unifac Group Contribution.* Aiche Journal, 1979. 25(1): p. 203-205.
257. Fredenslund, A., et al., *Computerized Design of Multicomponent Distillation-Columns Using Unifac Group Contribution Method for Calculation of Activity-Coefficients.* Industrial & Engineering Chemistry Process Design and Development, 1977. 16(4): p. 450-462.
258. Abrams, D.S. and J.M. Prausnitz, *Statistical Thermodynamics of Liquid-Mixtures - New Expression for Excess Gibbs Energy of Partly or Completely Miscible Systems.* Aiche Journal, 1975. 21(1): p. 116-128.

APPENDIX A: PERSMISSION TO REPRINT

ELSEVIER LICENSE
TERMS AND CONDITIONS

Nov 09, 2014

This is a License Agreement between Sina Behtash ("You") and Elsevier ("Elsevier") provided by Copyright Clearance Center ("CCC"). The license consists of your order details, the terms and conditions provided by Elsevier, and the payment terms and conditions.

All payments must be made in full to CCC. For payment instructions, please see information listed at the bottom of this form.

Supplier	Elsevier Limited The Boulevard,Langford Lane Kidlington,Oxford,OX5 1GB,UK
Registered Company Number	1982084
Customer name	Sina Behtash
Customer address	218 S. Marion St. Apt. B COLUMBIA, SC 29205
License number	3504980750506
License date	Nov 09, 2014
Licensed content publisher	Elsevier
Licensed content publication	Journal of Catalysis
Licensed content title	Microkinetic modeling of the decarboxylation and decarbonylation of propanoic acid over Pd(111) model surfaces based on parameters obtained from first principles
Licensed content author	Jianmin Lu,Sina Behtash,Muhammad Faheem,Andreas Heyden
Licensed content date	September 2013
Licensed content volume number	305
Licensed content issue number	n/a
Number of pages	11
Start Page	56
End Page	66
Type of Use	reuse in a thesis/dissertation

Figure A1. Evidence for the permission to reprint. Lu, J. M.; Behtash, S.; Faheem, M.; Heyden, A. Journal of Catalysis 2013, 305, 56.

Figure A2. Evidence for the permission to reprint. Lu, J. M.; Behtash, S.; Heyden, A. Journal of Physical Chemistry C 2012, 116, 14328.

RSC | Advancing the Chemical Sciences

Royal Society of Chemistry
Thomas Graham House
Science Park
Milton Road
Cambridge
CB4 0WF

Tel: +44 (0)1223 420 066
Fax: +44 (0)1223 423 623
Email: contracts-copyright@rsc.org

www.rsc.org

Acknowledgements to be used by RSC authors

Authors of RSC books and journal articles can reproduce material (for example a figure) from the RSC publication in a non-RSC publication, including theses, without formally requesting permission providing that the correct acknowledgement is given to the RSC publication. This permission extends to reproduction of large portions of text or the whole article or book chapter when being reproduced in a thesis.

The acknowledgement to be used depends on the RSC publication in which the material was published and the form of the acknowledgements is as follows:

- For material being reproduced from an article in *New Journal of Chemistry* the acknowledgement should be in the form:
  - [Original citation] - Reproduced by permission of The Royal Society of Chemistry (RSC) on behalf of the Centre National de la Recherche Scientifique (CNRS) and the RSC
- For material being reproduced from an article *Photochemical & Photobiological Sciences* the acknowledgement should be in the form:
  - [Original citation] - Reproduced by permission of The Royal Society of Chemistry (RSC) on behalf of the European Society for Photobiology, the European Photochemistry Association, and RSC
- For material being reproduced from an article in *Physical Chemistry Chemical Physics* the acknowledgement should be in the form:
  - [Original citation] - Reproduced by permission of the PCCP Owner Societies
- For material reproduced from books and any other journal the acknowledgement should be in the form:
  - [Original citation] - Reproduced by permission of The Royal Society of Chemistry

The acknowledgement should also include a hyperlink to the article on the RSC website.

The form of the acknowledgement is also specified in the RSC agreement/licence signed by the corresponding author.

Except in cases of republication in a thesis, this express permission does not cover the reproduction of large portions of text from the RSC publication or reproduction of the whole article or book chapter.

A publisher of a non-RSC publication can use this document as proof that permission is granted to use the material in the non-RSC publication.

VAT Registration Number: GB 342 1764 71 Registered Charity Number: 207890

Figure A3. Evidence for the permission to reprint.
Behtash, S.; Lu, J.; Faheem, M.; Heyden, A. Green Chemistry 2014, 16, 605.
Behtash, S.; Lu, J.; Heyden, A. *Catalysis Science & Technology* 2014, *4*, 3981.